2003

A Planar Laser-induced Fluorescence Study on the Effects of Unsteadiness and Fuel Lewis Number in Hydrogen Laminar Diffusion Flames

Marcos Chaos
University of Central Florida

A PLANAR LASER–INDUCED FLUORESCENCE STUDY ON THE EFFECTS OF UNSTEADINESS AND FUEL LEWIS NUMBER IN HYDROGEN LAMINAR DIFFUSION FLAMES

by

MARCOS CHAOS

B.S. University of Central Florida, 1998
M.S. University of Central Florida, 2000

A dissertation submitted in partial fulfillment of the requirements
for the degree of Doctor of Philosophy
in the Department of Mechanical, Materials, and Aerospace Engineering
in the College of Engineering and Computer Science
at the University of Central Florida
Orlando, Florida

Fall Term
2003

Major Professor: Dr. Ruey-Hung Chen

ABSTRACT

Studies on the effect of transport properties coupled with the interaction of fluid dynamics and combustion in acoustically forced laminar hydrogen jet diffusion flames have been performed using the planar laser-induced fluorescence (PLIF) technique. These unsteady diffusion flames are of particular interest because they are reproducible turbulent-like events that can be investigated to gain insight into turbulent combustion. Results reported herein add to the ongoing effort of understanding the complex transport processes taking place in the flames encountered in most modern heat-producing and power-producing devices.

Fuel transport properties (i.e. fuel Lewis number, Le_F) were varied by fuel dilution with various levels of helium (He) or argon (Ar). The fuel stream of Burke-Schumann type hydrogen flames was acoustically excited by using a loudspeaker and the two-dimensional OH and temperature fields were measured. PLIF measurements were performed using an intricate two-laser, two-camera system; digital image analysis was implemented to reduce the large image data set obtained.

The temperature of the unsteady flames departed significantly from the steady-state temperature as predicted by previous researchers. It was found that, regardless of Le_F, unsteady He-diluted flames had maximum flame temperatures at some point during the speaker oscillation that were always higher than the maximum temperatures of the

H_2-Ar flames. This was contrary to the trends seen in steady flames. An increased H_2 mass flux to the flame zone in the unsteady H_2-He flames was the reason for this observation since mass diffusion becomes important in the driven flames due to increased mass gradients and the difference in diffusivity of hydrogen in the diluents used.

Low turbulence intensities (i.e. low frequency) allowed the flames to respond steadily to the changing flowfield. The structure of the reaction zone of unsteady flames at this low frequency was altered (i.e. stretched or compressed) slightly and, in general, these flames resembled the steady flames structurally. At high frequency, however, the flames responded to the imposed flow oscillation by considerable reaction zone stretch/compression. Results obtained from the present experiments suggest that, depending on the Lewis number, the flame temperature responds differently to the stretch imparted on the flame by the unsteady flowfield. These Lewis number effects were evidenced by both the low and high frequency flames; however, they were most obvious in the high frequency cases. The temperature of flames with $Le_F \geq 1$ increased/decreased when the reaction zone thickened/thinned. On the other hand, flames with $Le_F < 1$ increased/decreased in temperature when the reaction zone thinned/thickened. These trends competed with the thermal and mass transport processes present in the high-curvature regions of the flames.

A mis padres, por todos sus sacrificios, con cariño.

ACKNOWLEDGEMENTS

Foremost, I would like to express my gratitude to my advisor, Dr. Ruey-Hung Chen, for his support, patience, and encouragement throughout my graduate studies. His technical and editorial advice was essential to the completion of this dissertation. He has taught me innumerable lessons and insights on the workings of academic research in general. It is not often that one can work with an advisor and colleague that always finds the time for listening to the little problems and roadblocks that unavoidably crop up in the course of performing research. I would also like to thank the members of my committee, Dr. Jay Kapat, Dr. Kevin D. Belfield, Dr. Lee Chow, and Dr. Michael H. Koenig for reading previous drafts of this dissertation and providing many valuable comments that improved the overall presentation and contents of this work.

My most sincere thanks go to Dr. William L. Roberts and Dr. Eric J. Welle for the use of their laser facility at North Carolina State University, which was vital to this research. Their guidance in a field that was relatively new to me is surely appreciated. I am also very appreciative of the many interesting email discussions relating to OH spectroscopy with Dr. Jerry M. Seitzman of Georgia Tech. In addition, I would like to acknowledge my colleagues at the Combustion Laboratory and the rest of the Mechanical, Materials, and Aerospace Engineering Department and thank them for contributing to such an inspiring and pleasant atmosphere.

Thanks to my wife Suzy for being by my side through this endeavor. My parents and my brother and sister-in-law, Carmen, José, Abel, and Vanessa, as well as the rest of my family receive my deepest gratitude and love for their dedication and the many years of support during my undergraduate and graduate studies that provided the foundation for this work. At last, to my cousins and nephews, Conchi, Chris, Amerigo, and Francesco, thanks for supporting me; you have been my family and my home away from home.

This work was supported, in part, by Siemens-Westinghouse Power Corporation. Marcos Chaos was awarded the 2000-2003 Siemens-Westinghouse Doctoral Fellowship.

TABLE OF CONTENTS

LIST OF FIGURES

LIST OF TABLES

NOMENCLATURE

A	Einstein coefficient First excited state designation
A_B	Burner area
A_b	Thermocouple bead area
B	Einstein coefficient
b	Absorption/emission rate constant
B_v	Molecular constant
C	Curvature
c	Speed of light (299,792,458 m/s)
CARS	Coherent anti-Stokes Raman spectroscopy
C_p	Heat capacity
D	Burner diameter Mass diffusivity
d	Thermocouple bead diameter
Da	Damköhler number
dA	Differential area
DFWM	Degenerate four-wave mixing
D_v	Molecular constant
E	Energy

F, f	Angular momentum energies for excited and ground states Fluorescence Rotational manifolds
F_{i-j}	View factor from surface i to surface j
FWHM	Full Width Half Magnitude
g	Degeneracy
G	Vibrational energy
h	Convective heat transfer coefficient Planck's constant ($6.62606876 \times 10^{-34}$ J s)
HAB	Height Above Burner
I	Irradiance
J	Angular momentum quantum number
K	Transition notation
k	Boltzmann constant ($1.3806503 \times 10^{-23}$ J/K) Thermal conductivity
l	Electron orbital angular momentum quantum number Separation distance projection
L	Radial distance Total orbital electronic angular momentum quantum number
LDV	Laser Doppler Velocimetry
Le	Lewis number
Le_F	Fuel Lewis number
LIF	Laser–induced fluorescence
LII	Laser–induced incandescence
m	Number of measurements (Chauvenet's criterion)

m_l	Axial orbital angular momentum quantum number
m_s	Axial spin quantum number
n	Principal quantum number
N	Total angular momentum, apart from spin, quantum number
N_a	Total number of molecules
Nd: YAG	Neodymium Yttrium Aluminum Garnet
N_e	Number of electrons
N_i	Number of molecules in state I
N_R	Population ratio
Nu	Nusselt number
PLIF	Planar laser–induced fluorescence
Pr	Prandtl number
Q	Partition Function Quenching Rate
q_B	Burner heat flux
q_b	Thermocouple bead heat flux
Q_e	Electronic partition function
Q_r	Rotational partition function
Q_v	Vibrational partition function
r	Radial distance from fuel tube axis
r_{max}	Maximum radial flame location
R	Rotational angular momentum quantum number Fuel tube radius

Re	Reynolds number
RET	Rotational energy transfer
s	Electron spin quantum number
S	Separation distance Total electronic spin quantum number
SLM	Standard liters per minute
T	Temperature
T_{ad}	Adiabatic temperature
T_B	Burner temperature
T_b	Thermocouple bead temperature
T_e	Electronic energy
T_f	Film temperature
T_F	Flame temperature
T_{max}	Maximum temperature
T_∞	Temperature of surroundings
TTL	Transistor-transistor logic
U	Velocity
u'	Velocity fluctuation
v	Vibrational quantum number
V	Voltage
VET	Vibrational energy transfer
X	Ground state designation
x	Radial distance

x_e	Molecular constant (vibrational anharmonicity)
y_v	Molecular constant
Y_v	Molecular constant

Greek

α	Thermal diffusivity Transition notation
β	Transition notation
$\Delta\varepsilon$	Energy separation
ε	Emissivity
ϕ	Angle between *l* and *x* Phase angle (speaker oscillation)
Λ	Quantum number of total electronic angular momentum
λ	Wavelength
μ	Viscosity
Π	OH ground state
θ	Elevation angle
ρ	Density
Σ	Quantum number of total spin along internuclear molecular axis OH first excited level
σ	Stefan-Boltzmann constant (5.6704×10^{-8} W m^{-2} K^{-4})
Ω	Quantum number of total electronic angular momentum along internuclear molecular axis

ω_e	Molecular constant (vibrational frequency)
ξ	Fractional area
Ψ	Transition notation

1 INTRODUCTION

1.1 Motivation and Overview of Research

Combustion of gaseous and liquid fuels is the primary energy source for most modern heat-producing and power-producing devices supporting the increasing demands of the ever-growing world population. Examples include industrial boilers, internal combustion engines, and gas turbines. The vast majority of these devices involve nonpremixed turbulent combustion, which is inherently complex due to the interaction of hydrodynamics and chemical kinetics. A jet diffusion flame is one of the simplest and better understood examples of nonpremixed combustion. Indeed, turbulent jet diffusion flames are used in many of the aforementioned devices.

Turbulence can be considered as an ensemble of vortices of different sizes and frequencies and, therefore, different length and time scales. This conceptual description has given rise to a variety of "flamelet" models for turbulent flames (Peters, 1984; Peters, 1986). A turbulent flame can be considered a collection of flamelets strained by the turbulent vortices, which are intrinsically unsteady in nature. A considerable amount of research has been conducted on unsteady jet flames in order to model and understand turbulent flame structure. If the turbulence in a jet flame can be controlled, then the

mixing, combustion, radiation, and generation of pollutants may possibly be altered favorably.

The use of hydrogen (H_2) in combustion devices is helpful in reducing pollutant emission since CO, CO_2 (greenhouse gas), and unburned hydrocarbon particulates such as soot are eliminated. Hydrogen also reduces emissions of oxides of nitrogen since the prompt NO formation path is eliminated (Turns, 1995; Glassman, 1996). Hydrogen is one of the most abundant elements in the universe. However, it is found mostly bound to other elements to form more stable molecules (such as water). Before it can be used as fuel, H_2 needs to be generated through different processes such as electrolysis, natural gas reforming or gasification of solid fuels like coal or biomass. The energy input for these processes is high making the use of H_2 not cost effective. Current technological improvements are reducing these costs, however, making H_2 more attractive in future applications.

Temperature and flame structure are fundamental parameters that determine chemical reaction rates and formation of pollutants such as NO_x. Here, NO_x refers to the sum of both common oxides of nitrogen, NO and NO_2. Fuel dilution with inert species or flue gas is a frequently used method to control and reduce flame temperature and nitric oxide emission in order to meet the increasing emission restrictions imposed by many industrialized countries. Dilution, however, may change thermal and mass transport properties of the fuel (i.e. Lewis number), which might either enhance or adversely affect the flame temperature. Flame unsteadiness (i.e. turbulence) affects flame structure (i.e. curvature and strain) and changes the way fuel and oxidizer reach the flame zone, which

may further modify the flame temperature when coupled with dilution. For example, a concave/convex flame zone (with respect to the fuel) may reduce/increase the flame temperature depending on whether the fuel Lewis number is greater/less than unity (Takagi *et. al.*, 1996). Similarly, unsteadiness is known to modify the flame temperature (Cuenot and Poinsot, 1996; Takahashi and Katta, 1996). However, the coupled effect of unsteadiness and fuel Lewis number is not thoroughly known.

In this study, a laminar hydrogen jet diffusion flame was pulsed at different frequencies and amplitudes (and, thus, various time and length scales). The flame, thus, was locally under the stretch/curvature effects of the instability artificially introduced. Different inert dilution levels were used to vary the thermal and mass transport properties of the fuel in an effort to better understand the coupled effect of fuel Lewis number and flame unsteadiness. Quantitative two-dimensional temperature and OH concentration fields were obtained using planar laser-induced fluorescence of the OH radical, which is present in high temperature regions. The results of this work contribute to the understanding of the role that unsteadiness, flow structure, and thermo-diffusive effects play in jet flames and may provide helpful data to validate turbulent flame models.

1.2 Background

Combustion processes can be generally categorized into premixed and non-premixed flames. In premixed flames, the reacting gases (i.e. fuel and oxidizer) are homogeneously mixed before they are ignited. Non-premixed flames (i.e. diffusion

flames) can be best described as the combustion process controlled by the diffusion of fuel and oxidizer into each other; reaction takes place while the reactants come in contact. Since the inception of the Burke-Schumann laminar flame-sheet model (Burke and Schumann, 1928), significant progress has been made in understanding laminar diffusion flames in the last few decades (see, for example, the review article of Williams, 2000). The understanding of laminar nonpremixed flames provides a basis for studies of important phenomena such as flame extinction, pollutant formation, and turbulent flames in general.

Many industrialized nations have imposed strict pollutant emission standards in an effort to minimize health and environmental risks. Industrial furnaces operate at fuel-lean conditions and devices that make use of diffusion flames utilize dilution to reduce emissions (e.g. flue-gas recirculation). It is of interest, thus, to investigate how dilution affects flame parameters, such as temperature. In small scale boilers (which utilize diffusion flames), it is more effective to introduce the diluent (whether inert gas or recirculated flue-gas) with the fuel (Hopkins *et. al.*, 1991). Studies on how fuel dilution affects thermal and mass properties are, therefore, needed. These properties can be expressed as a nondimensional parameter; the fuel Lewis number (Le_F), which is customarily defined as the ratio of the thermal diffusivity of the fuel-diluent mixture (α) to the mass diffusivity of the fuel (D) (i.e. $Le_F = \alpha/D$).

When coupled to an unsteady flowfield (such that of a turbulent flame), fuel Lewis number effects become increasingly more complex and difficult to determine. Vortex structures and vortex-flame interactions appear in most practical devices (as

discussed above) indicating that vorticity dynamics in combustion is of great practical importance. Relevant studies regarding Lewis number effects in flames and unsteady processes (such as vortex-flame interactions) will now be reviewed.

1.2.1 Lewis Number Effects

The effect of Lewis number (*Le*, whether fuel or oxidizer Lewis numbers) on laminar and turbulent diffusion flames as well as premixed flames has been the subject of several studies over the last few decades. In premixed flames, Lewis numbers effects are well established and are known to affect thermal structure, extinction behavior, tip opening in Bunsen flames, and are also responsible for the occurrence of cellular and pulsating flame structures (Sivashinsky, 1977; Joulin and Clavin, 1978; Sivashinsky, 1983; Williams, 1985; Sakai *et. al.*, 1996). This research work centers on diffusion flames and, thus, emphasis will be placed on them in the following review.

1.2.1.1 Laminar Flames

Perhaps, the most representative Lewis number study on laminar diffusion flames is that of Law and Chung (1982) and Chung and Law (1984). The authors conducted an analytical study (assuming no flame radiation) of the effect of Lewis number on flame structure and temperature for a variety of one-dimensional counterflow (i.e. opposing fuel

and oxidizer flows) diffusion flame configurations, where the flame takes the shape of a flat disk, as well as coflow diffusion flames. They reported that for $Le < 1$ the flame temperature was increased above the adiabatic flame temperature of a homogeneous product mixture (i.e. the temperature calculated by assuming $Le = 1$). The opposite was observed for $Le > 1$. This is due to the difference in thermal and mass diffusivities. For example, $Le < 1$ implies a retardation of the thermal diffusion relative to the mass diffusion. This results in a larger temperature gradient than the concentration gradient of the reactant (whose $Le < 1$) within the flame in order to balance the thermal enthalpy and the reactant mass (i.e. chemical enthalpy) flowing out of and into the reaction zone. This larger gradient yields a higher flame temperature. Law and Chung (1982) also noted the implications that their findings had on temperature sensitive processes such as NO_x formation.

Ishizuka and Sakai (1986) experimentally studied coflowing $H_2/CH_4/N_2$-air laminar diffusion flames and observed that changing the concentration of the diluents (i.e. Lewis number) yielded flame tip opening and changes in flame temperature. This phenomenon was caused by the difference in diffusivities of hydrogen and methane; hydrogen has a higher mass diffusivity than methane and its concentration was less than methane along the flame. This tendency of H_2 to be depleted faster is referred to as preferential diffusion. Preferential diffusion occurs when the fuel is made up of species having different mass diffusivities. The fuel with higher mass diffusivity will be consumed faster (i.e. it is preferred), leading to the stratification of fuel concentration across the flame. This fuel stratification is of special importance at the flame tip (i.e.

strong curvature), the concentration of the fuel may drop below the limiting value and the flame tip will open (i.e. local extinction). Ishizuka and Sakai (1986) attribute their findings to the preferential diffusion of H_2 while acknowledging that the phenomena they observed could be explained by the nonunity Lewis number theoretical model suggested by Law and Chung (1982) and Chung and Law (1984).

Chen *et al.* (1992) experimentally studied the effects of Le_F on laminar diffusion flames formed in Wolfhard-Parker burners. The fuel dilution level was varied (which changed the Lewis number) over a wide range of values. Effect of Lewis number on flame temperature was qualitatively found (i.e. for $Le_F < 1$ flame temperature was higher than adiabatic and vice versa for $Le_F > 1$). They reported on how low Lewis numbers extended extinction limits (due to the increase in flame temperature as reported by Law and Chung, 1982). Chen *et. al.* (1992) also observed that for near-extinction flames with Lewis number sufficiently lower than unity, laminar diffusion flames exhibited cellular structures similar to those found in premixed flames.

The opposite of this phenomenon with $Le_F > 1$ was reported in the numerical study of Cheatham and Matalon (1996) of spherical flames. Near-extinction diffusion flames with high Lewis numbers exhibit natural spontaneous oscillations (Kirby and Schmitz, 1966). As discussed above, a higher than unity Lewis number yields a lower flame temperature so that the chemical reaction rate is reduced (i.e. higher chemical time), lowering the Damköhler (*Da*) number. *Da* is defined as the ratio of the mixing or diffusion time to the chemical reaction time. In the study of Cheatam and Matalon (1996) a low *Da* caused the flame to broaden and move away from the fuel source. The

broader reaction zone was more sensitive to external disturbances due to the increased reaction time and nonequilibrium chemistry caused by low *Da*. If the flame was perturbed outwards, for example, its natural tendency was to move back and reestablish its unperturbed position. This motion was opposite to the propensity of the flame to move outward due to the high Lewis number and low *Da*, setting an oscillatory motion with a Lewis number dependent amplitude and frequency. Experimental evidence and numerical modeling of Lewis number induced diffusive-thermal instabilities leading to cellular and pulsating structures (as in premixed flames) has been the subject of several recent publications (see, for example, Kim and Lee, 1999, Kaiser *et. al.*, 2000, and Chaos and Chen, 2003a).

A recent study (Feese and Turns, 1998) documented the effect of dilution on nitric oxide emissions for a counterflowing (numerical model) and coflowing (experimental) laminar CH_4-air flames. N_2 diluent was added to either the fuel or air sides. In both flame configurations it was observed that adding the diluent to the fuel side yielded higher NO_x concentrations and higher flame temperature (i.e. T_F) than when the diluent was added to the oxidizer side. It was speculated that the Fenimore prompt NO mechanism (active in hydrocarbon flames) was affected, thus, yielding the results observed. However, it can be concluded from the study of Feese and Turns (1998) that adding the N_2 diluent to the fuel side affected molecular and thermal transport properties changing the Lewis number to a lower value than when it was added to the air side thus yielding the results reported of higher flame temperature and nitric oxide emission. The results of Feese and Turns (1998) do not follow the trend observed in small scale boilers

(Hopkins *et. al.*, 1991) where fuel dilution resulted in much greater NO_x reduction than when the air was diluted. This can be attributed to the difference in mixing and heat transfer mechanisms since industrial boilers use turbulent flames.

Numerical analyses have been developed in recent years that include multicomponent transport properties (i.e. diffusion of heat and species) in an effort to model Lewis number effects in flames. The works of Hermanson and Vranos (1991) and Hermason and Vranos (1992) extended the analysis of Law and Chung (1982) to include thermal transport effects in counterflow diffusion flames. Results of the studies of Hermanson and Vranos (1991, 1992) showed that temperature changes and fuel consumption rate were Lewis number dependent. Takagi and Xu (1994) took into account detailed chemical kinetics and multicomponent diffusion (i.e. Lewis number) in their model and obtained results in good agreement with Ishizuka and Sakai (1986). It was analytically quantified in the work of Takagi and Xu (1994) that excess enthalpy (and thus higher flame temperature) occurred as the concentration of H_2 in the fuel (the flame modeled was similar to that of Ishizuka and Sakai, 1986) varied along the flame (i.e. Lewis number). The results obtained running their model with $Le_F < 1$ yielded a flame temperature which was higher than the adiabatic flame temperature calculated assuming $Le_F = 1$, as observed by Law and Chung (1982).

Cuenot and Poinsot (1996) included finite rate chemistry and non-unity Lewis numbers into an asymptotic model (similar to that of Liñan, 1974) of planar (i.e. counterflow) flame configurations. The accuracy of their results was checked against numerical simulations using the same chemical and transport models. They showed that

fuel and oxidizer Lewis numbers do have an effect on heat release and flame temperature, changing the fuel and oxidizer Lewis numbers affected the location of the flame and the diffusion rate of both reactants (refer to Figure 17 in Cuenot and Poinsot's paper).

Takagi *et. al.* (1996) studied the effect of curvature and preferential diffusion (i.e. Lewis number) on diffusion flames by studying coflowing usual and "inverse" flames. Here, inverse flames denoted those flames formed by an air jet surrounded by fuel flow. Takagi *et. al.* (1996) looked at the temperature at the tip of these flames where concave/convex curvature effects (with respect to the fuel flow) could be observed in usual/inverse flames. The numerical and experimental analyses performed by the authors were in good agreement. Le_F for the flame studied was less than unity (i.e. high mass diffusivity). The results of Takagi *et. al.* (1996) showed that concave/convex curvature decrease/increase the fuel concentration at the flame tip leading to a decrease/increase in flame temperature. The opposite behavior is expected for $Le_F > 1$. Their results complement and help explain the tip opening phenomenon observed by Ishizuka and Sakai (1986).

To the author's knowledge, Chen *et. al.* (1997) were the first investigators to systematically document the effect of fuel Lewis number on temperature and NO_x in laminar jet diffusion flames. As explained earlier, Le_F has an effect on flame temperature and, thus, it will affect the thermal (i.e. Zeldovich) NO_x formation mechanism. In their experimental work, Chen *et. al.* (1997) studied laminar jet flames in which H_2, CH_4, and C_3H_8 were diluted with Ar or He. They showed that while NO_x emission decreased in hydrogen flames with increasing He dilution, it increased with Ar dilution. The authors

concluded that the effect of Le_F could overwhelm the effect of dilution; that is, an increase in fuel dilution which made $Le_F < 1$ lead to an increase in flame temperature (T_F). Therefore, for flames with the same degree of dilution of Ar and He, the inert that yielded lower Le_F also yielded higher flame temperature and, consequently, higher NO_x emission levels.

1.2.1.2 Turbulent Flames

All of the studies described in the previous section demonstrate that Le_F has the most important impact on flame temperature (and, thus, temperature dependent processes such as the thermal NO_x mechanism). The effect of Le_F has been less documented on turbulent diffusion flames. Vranos *et. al.* (1992) showed the diminishing importance of Le_F in turbulent CH_4/H_2 – air jet diffusion flames as compared with laminar flames and attributed this phenomenon to transient behavior, flamelet interactions, and unsteadiness associated with flow turbulence. Chen and Mansour (1996) compared measurements on flame structure and temperature of turbulent Ar-diluted hydrogen diffusion flames (78% H_2, 22% Ar with $Le_F > 1$) to flamelet calculations. It was found that molecular diffusion was unimportant since it could be dominated by the strong small-scale turbulent mixing. The results of Chen and Mansour (1996), thus, justify the use of unity Lewis number assumptions in numerical turbulent flame models (to be discussed below).

Fuel dilution and its effect on NO_x emission from turbulent diffusion flames has been investigated experimentally by several authors including Drake *et. al.* (1987), Chen

and Driscoll (1990), and Driscoll *et. al.* (1992). These authors studied the interaction between fluid dynamics, turbulence, combustion, and NO_x chemistry and their results were used later to validate numerical models such as the ones developed by Chen and Kollmann (1992) and Chen *et. al.* (1995). Drake *et. al.* (1987) extended nonequilibrium thermochemistry models to include turbulence and studied thermal (i.e. Zeldovich) NO_x emission in turbulent hydrogen flames experimentally using various chemiluminescence sampling probes. They observed that substituting Ar or CO_2 instead of N_2 as fuel diluents (i.e. different Le_F), yielded discrepancies in the emissions of nitric oxide when compared to numerical models (the NO_x levels measured were 25% higher than those predicted by the model). The experimental work carried out by Chen and Driscoll (1990) and Driscoll *et al.* (1992) yielded NO_x emission level measurements that were found to be lower than the ones predicted by thermal theory by as much as a factor of 4. H_2 and He-diluted H_2 flames were studied. In these flames, Le_F has a value near unity over a wide range of dilution. Therefore, fuel Lewis number effects could not be clearly discerned from these experiments.

Gabriel *et. al.* (2000) continued the work performed by Chen and Driscoll (1990) in order to quantify the effects of Le_F on temperature and NO_x emission in turbulent hydrogen flames. They used a burner similar to that of Chen *et. al.* (1997) and observed the variation in the Damköhler number scaling of NO_x as the Lewis number varied. In contrast to the results found by Chen *et. al.* (1997), the scaling exponent changed from negative to positive as the fuel Lewis number changed from higher than unity to sufficiently less than unity. This change in the scaling exponent had not been observed in

laminar flames or in the studies of Chen and Driscoll (1990) and Driscoll *et. al.* (1992) (which used pure H_2 or He-diluted H_2 flames with near-unity Lewis number). Gabriel *et. al.* (2000) concluded that the effect of Le_F on flame temperature was not as significant as in the laminar flame study of Chen *et. al.* (1997). However, the effects differed from those obtained by dilution alone while maintaining $Le_F = 1$.

The inherent complexity of turbulent diffusion flames, makes them hard to model numerically. However, numerical models of these flames have much improved from early attempts (Bush and Fendell, 1974; Oyegbesan and Algermissen, 1976) due to the advances in computer processing power and speed. A comprehensive treaty on turbulent flame computational research efforts can be found in Bilger (2000). Most of the current numerical models, though, apply a unity Lewis number assumption, which, as explained above, may be justified (Chen and Mansour, 1996).

Lee and Shin (1988) found, through numerical modeling of turbulent H_2/N_2-air jet diffusion flames relying on perturbation methods, that, as the Reynolds number increased, turbulent diffusion became dominant and molecular diffusion effects became negligible. Pitsch (2000) applied an unsteady flamelet model to a turbulent $CH_4/H_2/N_2$-air coflowing diffusion flame. It was concluded that introducing differential diffusion effects in a thin laminar region close to the burner exit and assuming a unity Lewis number throughout the flame, improved the agreement between model and experimental data (Bergmann *et. al.*, 1998). The results of Pitsch (2000) can also help explain the observations of Sanders and Gokalp (1997). Sanders and Gokalp (1997) tried to predict NO formation and temperature of diluted turbulent hydrogen diffusion flames using the

laminar flamelet concept. Introducing nonunity Lewis numbers in their model lead to the over prediction of NO and temperature in the far-field regions of the flame when compared to experimental data. Setting the Lewis numbers to unity lead to a better agreement in the far-field but underestimated the parameters in the near-field.

These results lead to the conclusion that if Lewis number effects are present in turbulent flames they will be found in the regions where turbulence is not developed (i.e. regions close to the burner exit), decaying fast as the turbulent flow develops.

1.2.1.3 Summary

In summary, it has been shown that Lewis number has an effect on flame temperature, NO_x formation and emission, extinction, flame tip opening, and cellular and pulsating structure formation in laminar and turbulent diffusion flames as well as premixed flames. However, there is a need to understand how flame-vortex interaction and Lewis number effects in turbulent flames impact temperature and flame structure. Some of the available numerical and experimental data on unsteady laminar flames relevant to this study will be reviewed in the next section.

1.2.2 Unsteady Processes (Vortex-Flame Interactions)

As reviewed above, Lewis number effects in turbulent flames are not as pronounced as in laminar flames. The reason as to why this happens is not well understood. Turbulent flames have various turbulent scales (i.e. size and intensity); the stochastic nature of these scales makes it difficult to determine specific effects such as that of Le_F. It seems that unsteadiness, vortex-flame interactions and the turbulent mixing processes of a turbulent flame control the characteristics and rate of combustion and overwhelm any Lewis number effects that may be present. Thus, the study of vortex-flame interaction is of great importance to our understanding of basic combustion mechanisms in turbulent flames. This problem has been extensively investigated in recent years; a comprehensive review of these investigations has been done by Renard *et. al.* (2000).

1.2.2.1 Premixed Flames

A brief review of vortex flame interaction in premixed flames will be presented in this section. The effect of heat and mass diffusion (i.e. Lewis number), flame curvature, and flame stretch on premixed flames has been reviewed by Law (1988). For example, it was reported how the concave curvature towards the fuel-oxidizer mixture in a Bunsen flame focuses heat on the incoming mixture and has a defocusing effect on the reactants

coming into the flame zone. If $Le > 1$, the concave curvature tend to raise the flame temperature since the heat focusing effect onto the reactants is greater than the diffusion rate at which the reactants approach the flame (i.e. the reactants are "defocused" due to the concave curvature). The opposite holds for $Le < 1$ which is responsible for flame tip opening (i.e. local extinction) in premixed flames (Sakai *et. al.*, 1996).

Extensive experimental work has been done by Roberts and Driscoll (1991), Roberts *et. al.* (1992), and Roberts *et. al.* (1993) to determine the effect of vortex size and strength on the structure of premixed flame fronts. Experiments indicated that reactant pocket formation and quenching (i.e. incomplete combustion or local quenching) are more likely to occur when large vortices disturb the flame as opposed to small vortices having the same strength and are Lewis number dependent, consistent with the simulation of Poinsot *et. al.* (1991) and the experiments of Renard *et. al.* (1998). Mixtures with $Le > 1$ were found to need much larger Karlovitz numbers (i.e. the ratio of the characteristic time scale for the reaction zone to the smallest time scale of the flow) for flame quenching than mixtures with $Le < 1$ (Roberts *et. al.*, 1993).

Lewis number was found to have an effect on premixed flame area growth and the intensity of the reactive layer marked by OH of flames interacting with a turbulent vortex (Lee *et. al.*, 1993; Lee *et. al.*, 1995). However, even though the effect of Lewis number was strong locally, probability density functions of flame curvature remained unchanged. This result led to the conclusion that the effect of turbulence on non-unity Lewis number premixed flames was to alter flame wrinkling and surface area but only slightly modify the burning rate (Lee *et. al.*, 1993).

1.2.2.2 Diffusion Flames

In the literature, few reports are found that specifically deal with Lewis numbers effects coupled with unsteadiness or vortex-flame interactions in nonpremixed flames. In addition, most of the theoretical and experimental efforts have treated counterflow diffusion flames as opposed to jet flames. A review of relevant numerical and experimental investigations of vortex-flame interactions and unsteady flames (laminar and turbulent) is given below.

Flame structure of acoustically forced laminar jet diffusion flames was studied by Lewis *et. al.* (1988), Gutmark *et. al.* (1989), Strawa and Cantwell (1989), and Kim *et. al.* (1993) in an effort to characterize mixing and structure of complex turbulent flames. Combustion was found to be enhanced since flame forcing promoted an earlier transition to small-scale turbulence (Gutmark *et. al.*, 1989) and mixing was enhanced at the exit of the fuel tube (Kim *et. al.*, 1993).

Although not the subject of the present research study, acoustic flame forcing has been found to have a strong effect on soot in CH_4-air laminar jet diffusion flames (Smyth *et. al.*, 1993; Shaddix *et. al.*, 1994). Laser-induced incandescence (LII) and laser-induced fluorescence (LIF) were used to obtain measurements of laminar flames forced at different amplitudes by a loudspeaker driven cavity. It was found that forcing produced flame tip clipping, which dramatically increased the soot signals. A later computational model developed by Kaplan *et. al.* (1996) yielded comparable results.

As explained above, unsteady (i.e. vortex-flame interaction) research on counterflow flames is extensive. Rolon *et. al.* (1995) used a counterflowing laminar flame (N_2-diluted hydrogen and N_2-diluted air) where a vortex was introduced from the oxidizer side. The paper presents mostly velocity field data and it was shown that, depending on the vortex strength, the reactive layer may be disrupted in such a manner that the flame was extinguished locally exhibiting specific patterns. Renard *et. al.* (1999) continued the investigation of Rolon *et. al.* (1995) by observing the structure of the OH radical using LIF as the vortex impinged the counterflow flame. Different mixtures (both hydrogen and air were diluted with nitrogen) were tested along with different vortices. Vortex size and strength affected flame surface geometry and residence time, which in turn affected flame strain, heat release (i.e. flame temperature), and promoted local quenching. Renard *et. al.* (1999) showed experimentally that when the vortex initially impinged on the flame zone, combustion was globally intensified due to flame strain. Thévenin *et. al.* (2000) further extended the investigations of Rolon *et. al.* (1995) and Renard *et. al.* (1999) to identify vortex-flame interaction regimes such as wrinkling and roll-up with emphasis placed on flame extinction.

Takagi *et. al.* (1996), Yoshida and Takagi (1998), and Yoshida and Takagi (1999) studied a counterflow H_2/N_2-air flame strained by a microjet impinging from either the fuel or air sides. Their results showed how microjet impingement lead to local flame extinction followed shortly by reignition (also observed by Rolon *et. al.*, 1995). However, with the microjet impinging from the air side, the temperature after reignition was considerably higher than that of a steady flame. The results were attributed to the

high mass diffusion (i.e. preferential diffusion) of H_2 coupled with flame curvature. Impingement from the air side curves the flame convexly with respect to the fuel side, thus focusing fuel in the convex region and increasing the temperature. A similar behavior was observed by Finke and Grünefeld (2000) on their experimental study of curved counterflow flames. Hydrogen flames diluted with different inert species were studied. All flames studied had a higher flame temperature when curved towards the air side (i.e. convex curvature with respect to the fuel). However, a relationship could not be established between flame curvature and flame quenching. A more recent study by Katta *et. al.* (2003) attributes the change in temperature of millimeter-size vortex/flame interaction (as in Takagi *et. al.*, 1996, Yoshida and Takagi, 1998, and Yoshida and Takagi, 1999) not to preferential diffusion but to non-unity Lewis number and the entrainment of combustion products into the flame region by the vortex. In addition, curvature effects alone could not explain the results of Katta *et. al.* (2003) when compared to an earlier study (Katta *et. al.*, 1998), which can further justify the results reported by Finke and Grünefeld (2000).

Experimental work on unsteady jet diffusion flames and vortex-flame interactions in these flames is limited. Hancock *et. al.* (1996) used coherent anti-Stokes Raman scattering (CARS) to measure temperature of steady and forced laminar H_2/N_2-air jet diffusion flames. Experimental results were compared to direct numerical simulations. It was found that, during forcing, the mass flux of hydrogen was increased, increasing the flame temperature. Areas where the flame was curved towards the fuel side exhibited higher temperatures. Visualization of the flame through particle image velocimetry (PIV)

(Schauer *et. al.*, 1998) further verified the results of Hancock *et. al.* (1996). Mueller and Schefer (1998) experimented with vortices of various sizes and strengths interacting with laminar methane flames diluted with nitrogen. They showed temporal evolution images on how the strain due to the vortex thickened or thinned the flame based on OH radical data (from laser-induced fluorescence). The OH data presented proved that the vortex convected products formed upstream of the flame downward changing local dilution; therefore one can conclude a local change in Lewis number as inferred by Katta *et. al.* (1994).

Recent experimental studies of laminar jet diffusion H_2/N_2-air flames attribute flame temperature changes to preferential diffusion of H_2 in regions where the unsteady nature of the vortex curves and thins or broadens the reaction zone layer (Kawabe, *et. al.*, 2000; Komiyama *et. al.*, 2001; Komiyama *et. al.*, 2003). Non intrusive laser techniques were utilized to measure temperature and characterize the flow (i.e. Rayleigh scattering, LIF, PIV). The flame studied was a 70% N_2, 30% H_2 mixture which has $Le_F < 1$. Thus, Lewis number effects might explain the results observed.

Turbulent vortex-flame interaction studies are scarce. As an example, the work of Rehm and Clemens (1998) is cited here. They used LIF and PIV to characterize the regions of high and low strain and how vorticity and strain affected the reaction zone marked by OH. Other works by Lovett and Turns (1993) and Hermason *et. al.* (2000) investigated the flame structure of pulsed (i.e. unsteady) turbulent diffusion flames in an effort to determine how forcing affected velocity, temperature, and mixing.

Considerable effort has been placed in the numerical modeling of unsteady flames and vortex-flame interactions. Cuenot and Poinsot (1994) used numerical simulation to model unsteadiness and curvature effects for Le_F=1. They compared temperature and reaction rate results obtained from their simulation to an asymptotic model that assumed negligible unsteady and curvature effects (laminar flamelet assumption, LFA). Cuenot and Poinsot (1994) showed that curvature effects were opposite to unsteadiness when compared to the LFA model results. In essence, curvature effects increased overall diffusion, which lead to a lower temperature when compared to the laminar flamelet model. Unsteadiness effects, which occur when the flow time scale is too small with respect to the chemical time scale (i.e. low Damköhler number), yielded a higher temperature than that of the LFA model. Cuenot and Poinsot's model showed the limits of LFA codes for turbulent diffusion combustion. Quenching by flame strain was also evidenced.

Katta *et. al.* (1994) numerically modeled a jet diffusion H_2–air flame with induced unsteady oscillations. They related the local variation in flame temperature as the flame bulged out (due to the presence of unsteadiness, also observed by Vilimpoc and Goss, 1988) to the local Lewis number change. The convective motion of the oscillations induced stretch along the flame surface; it was found that the lower local Lewis number due to the hydrogen molecules on the fuel side of the flame was responsible for increasing the temperature of the stretched region. It was also shown in their model that the results differed from unity Lewis number assumption. Katta and Roquemore (1995) continued the investigation of Katta *et. al.* (1994) and reported how as the flame was

stretched/compressed, the local temperature increased/decreased if the unsteadiness was introduced from the fuel side and decreased/increased if introduced from the air side. Although not reported, curvature effects could also explain the observed results (Cuenot and Poinsot, 1994; Yoshida and Takagi, 1996).

Takahashi and Katta (1996) introduced unsteady chemical kinetics of 17 different species to explain extinction of laminar methane jet diffusion flames due to vortex interaction. Their model provided an understanding of how diffusion, convection, and chemical kinetics may affect flame temperature. Explanation was given by Takahashi and Katta (1996) as to how the vortex thinned the thermodiffusive layer (i.e. reaction zone), gradually decreasing flame temperature. Katta *et. al.* (1998) showed through a time dependent numerical code and experiments on a flame similar to that of Rolon *et. al.* (1995) that specific quenching patterns might be observed for relatively strong vortices. It was argued that the flame quenching patterns observed might have stemmed from the combined effect of preferential diffusion and flame curvature.

1.2.2.3 Summary

This review illustrates the complexity inherent in unsteady and vortex-flame interaction processes. It seems that the interaction between combustion and time and length scales in unsteady flow is of great relevance since the diffusional scales of chemical reactions are affected. However, a clear picture is not yet available since authors seem not to settle on how heat and mass diffusion play a role in unsteady flames

(i.e. Lewis number versus preferential diffusion effects, flame curvature, strain rate, etc.). This controversy between different theories and predictions calls for further investigation. Future progress in cataloguing and modeling of vortex-flame interactions of several scales will provide means for a comprehensive treatment of turbulent combustion.

1.2.3 Spectroscopy

1.2.3.1 Introduction

The need for further unsteady flame investigations has been evidenced by the review above. However, the unsteady nature of these phenomena makes measurement of fundamental properties such as temperature and species concentration challenging. Traditional measurement methods using physical probes are intrusive and, in some cases, alter the problem being studied. Reliable physical probing methods require that the probe be significantly smaller than the reaction zone. In turbulent flames, unsteady flames, and flames during vortex-flame interactions, the flame size is of millimeter size (sometimes smaller). Probe insertion in such flames would change flame dynamics and transfer mechanisms (Becker, 1993). The spatial and temporal resolution of such probes is limited which makes them ineffective in situations where the measured quantity changes rapidly. The harsh environment of combustion processes (i.e. high temperatures)

promotes the degradation of physical probes, which adds to the disadvantages of their use.

The introduction of laser diagnostics techniques has greatly impacted combustion research. Laser diagnostics provide non-intrusive measurement means that have excellent spatial and temporal responses. Complex flows and large or small-scale structures (such as those found in a turbulent flame) can be studied without impacting flow structure of species chemistry. Two or three-dimensional data is possible with laser diagnostics as opposed to physical probes, which provide point measurements. Species concentration, temperature, and flow structure (among other parameters) can be obtained using several techniques such as laser-induced fluorescence (LIF), Raman and Rayleigh scattering, coherent anti-stokes Raman spectroscopy (CARS), and degenerate four-wave mixing (DFWM) among others. The reader is referenced to Eckbreth (1996) for the most comprehensive treatise found in the literature on these and other techniques. LIF will be further elaborated here since it was used in the present study.

The understanding of basic spectroscopic concepts is fundamental for the application of the laser diagnostics techniques discussed above. A concise background review on the physics of atomic and molecular spectroscopy is given below with emphasis placed on the OH molecule which is the species probed in this research using LIF.

1.2.3.2 Atomic and Molecular Spectroscopy

Quantum mechanics instructs that an electron can only take on discrete energy levels within an atom. Radiation spectra associated with changes in energy states is, thus, not continuous. The radiation pattern from atoms and molecules can be predicted quantum mechanically. In the sections below, a foundation on atomic spectroscopy will be laid which will be extended to molecular spectroscopy of the OH molecule in particular.

1.2.3.2.1 Atomic Quantum Numbers and Classification

An electron moving in a spherically symmetrical force field (such as that of an atom) can be characterized by the following quantum numbers: n, l, s, m_l, and m_s. Where n is the principal quantum number and it is a measure of the radius of the electron orbit, l is the orbital angular momentum quantum number, and s is the spin quantum number. In the presence of a magnetic field (which is usually the case), l and s become spaced quantized in which case they are represented by their components along the field direction, m_l and m_s respectively. The allowed values these numbers can assume are given below:

$$n = 0, 1, 2, \ldots \quad (1.1a)$$

$$l = 0, 1, \ldots, n-1 \quad (1.1b)$$

$s = \pm 1/2$ (1.1c)

$m_l = l, l-1, l-2, \ldots, -l$ (1.1d)

$m_s = \pm 1/2$ (1.1e)

According to the value of l, electrons are given the terms s ($l = 0$), p ($l = 1$), d ($l = 2$), f ($l = 3$), g ($l = 4$), and so on alphabetically. The Pauli Exclusion Principle (Herzberg, 1944), states that no two electrons can have the same four quantum numbers (i.e. n, s, m_l, and m_s). Therefore, in an atom, only a given number of electrons can have the same n and l values. The total number of atoms for a given n and l (i.e. a "shell") is $2(2l+1)$ since there are $2l+1$ possible values of m_l and two possible values of m_s. From this reasoning, a s shell ($l = 0$) can only have two electrons, a p shell, six, and so on.

Using the basis above, electrons can be characterized by the principal quantum number n (i.e. the energy level they occupy) followed by the letter corresponding to their angular momentum. The number of electrons in a given shell is represented by a superscript. As a shell is filled up, the next shell is occupied. As an example, take Boron (B), which has five electrons. The quantum representation of this atom is $1s^2 2s^2 2p^1$ with the 2p shell being an open shell since it is not fully occupied (note that the sum of the superscripts equal the number of electrons).

Atom spectra are generated from the electrons in the outermost shells (the 2p shell in the case of Boron) and are termed optical electrons. The energy level of an atom can be classified in terms of its total orbital angular momentum quantum number, L, the total spin angular momentum quantum number, S, and the total angular momentum quantum number, J, which arise from the coupling of the motion of the several different electrons.

These numbers need to be evaluated for the outermost electrons since, for the closed shells (i.e. fully occupied orbit), electron motions cancel each other resulting in zero values for L and S. Depending on the value of L and S, J can take on specific values. The allowed values for J and S are given below:

$$\begin{aligned} J &= (L+S),(L+S-1),(L+S-2),\ldots,|L-S| \\ S &= N_e/2,(N_e/2)-1,(N_e/2)-2,\ldots,1/2 \text{ or } 0 \end{aligned} \tag{1.2}$$

where N_e is the number of electrons in the outermost orbit. The value of L depends on the l quantum number of the outermost electrons (Eckbreth, 1996). The energy level term, thus can be classified by:

$$^{2S+1}L_J$$

where L is designated by the capital letters S, P, D, F, G, and so on for L values of 0, 1, 2, 3, 4, etc. Thus, for the Boron atom given as an example above, $L = 1$, $S = 1/2$, and J can take on the values of 3/2 and 1/2; therefore, the ground state classification is given by the term $^2P_{3/2,1/2}$. States that have different J values are multiplets such as in the case of the ground state of Boron presented here. Multiplet states are degenerate, that is, these states are in everyway equal except differing slightly in energy levels due to spin-orbit coupling. The degeneracy for a multiplet state with given J is $g = 2J+1$. Thus, for the case of the ground state of Boron, the total degeneracy of the state would be 6. This is

important in determining how large a population a given state can accommodate, which is significant for thermometry measurements.

1.2.3.2.2 Molecular Quantum Numbers and Classification

Molecular spectra are considerably more complicated than their atomic counterparts. Molecular nuclei can rotate and vibrate which add to the ways electron momenta can couple to the molecular motion. Molecules, thus, can exhibit spectra where electronic, rotational, and vibrational modes are excited. Once again, rotational and vibrational energies can take on discrete values and two new quantum numbers arise, R and v, the rotational and vibrational quantum numbers respectively. Standard nomenclature for R is J (Eckbreth, 1996) but it is not used here to avoid the unfortunate duplication of nomenclature for the total angular momentum quantum number.

The overall electronic molecular states emerging from the different electron configurations may be characterized much in the same way as atoms. As was mentioned above, only the outermost electrons are considered. Greek characters are used to differ molecular from atomic nomenclature. The quantum numbers used in molecular nomenclature are the total axial (i.e. projection along the internuclear axis) orbital angular momentum, Λ, the total electron spin, S, and the total axial spin, Σ. As with atoms, Λ can be represented by letters; Σ, Π, Δ, Φ, Γ for values of 0, 1, 2, 3,4 and so on. S can take on integer or half integer values and Σ can take on the following values:

$$\Sigma = S, S\text{-}1, S\text{-}2, \ldots, -S \tag{1.3}$$

The states can be classified by (Daily, 1997):

$$^{2S+1}\Lambda_{|\Lambda+\Sigma|}$$

Multiplets also arise in molecular electronic configurations. States with $\Lambda > 0$ split into components having slightly different energies due to orbital-spin interaction (i.e. spin splitting) with degeneracy $g = 2S+1$ and $g = 2$ for $\Lambda = 0$. In the presence of molecular rotation, the degeneracy that exists for $\Lambda \neq 0$ is further split (i.e. doubled; $g = 2(2S+1)$) due to the coupling between the orbital motion of the electrons and the molecular rotation, which referred to as Λ-doubling.

Coupling between molecular rotation and electron orbital motion can occur in several ways, the most important two of which will be reviewed here: Hund's cases (a) and (b) (Herzberg, 1950). In Hund's case (a), coupling between the orbital angular momentum, total electron spin, and molecular rotation is considered weak. In this case, a new quantum number is defined:

$$\Omega = \Lambda+\Sigma \tag{1.4}$$

and the total angular momentum is:

$$J = \Omega + R \tag{1.5}$$

The first rotational level, thus, corresponds to $J = \Omega$ (i.e. $R = 0$). In Hund's case (b), the coupling between the total spin and molecular rotation is strong (i.e. stronger than the coupling between the orbital angular momentum and the total spin). A new quantum number arises:

$$N = R + \Lambda \tag{1.6}$$

and the total angular momentum is:

$$J = N + S \tag{1.7}$$

As an example, take the OH molecule. In its ground state, $\Lambda = 1$, $S = 1/2$, and Σ can take on the values 1/2 or 3/2 (Eckbreth, 1996). Therefore, the ground state representation is given by:

$$^2\Pi_{3/2,1/2}$$

The first excited OH state happens when an electron from a closed shell jumps to an open shell in which case $\Lambda = 0$, $S = 1/2$, and $\Sigma = 1/2$ or $-1/2$. The excited state term is then:

$^2\Sigma^+_{1/2}$

The + superscript above denotes that the state is symmetric. Symmetry plays an important role in characterizing rotational level properties such as parity. Symmetry and parity of the rotational levels of a molecule are important in determining the selection rules for allowable transitions to the excited state. The procedure by which a state can be classified as symmetric or asymmetric will not be discussed here (the reader is referenced to Herzberg, 1950 and Eckbreth, 1996).

In spectroscopy, the ground state is denoted by X and the excited states by A, B, C, and so on. For the OH molecule, excitation from the ground state to the first excited state can be represented by $A^2\Sigma^+ \leftarrow X^2\Pi$ (subscripts are usually dropped). Naming standards for the vibrational energy levels use v' for the excited state and v'' for the ground state and are usually denoted by (v', v''). Thus, writing $A^2\Sigma^+ \leftarrow X^2\Pi$ (1,0) would denote excitation of the (1,0) vibrational band of OH. That is, exciting $v' = 1$ in the $^2\Sigma^+$ state from $v'' = 0$ in the $^2\Pi$ ground state. The single prime superscript for the excited state and the double prime superscript for the ground state notation will be used throughout the remainder of this work.

1.2.3.2.3 Selection Rules

The absorption and emission of radiation results from the transition of a molecule between electronic energy levels. The transition follows a certain selection criteria that can now be summarized based on the background provided above. While there are extensive selection rules, only those relevant to LIF transitions will be discussed here (i.e. rules pertaining to electric dipole transitions, Eckbreth, 1996). Selection rules are summarized in Table 1-1. In general, parity must change during the transition and states with different multiplicity do not combine.

Table 1-1: Selection rules

Total Angular Momentum	$\Delta J = 0, \pm 1$	$J = 0 \leftrightarrow J = 0$, not allowed
Electronic Quantum Numbers	$\Delta \Lambda = 0, \pm 1$	
	$\Delta S = 0$	
Hund's case (a)	$\Delta \Sigma = 0$, $\Delta \Omega = 0, \pm 1$	
Hund's case (b)	$\Delta N = 0, \pm 1$	
Parity	Must change	
Σ States	$\Sigma^+ \rightarrow \Sigma^+$, $\Sigma^- \rightarrow \Sigma^-$	$\Sigma^+ \leftrightarrow \Sigma^-$, not allowed

There is no strict rule for the vibrational quantum number, v. However, transitions where $\Delta v = \pm 1$ tend to be the strongest. Rotational energy level transitions following the rules in Table 1-1 can be classified as follows:

P–branch	$J' = J'' - 1$
Q–branch	$J' = J''$
R–branch	$J' = J'' + 1$

P, Q, and R branches are termed main branches.

1.2.3.3 OH Molecule

In this section, the spectroscopic background presented above is extended and applied to the OH molecule, which was the species probed in this study through LIF. More specifically, the $A^2\Sigma^+ \leftarrow X^2\Pi$ transition is examined. A discussion of OH energy levels, allowed transition terminology, transition strengths, and state population distributions will be discussed below.

1.2.3.3.1 Energies

As discussed above, molecular transitions may involve electronic, rotational, and vibrational excitations. Thus, the total energy of a molecule might be written as:

$$E = T_e + G(v) + F(J) \tag{1.8}$$

Where E is the total energy, T_e is the electronic energy, G is the vibrational energy, and F is the angular momentum energy. For given Λ and S, J is dependent on the rotational energy level of the molecule (see Equations (1.5) and (1.7)), thus, F is also referred to as the rotational energy term. Explicit equations can be written for each energy term in Equation (1.8). Due to complexities modeling the electronic energy, T_e is usually obtained from appropriate tables. The vibrational energy may be modeled by Equation (1.9) below (Dieke and Crosswhite, 1962):

$$G(v) = \omega_e (v + 1/2) - x_e (v + 1/2)^2 \qquad (1.9)$$

Where ω_e and x_e are molecular constants and are usually tabulated. Expressions for $F(J)$ will depend on the coupling between the electronic, rotational, and vibrational states as discussed above. Modeling of the rotational term energy is given in the next sections.

For the OH molecule, states are usually between Hund's cases (a) and (b) and either terminology maybe used to represent state nomenclature. Both the Σ^+ and Π states are doublets, that is, the multiplicity of the states is 2 (i.e. $2S+1 = 2$). Recall that for $\Lambda \neq 0$ these states are further doubled. Therefore, a manifold of rotational levels arise for given Λ and S. Following the designation of Dieke and Crosswhite (1962), for the Σ^+ state, the two components of the doublet are characterized by the rotational term energies F_1 and F_2 and, for the Π state, f_1 and f_2.

1.2.3.3.2 The $A^2\Sigma^+$ State

For this excited state recall that $\Lambda = 0$ and, thus, electron spin couples to the rotation of the molecule, that is, Hund's case (b) is applicable. This level is a doublet, as discussed above, due to the spin-orbit interaction. However, since $\Lambda = 0$, Λ–doubling does not occur. Since $S = 1/2$, the total angular momentum may be expressed by Equation (1.7) for each of the two components in the doublet:

$$J = N \pm S \text{ or } J = N \pm 1/2 \quad (1.10a)$$
$$J = N + 1/2 \text{ for } F_1 \quad (1.10b)$$
$$J = N - 1/2 \text{ for } F_2 \quad (1.10c)$$

Where N depends on the rotational quantum number R since $\Lambda = 0$ (see Equation (1.6)). The rotational term energy in Equation (1.8) for each of the levels in the doublet (i.e. F_1 and F_2) can then be modeled by (Dieke and Crosswhite, 1962):

$$F_1(N) = B_v N(N+1) - D_v[N(N+1)]^2 + y_v(N+1) \quad (1.11)$$
$$F_2(N) = B_v N(N+1) - D_v[N(N+1)]^2 - y_v(N+1) \quad (1.12)$$

where B_v, D_v, and y_v are molecular constants which can be a function of the vibrational level. As one can see, the spin-split states have nearly identical energies. Graphically, the first few rotational energy levels of the Σ^+ state may be represented as in Figure 1-1. In this figure, the parity of the states is shown (i.e. *par*). The Σ^+ state is symmetric,

hence, when N is even, the corresponding rotational level has positive parity and vice versa when N is odd. Note that the first rotational level corresponds to $J = 1/2$.

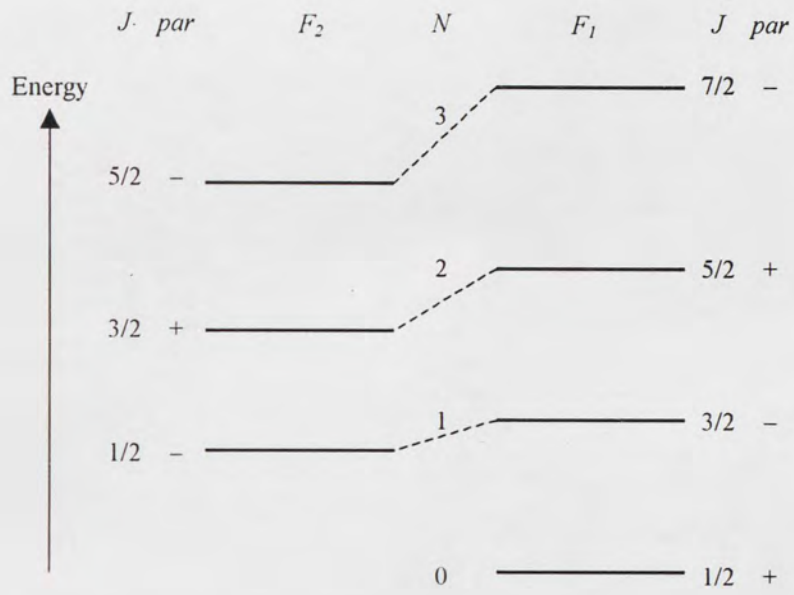

Figure 1-1: Energy level progression for the excited $A^2\Sigma^+$ state.

1.2.3.3.3 The $X^2\Pi$ Ground State

Since $\Lambda = 1$ for the Π level, Hund's cases (a) or (b) may be applied. OH spectroscopy at this level is quite complicated starting as case (a) for low J and transitioning to case (b) as J increases (i.e. as the nuclear rotation increases) (Eckbreth, 1996). Recall that for this ground level and from Equation (1.4) the two spin-split levels of the ground state doublet have different Ω quantum numbers, namely, $\Omega = 1/2, 3/2$. According to Equation (1.5), the total angular momentum can now be given by:

$$J = \Omega, \Omega + 1, \Omega + 2, \ldots \tag{1.13}$$

The manifold of rotational energies (now given by f_1 and f_2) can be modeled by (Dieke and Crosswhite, 1962):

$$f_1(N) = B_v\left\{(N+1)^2 - \Lambda^2 - \frac{1}{2}\left[4(N+1)^2 + Y_v(Y_v-4)\Lambda^2\right]^{1/2}\right\} - D_v\left[N(N+1)\right]^2 \tag{1.14}$$

$$f_2(N) = B_v\left\{N^2 - \Lambda^2 - \frac{1}{2}\left[4N^2 + Y_v(Y_v-4)\Lambda^2\right]^{1/2}\right\} - D_v\left[N(N+1)\right]^2 \tag{1.15}$$

where Y_v is a molecular constant. Note that as N increases, f_1 approaches f_2 indicating the transition to Hund's case (b). A list of the molecular constants is given in Table 1-2. Data in Table 1-2 was obtained from Dieke and Crosswhite (1962). These constants are useful in evaluating the total energy of the state using Equations (1.8), (1.9), (1.11), (1.12), (1.14), and (1.15). Even though the ground level of OH exhibits characteristics of both Hund's cases (a) and (b), case (b) notation is used throughout. For this reason, Equations (1.14) and (1.15) are expressed in terms of N and, thus, Equations (1.10b) and (1.10c) can be used to characterize the rotational levels.

Table 1-2: OH molecular energy constants (in cm^{-1})

$X^2\Pi$ State			
	T_e	ω_e	x_e
	0.0	3735.21	82.21
v''	B_v	D_v	Y_v
0	18.515	0.00187	-7.547
1	17.807	0.00182	-7.876
2	17.108	0.00182	-8.214
3	16.414	0.00182	-8.568
$A^2\Sigma^+$ State			
	T_e	ω_e	x_e
	32682.0	3184.28	97.84
v'	B_v	D_v	y_v
0	16.961	0.00204	0.1122
1	16.129	0.00203	0.1056
2	15.287	0.00208	0.0997
3	14.422	0.00206	0.0980

Since $\Lambda \neq 0$ for the ground state, each level in the doublet is Λ-doubled as discussed above. Therefore, for given J and N, the specific configuration consists of two Λ-doubled sublevels. A graphical representation of the rotational energy levels in the ground state of OH is shown in Figure 1-2. Notice that each Λ-doubled state has different parity. For a more comprehensive view of the energy levels of the OH

molecule, refer to Figure 1-3. In this figure, both rotational and vibrational structures are represented. Note that Λ-doubling for the $X^2\Pi$ state and the spin-split levels of the $A^2\Sigma^+$ state are not shown; in diagnostics applications doubling and splitting of the states are usually unresolved since they are very small.

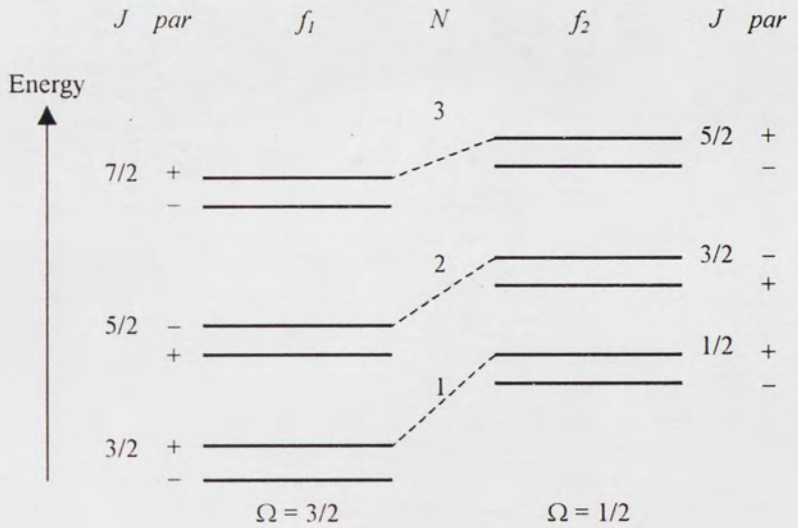

Figure 1-2: Energy level progression for the ground $X^2\Pi$ state.

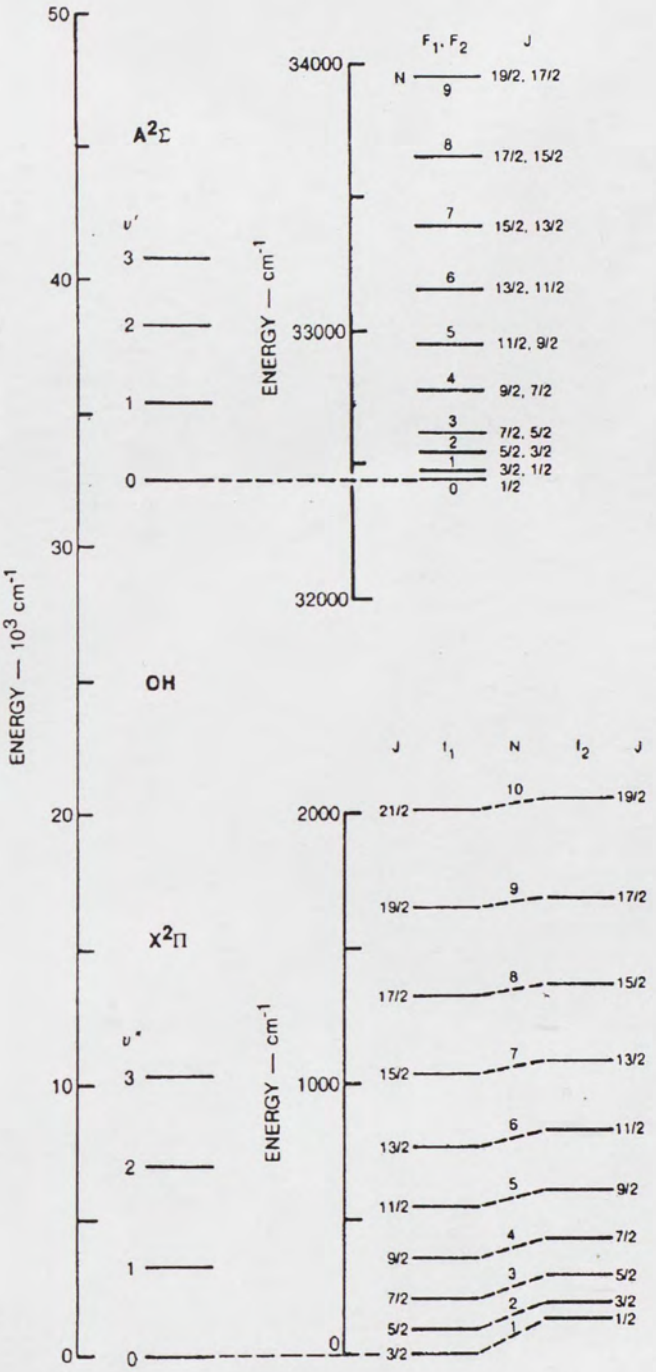

Figure 1-3: Energy level diagram of the ground and first excited states of the OH molecule in the (0,0) vibrational band (adapted from Eckbreth, 1996).

1.2.3.3.4 Notation of the $A^2\Sigma^+ \leftarrow X^2\Pi$ Transitions

Following the general selection rules in Table 1-1, a nomenclature standard can be generated to denote the different transitions between ground and excited states. In general, for the $A^2\Sigma^+ \leftarrow X^2\Pi$ (v', v'') transition, a symbol of the form ${}^{\Psi}K_{\alpha,\beta}$ (N'') can be written. Here, Ψ represents ΔN (O, P, Q, R, or S for ΔN = -2 to 2), K represents ΔJ (P, Q, or R for ΔJ = -1 to 1), α represents the manifold in the excited state (i.e. either 1 or 2 for F_1 and F_2 respectively), and β represents the manifold in the ground state (i.e. either 1 or 2 for f_1 and f_2 respectively). The last term denotes the specific N states being considered. For example, the term ${}^{S}R_{21}(10)$ is a transition from $N'' = 10$, $J'' = 10.5$ (i.e. $\beta = 1$ therefore f_1 is the manifold of interest for which $J = N + 1/2$ from Equation (1.10b)) to $N' = 12$, $J' = 11.5$ (in the manifold F_2). One should note that when $\Delta N = \Delta J$, the Ψ symbol is suppressed, and when $\alpha = \beta$, the β symbol is suppressed. Usually the Ψ symbol is omitted although some authors may omit either the Ψ or K symbols.

Figure 1-4 illustrates the application of the selection rules and the transition notation to the $A^2\Sigma^+ \leftarrow X^2\Pi$ system. All possible transitions from states with $N'' = 10$ are labeled. In total, 12 bands are possible with three bands originating from each Λ-doubled, spin-split $X^2\Pi$ state. Two kinds of branches are evident, the main branches ($\alpha = \beta$) and satellite or cross branches ($\alpha \neq \beta$). Note that some branches violate some of the selection rules in Table 1-1 (i.e. the branches with $\Delta N = 2$ or -2). These branches are weak but present in OH molecular transitions. As N increases, the satellite branches

weaken and the six main branches contain the only significant transition strengths (Dieke and Crosswhite, 1962). Also note that because of the parity selection rule, transitions between two Λ-doubled states (i.e. Π↔Π transitions) would have 24 possible branches and transitions between two Σ states would have 6 possible branches.

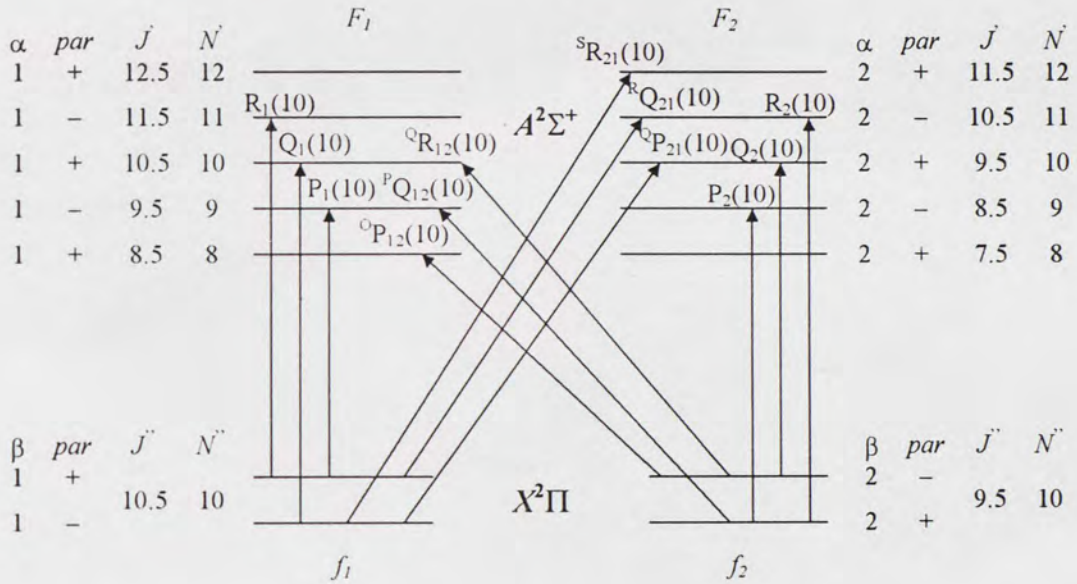

Figure 1-4: Allowed transitions from $N'' = 10$ in the $A^2\Sigma^+ \leftarrow X^2\Pi$ system.

1.2.3.3.5 State Populations

Laser diagnostics such as LIF where temperature may be measured rely on the proper modeling of the possible number of molecules occupying the energy level of the ground state being probed. Here, it will be assumed that temperatures are low enough such that only the ground state is populated, which is usually the case in combustion

$$\frac{N_i}{N_a} = \frac{e^{-hcT_e/kT}}{Q_e}\frac{e^{-hcG/kT}}{Q_v}\frac{(2J''+1)e^{-hcf(N'')/kT}}{Q_r} \tag{1.18}$$

where T_e and G are the electronic and vibrational energy terms (Equations (1.8) and (1.9)), $f(N'')$ is the rotational energy of the level (i.e. either f_1 or f_2 from Equations (1.14) and (1.15)). Q_e, Q_v, and Q_e are the electronic, vibrational, and rotational partition functions and can be approximated by (Eckbreth, 1996)

$$Q_e = 2(2S''+1) \tag{1.19}$$

$$Q_v = \frac{e^{-hc\omega_e/2kT}}{1-e^{-hc\omega_e/kT}} \tag{1.20}$$

$$Q_r = \frac{T}{B_v hc/k} \tag{1.21}$$

Note in Equation (1.19) that the electronic partition function is approximated as the degeneracy of the ground state (a factor of 2 is included to account for the Λ-doubling of the ground state). This is a good approximation in this case, however, for extremely high temperatures or transitions that involve configurations where both the ground and excited states are populated, this expression would not be valid.

As an example take the $R_1(10)$ transition of the ($v' = 0$, $v'' = 1$) vibrational band at a temperature of 1500 K of the $A^2\Sigma^+ \leftarrow X^2\Pi$ system. Here, $S'' = 1/2$, therefore $Q_e = 4$ from Equation (1.19). Using the data in Table 1-2 for $v'' = 1$ in Equations (1.20) and (1.21) yields $Q_v = 0.171$ and $Q_r = 58.55$. Since $N'' = 10$ and $J'' = 10.5$, $f_1(10) = 1{,}901$ cm^{-1} and

the result for Equation (1.18) is 0.014 (note that G is 1,847 cm^{-1} from Equation (1.9) and the data in Table 1-2). Therefore, about 1.4% of the OH molecules occupy the level with $N'' = 10, J'' = 10.5$ (positive parity).

1.2.3.4 Summary

As a more comprehensive illustration of the information presented in this section, Figure 1-5 shows line strengths for the transitions in the (1,0) vibrational band of the $A^2\Sigma^+ \leftarrow X^2\Pi$ OH system. The data presented in this figure was generated using data from Earls (1935), Kovács (1969), Whiting *et. al.* (1973), and Luque and Crosley (1999); line strength calculation procedures are beyond the scope of this report. In Figure 1-5, vertical lines are plotted for each transition (i.e. $Q_1(1)$, $R_2(9)$, etc.) with the height representing the line strength. Lines corresponding to a specific branch are connected, each branch is labeled using standard notation where the Ψ symbol has been dropped (see Section 1.2.3.3.4). One can note the strength of the main branches with respect to the cross branches.

The information presented here will be useful in determining which rotational levels provide the best fluorescence signals, temperature sensitivity, and temperature dependence of state populations. As temperature increases, the molecular energy increases and populations shift to higher rotational levels. This population dependency on temperature is exploited in the LIF technique, which will be discussed in the next

section. If the equilibrium population distribution can be obtained through LIF, the temperature can be calculated using the expressions developed in this section.

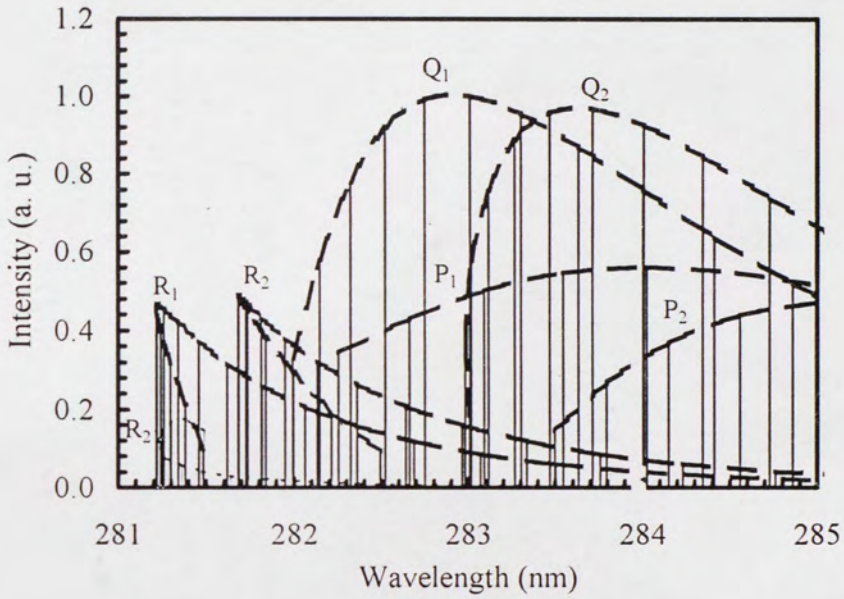

Figure 1-5: OH transition strengths for a selected region of the $A^2\Sigma^+ \leftarrow X^2\Pi$ (1,0) transition at 2000 K.

2 LASER–INDUCED FLUORESCENCE

Fluorescence is the spontaneous emission of radiation (i.e. photon or light emission) from atoms or molecules from an upper energy that has been excited (i.e. with the use of a laser) to a lower energy level. Lasers are the most convenient sources of spectrally resolved excitation, which leads to the laser-induced fluorescence (LIF) technique. A laser source tuned to the wavelength where transition occurs and a camera capable of detecting fluorescence emission is one of the simplest systems that can be used to perform LIF. Due to the relatively high laser energies required for LIF measurements, continuous wave (CW) lasers are not desirable; thus, the use of pulsed laser that provide high energy pulses of short duration (in the nanosecond range) are extensively used (Eckbreth, 1996). Fluorescence may occur from the excited state populated by the laser excitation (i.e. resonance fluorescence); however, this presents complications as emission and excitation wavelengths are the same and interference may occur. In general, the fluorescence wavelength occurs primarily at longer wavelengths than that of the laser excitation used (i.e. Stokes shift). For diagnostics applications, one generally views spectrally shifted fluorescence to avoid interferences. Figure 2-1 shows a schematic of the laser induced fluorescence process used in this investigation; rotational levels are not resolved in this figure.

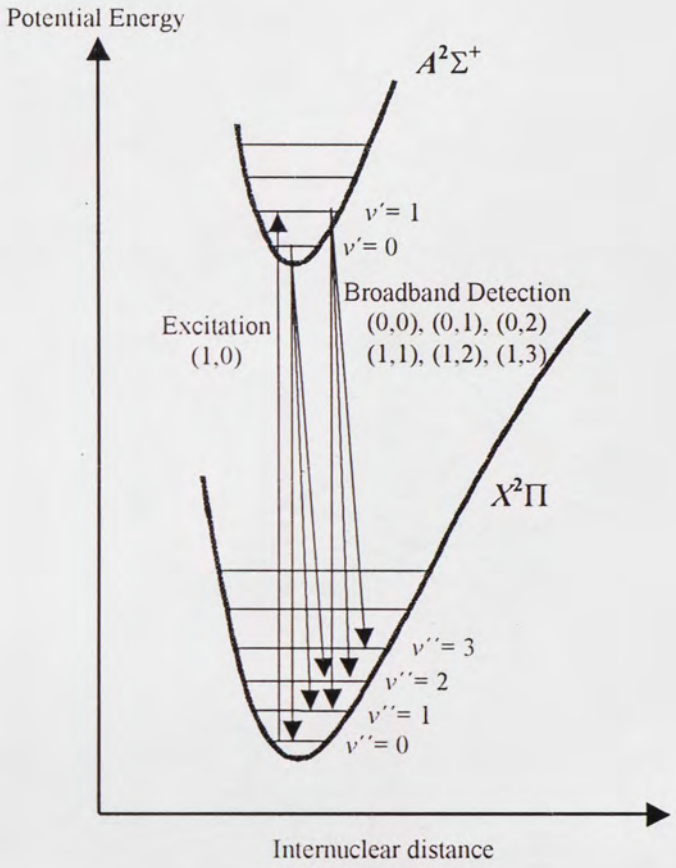

Figure 2-1: Laser-induced fluorescence (LIF) for the present study. Potential energy curves are shown for the ground and excited states. Excitation occurs in the (1,0) vibrational band. Broadband fluorescence is collected.

Once a molecule is excited to an upper electronic energy state, several processes may occur. Fluorescence may take place from the energy level directly excited by the laser, or collisional energy transfer may first cause the molecule to transition to a different electronic, rotational or vibrational state and then fluorescence occurs from that state to the ground state. If inelastic collisions cause the molecule to change its electronic energy level, it is referred to as quenching, as no photon is released. Internal atomic

collisions within the molecule can produce internal energy transfer and even dissociation of the molecule (i.e. predissociation).

Temperature and species concentration are directly related to the ground state population density as discussed in Section 1.2.3 above. The ground state population can be related to the fluorescence signal if the excited molecular state is populated by a laser exciting a transition allowed by the quantum mechanical selection rules. However, due to collisional effects, it is necessary to know not only the rate of radiative decay (fluorescence) from the excited state, but also vibrational and rotational energy transfer rates and electronic quenching rates, which are dependent on thermodynamic and chemical parameters. From these rate models, the observed fluorescence can be related to the undisturbed ground state population. Therefore, an important criterion in selecting a species to perform LIF measurements is that the rates of radiative decay for selected transitions be known.

2.1 LIF Research in Combustion Applications

One of the requirements for performing LIF measurements is that the species used must have well known spectral emission characteristics and absorption wavelengths that are accessible with tunable lasers. Experiments can be found where OH, NO, CO, and CH molecules have been used. Temperature and species concentration have been successfully determined employing LIF in premixed flames as well as turbulent diffusion flames (Goldsmith and Laurendeau, 1986; Arnold *et. al.*, 1992; Meier *et. al.*, 1992;

Kelman and Masri, 1994; Reisel and Laurendeau, 1994; Palmer and Hanson, 1996). Some qualitative LIF measurements of turbulent diffusion flame structure are also available (Seitzman *et. al.*, 1990; Seitzman *et. al.*, 1994).

The hydroxyl molecule (OH) has been the one of the most used LIF probing species. OH provides high fluorescence yield and is present in high concentrations in flames. Several researchers have performed extensive studies on OH emission spectra and an extraordinarily large database exists making OH ideal for LIF in combustion applications (Dieke and Crosswhite, 1962; Lengel and Crosley, 1977; Lengel and Crosley, 1978; Dimpfl and Kinsey, 1979; Luque and Crosley, 1999). OH is also an important intermediate species in combustion because it is formed in almost all flames, is relatively stable and marks the reaction zone in diffusion flames (Crosley and Smith, 1982; Kelman and Masri, 1994; Palmer and Hanson, 1996). For these reasons, OH LIF provides excellent qualitative information, including visualization of turbulent structures and flame location.

2.2 Fluorescence Regimes

Once a target molecule has been identified for LIF measurements, the use of linear or saturated fluorescence has to be considered. In the linear fluorescence regime, the fluorescence yield is proportional to the laser energy (i.e. intensity). In the saturated fluorescence regime, the fluorescence signal is independent of the laser intensity, as the population of the excited state is driven to saturation (i.e. state is "filled"). Saturated

fluorescence measurements solve many of the complications in performing quantitative such as collisional quenching, vibrational energy transfer (VET), and rotational energy transfer (RET) occurring in the excited state since laser absorption and fluorescence emission dominate these energy transfer modes. Fast energy transfers, however, may impair saturated LIF measurements (Campbell, 1984a; Campbell, 1984b). Lucht, et. al. (1982) used saturated LIF measurements to measure temperatures with an accuracy of approximately 5%. Saturated LIF measurements, however, are somewhat difficult to obtain. Laser sources have limited energies and suffer from temporal and spatial energy variations. Laser beams have a Gaussian profile and, at the edges of the beam, saturation may not be achieved due to low laser power. Temporally, a laser might not be able to saturate the transition for the entire duration of a pulse.

Due to the complications discussed above, LIF measurements in the linear fluorescence regime are more common. Thus, rates of electronic quenching, RET and VET must be taken into account in order to correct LIF signals and obtain accurate quantitative measurements. Linear LIF was employed in this study. The sections below will discuss methods to account for these energy transfer modes along with possible sources of error and procedures to select appropriate transitions.

2.3 Error Sources

2.3.1 Laser Non-Uniformities

Spatial and temporal laser beam variations can lead to systematic errors of the measured fluorescence signals. As mentioned above, laser beam usually have a Gaussian energy profile, therefore, at the edges of the laser beam the energy is lower than at the center of the beam. In the linear fluorescence regime, fluorescence intensity is proportional to laser energy, therefore, higher fluorescence signal will be obtained at the center of the beam than at the edges.. Optic used to steer and focus the laser beam might further contribute to the spatial variation in laser energy. This presents a source of error and must be accounted for by measuring the energy profile of the laser. A spatial beam profile can be obtained from an average of scattering laser signals from a uniform field (Hanson *et. al.*, 1990; Seitzmann and Hanson, 1993a; Seitzman *et. al.*, 1994). Further discussion on how beam spatial non-uniformities were corrected for in this project can be found in Section 5.1.2 below.

Energy variations from pulse to pulse (i.e. shot to shot) are also a source of error; these temporal laser energy fluctuations are due to lasing inefficiencies. Shot to shot variations, though, can be minimized by gathering and averaging several fluorescence signals. In this research project forty fluorescence images were taken of each condition investigated. Shot to shot energy fluctuations were monitored and accounted for as described in Section 5.1.1.

2.3.2 Laser Beam Attenuation and Fluorescence Trapping

As a laser beam travels through a medium containing the species being probed (OH in the present case), it is attenuated due to molecular absorption and, thus, the excitation power of the laser is reduced. This results in higher fluorescence signals where the laser first encounters the medium than where it leaves it behind. Attenuation is affected by the concentration of the species being probed, the path length the laser has to travel through the medium, and the line strength of the transition being excited. Attenuation can be minimized if a weak line is excited. However, this would lower signal-to-noise ratio and interpretation of the fluorescence signals would be impaired (Quagliaroli *et. al.*, 1993). The symmetry of axisymmetric flames (as the ones studied here) provides means of correcting for attenuation since fluorescence signal at both edges of the flame should be identical (refer to Section 5.1.4).

Fluorescence photons emitted by the excited molecules might be absorbed by other molecules; this is referred to as trapping. At high temperature and for transitions in low vibronic states (i.e. low v), fluorescence might be absorbed by molecules populating the ground state (Quagliaroli *et. al.*, 1993). As a result, the fluorescence signal is attenuated as seen by the detector (i.e.camera). Measurement of OH fluorescence in the (0,0) band of the $A^2\Sigma^+ \leftarrow X^2\Pi$ transition is difficult since most the fluorescence is emitted in the same vibrational band, which maximizes trapping. The (0,0) band of OH has the highest transition probability as seen in Figure 2-2, but due to fluorescence trapping, weaker bands such as (1,0) and (1,1) have been used by researchers (Seitzman and

Hanson, 1993a). Trapping is also affected by the path length through the medium. Therefore, large flames result in larger fluorescence trapping due to the presence of more absorbing species. Correcting for fluorescence trapping would require knowledge of temperature and molecular concentration distribution (precisely the quantities sought by using LIF). Therefore, LIF experiments are usually designed to minimize fluorescence trapping by careful selection of excitation transitions.

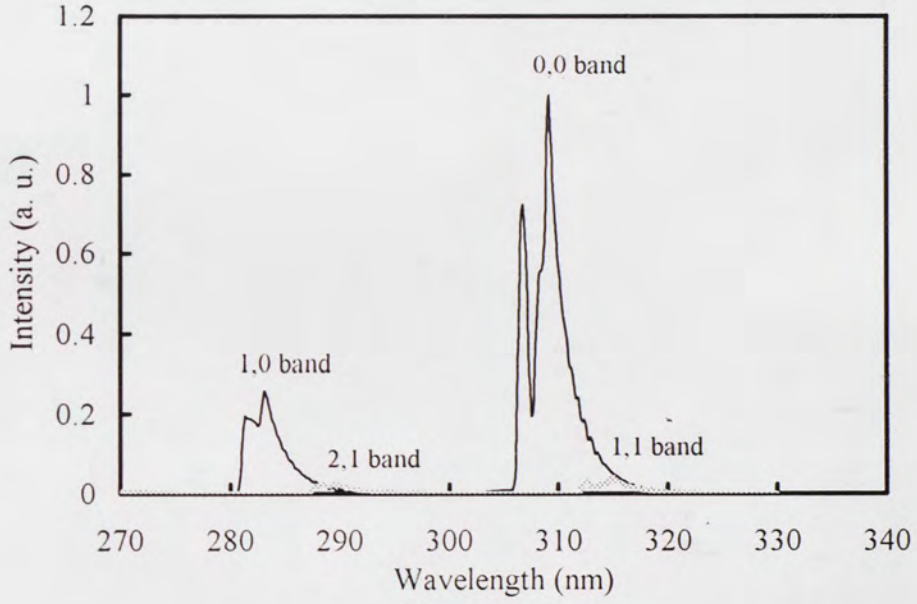

Figure 2-2: Vibrational band transition strengths of the $A^2\Sigma^+ \leftarrow X^2\Pi$ System.

2.3.3 Interference

Fluorescence may interact with other species present in the flame or medium being probed. Radical species, soot, and other molecules may present signal interference. Interference can be caused by scattering, laser induced incandescence (LII, Eckbreth, 1996), and LIF from other molecules. Laser beam scattering off experimental surfaces may be minimized or eliminated by proper optical setup and access. Rayleigh scattering (elastic scattering of light quanta from molecules or particles) and Raman scattering (inelastic scattering) from other species and particles can pose more of a concern.

Rayleigh scattering of the laser beam becomes important when detecting fluorescence in the same band as the excitation. When fluorescence is detected in different bands than the pump (as it is the case in this study), use of spectral filters to block out the incident laser beam will also block Rayleigh scattered signals. Raman scattering signals are shifted in frequency by an amount corresponding to the rotational and/or vibrational motions of the molecule (Daily, 1997). According to Eckbreth (1996) minimization of the Raman signals can be achieved by selecting transitions that avoid Raman bands, for example exciting the (1,0) band and collecting the fluorescence in the (1,1) band. This approach was taken in this study; Raman signals, however, are usually much weaker than fluorescence signals (Eckbreth, 1996). In addition, soot interference was not of concern in this study since hydrogen was used and no carbon species were present.

2.4 Two-Line Planar Laser-Induced Fluorescence (PLIF) Thermometry

The technique adopted in this study in order to extract temperature information from gathered fluorescence signals was PLIF. Here, a laser beam was formed into a sheet and two-dimensional fluorescence images were gathered. The two-line fluorescence technique for temperature measurement involves sequential excitation scans to a common vibrational level in an excited electronic state from two different rotational levels in the ground electronic state. Figure 2-3 illustrates the basic concept of two-line fluorescence. First, the molecule is excited by laser pumping from level 1 to level 3 and the fluorescence from level 3 to 2 is collected, then, the molecule is pumped from level 2 to level 3, and the fluorescence from 3 to 1 is detected. Two different rotational levels in the excited electronic state are pumped. However, because the same excited vibronic state is pumped, collisional rates are assumed to be the same. Scattering interference is minimized because fluorescence detection occurs in a different vibrational band than the laser excitation.

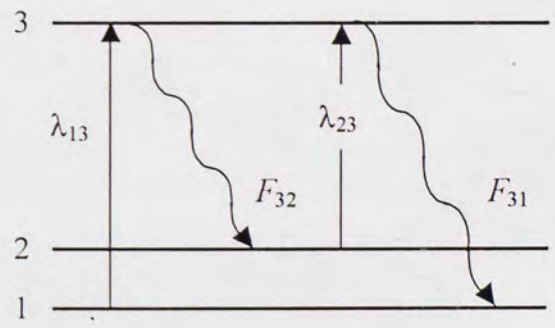

Figure 2-3: Two-line fluorescence.

Assuming steady-state and pumping level 1 to level 3, the fluorescence from level 3 to level 2 is given by (Eckbreth, 1996):

$$F_{32} \sim N_3 A_{32} = \frac{N_1 b_{13} A_{32}}{b_{31} + A + Q} \tag{2.1}$$

where N_i (i.e. N_1, N_2, etc.) is the population of the i^{th} level, A_{32} is the transition probability (or Einstein coefficient) for spontaneous emission, b_{13} is the absorption rate, and b_{31} the rate for stimulated emission. In the above equation, $A = A_{31} + A_{32}$ and the quenching rate $Q = Q_{31} + Q_{32}$. Similarly, pumping level 2 to level 3, the fluorescence from level 3 to level 1 is given by:

$$F_{31} \sim N_3 A_{31} = \frac{N_2 b_{23} A_{31}}{b_{32} + A + Q} \tag{2.2}$$

Einstein showed that for transitions between two states, i and j, the Einstein coefficients are related by following relationships (Eckbreth, 1996):

$$b_{ij} = \frac{B_{ij} I_{ij}^{\nu}}{c}; \quad \frac{A_{ij}}{B_{ij}} = \frac{8\pi h}{\lambda_{ij}^3}; \quad g_i B_{ij} = g_j B_{ji} \tag{2.3}$$

where the B's are the Einstein coefficients for stimulated emission, I^{ν}_{ij} is the spectral irradiance (laser intensity per unit frequency interval), c is the speed of light, h is Planck's constant, λ is the excitation wavelength, and g_i is the degeneracy of state i.

The fluorescence ratio is proportional to the relative population in the absorbing states and hence is a function of temperature through Boltzmann statistics (see Section 1.2.3.3.5). Using Equation (1.16) and taking the ratio N_2/N_1 for the two transitions yields:

$$\frac{N_2}{N_1} = \frac{g_2}{g_1} e^{-\frac{hc}{kT}(E_2 - E_1)} \tag{2.4}$$

Taking the ratio of the fluorescence signal from the two transitions (Equations (2.1) and (2.2)), substituting the expressions of Equations (2.3) and (2.4), and assuming that, for the linear fluorescence regime, $b << A + Q$ (Eckbreth, 1996), a number of parameters which are affected by trapping and collisional rates cancel out (Eckbreth, 1996):

$$\frac{F_{31}}{F_{32}} = \frac{N_2 B_{23} I_{23} A_{31}}{N_1 B_{13} I_{13} A_{32}} = \frac{N_2 g_3 g_1 B_{32} I_{23} A_{31}}{N_1 g_2 g_3 B_{31} I_{13} A_{32}} = \frac{I_{23} \lambda_{32}^3}{I_{13} \lambda_{31}^3} e^{-\frac{hc}{kT}(E_2 - E_1)} \tag{2.5}$$

If the lower states of the two transitions differ only by rotational quantum number, then the measurement is of rotational temperature. Thermodynamic (translational) temperature can be assumed to be in equilibrium with rotational temperature in most combustion conditions. Thus, a direct relationship between temperature and fluorescence

signals of two different rotational transitions is given by Equation (2.5). The two-line method eliminates the need to know quenching, rotational, and vibrational energy transfer rates.

Two-line OH LIF has been used successfully by Cattolica (1981) to measure temperature in a methane-air flat flame accurate to within 5% (at 2,000K). Lucht, *et. al.* (1982) reported errors of 3-5% in temperatures measured using two-line OH saturated LIF as compared with absorption and corrected thermocouple measurements. Two-line thermometry has been successfully employed by several researchers in sooting environments (Lucht et. al., 1985; Santoianni *et. al.*, 2001) and in situations involving supersonic flows (Seitzman and Hanson, 1993b; Palmer and Hanson, 1996).

2.5 Transition Selection

When performing two-line thermometry, transitions need to be selected carefully in order to obtain the best possible signals. Transitions need to be accessible with available laser sources. In addition, the strength of the transition needs to be high enough to have a good signal-to-noise ratio. Transitions in the $A^2\Sigma^+ \leftarrow X^2\Pi$ (1,0) OH system were used in this research. These transitions have been commonly used (Seitzman *et. al.*, 1994) since scattered light can be rejected with the use of proper spectral filters (fluorescence occurs at different wavelengths from excitation) and signal strength is good (see Figure 2-2). Referring to Figure 1-5, the strongest signals typically are encountered in the Q branch ($J' = J''$) transitions. Transitions in this branch were chosen for this study

in order to maximize signal-to-noise ratio. One further concern is the proper isolation of transitions needed to avoid excitation of lines close to the transitions being pumped by the laser. It has been recommended that the minimum line separation should be on the order of 1 cm^{-1} for atmospheric pressure flames (Seitzman *et. al.*, 1994; Palmer and Hanson, 1996). From data obtained from Luque and Crosley (1999) and Dieke and Crosswhite (1962), several transitions do not meet this criterion such as $R_1(6)$, $Q_1(9)$, or $Q_2(4)$.

The temperature sensitivity of the selected lines needs to be considered. Figure 2-4 shows the temperature sensitivity and range of various Q-branch transition pairs in the $A^2\Sigma^+ \leftarrow X^2\Pi$ (1,0) OH system. Using Equation (2.4) the slope sensitivity of the ratio of the population in the ground states being pumped is:

$$\left|\frac{dN_R}{N_R}\right| = \left|\frac{\Delta\varepsilon_{12}}{T}\frac{dT}{T}\right| \tag{2.6}$$

where N_R represents the ratio of the two populations (N_2/N_1) and $\Delta\varepsilon_{12} = hc(E_2-E_1)/k$ is the energy separation of the selected transitions (in degrees Kelvin). With high slope sensitivity (i.e. $|\Delta\varepsilon_{12}/T|$) errors in the measured ratio produce small errors in the calculated temperature, thus, a large value of $\Delta\varepsilon_{12}$ is desirable. However, to increase fluorescence yield and maximize signal-to-noise ratio, transitions with large population fractions (and, thus, low energy separations) are needed. This presents a trade-off and it is usually handled by selecting transitions where $\Delta\varepsilon_{12}$ is of the same order as the maximum

temperature expected in the flame being measured (Seitzman *et. al.*, 1994). The $Q_1(5)/Q_1(14)$ pair was chosen in this research for its proper temperature range and high slope sensitivity. The transitions are also well isolated, as shown by the absorption spectrum in Figure 2-5 (calculated from data in Dieke and Crosswhite, 1962 and Luque and Crosley, 1999). To minimize fluorescence trapping (Section 2.3.2), broadband fluorescence was collected after excitation of the $Q_1(5)$ and $Q_1(14)$ lines (see Figure 2-1) to obtain signal ratios which are relatively insensitive to trapping (Cattolica, 1981; Seitzman *et. al.*, 1994).

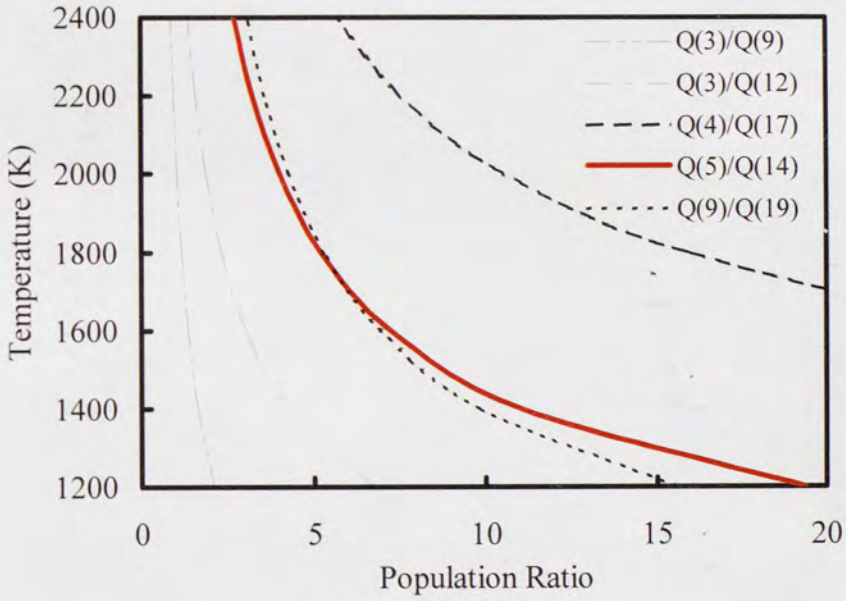

Figure 2-4: Temperature sensitivity of OH $A^2\Sigma^+ \leftarrow X^2\Pi$ (1,0) transition pairs in the Q branch; red denotes pairs used in this study.

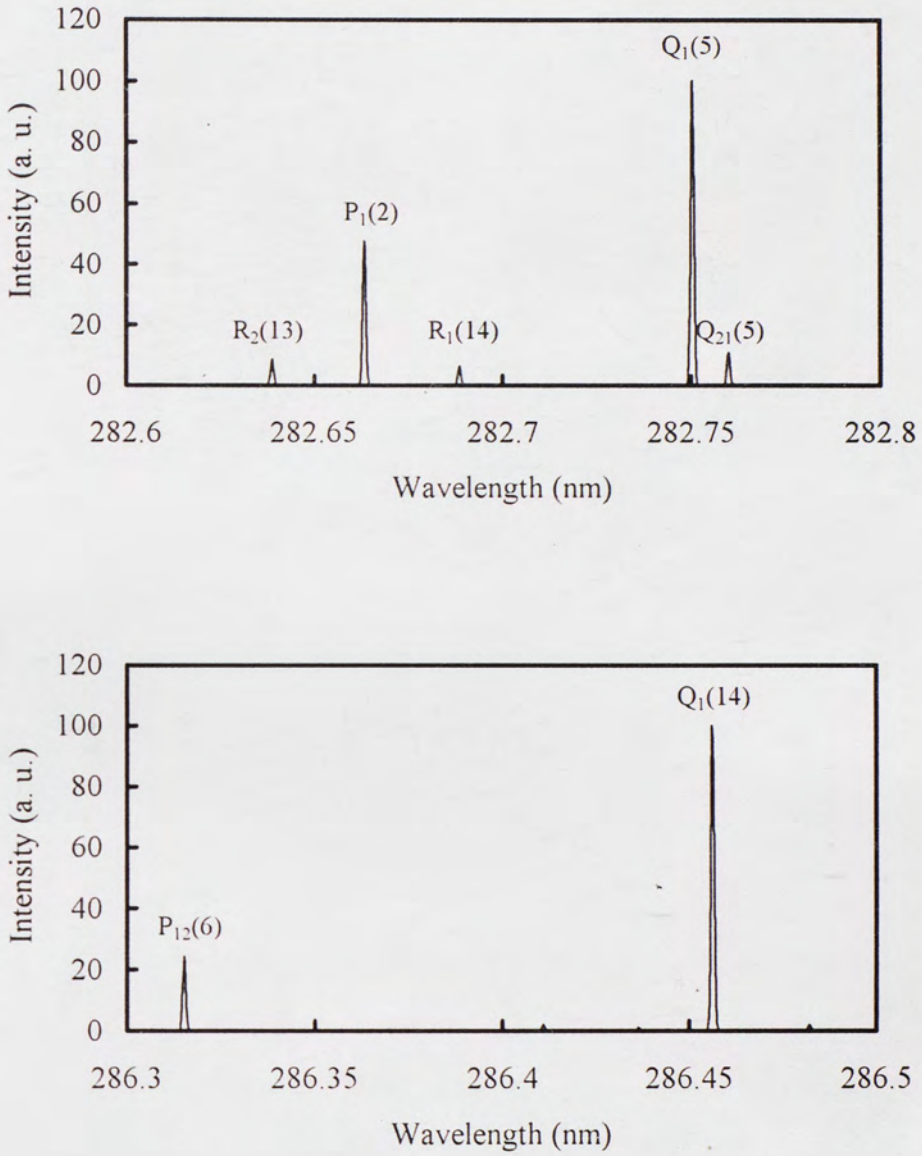

Figure 2-5: OH absorption spectrum at 1500 K. Note the separation and strength of the selected Q-branch lines relative to nearby cross branches.

3 EXPERIMENTAL SETUP

This research work studied a flame similar to those presented by Chen *et. al.* (1997) except controlled vortices (i.e. frequency and amplitude) were generated acoustically by using a loudspeaker. These pulsed flames were to simulate the unsteady nature of most practical flames, which are frequently turbulent. The controlled vortices allowed for a deterministic study on the effects of various turbulent scales.

Several experimental procedures were implemented in this work to measure velocity, temperature, and planar laser-induced fluorescence (PLIF) of the hydroxyl molecule (OH) of unsteady hydrogen flames diluted with helium or argon. The temperature data discerned from these experiments along with OH concentration data will allow for the determination of the coupled effect of transport properties and flame dynamics on reaction zone structure and flame temperature. A description of the laminar flame burner along with the apparatus for each experimental procedure performed in this study is given below.

3.1 Pulsed Laminar Flame Burner

The main burner used in this research project is depicted in Figure 3-1. A laminar diffusion flame was generated by ejecting hydrogen (99.995 % purity) diluted with either

helium or argon vertically upward from a straight circular tube into coflowing air. Dilution levels (by volume) and fuel Lewis numbers tested were similar to those of Chen *et. al.* (1997) and are listed in Table 3-1. The Lewis numbers (i.e. Le_F) shown in Table 3-1 were calculated from thermodynamic properties (i.e. binary mass diffusivity and thermal diffusivity) obtained from a website (Dandy, 2003). Table 3-1 also lists the adiabatic flame temperatures (T_{ad}) of the fuel mixtures used, which were calculated using CHEMKIN (Kee *et. al.*, 2000). The fuel tube was made of stainless steel with inside and outside diameters of 4.6 and 6.5 mm respectively, the outside diameter tapered down to 5.5 mm towards the tube exit. The coflowing air annulus had an inside diameter of 60 mm. Solid glass beads (Fisher Scientific) 1 mm in diameter and stainless steel screens were used to ensure uniform flow velocities. The flame and combustion products were confined in a vycor glass tube to shield them from any room drafts and to allow optical access.

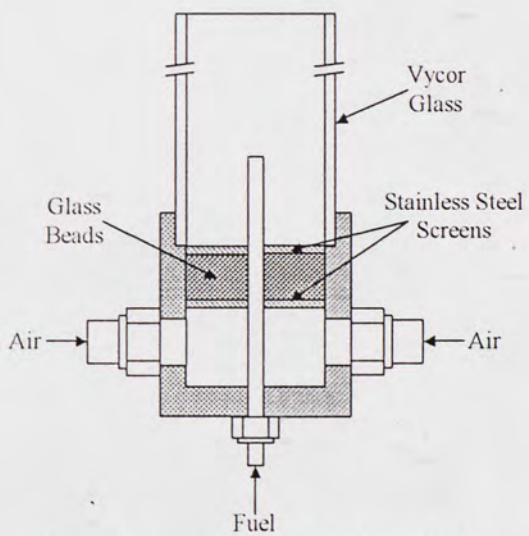

Figure 3-1: Laminar flame burner.

Table 3-1: Fuel Lewis numbers (Le_F) and adiabatic flame temperatures

Dilution Level*	Diluent		T_{ad} (K)**
	He	Ar	
20%	0.998	1.389	2323
40%	1.012	1.012	2226
60%	1.035	0.718	2041

*Degree of dilution by volume
**Adiabatic flame temperature calculated using CHEMKIN (Kee *et. al.*, 2000)

Figure 3-2 shows the schematic of the pulsed flame burner. The fuel tube was connected to a Plexiglas plenum to which a 50 Watt, 203.2 mm diameter polypropylene woofer speaker was attached (Radio Shack, Cat. No. 40-1024A) with a frequency response of 35 Hz to 3000 Hz. Motion of the speaker cone modulated the pressure within the Plexiglas plenum and, thus, the exit fuel flow. The speaker was lined with a 40A Durometer latex rubber sheet 0.203 mm thick. The plenum cavity was a rectangular parallelepiped of size 263.5 x 263.5 x 5.56 mm. Controlled fluctuations of the fuel flow were accomplished by applying an amplified sine wave to the speaker. The sine wave was generated by a Stanford Research Systems (SRS) DS335 3.1 MHz synthesized function generator. The function generator had an amplitude limit of 20 volts peak-to-peak and could not supply enough current to drive the speaker; therefore, an Optimus MPA-125 100 Watt power amplifier was used to provide a 2:1 amplification of the voltage of the sinusoidal signal. The amplifier response was slightly frequency dependent; thus, as different frequencies were tested, the amplifier output had to be adjusted to maintain the 2:1 amplification. Fuel, diluent, and air flowrates in the laminar

flame burner were measured and controlled using MKS mass flow controllers with an accuracy of ± 1% of their full scale range. Flowrates supplied to the burner for each specific dilution level are listed in Table 3-2. A matrix of the experimental conditions listing the speaker parameters tested is given in Table 3-3.

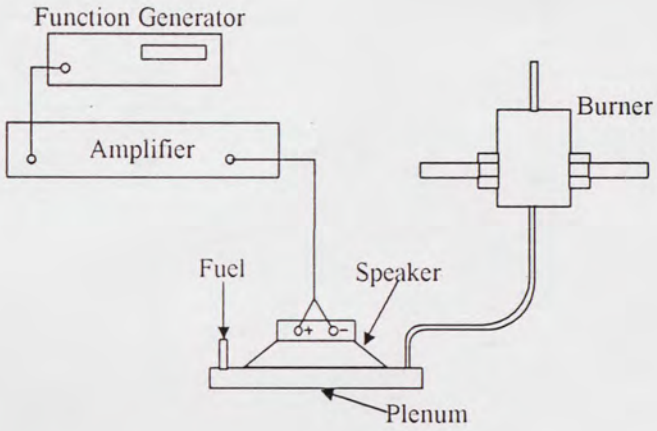

Figure 3-2: Laminar flame burner setup.

Steady air and fuel velocities were kept equal to avoid any shear instabilities and flame flicker (i.e. Burke-Schumann flame conditions). Thus, the only strain induced in the flame would be a result of the vortices introduced by the loudspeaker. The mean exit velocity was kept constant at 30 cm/s for all the experiments herein described. Flames were short (approximately 10 mm) and converged toward the axis of symmetry (i.e. overventilated flames, Glassman, 1996) since air was in abundance (i.e. fuel-limited flames). The Reynolds number based on the fuel tube diameter and the fuel mixture properties at atmospheric conditions varied between 10 and 60 approximately assuring a laminar flame.

Table 3-2: Laminar flame burner flowrates

Dilution Level	H_2 (cm^3/min)	Diluent (cm^3/min)	Air Coflow (L/min)
20%	239	60	50.6
40%	179	120	50.6
60%	120	179	50.6

30 cm/s constant exit velocity

Table 3-3: Pulse test conditions

Frequency	Amplitude*	20% Dilution	40% Dilution	60% Dilution
10 Hz	low	0.4 V	0.3 V	0.25 V
	high	0.7 V	0.6 V	0.5 V
100 Hz	low	12.5V	10 V	5 V
	high	25 V	20 V	10 V

*Voltages listed are as measured at the speaker

3.2 Thermocouple Measurements of Steady Flames

Temperature measurements were taken of steady flames for comparison with data obtained from the laser-induced fluorescence experiments discussed below. Radial temperature profiles were obtained at 2 mm intervals along the flame axis of hydrogen flames diluted with helium or argon (see Table 3-1 and Table 3-2 for test conditions). Temperatures were measured with a fine wire R-type (Pt – Pt/13 % Rh) thermocouple with a bead size of approximately 200 μm. The thermocouple was mounted on a

computer controlled traversing table with a resolution of 5 μm. Radial temperature profiles were taken with a thermocouple traversing speed of 200 μm/s. Thermocouple voltages were read by a computer-based data acquisition board (National Instruments, PCI-6034E) programmed to take data at a fixed rate of 25 Hz, thus providing eight measurements per μm. The board was controlled with the help of LabView, a software package from National Instruments. LabView is a graphical user interface that can be used to create "virtual" instruments to acquire, analyze and display data. The graphical diagram of the program developed for data acquisition is shown in Appendix A.

Raw thermocouple data was corrected for radiation losses following the procedures of Bradley and Matthews (1968) which are discussed in-depth in Section 4.1. For radiation exchange purposes, the thermocouple was assumed to interact only with the surroundings, which were treated as a black body. Thermodynamic gas properties used for correction were those of the stoichiometric combustion products and were calculated using software located on a website (Dandy, 2003) which is based on the CHEMKIN database (Kee *et. al.*, 2000). Thermodynamic data used can be found in Table 3-4 and Table 3-5 for He and Ar dilutions respectively. Emissivity values for the R-type thermocouple used were obtained from Glawe and Shepard (1954). As will be discussed in Section 4.1, the correction process was iterative.

Table 3-4: Thermodynamic properties of combustion gases (He dilution)

T (K)	ρ (kg/m^3)	μ (kg/ m s)	k (W/m K)	C_p (J/kg K)
		20 % Dilution		
1400	0.19936	5.18057 E-05	0.13145	1619.8
1600	0.17444	5.70297 E-05	0.14804	1663.0
1800	0.15506	6.20178 E-05	0.16402	1699.3
2000	0.13955	6.67956 E-05	0.17939	1729.7
2200	0.12687	7.13974 E-05	0.19419	1755.1
		40 % Dilution		
1400	0.18004	5.25123 E-05	0.14760	1701.0
1600	0.15753	5.77867 E-05	0.16535	1743.3
1800	0.14003	6.28231 E-05	0.18246	1778.7
2000	0.12603	6.76529 E-05	0.19892	1808.4
2200	0.11457	7.22994 E-05	0.21479	1833.2
		60 % Dilution		
1400	0.15242	5.35665 E-05	0.17507	1852.8
1600	0.13337	5.89095 E-05	0.19484	1893.3
1800	0.11855	6.40111 E-05	0.21387	1927.2
2000	0.10669	6.89036 E-05	0.23221	1955.6
2200	0.09699	7.36214 E-05	0.24992	1979.3

Table 3-5: Thermodynamic properties of combustion gases (Ar dilution)

T (K)	ρ (kg/m^3)	μ (kg/ m s)	k (W/m K)	C_p (J/kg K)
20 % Dilution				
1400	0.22435	5.30251 E-05	0.11501	1439.4
1600	0.19630	5.83305 E-05	0.12986	1477.8
1800	0.17449	6.33905 E-05	0.14415	1510.1
2000	0.15704	6.82402 E-05	0.15790	1537.1
2200	0.14277	7.29084 E-05	0.17112	1559.6
40 % Dilution				
1400	0.23884	5.52676 E-05	0.10727	1282.2
1600	0.20898	6.07233 E-05	0.12083	1314.1
1800	0.18576	6.59244 E-05	0.13387	1340.8
2000	0.16719	7.09103 E-05	0.14641	1363.2
2200	0.15199	7.57062 E-05	0.15847	1381.9
60 % Dilution				
1400	0.25955	5.83105 E-05	0.09650	1088.1
1600	0.22711	6.39655 E-05	0.10827	1111.8
1800	0.20187	6.93504 E-05	0.11958	1131.7
2000	0.18169	7.45147 E-05	0.13045	1148.4
2200	0.16517	7.94782 E-05	0.14090	1162.3

3.3 Laser Doppler Velocimetry

In an effort to characterize the flow disturbance introduced by the speaker, velocity measurements were performed using a Laser Doppler Velocimetry (LDV) system. The LDV system layout is shown in Figure 3-3. A TSI 9100 LDV system was used. The entire system was mounted on a three-axis traversing table (TSI model 9500) with a resolution of 2.5 μm while the burner remained stationary mounted on a separate surface. The system consisted of a Spectra-Physics Model 2020 Argon Ion laser, which provided two colors of laser light at 514.5 and 488 nm, two polarization rotators (TSI 9101 and TSI 9102-12), an attenuator (TSI 9136), a dispersion prism and mirror (TSI 9106), a steering mirror (TSI 9107), a beamsplitter (TSI 9115), a Bragg cell (TSI 9182), a beam spacer (TSI 9207), and a focusing lens (TSI 9169-250). Scattered laser light was collected using a TSI 9160 photomultiplier system. Photomultiplier signals were gathered and analyzed using a TSI 1990C counter-type signal processor interfacing with a personal computer. The system was operated in the forward scattered mode.

Only the axial velocity at the centerline of the fuel tube axis was measured. Therefore, only one line of the laser light emission was used (the 514.5 nm green component) which was separated from the 488 nm line by the dispersion prism. The 514.5 nm beam was split and the two resulting beams had a separation of 100 mm. Since the focusing lens had a focal length of 250 mm, the crossing of these beams generated a probe volume of 130 μm in diameter and 650 μm in length approximately with fringe

spacing of 1.31 μm. The beams were polarized in a plane normal to and were crossed in a plane parallel to the centerline of the burner.

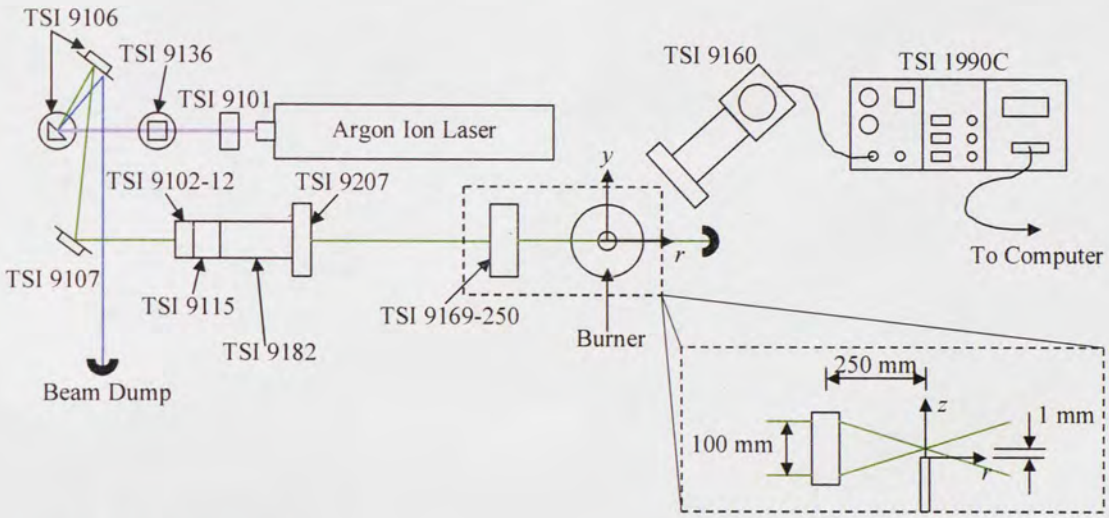

Figure 3-3: LDV layout.

Velocity was measured in a cold isothermal air flow (i.e. in the absence of combustion) 1 mm above the fuel tube exit. Measurements at the exit plane of the fuel tube could not be performed since the tube interfered with one of the laser beams. A Bragg cell was used to frequency shift one of the beams. Fringes at the measurement location, thus, were not stationary but moved at a selected frequency. The direction of fringe movement was in the negative z-direction (i.e. towards the fuel tube, see Figure 3-3). The net frequency shift was 1 MHz which allowed for velocity measurements down to approximately –1.3 m/s.

The flow was seeded with atomized water particles using a TSI Model 9306 6-jet atomizer. The atomizer provided a high concentration of 1- 2 μm particles needed for the

measurements. Atomized particles were introduced upstream of the speaker plenum (more precisely, between the plenum and the flow controller delivering gas to the fuel tube) as seen in Figure 3-4. Once the atomizer pressure and flowrate were optimized for maximum seeder concentration (i.e. high data rate), the flow controller was adjusted to provide an exit velocity of 30 cm/s, which was the mean exit velocity used in the unsteady experiments.

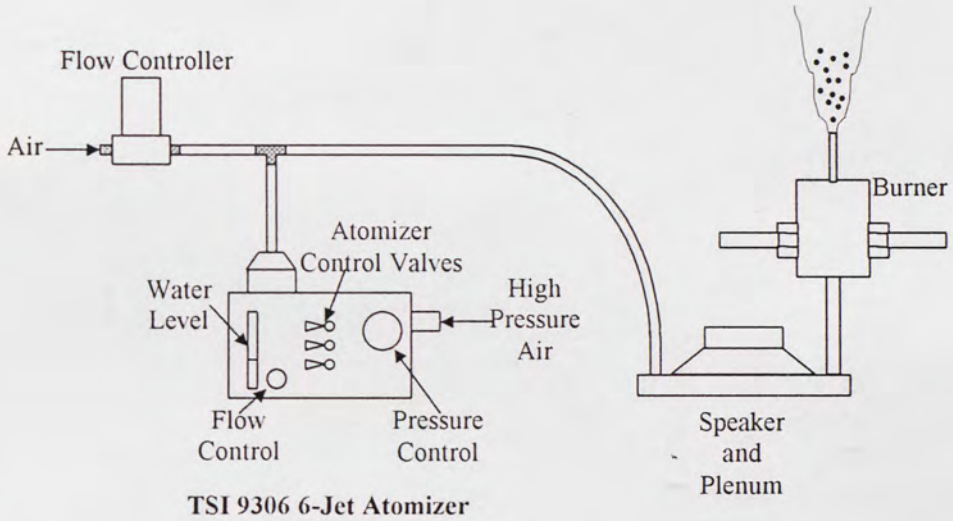

Figure 3-4: Atomizer setup.

LDV data was gathered in the continuous mode where velocity was measured as the particles crossed a specified number of fringes. Therefore, high data rates were needed (i.e. higher than the pulsing frequency of the speaker) in order to meet the Nyquist criterion. Data rates were on the order of 1000 – 2000 Hz, which were 5 to 10 times the maximum speaker forcing frequency tested (i.e. 200 Hz).

It was of interest to extract the amplitude of the velocity oscillation generated by the speaker and, thus, obtain a measure of the turbulence intensity introduced in the laminar flow. A time history of the signal was needed for this purpose. Two outputs were used from the TSI 1990C counter in order to record the arrival time of the signals and the magnitude of the measured velocity. The data collection setup is shown in Figure 3-5. A LabView program was written to read data from a computer based acquisition board (National Instruments PCI – 6034E). The board was wired to an external connector block where the signals were attached (National Instruments CB-68LP). The graphical LabView interface environment developed can be found in Appendix A.

The data acquisition board has a high resolution counter capable of making time measurements with an accuracy of 50 ns. The MONITOR signal from the 1990C counter is an analog 0-10 V signal proportional to the measured Doppler frequency. This signal cannot be continuously recorded since it only updates once a particle produces a valid Doppler signal. Therefore, the DATA READY signal from the 1990C was used to latch data into the computer. This signal is a positive TTL (Transistor Transistor Logic) signal and is issued every time the MONITOR signal is updated. The trailing edge of this signal was used to trigger the data acquisition board and the counter (see Figure 3-5). Thus, the counter measured the time between incoming signals.

Data collected by the process described above was analyzed using the procedures described in Adrian and Yao (1987), Nobach (2000), and Benedict *et. al.* (2000) with the help of a computer program found on a website (Nobach, 2003).

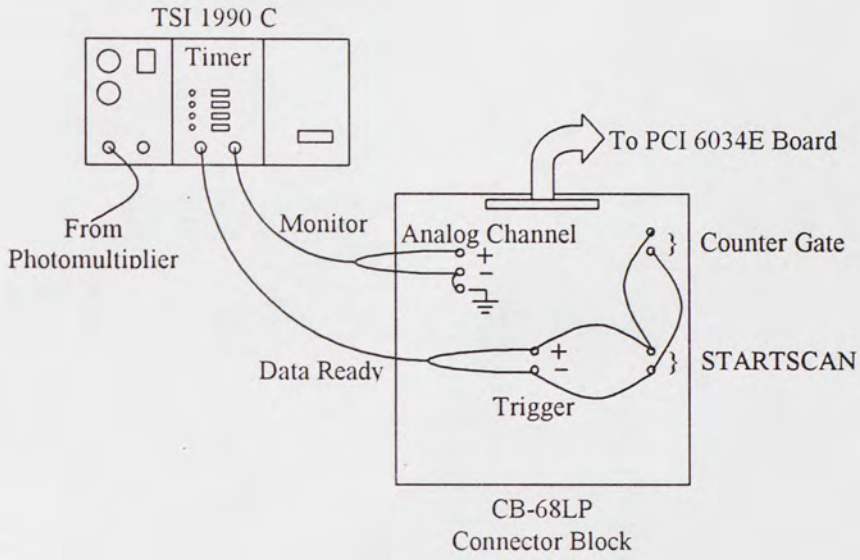

Figure 3-5: LDV data collection.

3.4 Planar Laser–Induced Fluorescence (PLIF) Experiment

3.4.1 Summary

Laser-induced fluorescence of the OH radical was performed on steady and unsteady hydrogen laminar flames. The selected transitions ($Q_1(5)$ and $Q_1(14)$ as discussed in Section 2 above) were accessed by using an elaborate ultraviolet (UV) two-laser two-camera system. Images of broadband fluorescence of steady and unsteady flames were gathered and were related to temperature by proper calibration. A detailed description of the components and optical setup of such system is provided in the sections below as well as procedures to ensure proper timing of the system to capture the unsteady nature of the flames studied, laser tuning, laser energy monitoring, and calibration issues.

3.4.2 Optical Layout

Excitation of the $Q_1(5)$ and $Q_1(14)$ transitions of the $A^2\Sigma^+ \leftarrow X^2\Pi$ (1,0) band of OH was carried out using a YAG-pumped dye laser system. A schematic of the system setup is shown in Figure 3-6. Two pulsed Continuum Surelite III Nd: YAG lasers were used to separately pump a Lambda Physik FL3002 dye laser ($Q_1(5)$ excitation) and a Continuum Jaguar dye laser ($Q_1(14)$ excitation). The YAG lasers were Q-switched to produce short pulses (approximately 8 ns) at a repetition rate of 10 Hz. The second harmonic (532 nm) was used on both the YAG lasers; at this wavelength, the maximum energy output of the lasers was 425 mJ approximately. The dye lasers, which cannot lase independently and, thus, must be pumped by another laser source, were capable of producing a range of wavelengths depending on the dye used. Rhodamine 6G (i.e. Rhodamine 590 chloride, $C_{28}H_{31}0_3N_2$) was used in this experiment to pump the selected OH transitions. This dye has a tuning range of 555-585 nm. The energy conversion efficiency of the dye laser varies and is a function of the dye, the tuning of the optical cavity, and the beam quality of the pump. Typical efficiency of the YAG-dye laser system used was 20 percent approximately.

In order to extract ultraviolet (UV) radiation from the output of the dye lasers to excite the $Q_1(5)$ (282.75 nm; 35,367 cm^{-1}) and $Q_1(14)$ (286.46 nm; 34,909 cm^{-1}) transitions of OH, the output laser beams, which were in the visible range, were passed through beta-barium borate (BBO) doubling crystals (6x5x7 mm, Type I, 43.5 degrees) where approximately 10 percent of the beams radiation was frequency doubled to UV.

The UV and visible wavelengths leaving the doubling crystals were separated using Pellin-Broca prisms. The visible wavelength beams were routed to beam dumps and the UV beams were steered to the interrogation region of the flame as shown in Figure 3-6. The laser linewidth of the dye lasers used was approximately 0.5 cm^{-1}. Since the separation of the selected transitions with respect to nearby transitions was on the order of more than 2 cm^{-1} (see Figure 2-5), inadvertent excitation of these transitions was eliminated.

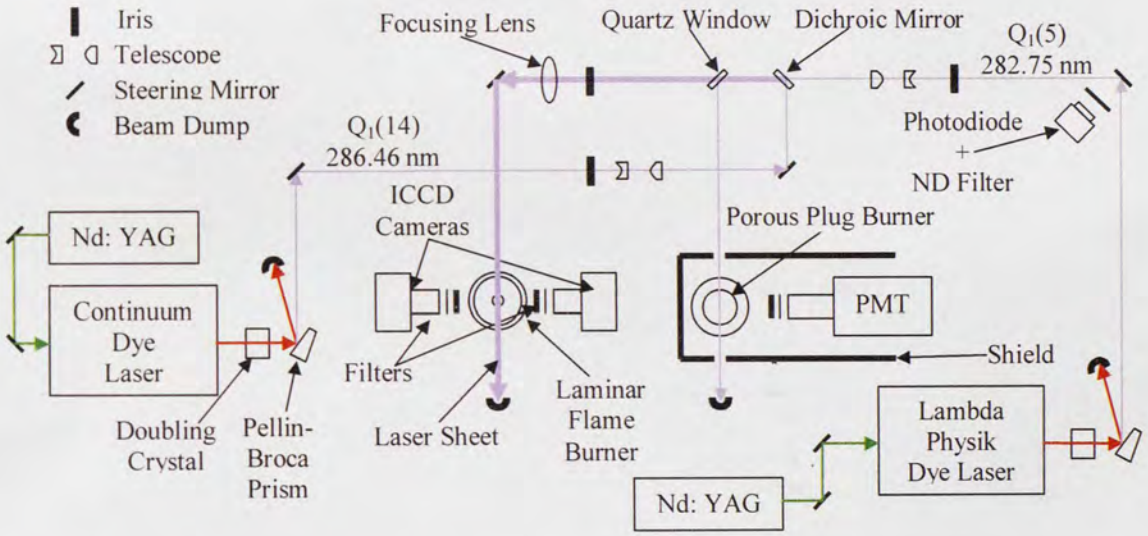

Figure 3-6: PLIF optical layout.

Facing one of the steering mirrors, a photodiode (Thor Labs DET2-SI High Speed Silicon Detector) was placed for timing purposes as will be explained in Section 3.4.4 below. A neutral density (ND) filter was placed on front of the photodiode to eliminate beam variances. After passing through iris type apertures, both UV beams were expanded using a telescope system comprising of two spherical lenses. One spherical

lens (25.4 mm diameter, -75 mm focal length) expanded the beams while the second lens (38.1 mm diameter, 127 mm focal length) recollimated them. Both UV pulses were then combined into a single beam using a dichroic mirror. Approximately 8 percent of the combined beam was reflected by a quartz (i.e. fused silica) window and directed across the surface of a porous plug burner. The porous plug burner burned the same fuel that was being used by the laminar flame burner (i.e. hydrogen-air flame) and it was used to ensure proper tuning on the selected OH transitions

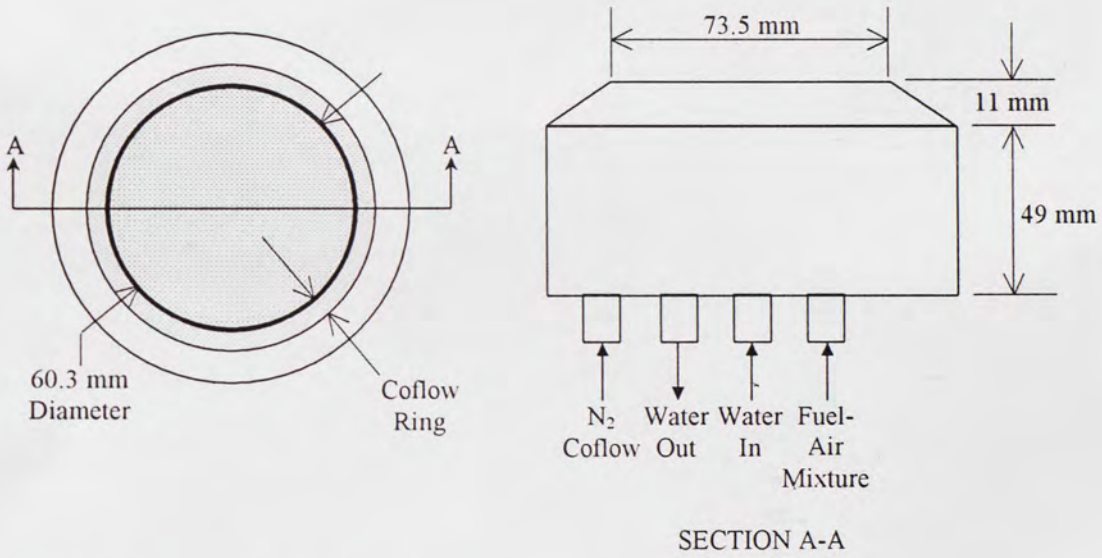

Figure 3-7: Porous plug burner schematic.

A schematic of the porous plug burner is shown in Figure 3-7. The porous plug burner was made of sintered bronze, which established a premixed flat flame slightly above the burner surface. A coflow ring around the central burner allowed a nitrogen curtain to isolate the flame from entrainment of ambient air, which would locally change

the stoichiometry. The burner was water cooled to protect the bronze plug. A photomultiplier (PMT) (Products for Research, Inc.) was positioned 90 degrees to the beam passing over the porous plug burner and collected the OH fluorescence signal. The PMT is a high-gain, low-noise light detector that can detect single photons over a wide spectral range. Filters were placed in front of the PMT to block wavelengths below 290 nm including the laser pump itself (Melles Griot WG-305), and visible wavelength (i.e. room lights) (Melles Griot UG-11). Therefore, the majority of the radiation collected was a result of the broadband fluorescence of the OH radical (mostly from the (0,1) and (1,2) vibrational bands). Spectral curves for the WG-305 and UG-11 filters are shown in Figure 3-8. The PMT was shielded from stray laser light by black cardboard fencing.

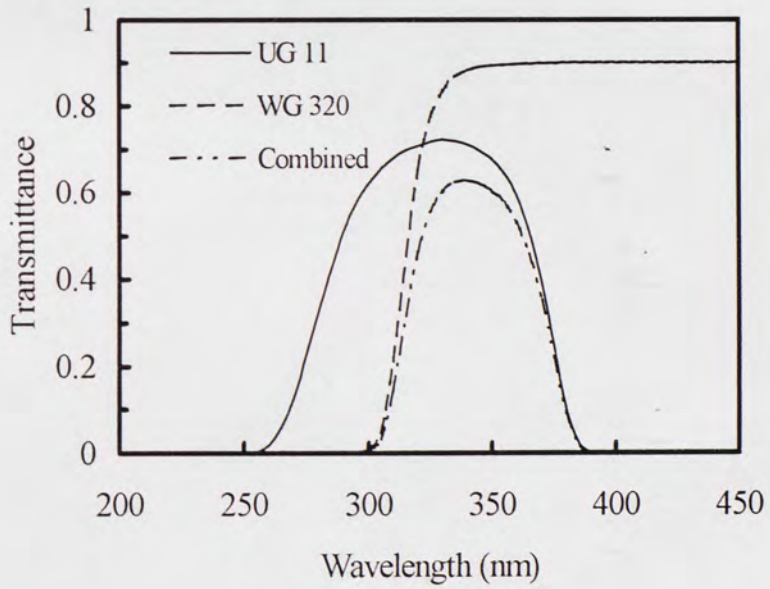

Figure 3-8: Spectral filters transmission curves.

Once the combined UV beam passed through the quartz window, it passed through an iris aperture and a plano-convex focusing lens (25.4 mm diameter, 1.1 m focal length) to form a thin laser sheet 10 mm tall and 200 μm thick. The laser intensity of the UV beams was measured before and after each set of data was taken with a Molectron UV energy meter. The energies of the YAG lasers were adjusted as needed to maintain the UV intensity at a constant level. Since the dye laser efficiency is higher at 282 nm than 286 nm, the energy of the YAG laser used to pump the $Q_1(14)$ transition was always larger than that of the YAG laser pumping the $Q_1(5)$ transition. The dye lasers were tuned to their respective transitions and then the doubling crystals were adjusted to yield the maximum UV energy in the pulse. Tuning the doubling crystals in this way caused the peak UV energy to occur at the same wavelength as the maximum fluorescence signal. Even within the small spectral width of the transition scans (which will be discussed in Section 3.4.3), the UV energy was not uniform over the entire scan due to walk-off in the doubling crystals. This procedure was followed when taking all measurements (i.e. calibration and unsteady laminar flame images). By tuning the laser system in this manner, it permitted the UV intensity to be adjusted so that the signals were in the fluorescence linear regime (i.e. fluorescence signal is proportional to laser intensity). All the PLIF measurements taken were done with a laser power of approximately 6 mJ/pulse, which provided a spectral power density in the aforementioned linear regime.

The OH fluorescence signal from the laminar flame burner was captured by two Princeton Instruments ICCD (Intensified Charged Coupled Device) cameras (512x384

pixels, 14 bit resolution) positioned normal to the laser sheet path. The cameras were fitted with UV Nikkor lenses (105 mm, f = 1:4.5). The ICCD cameras captured two-dimensionally resolved information. As with the PMT, UG-11 and WG-305 filters were placed on front of the camera lenses to filter out wavelengths not pertaining to OH fluorescence. The fluorescence images from the cameras were acquired using the scientific image processing software package IPLab, from Scanalytics, Inc., run on two separate desktop computers (each computer controlled one camera). The gain setting was not the same on both cameras, which will affect calibration data obtained with this system as discussed in Section 4.2 below.

3.4.2.1 Calibration Setup

Fluorescence images and thermocouple data were taken on a porous plug burner as the one depicted in Figure 3-7. The calibration curves resulting from these images were used to relate fluorescence yield ratios from the OH PLIF images acquired in the unsteady laminar diffusion flame to temperature. The thermocouple calibration process will be discussed in more detail in Section 3.5 below. The optical setup for the calibration images (Figure 3-9) was identical to that shown in Figure 3-6, except the porous plug burner, which was probed by the thermocouple, replaced the laminar flame burner. The photodiode was not used since the calibration flame was steady and unsteady timing issues were not of concern.

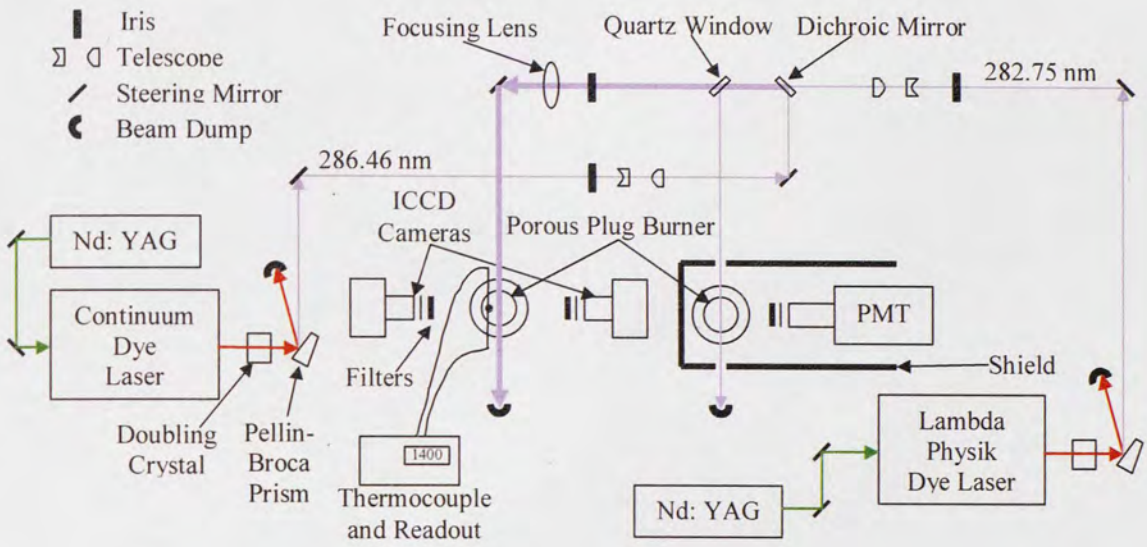

Figure 3-9: Optical setup for calibration measurements.

3.4.3 OH Transition Tuning

The dye lasers used in this experiment were equipped with digital indicators for tuning to a selected wavelength. However, minor adjustments had to be made from day to day in order to ensure continuous tuning to the selected OH transitions. The indicators, thus, were just a coarse measure of the output photon wavelength and, as observed, were not particularly repeatable or reliable. Therefore, in order to ensure proper tuning to the selected excitation wavelengths, the output of the PMT collecting fluorescence signals from the porous plug burner (see Figure 3-6 and Figure 3-9) was monitored. The signal was displayed on a Hewlett Packard Infinium oscilloscope. The dye lasers were "walked" through a range of wavelengths (i.e. transition scan) containing

the excitation wavelength (i.e. for either the $Q_1(5)$ or $Q_1(14)$ transitions) until the signal displayed on the oscilloscope was maximized. This procedure was performed for both calibration and unsteady laminar flame measurements.

3.4.4 Timing

The YAG lasers were designed to pulse at a rate of 10 Hz for maximum output power. This laser feature only allowed for forcing frequencies (i.e. frequencies at which the speaker pulsed the laminar flame) to be multiples of 10 Hz. In order to capture different temporal positions (i.e. phases) within the unsteady laminar flame, the lasers were triggered externally. Two Stanford Research Systems (SRS) DG535 digital delay generators (DDG #1 and DDG #2) triggered the YAG lasers. Figure 3-10 shows a schematic of the wiring setup used for timing purposes.

As shown in Figure 3-10, DDG #1 operated in internal trigger mode. After each internal trigger, DDG #1 sent two negative TTL pulses 10 μs in duration to the YAG laser pumping the $Q_1(14)$ transition, a command to fire the laser flashlamps (Fire command) and a command for the Q-switch to open (Q-switch command). The delay between the Fire and Q-switch commands determined the energy output of the laser; although varied, the delay was kept around a value of 250 μs. The Fire command signal was also used to trigger DDG #2 operated in external trigger mode. After receiving the trigger, DDG #2 sent Fire and Q-switch commands to the YAG laser pumping the $Q_1(5)$

transition after a user-specified delay of 1 μs. This delay was short enough compared to the speaker forcing periods tested (see Table 3-3) and to the time scale of the flame (i.e. the approximate ratio of the fuel tube diameter to the mean velocity, i.e. 30 cm/s, is approximately 15 ms) that the $Q_1(5)$ and $Q_1(14)$ pulses could be considered simultaneous. The delay between the Fire and Q-switch commands sent by DDG #2 could also be changed to vary the laser energy.

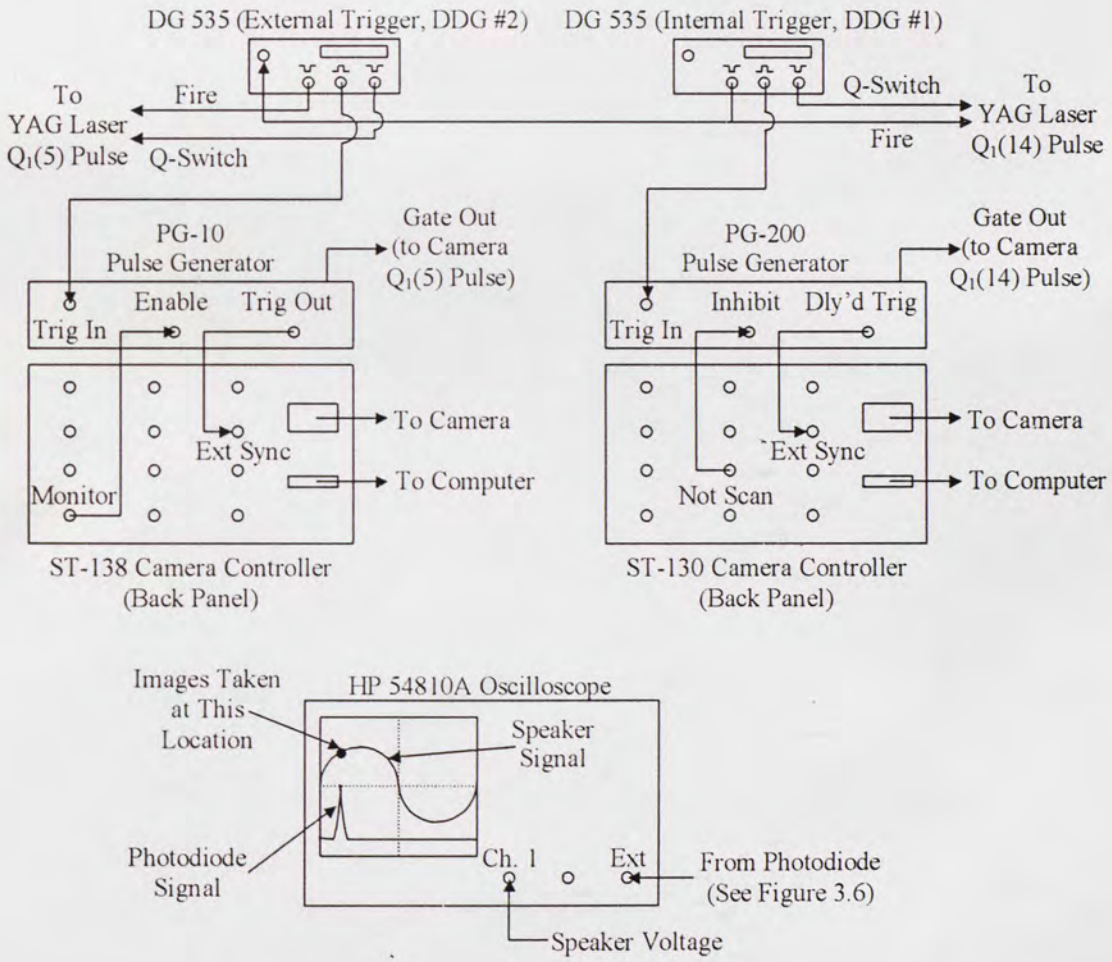

Figure 3-10: Wiring diagram for unsteady timing and PLIF image acquisition.

Both DDGs were also used to trigger the ICCD cameras. DDG #1 and DDG #2 sent a positive TTL signal 10 μs in duration simultaneously with their respective Q-switch commands to two Princeton Instruments Programmable Pulse Generators (PG-200 and PG-10, respectively) that controlled the intensifier gate pulses to the ICCD cameras. The pulse generators sent a high voltage pulse of user-specified duration to their respective camera intensifiers after a user-specified delay. As shown in Figure 3-10, Princeton Instruments ST-138 and ST-130 controllers were used. The controllers controlled the array readout and cooled the camera detectors.

Figure 3-11 shows one timing cycle where the relationship between laser and camera pulses can be better visualized. After the PG-200 sent a high voltage pulse to the camera intensifier, it sent a negative TTL signal (Ext. Sync.) to the ST-130 controller for image exposure. After the intensified array had been exposed, the shutter closed, and the ST-130 read the array while sending an "inhibit" signal to the PG-200 preventing it to send any more pulses to the camera. Similarly, after the PG-10 sent a high voltage pulse to the camera it controlled, it sent an External Sync pulse to the ST-138 controller. After exposure, the shutter closed and the Shutter Monitor signal went low disabling the PG-10.

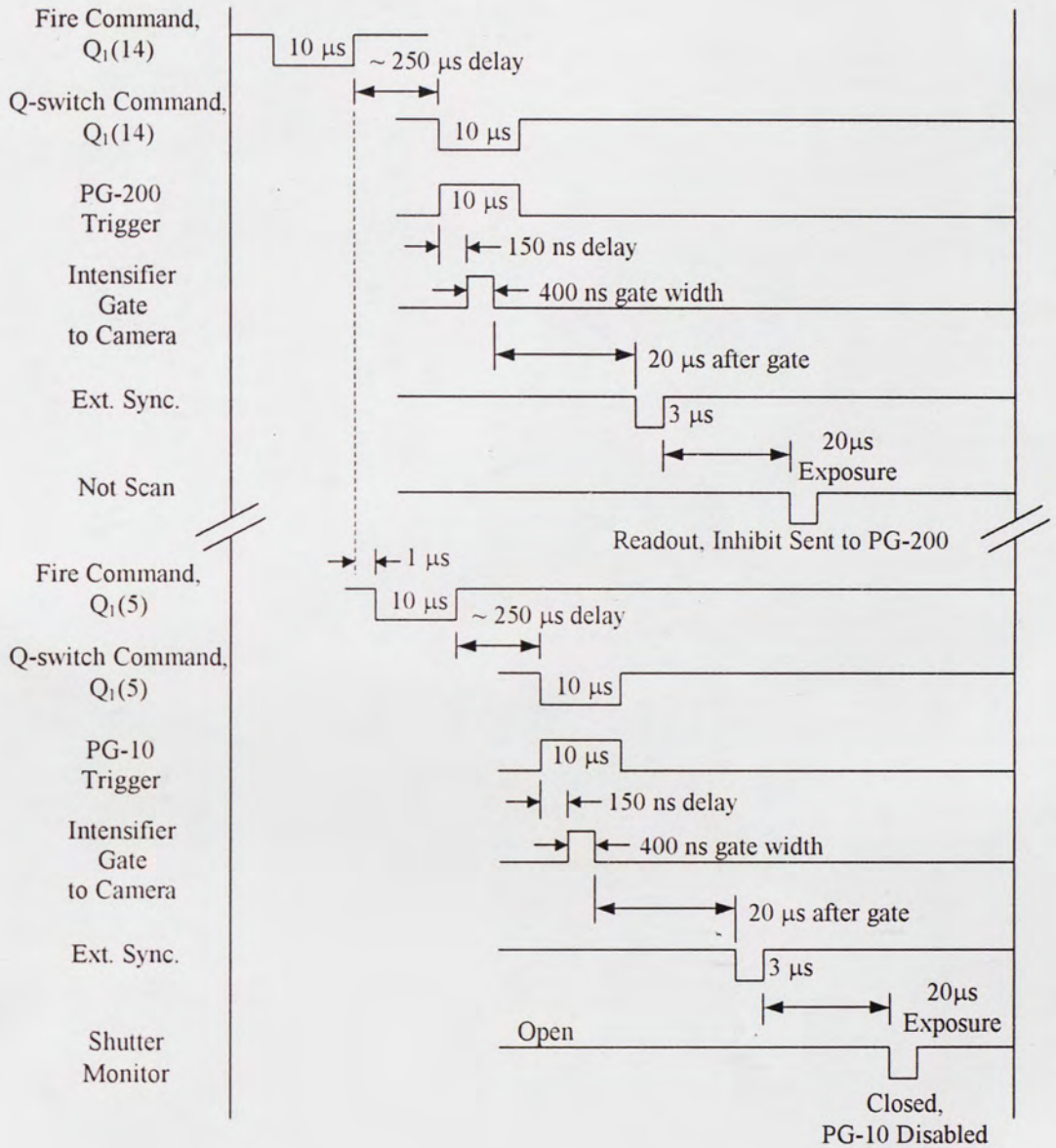

Figure 3-11: Camera gate timing.

Fluorescence images were acquired by the gated operation of the ICCD cameras. The gate signals (from the programmable pulse generators) had to be timed such that they would lie temporally within a specified phase of the speaker oscillation and were

coincident with their respective laser pulses. Since the cameras were being triggered by the same DDGs that controlled the laser pulses, once the camera gates were overlapped with their respective laser pulses (i.e. OH signal), they would stay so for every shot. In order to do this, the signal from the PMT (see Figure 3-6), the Gate Monitor signal from the PG-200, and the Pulse Monitor signal from the PG-10 were displayed on a Hewlett Packard 54501A 4-channel digitizing oscilloscope, which was triggered by the PG-200 signal as shown in Figure 3-12.

The Gate Monitor and Pulse Monitor signals were located on the back panels of the PG-200 and PG-10 respectively. These signals were negative TTL pulses with the same delay and width as the high voltage pulses sent to the cameras. The delay and width of the gate pulses were adjusted individually so that each of the fluorescence peaks from the PMT signal (i.e. $Q_1(14)$ and $Q_1(5)$ transitions) were located within their respective camera pulse gates. The delay was set to 150 ns and the width to 400 ns approximately (see Figure 3-11) for both pulse generators. Since fluorescence lifetime is on the order of 100 ns, a gate width of 400 ns centered on the fluorescence signal was sufficient to capture the OH signal.

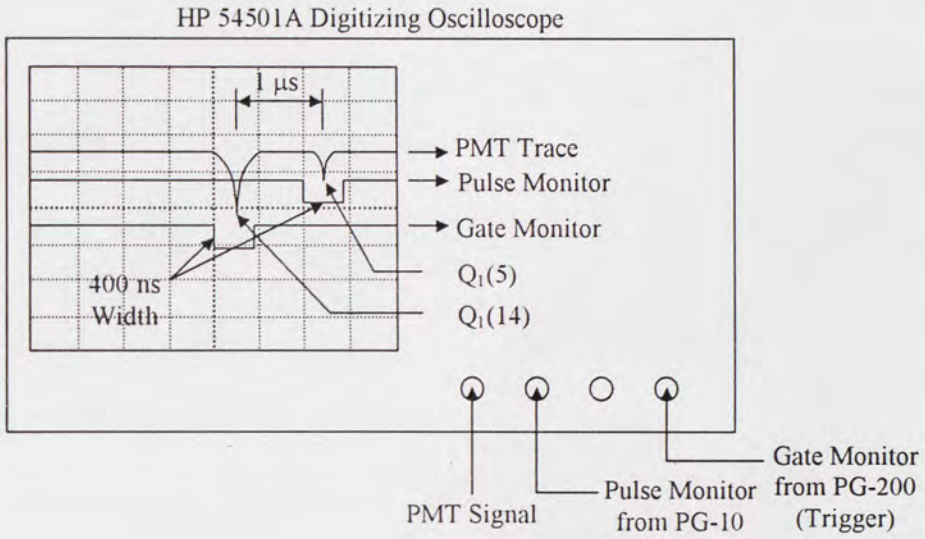

Figure 3-12: Fluorescence timing.

With the camera gate signals correctly positioned to capture OH fluorescence, unsteady measurements could be performed. For this purpose, the speaker voltage signal was displayed on a HP 54810A digitizing oscilloscope, which was triggered by the rising edge of the laser pulse as detected by the photodiode (see Figure 3-10). The speaker forcing the flame was considered the "master clock" from which the experiment was timed. The signal from the photodiode also represents one of the camera gate signals since the laser pulses and camera gates had been previously overlapped as discussed above. Therefore, the temporal position of the PLIF measurement (i.e. image capture) was when the peak photodiode signal occurred within the speaker oscillation. The position of the photodiode pulse was moved to different temporal locations within the speaker oscillation by increasing the delay between the internal trigger of DDG #1 and its outgoing TTL Fire Command signal. When this delay was increased, the speaker signal

shown on the oscilloscope shifted relative to the photodiode signal. It is noted that the phase of the speaker voltage relative to the internal trigger of DDG #1 changed every time the system was powered down. Therefore, the temporal position of the photodiode signal with respect to the speaker oscillation when there was a zero delay between the internal trigger of DDG #1 and the laser Fire Command changed when the equipment was shut off.

PLIF images were collected at eight temporal positions within the speaker voltage oscillation. First, DDG #1 was set so that the delay between its internal trigger and the Fire Command was such that the photodiode signal was located at the zero voltage location with positive slope of the speaker oscillation. The delay was then increased by a time equal to 12.5 percent of the speaker oscillation period to acquire images at the next temporal location. This step was repeated to acquire images through the remainder of the speaker oscillation. For each temporal position, a series of 40 images were taken of the $Q_1(5)$ and $Q_1(14)$ transitions (i.e. fluorescence shots). Off-transition (i.e. background) images were not taken since flame luminosity was very low in the hydrogen flames studied.

There were a few complications in timing the PLIF system. There was a phase difference between the speaker voltage and the actual flow oscillation at the burner exit. This phase difference was not measured and for this reason images at eight different temporal locations were taken as to obtain better information of the flow oscillation. In addition, it was found that the sine wave from the signal generator (running the speaker)

drifted relative to the internal trigger of DDG #1. This drift was managed by fine adjusting the delay on DDG #1 before and after each set of images was acquired.

3.4.4.1 Calibration Timing

In order to take calibration images, a similar setup as the one described above was utilized. In the calibration case, the flame is steady and DDG #1 can be considered the master clock. The wiring diagram is the same as in Figure 3-10 but the oscilloscope was not used since the speaker voltage did not need to be monitored. Hence, the delay between the internal trigger of DDG #1 and its Fire Command was set to a fixed value and was not varied throughout the image acquisition process.

3.4.5 Shot-to-shot Energy Monitoring

As mentioned above, the PLIF system was operated in the linear fluorescence regime. In this case, a measure of the shot-to-shot laser energy variations was needed so that it could be taken into account when analyzing fluorescence images since any drop-off in UV energy would result in a proportional decrease in fluorescence signal. In order to do this, a data acquisition system comprised of a National Instruments BNC-2090 assembly connected to a GPIB data acquisition (DAQ) board, two Stanford Research Systems (SRS) SR 250 Gated Integrators and Boxcar Averagers, a SRS SR240 300 MHz

Preamplifier, and a SRS R280 Power Supply and Display Module was used to acquire fluorescence data from the PMT. Figure 3-13 shows the wiring diagram of the system. The DAQ system worked in conjunction with a desktop PC (Gateway 133 MHz) to save and display data.

The SR 250 gated integrator and boxcar averagers were used to integrate and average the PMT signal. A gated integrator amplifies and integrates an analog signal that is present during the time a gate of user-specified width is open, ignoring noise and interference that maybe present at other times. The SR 240 preamplifier was used to first amplify the PMT signal. The fast rise time, low noise and DC accuracy of the preamplifier made it ideally suited to increasing the PMT signal. The amplified signal was then sent to both the SR 250 boxcars.

The boxcars were triggered by the Gate Monitor signal from the back panel of the PG-200. Recall that this signal occurred at the same time as a high voltage pulse was sent to the camera intensifier capturing the $Q_1(14)$ laser pulse (see Figure 3-10). The width and delay of the gate over which the boxcars performed signal integration could be set independently so that it could be overlapped over the signal of interest. Thus, the Gate signals from SR 250 #1 and #2 along with the PMT signal were displayed on a HP 54501A oscilloscope triggered by the PG-200 Gate Monitor signal as shown in Figure 3-13. The gate delay and width was then set on both boxcars accordingly so that they could capture the $Q_1(5)$ and $Q_1(.14)$ peaks from the PMT signal and their output was maximized.

The DAQ board read the averaged signal output from the boxcars and it was triggered by the Busy signal from SR 250 #1. The software package LabView by National Instruments was used as the interface between the PC and the DAQ board. A program was written which read the signal from the boxcar every time the DAQ board was triggered. The digitized data was saved to an Excel spreadsheet. This spreadsheet displayed the shot-to-shot energy for each of the 40 fluorescence images taken. Shot averaging and signal analysis was performed with post-processing of the digitized data. The LabView program diagram is shown in Appendix A.

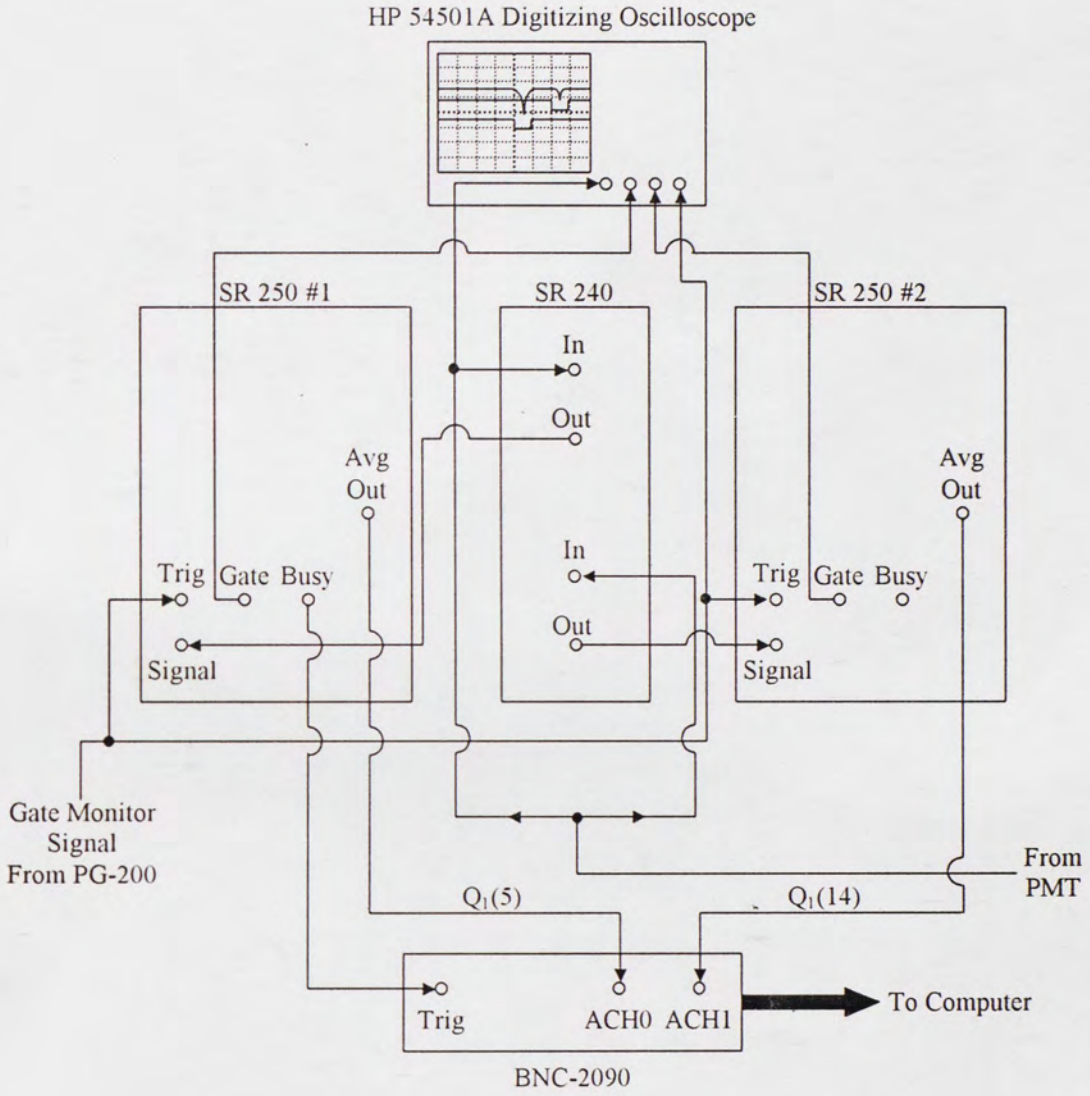

Figure 3-13: Wiring diagram for boxcar data acquisition system.

3.5 Experimental Uncertainties

Care was taken to minimize systematic errors by thorough design and calibration of the experiments performed in this research. This section summarizes the expected uncertainty in the experimental measurements taken. The uncertainty in the LDV velocity measurements is estimated to be ±5 cm/s. This uncertainty is due primarily to the resolution of the timer used to measure the Doppler laser signal (i.e. ± 5 ns). The thermocouple measurements had to be corrected for the environment the thermocouples were in (i.e. radiation correction) as will be discussed in the next section. This correction scheme relies on relationships derived from empirical data (i.e. Nusselt number relationships). It is estimated that the temperature obtained from the thermocouple measurements is accurate to within 15 K.

The possible sources of error in the PLIF measurements are many as discussed in Sections 2.3 and 5. The effect of these sources were considered and accounted for (refer to Section 5). As explained above, 40 flame images were taken at every temporal location within the speaker oscillation. In these images, the flame tended to move slightly from shot to shot; however, this was on the order of 0.2 mm (i.e. 5 pixels). The laser energy during the image collection process varied by approximately ±6%. This variation had to be accounted for since the system was operated in the linear fluorescence regime (see Section 5.1.1). The narrow linewidth of the dye lasers used along with the separation of the selected transitions with respect to nearby transitions suggest that the error in the ratio from the $Q_1(5)$ and $Q_1(14)$ images was, on the average, approximately 3-

5% (Seitzman *et. al.* 1994) which corresponds to ±5 - 15K based on the calibration curve generated for the PLIF measurements (See Section 4.2).

4 PLIF THERMOCOUPLE CALIBRATION

Fluorescence and thermocouple measurements were taken in a porous plug burner (see Figure 3-9) to provide calibration data to relate fluorescence yield ratios from the images taken in the unsteady laminar flame. The optical setup for the thermocouple calibration was discussed in Section 3.4.2.1 above. The premixed flat flame produced on the porous plug burner provided a suitable environment for thermocouple measurements because the flame was steady and highly repeatable. The flame size was large compared with the thermocouple diameter, and the temperature at any given height within the flame was uniform across the burner surface. Subsequent ignitions (from day to day) of the flame at a given fuel and air flowrates yielded thermocouple measurements that varied by less than one percent.

A fine wire thermocouple was used to measure the gas temperature. A type B, 70% platinum-30% Rhodium versus 94% Platinum-6% Rhodium thermocouple with a wire diameter of 380 μm was selected because of its upper temperature limit was the highest available, with a range of 800 – 2090 K. A digital meter (Omega Engineering, Inc.) connected to the thermocouple displayed the measured temperature in °C. The thermocouple bead was positioned at the center of the burner and its two leads stretched across the burner diameter. The flame temperature was varied by changing the fuel and air flowrates.

Measurements were taken in hydrogen-air flames. Raw thermocouple measurements ranged from 1250 to 1500 °C, as read by the thermocouple. Fuel and air flowrates supplied to the burner and used for calibration along with uncorrected thermocouple temperatures are listed in Table 4-1. Once the flowrates were set, a picture of the radiant thermocouple bead was taken. The thermocouple was then removed from the flame and the fluorescence images for the $Q_1(5)$ and $Q_1(14)$ transitions were taken (40 shots for each transition). This procedure was repeated for all flowrates. The bead image served as a way to locate the bead within the flame since as temperature changed the thermocouple material expanded or contracted changing the position of the bead. The ratio of the post-processed $Q_1(5)$ and $Q_1(14)$ images (post-processing of these images will be discussed in Section 5) was calculated using IPLab. The area in the image corresponding to the thermocouple bead would have the value of the $Q_1(5)/Q_1(14)$ ratio corresponding to the measured temperature.

Table 4-1: Fuel and air flowrates for thermocouple calibration

N_2 Coflow (SLM)	Air (SLM)	Fuel (SLM)	Temperature* °C
6.0	59.0	21.1	1480
6.0	59.0	20.0	1453
6.0	59.0	18.7	1418
6.0	59.0	17.7	1394
6.0	59.0	16.0	1350
6.0	59.0	15.0	1324
6.0	59.0	13.7	1290
6.0	59.0	12.5	1257

*Not corrected for radiation

4.1 Thermocouple Correction

The temperature of the thermocouple is not precisely the true local temperature of the surrounding gas due to heat losses. The effects of radiant heat transfer between the thermocouple bead, surrounding gas and surrounding environment, and conductive and convective heat transfer can significantly alter the temperature measured by the thermocouple. All these effects result in a temperature lower than the actual gas temperature. As the gas temperature increases, these effects introduce greater errors.

In a well designed thermocouple the junction will only be cooled a few degrees by conduction along the fine wires. However, if the fine wires are too short, significant cooling of the thermocouple junction can take place (Bradley and Matthews, 1968).

Bradley and Matthews found that for fine wire Platinum-Rhodium thermocouples the effect of conduction cooling was negligible with a lead wire length of 3.2 mm approximately. In the case of the measurements performed in this research, the burner radius is approximately 30 mm, and the temperature was uniform across the burner surface. With the thermocouple bead located at the center of the burner, the effective lead wire length was well above the 3.2 mm reported by Bradley and Matthews (1968); therefore, conduction effects could be neglected. A correction to the thermocouple temperature can then be applied by assuming a steady state balance between the radiant and convective heat transfer modes. The flame gas can also be assumed to be transparent to radiation. Emission from the gas in the flame would reduce the temperature discrepancy between the thermocouple and the surrounding flame gases. Therefore, the temperature correction reported here provides a conservative estimate of the error in the thermocouple measurements.

4.1.1 Radiation Energy Exchange

The thermocouple radiated heat away to the surroundings, which could be considered a black body for radiation exchange purposes. However, the thermocouple was placed close to the burner surface, which was made of sintered bronze. The burner, thus, cannot be considered a black body and its radiant heat exchange with the thermocouple needs to be taken into account. This section develops equations that will be used to obtain the true gas temperature.

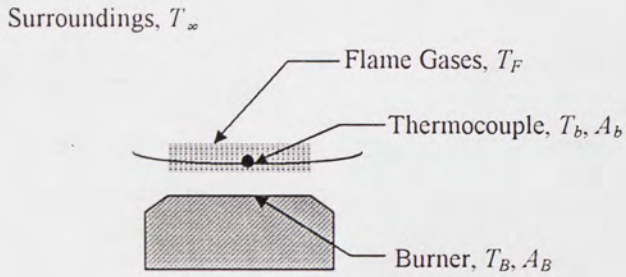

Figure 4-1: Thermocouple radiation exchange.

As shown in Figure 4-1, the radiation problem can be treated as an enclosure comprising of three surfaces: the burner, the thermocouple, and the "black" surroundings. The flames gases are assumed transparent and do not participate in the radiation exchange. The thermocouple bead has a surface area A_b and temperature T_b, the burner has a surface area A_B and temperature T_B, the surroundings have a temperature T_∞, and the flame temperature of the combustion gases is T_F. Assuming a steady state balance of all heat transfer modes, the heat lost by the thermocouple bead by means of radiation must be supplied convectively:

$$h(T_F - T_b) = q_b \tag{4.1}$$

Where h is the convective heat transfer coefficient and q_b is the surface heat flux (i.e. heat per unit area) of the thermocouple bead. If all surfaces are treated as diffuse-gray (i.e. emissivity is not a function of direction or wavelength) a system of equations can be

written that relate surface heating to surface temperature and can be used to calculate q_b (Siegel and Howell, 2002):

$$\sum_{j=1}^{N}\left(\frac{\delta_{kj}}{\varepsilon_j}-F_{k-j}\frac{1-\varepsilon_j}{\varepsilon_j}\right)q_j=\sum_{j=1}^{N}F_{k-j}\sigma\left(T_k^4-T_j^4\right) \tag{4.2}$$

Equation (4.2) is applied to the kth surface; here, δ_{kj} is the Kronecker delta, ε_j is the emissivity of the jth surface, F_{k-j} is the view factor from surface k to surface j, σ is the Stefan-Boltzmann constant, and T_k and T_j are the temperatures of the kth and jth surface respectively. If temperatures are specified, the heat fluxes, q_j, can be determined.

Application of Equation (4.2) to the bead and burner surfaces leads to the following system of equations:

$$q_b\frac{1}{\varepsilon_b}-q_B\left(F_{b-B}\frac{1-\varepsilon_B}{\varepsilon_B}\right)=\sigma\left[F_{b-B}\left(T_b^4-T_B^4\right)+F_{b-\infty}\left(T_b^4-T_\infty^4\right)\right] \tag{4.3a}$$

$$q_B\frac{1}{\varepsilon_B}-q_b\left(F_{B-b}\frac{1-\varepsilon_b}{\varepsilon_b}\right)=\sigma\left[F_{B-b}\left(T_B^4-T_b^4\right)+F_{B-\infty}\left(T_B^4-T_\infty^4\right)\right] \tag{4.3b}$$

where q_B is the burner heat flux, ε_B is the burner emissivity, ε_b is the bead emissivity, $F_{b\text{-}B}$ is the bead-to-burner view factor, $F_{b\text{-}\infty}$ is the bead-to-surroundings view factor, $F_{B\text{-}b}$ is the burner-to-bead view factor, and $F_{B\text{-}\infty}$ is the burner-to-surroundings view factor. An important point to note here is that since the burner was water cooled, the temperature at

the burner surface was very close to room temperature (i.e. $T_B \approx T_\infty$). Introducing this simplification, eliminating q_B, and solving for q_b, Equations (4.3a) and (4.3b) yield:

$$q_b = \frac{\sigma\varepsilon_b\left[\left(F_{b-\infty} + F_{b-B}\varepsilon_B\right)\left(T_b^4 - T_\infty^4\right)\right]}{1 - F_{b-B}F_{B-b}\left(1-\varepsilon_b\right)\left(1-\varepsilon_B\right)} \tag{4.4}$$

A comprehensive development of the view factors is presented in Section 4.1.1.1 below, however, Equation (4.4) can be further simplified by introducing view factor reciprocity and algebra (Siegel and Howell, 2002):

$$A_k F_{k-j} = A_j F_{j-k} \tag{4.5a}$$

$$\sum_{j=1}^{N} F_{k-j} = 1 \tag{4.5b}$$

Applying the expressions in Equations (4.5a) and (4.5b) to the three surface enclosure problem being treated, $F_{b-\infty}$ and F_{B-b} can be expressed in terms of the view factor from the thermocouple bead to the burner, F_{b-B}:

$$F_{B-b} = \frac{A_b}{A_B} F_{b-B} \tag{4.6a}$$

$$F_{b-\infty} = 1 - F_{b-B} \tag{4.6b}$$

Introducing Equations (4.6a) and (4.6b) in Equation (4.4), Equation (4.1) can be written, in final form, as:

$$h(T_F - T_b) = \frac{\sigma\varepsilon_b \left\{ \left[1-(1-\varepsilon_B)F_{b-B}\right]\left(T_b^4 - T_\infty^4\right)\right\}}{1-\frac{A_b}{A_B}F_{b-B}^2(1-\varepsilon_b)(1-\varepsilon_B)} \tag{4.7}$$

Values for the bead and burner emissivity were 0.2 and 0.55 respectively and were obtained from Touloukian and Ho (1970). The heat transfer coefficient, h, was estimated by modeling the thermocouple as a circular cylinder in crossflow (since the thermocouple was stretched across the burner), the empirical Nusselt number (Nu_d) relation developed by Churchill and Bernstein (1977) is well suited to the thermocouple measurements since it covers a wide range of Prandtl and Reynolds numbers:

$$\overline{Nu}_d = \frac{hd}{k} = 0.3 + \frac{0.62\,Re_d^{1/2}\,Pr^{1/3}}{\left[1+(0.4/Pr)^{2/3}\right]^{1/4}}\left[1+\left(\frac{Re_d}{282000}\right)^{5/8}\right]^{4/5} \tag{4.8}$$

$$Re_d\,Pr > 0.2$$

Where d is the thermocouple bead diameter, k is the thermal conductivity of the gas, $Re_d = Ud\rho/\mu$ is the Reynolds number for the cylinder, $Pr = \mu C_p/k$ is the gas Prandtl number, U is the average gas velocity, ρ is the gas density, μ is the gas viscosity, and C_p is the gas specific heat. Churchill and Bernstein's relation is recommended for all $Re_d Pr > 0.2$. The

value of $Re_d Pr$ for all flames listed in Table 4-1 was approximately 2. All gas properties need to be evaluated at the film temperature T_f:

$$T_f = \frac{1}{2}(T_b + T_F) \tag{4.9}$$

Gas properties of the stoichiometric combustion products were used. For a H_2 – air flame, the product species considered were H_2O and N_2 (2 and 79/21 moles respectively). The density, viscosity, thermal conductivity, and heat capacity of this mixture were calculated over a temperature range of 1500 – 2200 K using software located on a website (Dandy, 2003). The results at representative temperatures are listed in Table 4-2. Fourth degree polynomials were fitted to the data in Table 4-2 so that the calculated properties could be expressed as a function of temperature. The polynomials deviated from the data by no more than 0.05%.

Table 4-2: Thermodynamic properties of combustion products (premixed flame)

T (K)	ρ (kg/m^3)	μ (kg/m s)	k (W/m K)	Cp (J/kg K)
1400	0.21364	5.13060 E-05	0.12881	1592.1
1600	0.18693	5.64921 E-05	0.13665	1613.1
1800	0.16616	6.14410 E-05	0.15190	1649.9
2000	0.14955	6.61878 E-05	0.16656	1680.7
2200	0.13595	7.07497 E-05	0.18066	1706.4

Since the heat balance equation expresses the flame temperature T_F in terms of the convective heat transfer coefficient h, which in turn is dependent on the gas properties, which are dependent on T_F (see Equation (4.8) and Equation (4.9)), an iterative calculation procedure was needed to calculate the flame temperature. Correction calculations were carried out in an Excel spreadsheet using the equations listed above. An initial flame temperature guess was introduced to calculate the film temperature T_f at which all gas properties were evaluated (using the polynomials) and a new flame temperature calculated. The temperature guess was changed iteratively until the guess flame temperature and the calculated flame temperature converged. The iteration process was performed until the guess and calculated temperatures differed by less than 0.01%.

4.1.1.1 View Factors

As explained above, the thermocouple bead was in close proximity to the burner surface. Thus, a large fraction of the energy emitted by the thermocouple reached the burner. Since the burner cannot be treated as a black body, its contribution to the heat transfer exchange has to be taken into account. When calculating radiative transfer between surfaces, geometric relations are needed to account for how surfaces view each other. View factors represent the fraction of radiative energy leaving one surface that is intercepted by another surface. In this section, the geometric view factor from the thermocouple bead to the burner surface will be developed using the mathematical unit-

hemisphere technique (Siegel and Howell, 2002). This expression will help evaluate Equation (4.7).

Even though effort was placed in positioning the thermocouple above the center of the burner, the thermocouple wires sagged and the bead moved away from its original position as it was heated by the combustion gases as discussed above. The two surfaces (i.e. bead and burner) can be treated as a sphere and a disk respectively. View factors from a sphere to a coaxial disk can be found in most references (see, for example, Siegel and Howell, 2002 and Howell, 1982). The view factor from a sphere to a non-coaxial disk has been published by Feingold and Gupta (1970); however, the authors used a different analytical method from the one adopted here. For this reason, it was thought worthwhile to develop view factors using the unit-hemisphere technique.

Figure 4-2 shows the geometric configuration of the thermocouple bead with respect to the burner surface. The view factor from the thermocouple bead to the burner can be obtained using the unit hemisphere method. With this method, a unit hemisphere is placed centered over a differential area on the burner (dA_B), the view factor from the bead to the burner is proportional to the projection of the bead onto the unit hemisphere, and then the projection from the unit hemisphere down to the unit circle on the burner surface (i.e. dA_b'').

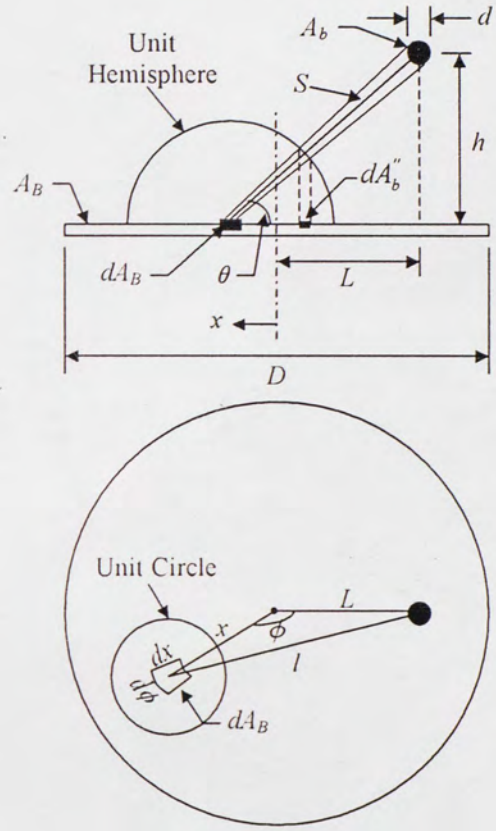

Figure 4-2: View factor geometry.

Using the geometry presented in Figure 4-2, the projection of the bead onto the hemisphere is a circle of diameter (non-dimensional) d/S and area $(\pi/4)(d/S)^2$ (by similar triangles), where d is the bead diameter and S is the distance from the bead to the differential area dA_B. The projection from the unit hemisphere down to the burner surface is an ellipse of area:

$$dA_b'' = \frac{\pi}{4}\left(\frac{d}{S}\right)^2 \sin\theta \tag{4.10}$$

Where θ is the angle formed by S and the burner surface. The area of the unit circle is π, therefore the fraction that dA_b'' occupies on the unit circle is:

$$\xi = \frac{dA_b''}{\pi} = \frac{1}{4}\left(\frac{d}{S}\right)^2 \sin\theta \tag{4.11}$$

Noting from the geometry in Figure 4-2 that $S^2 = h^2 + l^2$, where l is the projection of S onto the burner surface, the view factor from the bead to the burner can then be expressed as (Siegel and Howell, 2002):

$$A_B F_{B-b} = A_b F_{b-B} = \int_{A_B} \xi dA_B \tag{4.12a}$$

$$F_{b-B} = \frac{1}{A_b}\int_{A_B} \frac{1}{4}\frac{d^2}{h^2 + l^2} \sin\theta dA_B \tag{4.12b}$$

Reciprocity was used to solve for F_{b-B} in Equation (4.12a). Expressions for l and $\sin\theta$ are given below:

$$\sin\theta = \frac{h}{S} = \frac{h}{\sqrt{h^2 + l^2}} \tag{4.13}$$

Where $l^2 = L^2 + x^2 - 2Lx\cos\phi$ (i.e. Law of Cosines) and L and x are the radial distances from the center of the burner surface to the projection of the bead onto the surface and to

the differential area dA_B respectively and ϕ is the angle between L and x. From Figure 4-2, dA_B is:

$$dA_B = x\,dx\,d\phi \tag{4.14}$$

Substituting Equation (4.13) and Equation (4.14) into Equation (4.12b), the expression for the view factor is:

$$F_{b-B} = \frac{d^2 h}{4A_b}\int_0^{2\pi}\int_0^{D/2} \frac{x}{\left(h^2 + L^2 + x^2 - 2Lx\cos\phi\right)^{3/2}}\,dx\,d\phi \tag{4.15}$$

Equation (4.15) leads to elliptic integrals and cannot, therefore, be integrated in terms of elementary functions. A numerical approach was used to evaluate Equation (4.15) (i.e. trapezoidal rule; Chapra and Canale, 2002). Values for h and L were obtained from the bead images taken during the calibration process (see Section 3.5 above). The results from the numerical integration were in good agreement with those of Feingold and Gupta (1970). For the calibration flames studied (see Table 4-1), view factors ranged from 0.361 to 0.378. Thus, almost 40% of the radiant energy leaving the thermocouple reached the burner. This further verifies the validity and the need to calculate the flame temperature measured by the thermocouple using Equation (4.7).

4.2 Calibration Curves

Once the thermocouple measurements for the flame temperature were corrected, each $Q_1(5)/Q_1(14)$ ratio obtained from the image reduction procedure (discussed in Section 5) had a corresponding flame temperature. These values were plotted as a calibration curve and compared to the simple Boltzmann distribution. This plot is shown in Figure 4-3. The calibration curve follows the general trend of the Boltzmann curve but is shifted from it. This is due largely to the fact that the cameras used were operated at different gain settings, as mentioned above. In addition, the Boltzmann distribution does not account for excited state dynamics that are rotational-level dependent, which, possibly, further contributes to the observed shift.

One additional factor contributing to the shift in the calibration curve is catalytic reactions on the thermocouple surface. In some flames, platinum acts as a hydrogenation catalyst causing a reaction between hydrogen and the thermocouple material (i.e. platinum) (Rylander, 1967). Therefore, in hydrogen flames, this platinum property makes the thermocouple prone to these catalytic reactions, which would take place on the thermocouple surface causing a rise in surface temperature that deviates from the actual gas temperature. The thermocouple would then overestimate the temperature. Besides the catalytic effect, platinum-rhodium thermocouples are also susceptible to element contamination in a high temperature environment by hydrogen, carbon monoxide, and methane among other elements. This leads to thermocouple embrittlement altering its calibration (Kent, 1970).

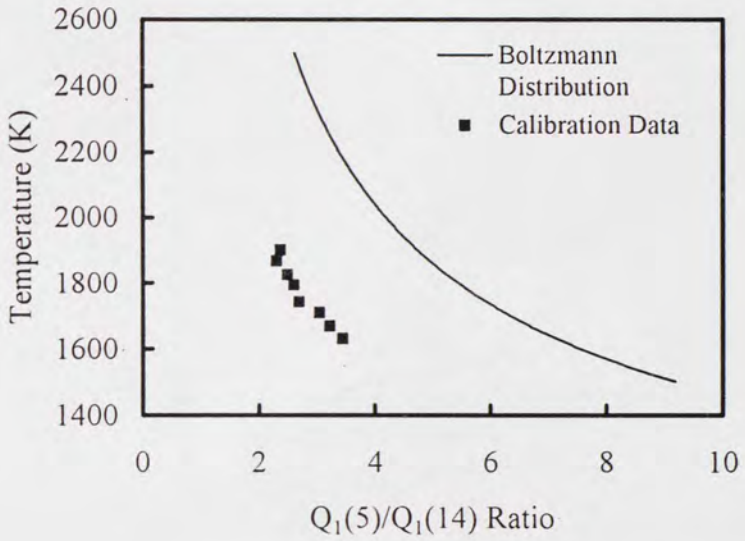

Figure 4-3: Calibration curve and Boltzmann distribution.

The thermocouple used in this research project was coated with a thin layer of silica. Coating the thermocouple can help reduce the effects of catalytic hydrogenation and element contamination described above. However, at the high temperatures encountered in flames, silica might be reduced by hydrogen in the flame causing an embrittling silicide that degrades the thermocouple (Pollock, 1991). Other coatings such as combination of yttrium oxide and beryllium oxide (Y_2O_3-BeO) have been successfully used and shown to provide an effective coating, which prevents thermocouple contamination (Kent, 1970). Thermocouple coating, however, might present a problem when determining the emissivity of the thermocouple. The emissivity is dependent on the thermocouple diameter and the thickness of the coating (Bradley and Matthews, 1968). If no emissivity data were available for the particular thermocouple material-

coating combination, measurements to determine this value would have to be taken. This might prove to be a difficult task since coatings behave differently as temperature changes. The coating becomes transparent to the energy radiated in the shorter wavelengths (i.e. high temperature) and wire emissivity is close to that of an uncoated wire. On the other hand, at lower temperatures, the emissivity is increased as a consequence of the high absorption at the longer wavelengths (Bradley and Matthews, 1968). In the case of the thermocouple used in this experiment, measurements were taken at high enough temperatures as to assume an emissivity equal to that of an uncoated wire (emissivity values were obtained from Touloukian and Ho, 1970). The emissivity can also be considered constant (a value of 0.2 was used) over the temperature range investigated.

5 DIGITAL IMAGE POST-PROCESSING

Planar laser-induced fluorescence images were taken in steady and unsteady hydrogen laminar diffusion flames as well as premixed flames (for calibration purposes). The steady diffusion flames will be used as a baseline to compare with previously published data (Chen *et. al.*, 1997; Rørtveit *et. al.*, 2001) as well as with the unsteady images. Images were taken of unsteady flames forced at 10 Hz and 100 Hz at two different forcing amplitudes. Hydrogen was diluted with argon or helium to change its fuel Lewis number.

The ICCD camera and lens arrangement allowed for a spatial resolution of approximately 50 μm (i.e. 19 pixels/mm). The camera full field of view was 584 x 384 pixels corresponding to an image 31.2 mm wide by 20.5 mm tall. The camera field of view was cropped to an area of 330 x 135 pixels since the image width of the camera full field of view extended well beyond regions where the flame existed. Therefore, all flame images were taken in a 17.6 x 7.2 mm frame. Calibration images had a field of view of 515 x 135 pixels in order to capture the wide premixed flat calibration flame. The image processing discussion below applies to both flame calibration and the actual unsteady laminar diffusion flame images.

5.1 Image Modification

5.1.1 Image Statistics, Filtering, and Background Subtraction

A set of 40 images was taken of each of the $Q_1(5)$ and $Q_1(14)$ transitions. Off-transition images (i.e. background or "dark" images) were also taken of the flames with the lasers blocked off. This was done since the only purpose of the off-transition image is to subtract background noise from the OH image.

The data obtained from the shot-to-shot energy variation using the boxcar data acquisition (DAQ) system (see Section 3.4.5 above) was analyzed prior to manipulating the images. The spreadsheet data files obtained from the boxcar data were statistically analyzed to reject any images that might have corresponded to a laser energy intensity being too high or too low. The average and standard deviation for each set of 40 readings (for every image set) was calculated. Chauvenet's criterion (Holman, 1994) was then applied to the data set. Assuming that the readings follow a Gaussian error distribution, out of a set of m measurements a reading may be rejected if the probability of obtaining its particular deviation from the mean is less than $1/(2m)$. For a set of 40 measurements and after referring to a table of Gaussian normal error function integrals (Holman, 1994), a value could be rejected if the ratio of its particular deviation from the mean to the standard deviation was greater than or equal to 2.498. Chauvenet's criterion was applied only once to each data set. The images corresponding to the rejected values from the boxcar data set were deleted. Images with saturated pixels were also deleted and the

corresponding boxcar data point was removed. After all dubious data points and corresponding images were eliminated; a new mean and standard deviation was calculated.

After the statistical analysis was performed, each image set was averaged. Filtering was used on the averaged images to eliminate anomalous pixels and smooth out the images (i.e. to get rid of the "salt and pepper" effect). A linear filter was used which replaced the value of each pixel with a weighted average of its nearest eight neighbors and itself; with the center pixel having the most weight. The averaged and filtered off-transition (background) images were then subtracted from the averaged and filtered on-transition fluorescence images (both $Q_1(5)$ and $Q_1(14)$ transitions). Off-transition boxcar data was also subtracted from its on-transition counterpart. Background images consisted primarily of the camera dark current since flame luminosity was not of concern in the hydrogen flames studied. Thus, when background was subtracted form an on-transition image, only the OH signal remained. The images resulting from the background subtraction may have pixels with very low, zero, or even negative values. Taking the Q1(5)/Q1(14) ratio of these images may produce anomalous and meaningless pixel values. To prevent this all pixels with values below 1.0 were assigned a value of unity.

The boxcar data also served to normalize the fluorescence images. The entire boxcar data set (i.e. steady, unsteady, and calibration boxcar data) obtained after the statistical analysis discussed above was normalized by the maximum value obtained after off-transition subtraction. Normalization factors were thus generated which ranged between 0.85 and 1. These factors were divided into the corresponding fluorescence

images (i.e. for each of the $Q_1(5)$ and $Q_1(14)$ transitions). This process assured consistent fluorescence intensity for all images (i.e. as if the images were taken with a constant, non-varying laser power), which is important in this case since the images were taken in the linear fluorescence regime (see Section 2.3).

5.1.2 Beam Energy Profile

Further corrections had to be made to the images in order to take image ratios of the $Q_1(5)$ and $Q_1(14)$ transitions and determine temperature fields from them. The spatial energy distribution of both of the laser pulses was not uniform. The laser sheets carried an energy profile that was Gaussian with energy dropping off at the "wings" of the laser sheet. Since the fluorescence was in the linear regime, areas where the laser intensity was higher/lower would result in a stronger/weaker fluorescence signal (see Section 2.3.1). Not correcting for the energy variations in the laser sheet would artificially indicate peaks and valleys of OH concentration where none physically existed.

One way of determining beam spatial profiles is to collect the scattering signal in a uniform medium. In the past, UV signals scattering off acetone molecules inside a closed container were used to determine the beam profile (Santoianni, 1999). In this project the left hand side of every picture taken of the unsteady laminar flame had a band of UV signals scattering from the vycor glass enclosing the flame (see Figure 5-1). This signal contains the information about the beam profile. Figure 5-2 shows a plot of a typical beam profile. The laser sheet profiles for the Q1(5) and Q1(14) transitions were

normalized by their respective maximum values and values below 0.3 were set to unity for the correction to avoid dividing the fluorescence images by low pixel values. Each column on the PLIF images was divided by these normalized beam profiles in the following way. A FORTRAN program was written (and found in Appendix B) to read the normalized beam profile and form an array in which each column was the beam profile. This array matched the dimensions of the images it would correct (i.e. 330 x 135 and 515 x 135 for unsteady and calibration images respectively). IPLab could read this array and turn it into an image, which was then divided into the uncorrected PLIF images.

Figure 5-1: Laser sheet.

The calibration images taken of the premixed flame did not have the vycor glass scattering. However, the OH field in these flames can be considered uniform since the temperature is constant across the burner surface and the beam profile can be obtained simply from the OH fluorescence. In fact, beam profiles obtained from the vycor glass scattering and from the OH field in the calibration images were almost identical.

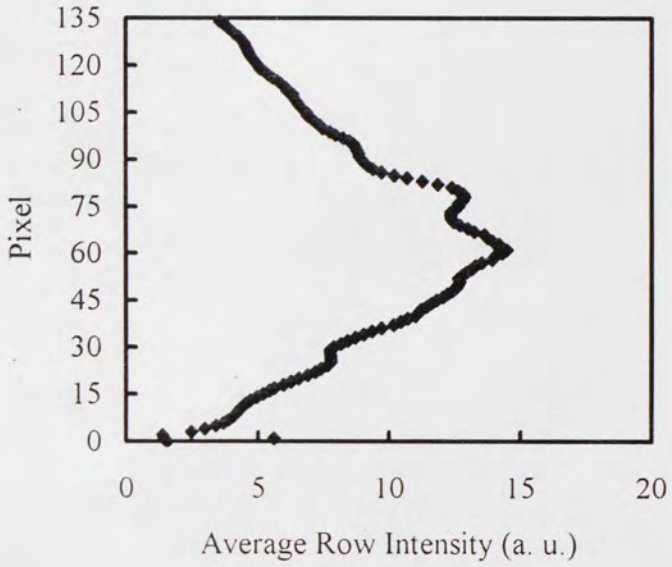

Figure 5-2: Laser sheet energy distribution.

5.1.3 Camera Flat-Field

The ICCD cameras were composed of two-dimensional arrays of light sensitive detectors or pixels. A CCD array is mechanically quite stable with the pixels retaining a rigidly fixed geometric relationship. Each pixel within the array, however, has its own unique light sensitivity characteristics, that is, if the array is illuminated uniformly, the acquired image may not be so; this is referred to as flat-field variation. As these characteristics affect camera performance, they must be removed through calibration. Thus, images were taken to correct for camera flat-field non-uniformities.

Images were obtained for both cameras of a laser sheet scattering off a uniform gas field (i.e. Rayleigh scattering). Propane was used for its large scattering cross-section

(Eckbreth, 1996). The images were corrected by the laser beam profile. Each column in the resulting images was then averaged providing the flat-field profile of the camera as shown in Figure 5-3. This profile was normalized and divided into each row in the PLIF images. Similar to the procedure discussed above for beam profile correction, a FORTRAN program (see Appendix B) was used to generate an array in which each row was the flat-field profile. IPLab used this array to form a flat-field correction image to be divided into the uncorrected PLIF images.

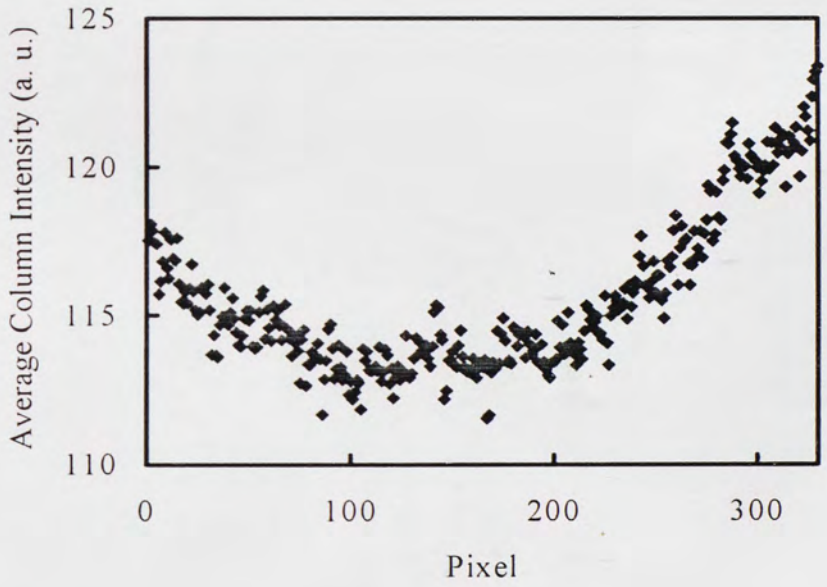

Figure 5-3: Camera flat-field.

5.1.4 Beam Attenuation and Fluorescence Trapping

As the laser passes through the flame, it is absorbed primarily by OH radicals and is therefore attenuated, producing stronger fluorescence signals where the laser sheet enters the flame and weaker signals where it exits (see Section 2.3.2). The laminar flame burner used produced axisymmetric flames and, in the absence of any laser attenuation, it is expected to have identical OH fluorescence signals at both edges of the flame. Figure 5-4 shows a plot of the averaged signal intensity over a specified region of one of the flame images. In this figure, the peak on the left-hand side has a higher intensity than that on the right-hand side. This was the case in all images collected. The drop in intensity, however, was always less than 3 % since the flames studied had thin reaction zones. Therefore, the images gathered from the laminar flame burner were not corrected for attenuation and the flames were considered optically thin.

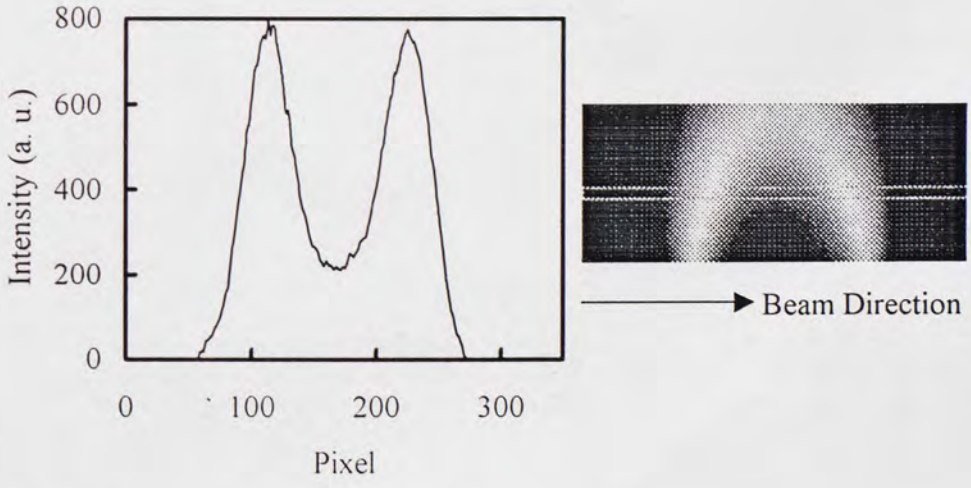

Figure 5-4: Laser attenuation in laminar flame.

The calibration images, on the other hand, had to be corrected for laser attenuation since the premixed flat flame produced by the calibration burner was large and the laser sheet had to travel across the burner's diameter. As explained in Section 3.5 above, the temperature (and, thus, the OH field) at any given height above the burner was uniform across the burner surface. Employing this assumption, the drop-off in laser energy as the sheet passed through the flame should be linear. The average of each column in the calibration images was calculated. Figure 5-5 shows a plot of the normalized column averages where the linear drop in intensity can be appreciated. Each row in the fluorescence images was divided by this linear ramp (see Figure 5-5). A beam attenuation correction image (i.e. linear ramp image) was calculated for each on-transition PLIF image, as the amount of attenuation varied with transition (i.e. $Q_1(5)$ or $Q_1(14)$) and strain imparted on the flame. Figure 5-6 shows one of the calibration images obtained for hydrogen before and after correcting for beam attenuation.

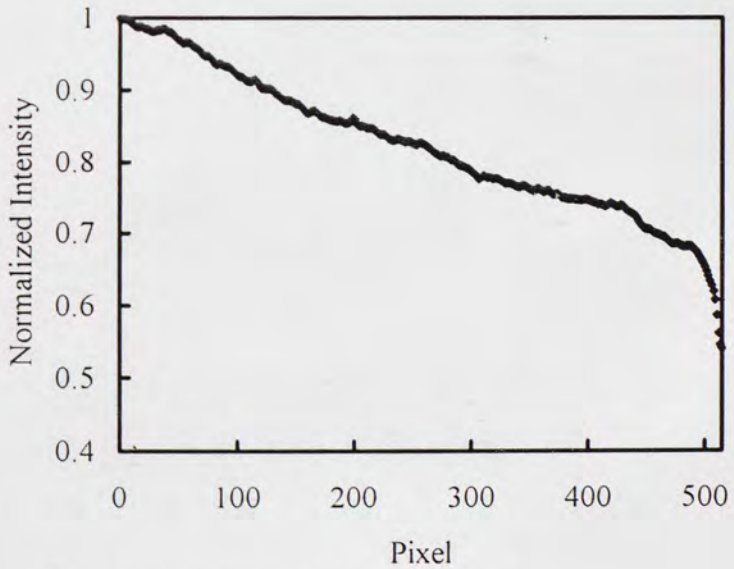

Figure 5-5: Linear laser attenuation (calibration flame).

Fluorescence trapping (i.e. quenching) can be accounted for in a similar manner. Since the flame is axisymmetric and trapping is due to OH molecules, the fluorescence signal should be uniform over areas of uniform OH concentration. As mentioned above, the size of the flames studied in this project are small such that trapping can be considered insignificant. Thus, the images gathered in this study were not corrected for fluorescence trapping.

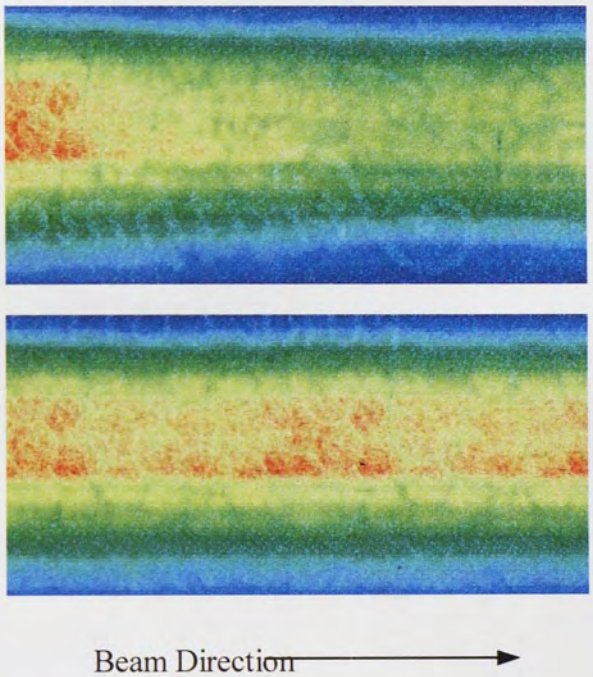

Figure 5-6: Premixed hydrogen-air PLIF calibration image before correction (top) and after correction (bottom) for beam attenuation (red indicates highest signal intensity).

5.1.5 Image Ratios

The $Q_1(5)$ and $Q_1(14)$ transition images needed to be spatially coincident before taking their ratio (i.e. both images overlapped). Even though the flames were repeatable, there was some slight movement of the flame from shot to shot. This movement was captured by the high resolution of the camera. Many of the images for the two transitions were slightly offset spatially from each other due to this. Usually this offset was not more than five pixels (i.e. 0.3 mm). Various tools in IPLab were used to line up the images to solve this problem.

When taking the ratio of the two transitions, pixels outside the reaction zone tended to have a value of unity since the signal values outside the flame were usually the same on both $Q_1 5$ and $Q_1 14$ transitions. As can be seen from the calibration curves in Figure 4-3, as the value of the population ratio decreases, temperature increases. However, low ratios are non-physical since they would correspond to temperatures in the order of 3000 K and above. Therefore, pixel values in the ratio images lower than 0.5 were treated as ambient temperature. Once all corrections and image adjustments had been made and the $Q_1(5)/Q_1(14)$ ratio was taken, the temperature field could be determined using the calibration curve obtained during the thermocouple calibration. All the images taken for the steady and unsteady laminar flames were normalized to the same color scale (which was a user defined color table in IPLab) in order to compare temperature fields of a flame at different pulsation frequencies, amplitudes, and dilution levels.

6 RESULTS AND DISCUSSION

The following results present the findings of the experiments described in Section 3 above. Lewis number effects coupled with the unsteady nature of the flames studied will be shown in this section by examining the images obtained from PLIF measurements. These images help determine the shape and strength of the reaction zone as well as the temperature of the flames studied. The systematic variation of diluents, dilution levels, and pulsing frequencies and amplitudes will help the effort of correlating transport processes with flame structure and dynamics.

6.1 Velocity fluctuations

The axial velocity disturbance introduced by the speaker was measured by LDV as described in Section 3.3. Only the centerline axial velocity 1 mm downstream from the exit of the fuel tube was measured to determine the velocity amplitude of the oscillation introduced by the speaker. As the unsteady fuel mixture emanates from the fuel tube, viscous dissipative forces will change its velocity and structure as it travels downstream. Future PIV (particle image velocimetry) measurements will be performed on the burner setup used in this project to determine the velocity field structure of the introduced unsteadiness.

It should be noted that the burner's fuel tube was long enough to assure a fully developed fuel flow throughout all experimental conditions. As mentioned in Section 3.1, the Reynolds number *Re* (based on the fuel tube diameter) in the experiments described in this study ranged between 10 and 60. For a laminar flow, the necessary tube length to assure a fully developed flow is 0.12 *Re R* (Schlichting, 1979), where *R* is the fuel tube radius. Thus, the minimum fuel tube length for fully developed flow should be approximately 17 mm. The actual length of the tube was 30 cm, approximately 17 times the required length for fully developed flow.

Plots of the amplitude of the axial velocity fluctuations (u') obtained from LDV measurements (Section 3.3) as a function of the voltage applied to the speaker (V) for frequencies listed in Table 3-3 are shown in Figure 6-1 and Figure 6-2. One can note the linear behavior of the velocity fluctuations with voltage. In fact, this linear trend was observed for other frequencies tested, which are not reported here to avoid drudgery. Linear data fits are also shown in Figure 6-1 and Figure 6-2. For a forcing frequency of 100 Hz, voltages had to be increased in order to obtain the same amount of fluid displacement (i.e. u'), as expected since the speaker cone is moving more rapidly at this frequency and does not travel as much as when forced at 10 Hz. Using the data fits, the voltages listed in Table 3-3 can be converted to velocity and the amount of flame pulsing can be characterized. As shown in Table 6-1, the centerline average exit velocity ($\bar{U} = 30$ cm/s) of the flame was modulated with amplitudes (u') ranging from 20% to 100% of the exit velocity.

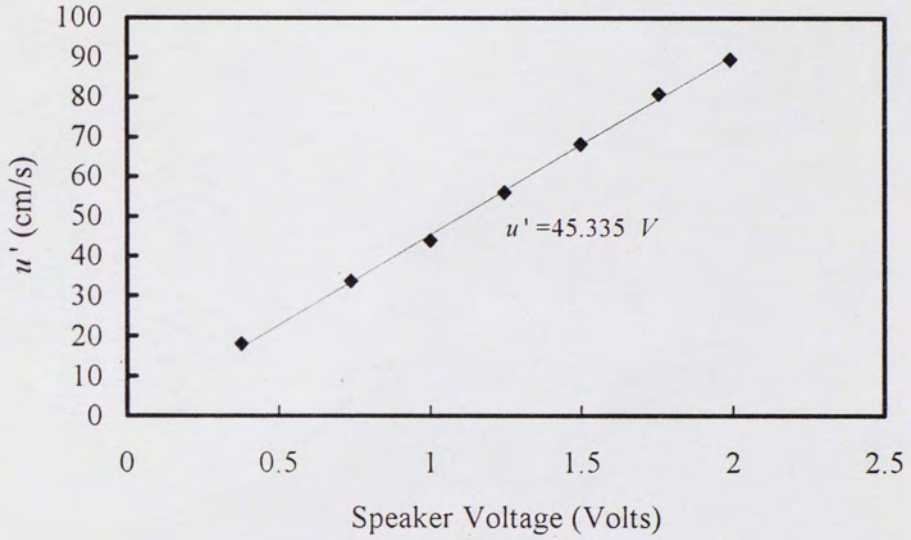

Figure 6-1: Amplitude of imposed exit velocity fluctuations for a speaker forcing frequency of 10 Hz.

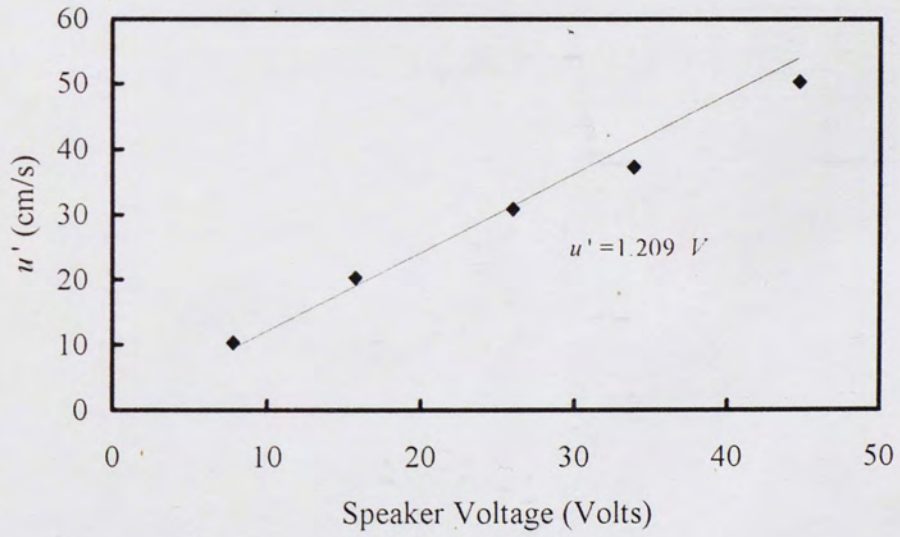

Figure 6-2: Amplitude of imposed exit velocity fluctuations for a speaker forcing frequency of 100 Hz.

High pulse strengths (i.e. close to 100% of the exit velocity) were possible for stronger flames (i.e. 20% dilution). As dilution increased, the maximum forcing level that could be sustained by the flame decreased as expected. The high amplitudes for the tests reported herein (listed in Table 6-1) were selected by increasing the speaker voltage until the flame was extinguished due to the strength of the speaker forcing for each specific dilution. As will be discussed in the next sections, flames diluted with helium tended to be more unstable than flames diluted with argon for the same speaker oscillation strength. In fact, during the tests performed to select pulse strengths (as described above), helium diluted flames always extinguished at a lower voltage than argon diluted flames.

A voltage close to the extinction value where the flame (whether Ar or He diluted) could still exist and be repeatable from cycle to cycle (as observed from LIF images) was selected. Thus, the high amplitudes reported in Table 6-1 are close to the extinction voltage for H_2-He fuel mixtures. The low amplitudes were chosen to be half of the high amplitudes. Within a specific dilution level, both Ar and He dilutions were pulsed at the same amplitude for direct comparison of results. Large and small-scale disturbances could be introduced by the pulse strength selection procedure described above. Note that at a forcing frequency of 100 Hz, all flames tested could not sustain the same high pulse strength used at a frequency of 10 Hz. This phenomenon becomes more evident as dilution increases. It can be seen that at 100 Hz, the high amplitude is 5 to 50% lower than that at 10 Hz.

Table 6-1: Test conditions

Frequency	Amplitude	$u'/\overline{U}$*		
		20% Dilution	40% Dilution	60% Dilution
10 Hz	low	0.604	0.453	0.378
	high	1.058	0.907	0.756
100 Hz	low	0.504	0.403	0.201
	high	1.007	0.806	0.403

* $\overline{U}$ = 30 cm/s

6.2 Steady Temperature Thermocouple Measurements

Flame temperatures of steady flames with fuel mixtures listed in Table 3-2 were measured via thermocouple probing as discussed in Section 3.2. These measurements will provide a basis for comparison with temperature fields obtained from LIF data. Temperature was measured at 2 mm intervals along the flame length. The radial temperature profiles obtained for 20, 40, and 60% dilutions can be found in Figure 6-3, Figure 6-4, and Figure 6-5, respectively.

Note that the maximum flame temperatures for every specific dilution level were always lower than the adiabatic flame temperatures listed in Table 3-1, including cases with $Le_F < 1$ (i.e. the 60% Ar flame). This trend becomes more evident as dilution increases. The large air coflow velocity used in this research project coupled with how hydrogen diffuses to the flame zone might explain this. The presence of convection in

the coflow flame decreases reactant residence time and might lead to reduced flame temperatures, increased reactant leakage, and reduced flame thickness (Law, 1988). In addition, as fuel dilution increases, it becomes harder for hydrogen to diffuse to the reaction zone due to the presence of the diluent species. Other studies on coflow jet flames have reported maximum temperatures that were approximately 250 K lower than the corresponding adiabatic flame temperature (Kawabe *et. al.*, 2000). Counterflow flames, on the other hand, do not exhibit the large convective heat transfer modes seen in coflow flames; thus, temperatures measured in counterflow flames are close to adiabatic temperatures (see Rørtveit *et. al.*, 2001). In fact, as discussed in the introduction section of this report, a large number of numerical studies have been done using the counterflow flame configuration.

Table 6-2 presents a summary of steady thermocouple data gathered in this research project compared to data obtained in counterflow flames (Chaos and Chen, 2003b; Rørtveit *et. al.*, 2001) and the present results from laser-induced fluorescence measurements of steady flames (to be discussed below). One can see the good agreement (within 40 K) between the temperature measured by the thermocouple and the steady temperature obtained from LIF in the Burke-Schumann burner. The temperatures reported for the counterflow diffusion flame (CFDF) were obtained at a strain rate of 100 s^{-1} based on a momentum balance of fuel and oxidizer flows (Seshadri and Williams, 1978). As discussed above, CFDF temperatures were always higher than temperatures measured in the Burke Schumann flames.

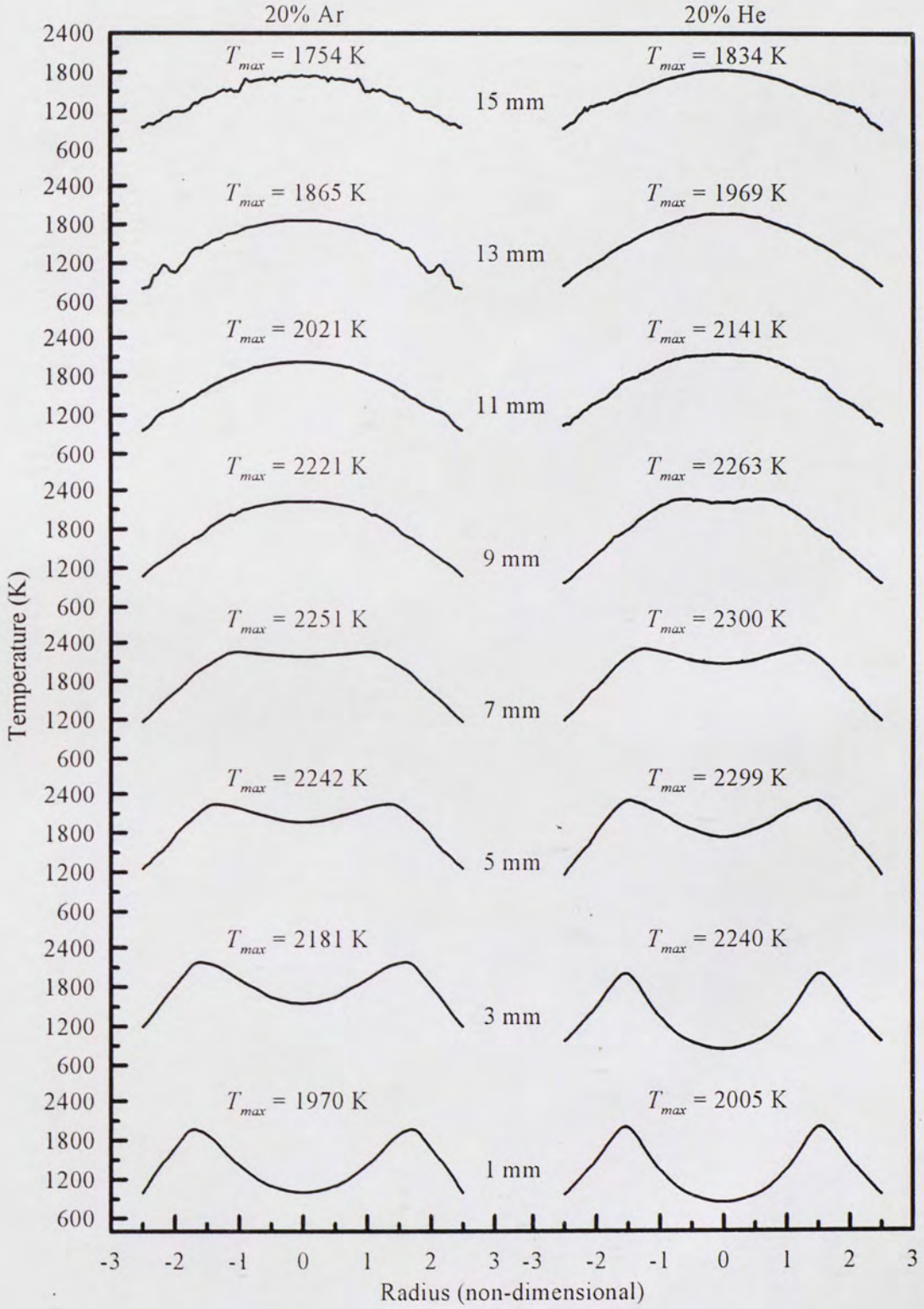

Figure 6-3: Radial temperature profiles for 20% fuel dilution.

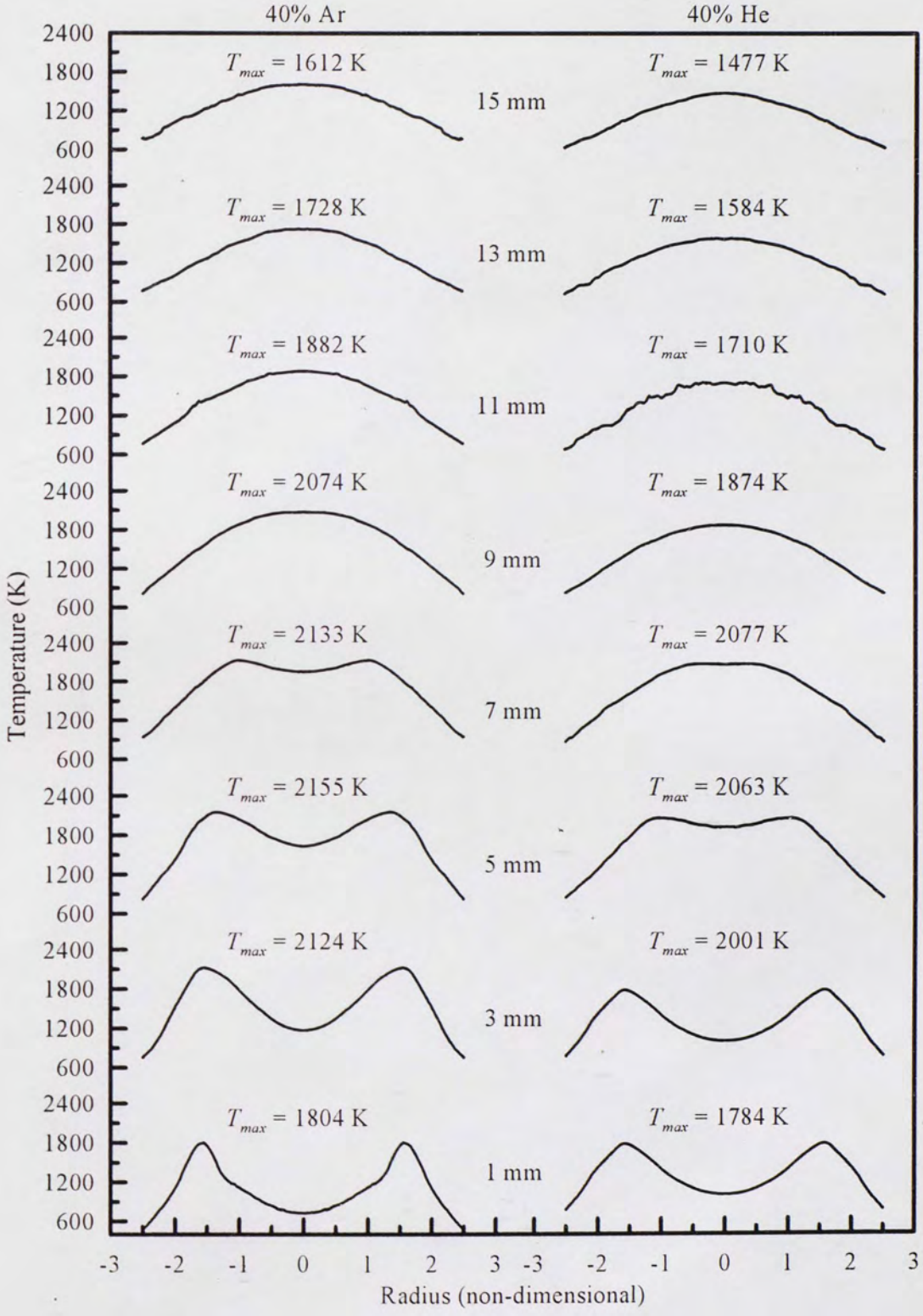

Figure 6-4: Radial temperature profiles for 40% fuel dilution.

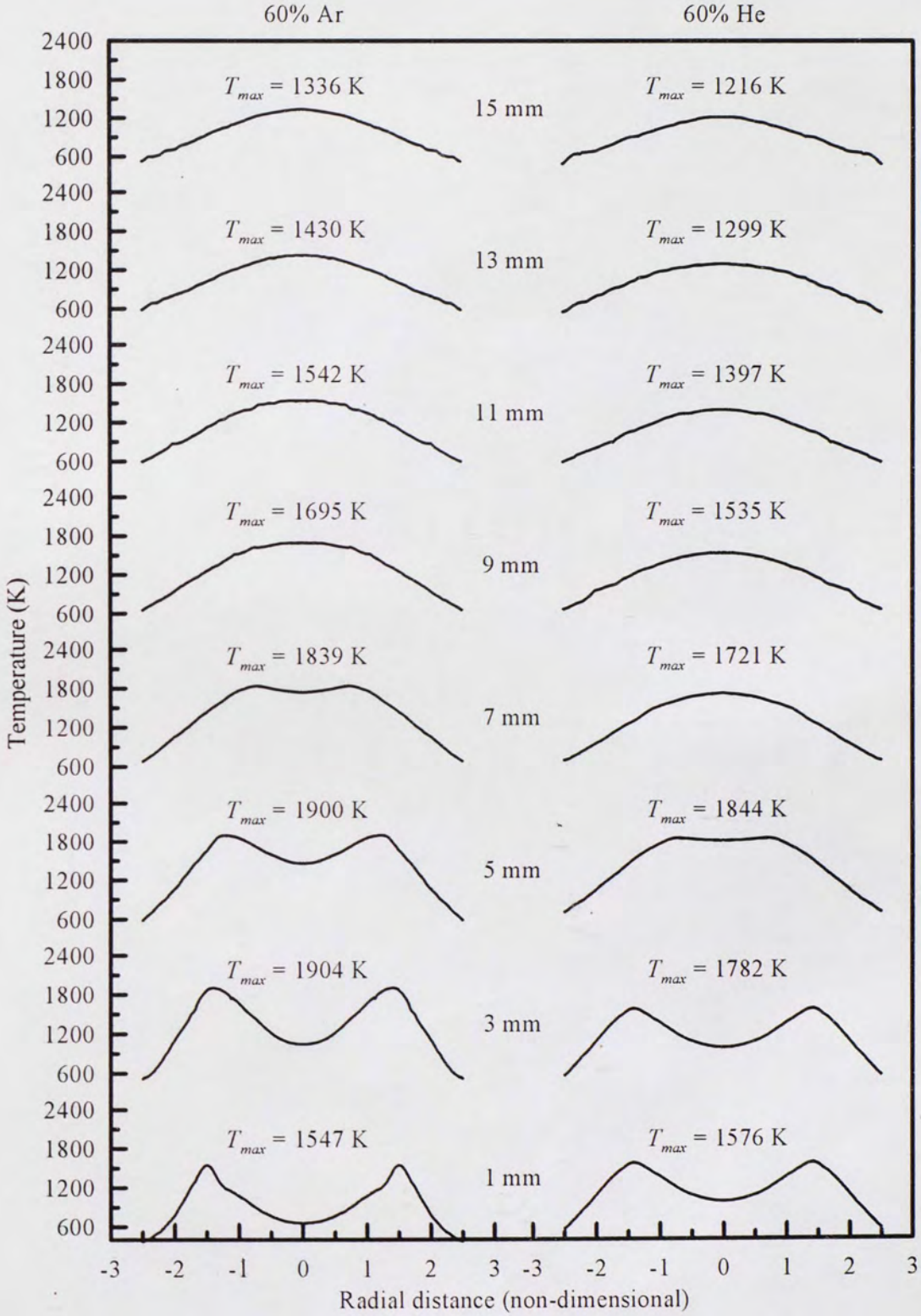

Figure 6-5: Radial temperature profiles for 60% fuel dilution.

Table 6-2: Summary of steady temperature measurements

Fuel Stream (mol %)				Le_F[a]	T_{ad} (K)[b]	T_{max} (K) BSF TC[c]	T_{max} (K) CFDF TC[d]	T_{max} (K) BSF LIF[e]
H_2	He	Ar	N_2					
80	20	---	---	0.998	2323	2300	2331	2276
60	40	---	---	1.012	2226	2077	2172	2080
40	60	---	---	1.035	2041	1844	2039	1880
80	---	20	---	1.389	2323	2251	2298	2267
60	---	40	---	1.012	2226	2155	2187	2139
40	---	60	---	0.718	2041	1904	2118	1969
80	---	---	20	1.387	2288	2212	2246	---
60	---	---	40	0.974	2137	2005	2172	---
40	---	---	60	0.677	1870	1731	2029[f]	---

[a] Fuel Lewis number calculated from Dandy (2003)
[b] Adiabatic flame temperature calculated using CHEMKIN (Kee *et. al.*, 1999)
[c] Thermocouple data of Burke-Schumann flames (i.e. jet flames studied in this project)
[d] Thermocouple data of counterflow diffusion flames at a constant strain rate of 100 s^{-1} (unpublished data of Chaos and Chen, 2003b)
[e] LIF measurements of steady Burke-Schumann flames (i.e. jet flames studied in this project)
[f] A temperature of 2039 K was reported by Rortveit *et. al.* (2001) for this same fuel composition and strain rate

It is expected that the maximum flame temperature of fuel mixtures with the same degree of dilution of He and Ar will be the same, since the specific heat of these inert gases is equal (20.8 J/mol K; Lide, 1993). Thus, any deviations in flame temperature between flames diluted with He and Ar can be attributed to Lewis number effects. As can be seen from Table 6-2, a lower Lewis number leads to higher maximum flame temperature within a specific dilution level. For $Le_F < 1$, thermal diffusivity is lower than the mass diffusivity of the reactants approaching the flame. In order to balance the chemical energy flux (i.e. mass flux) coming into the flame zone with the thermal energy

flux leaving the flame zone, an increased thermal gradient is generated which, in turn, leads to a higher flame temperature (Law and Chung, 1982). Flames with 60% dilution of He and Ar support this conclusion (Le_F = 1.035, 0.718 and T_{max} = 1844, 1904 K for He and Ar-diluted flames respectively based on thermocouple data). The opposite is true for $Le_F > 1$ as evidenced by the 20% He and Ar-diluted flames.

It is noted from the data in Table 6-2 that mixtures with similar Lewis numbers may differ in temperature. This was also observed by Katta *et. al.* (2003). As an example, take the case of 40% dilution with Ar or He. Le_F for these mixtures is identical (i.e. Le_F = 1.012), however, the flame temperature observed in all flames configurations was higher for the Ar dilution (e.g. T_{max} = 2077 K, 2155 K for 40% He and Ar dilutions, respectively, based on thermocouple data of Burke-Schumann flames). When the Lewis number is close to unity, which is the case for the 40% diluted flames, heat and mass diffuse similarly provided the gradients for heat and mass are also the same since the diffusive flux is the product of the diffusion coefficient and the thermal (i.e. enthalpy) or mass gradient. As will be shown in Section 6.3.2, the steady 40% diluted Ar flame has a wider temperature profile when compared to the steady 40% diluted He flame. The thermal gradient for this flame Ar-diluted flame is thus smaller. In addition, the thermal diffusivity, α, of H_2-40%Ar mixtures is less than that of H_2-40%He mixtures (see Figure 6-6). Therefore, assuming the heat flux leaving the flame is the same for H_2-40% Ar and H_2-40% He flames, the flame temperature of the H_2-40%Ar flame needs to be higher in order to account for the reduced gradient and thermal diffusivity. This explains the larger flame temperature exhibited by H_2 flames with 40% Ar dilution as compared with 40%

He-diluted flames (i.e. 78, 15, and 59 K difference for BSF TC, CFDF, and BSF LIF experiments, respectively when comparing thermocouple data of 40% Ar and He dilutions).

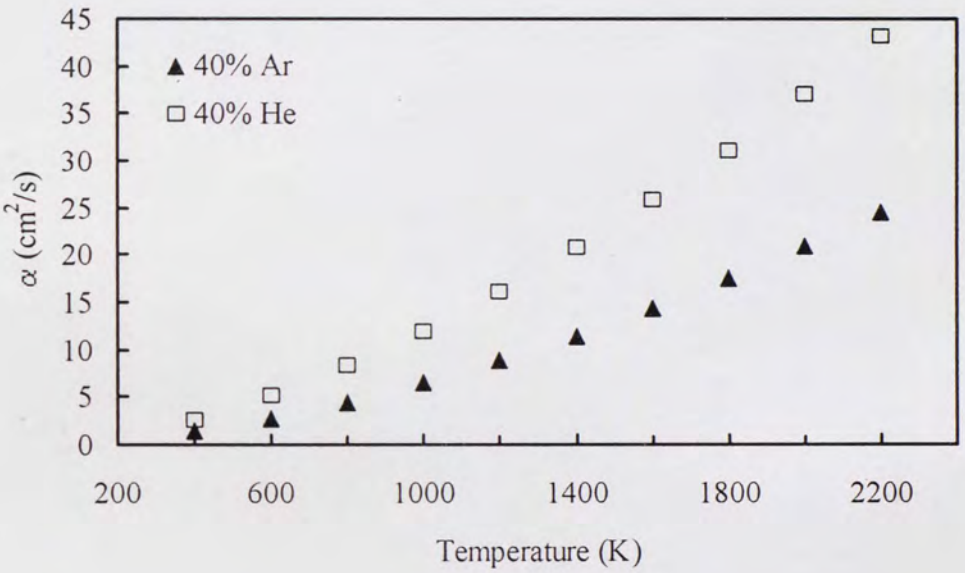

Figure 6-6: Thermal diffusivity of 40% diluted H_2-Ar and H_2-He mixtures over a selected temperature range.

Temperature data obtained in H_2-N_2 fuel mixtures is given in Table 6-2 for comparison with data from other experimental studies (Rørtveit *et. al.*, 2001). The good agreement with these experimental studies (i.e. 2029 K for 60% N_2-diluted H_2 CFDF vs. 2039 K reported by Rørtveit *et. al.*, 2001) serves as proof of concept that the temperature correction scheme followed in this research work yielded reliable measurements. The lower temperatures reported for the N_2 dilution are due to the higher heat capacity of this molecule (29.1 J/mol K; Lide, 1993). Note the Lewis number effect on the flame

temperatures of the counterflow N_2-diluted flames compared to the adiabatic flame temperatures. For 20% N_2 dilution, $Le_F = 1.387 > 1$ and $T_{max} = 2246$ K which is 42 K lower than T_{ad}. For 60% N_2 dilution, $Le_F = 0.677 < 1$ and $T_{max} = 2029$ K which is 159 K higher than T_{ad}.

Lewis number effects on the steady Burke-Schumman jet flames investigated in this research can be further evidenced by considering the temperature along the centerline of the flames. Plots of centerline temperatures (based on thermocouple data) can be found in Figure 6-7, Figure 6-8, and Figure 6-9 for 20%, 40%, and 60% inert dilutions, respectively. The location of the maximum flame temperature in these figures denotes the thermal flame length (i.e. flame tip), which, as mentioned above, was in the order of a few millimeters. Note that for 20% and 40% dilutions of Ar and He as well as 60% He dilution (i.e. $Le_F \gtrsim 1$), the flame tip temperatures are close to the corresponding maximum flame temperatures listed in Table 6-2 (2251, 2300, 2155, 2077, and 1844 K for 20% Ar, 20% He, 40% Ar, 40% He, and 60% He respectively). However, for 60% Ar dilution, the flame tip temperature (i.e. 1740 K) is more than 150 K lower than the maximum flame temperature (i.e. 1904 K). Qualitatively, these results are in agreement with the experiments of Chen *et. al.* (1997). The temperatures reported by Chen *et. al.* (1997), though, were higher than the ones presented here, however, the temperature trends at the tip of the flames were similar to the present results. Lewis number effects at the flame tip reported here were also observed in the experiments of Ishizuka and Sakai (1986) and were modeled numerically by Chung and Law (1984). This can be explained

by the disparity of heat and mass transport rates for nonunity Lewis numbers and the curvature present at the flame tip as discussed below.

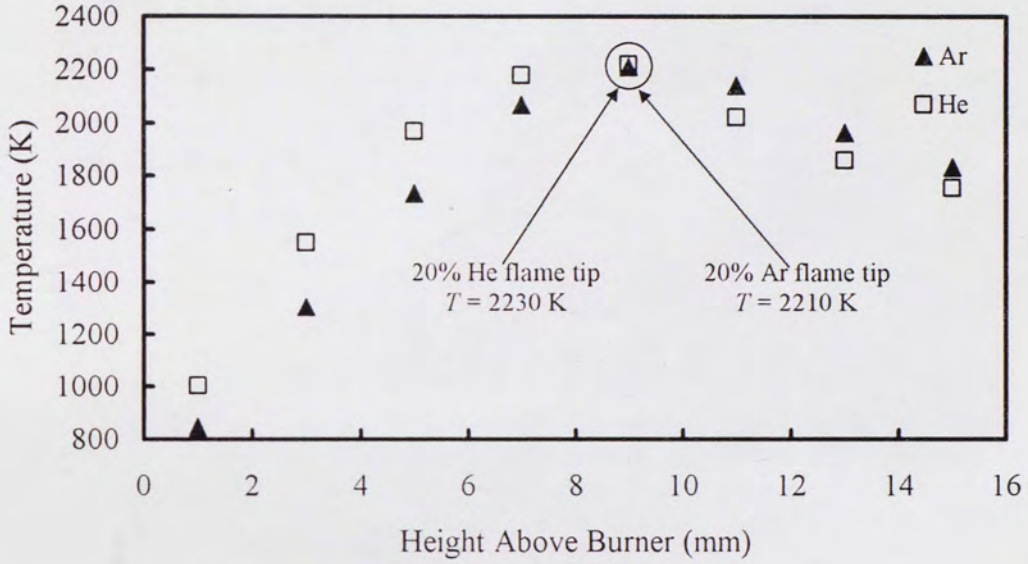

Figure 6-7: Centerline temperature of steady flames with 20% inert dilution.

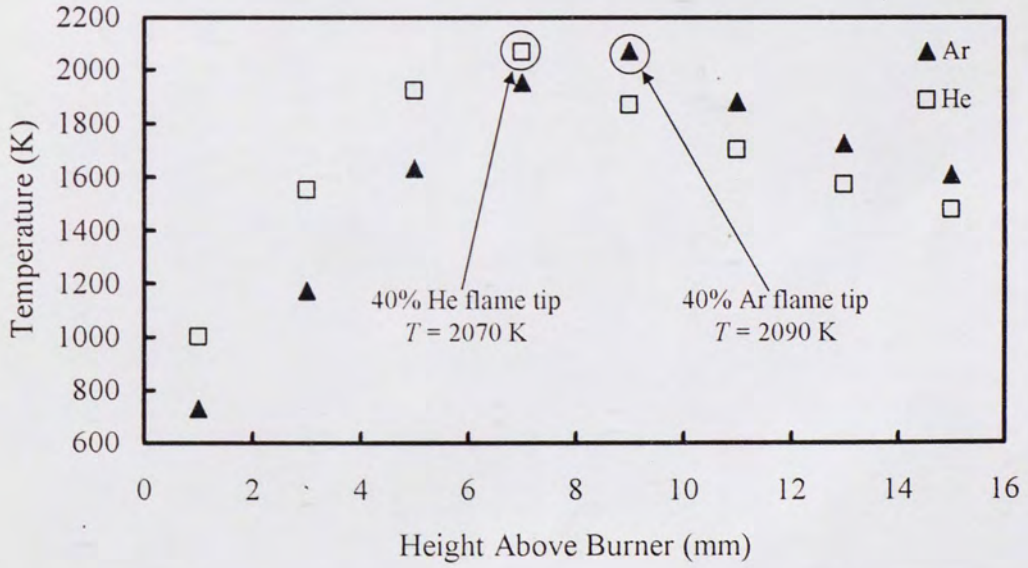

Figure 6-8: Centerline temperature of steady flames with 40% inert dilution.

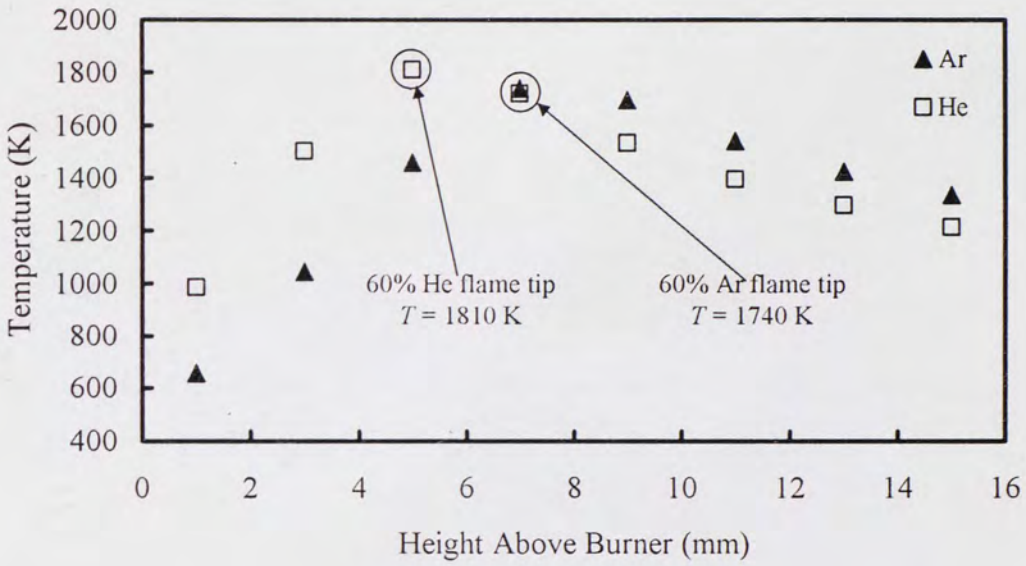

Figure 6-9: Centerline temperature of steady flames with 60% inert dilution.

At the flame tip, the flame curves towards the incoming fuel (i.e. concave curvature) as shown in Figure 6-10. This curvature helps focus heat onto the incoming reactant whereas it also has a defocusing effect on the diffusional mass transport to the flame zone. For $Le_F > 1$, thermal diffusivity is higher than mass diffusivity, the reactants are, thus, heated and the flame tip burns more intensely than the shoulder regions of the flame where curvature is small and heat and mass diffusion is parallel. For $Le_F < 1$, the defocusing effect on the reactants reaching the flame tip is stronger since the mass diffusivity is greater than the thermal diffusivity of the fuel mixture. Thus, there is a cooling effect and the flame tip has a lower temperature, which may lead to local extinction and flame tip opening (Ishizuka and Sakai, 1986).

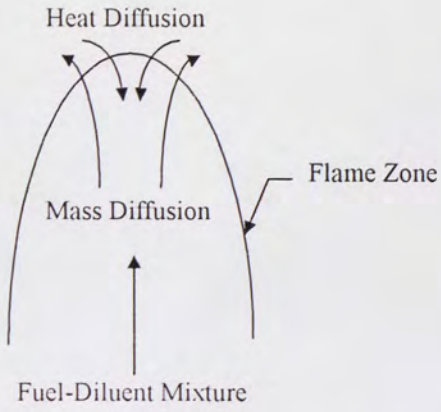

Figure 6-10: Flame tip schematic showing competing transport mechanisms.

Lewis number effects on steady flames have been established in this section. The subsequent sections below will present data collected with the help of PLIF on unsteady flames. Effort and emphasis will be placed in understanding how Lewis number and unsteadiness affect flame structure and temperature.

6.3 Laser–Induced Fluorescence Measurements

The sections below will present and discuss the results obtained from the fluorescence images gathered following the procedure described in Section 3.4. The flame structure will first be investigated by presenting OH intensity images. It is known (Crosley and Smith, 1982) that OH is present in the high temperature regions of the flame (i.e. the flame zone). By tracing OH from the fluorescence images, one can determine how the imposed unsteadiness affects flame structure and reaction intensity. Note, however, that proper transition selection has to be taken into account since the population

of different rotational states have different dependencies on temperature as can be inferred from Equation (1.18). A rotational state with a population that increases with temperature is desirable. Figure 6-11 shows the fraction of OH molecules occupying the rotational levels selected for this research (i.e. $N'' = 5$ and $N'' = 14$) as a function of temperature (using data from Luque and Crosley, 1999). Note that the population of the $Q_1(5)$ transition (i.e. rotational level $N'' = 5$) reaches a maximum around 700 K and then decreases with temperature. On the other hand, the population of the $Q_1(14)$ transition monotonically increases with temperature. Thus, the OH images presented here are those of the $Q_1(14)$ transition where OH population and temperature follow the same trend.

Temperature field images obtained from the ratio of the $Q_1(5)$ and $Q_1(14)$ transitions will also be presented in this section. The ratio of the fluorescence yield from the two rotational transitions pumped by the laser system discussed in Section 3.4 can be correlated to temperature using a simple Boltzmann distribution (see Section 1.2.3.3.5). As discussed above, images were taken at eight temporal locations within the speaker pulse and forty images were taken at each temporal location for each specific dilution/frequency/amplitude combination. Therefore, overall, the data presented in this section is the result of the reduction of a set of approximately 8,000 images following the procedures described in Section 5. All images are presented using pseudo color scales. In the case of OH, the intensity of all images has been normalized by the maximum intensity found in the entire data set.

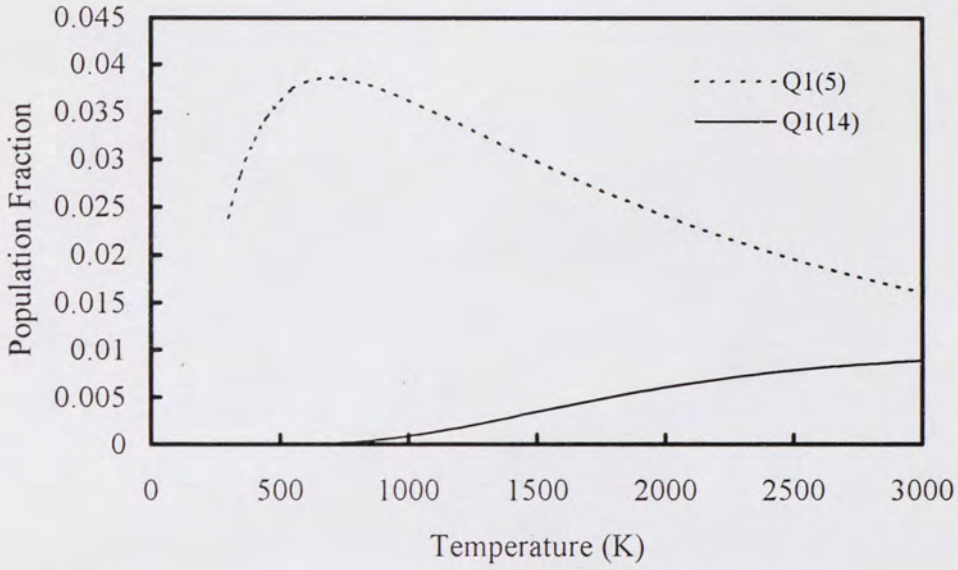

Figure 6-11: Population fractions vs. temperature for selected transitions.

6.3.1 Final Image Set

The image set consisting of OH intensity images and temperature field images is presented in its entirety in Figure 6-12 through Figure 6-61 below. Images of the steady flames are shown first followed by the OH intensity and temperature images for the unsteady flames. In these latter images, the phase angle within the speaker pulse is denoted by ϕ. Note that the interrogation region in all the images extends from 3 mm to approximately 10 mm above the fuel tube. In all images presented in this section, r denotes the radial distance from the fuel tube axis and R is the fuel tube radius.

Note that, at low frequency, the flames have structures similar to the steady flames. The flames respond steadily to the imposed speaker forcing and either bulge out

or come close to the burner centerline depending on the phase angle of the oscillation. High frequency flames are, in general, substantially different from low frequency flames. The reaction zones (as seen in the OH images) are thinner and a greater amount of curvature seems to be present. In some cases (see, for example, Figure 6-18), the flame is stretched and "pinched off" and a pocket seems to be formed. In addition, for high forcing amplitudes, some phases do not show a flame (e.g. Figure 6-29). This might not necessarily mean that the flame has extinguished but that the flame is out of the field of view of the camera.

Flames diluted with He seem to be more affected by the speaker forcing than Ar-diluted flames. For the same pulsing amplitude, He-diluted flames are displaced to a further radial location than Ar-diluted flames (e.g. Figure 6-14 and Figure 6-15). Regardless of the value of Le_F, He-diluted flames always yield a maximum temperature at some point during the oscillation cycle that is greater than the maximum temperature for the Ar-diluted flames for the same dilution level and at the same pulsing frequency and amplitude (e.g. Figure 6-54 and Figure 6-55). The sections below will discuss these issues in more detail.

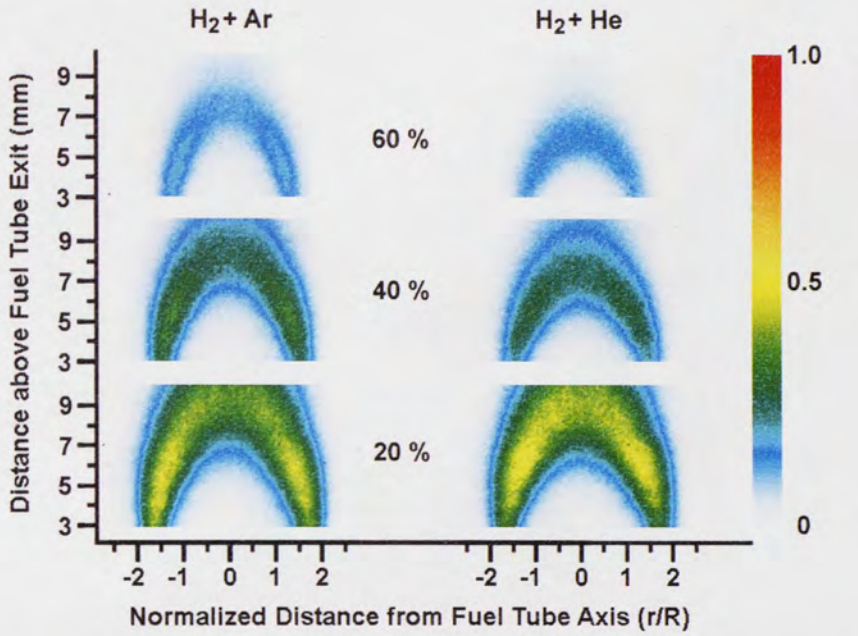

Figure 6-12: Two-dimensional OH field images of steady flames (percentages indicate level of inert gases).

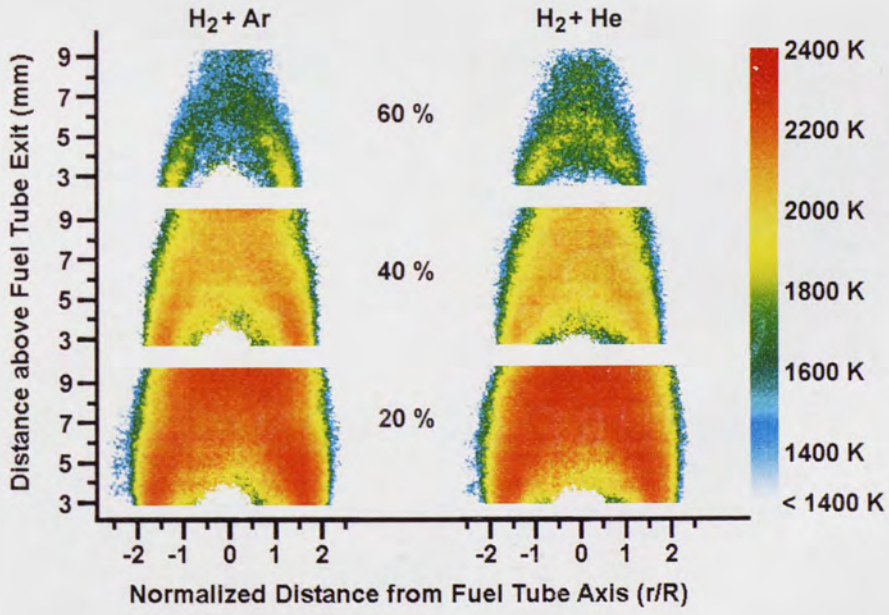

Figure 6-13: Two-dimensional temperature field images of steady flames (percentages indicate level of inert gases).

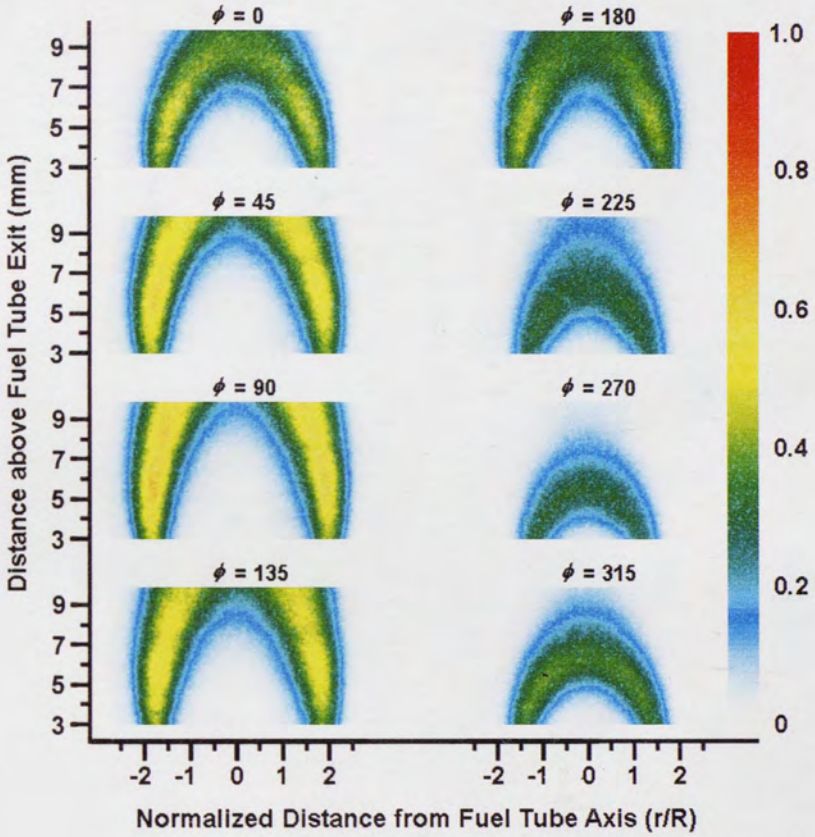

Figure 6-14: Two-dimensional OH field images for 20% Ar dilution, 10 Hz, low amplitude.

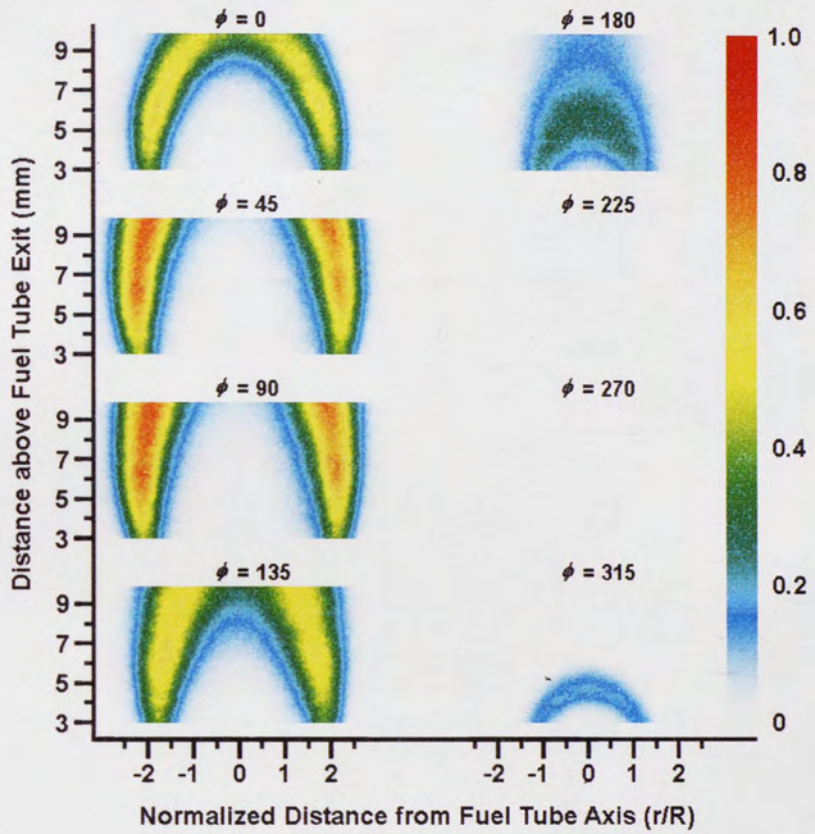

Figure 6-15: Two-dimensional OH field images for 20% He dilution, 10 Hz, low amplitude.

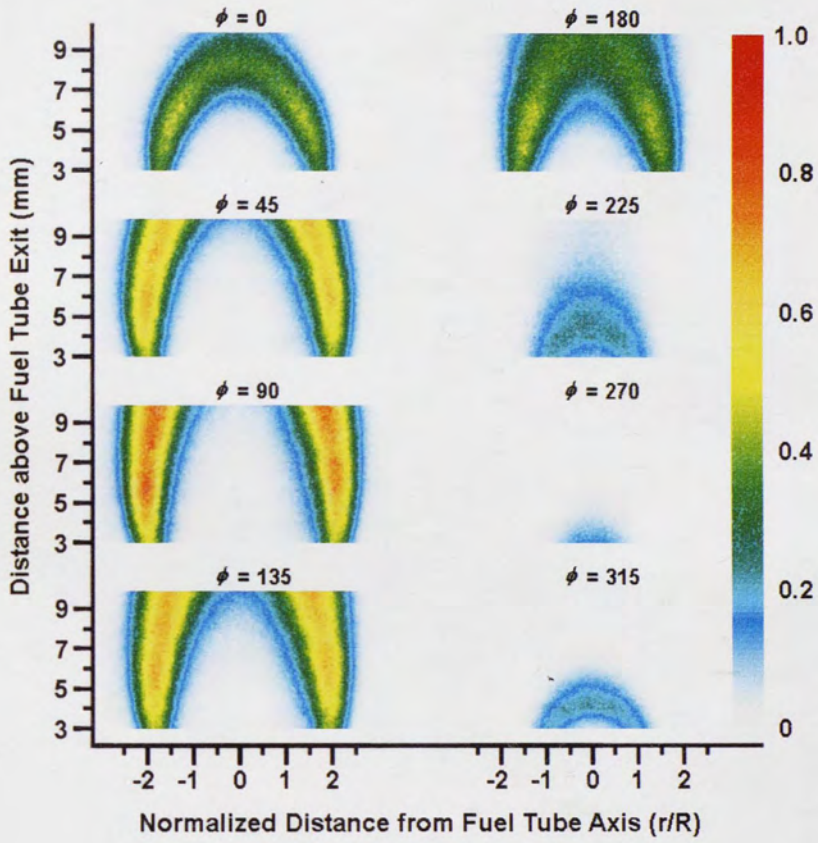

Figure 6-16: Two-dimensional OH field images for 20% Ar dilution, 10 Hz, high amplitude.

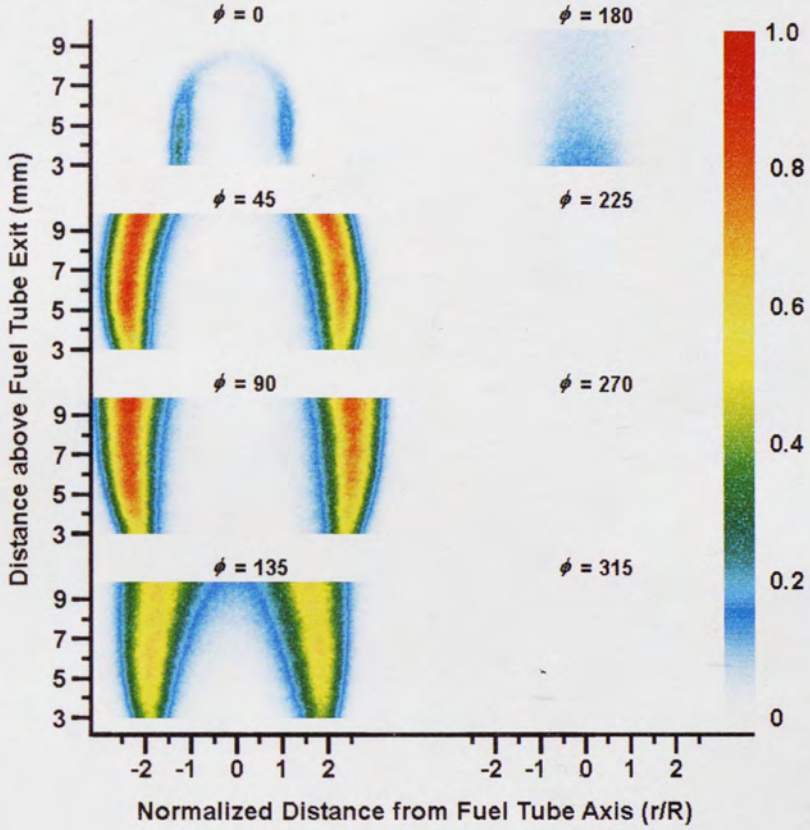

Figure 6-17: Two-dimensional OH field images for 20% He dilution, 10 Hz, high amplitude.

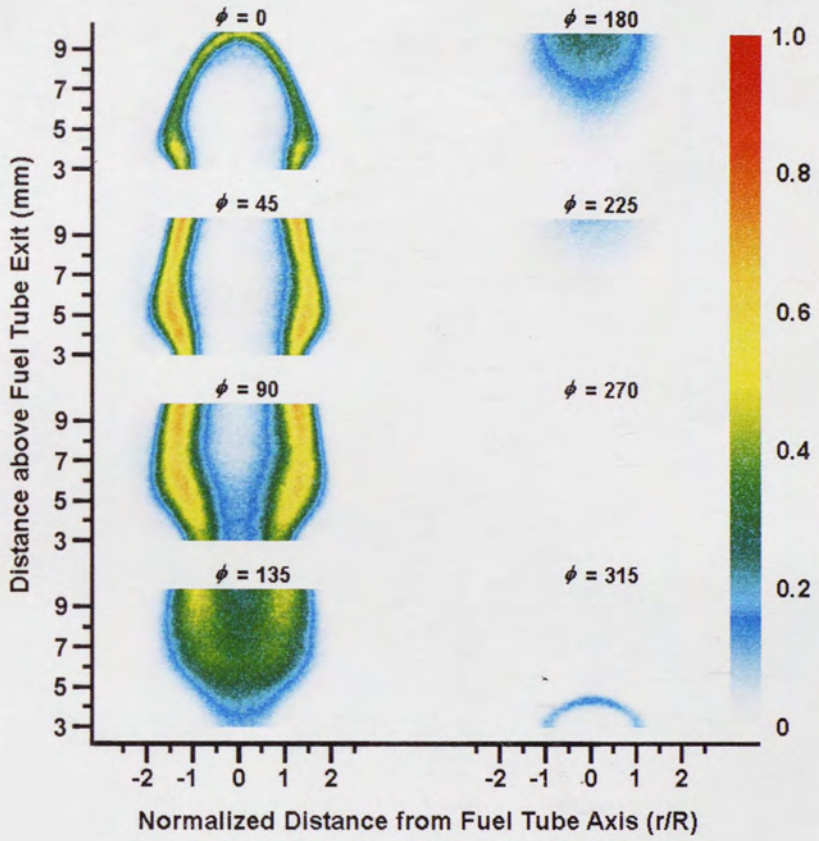

Figure 6-18: Two-dimensional OH field images for 20% Ar dilution, 100 Hz, low amplitude.

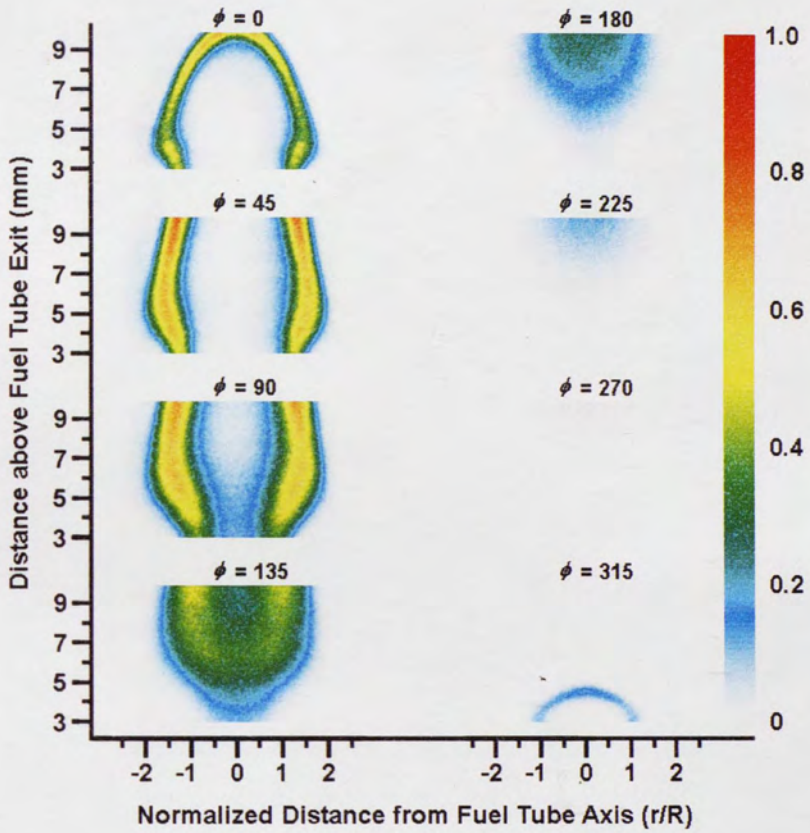

Figure 6-19: Two-dimensional OH field images for 20% He dilution, 100 Hz, low amplitude.

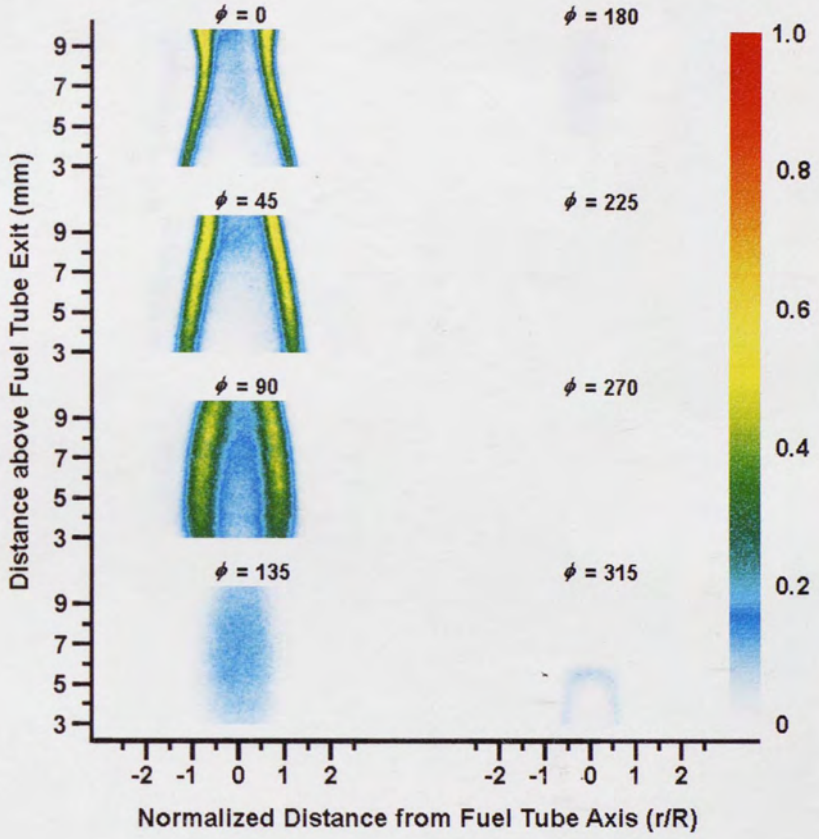

Figure 6-20: Two-dimensional OH field images for 20% Ar dilution, 100 Hz, high amplitude.

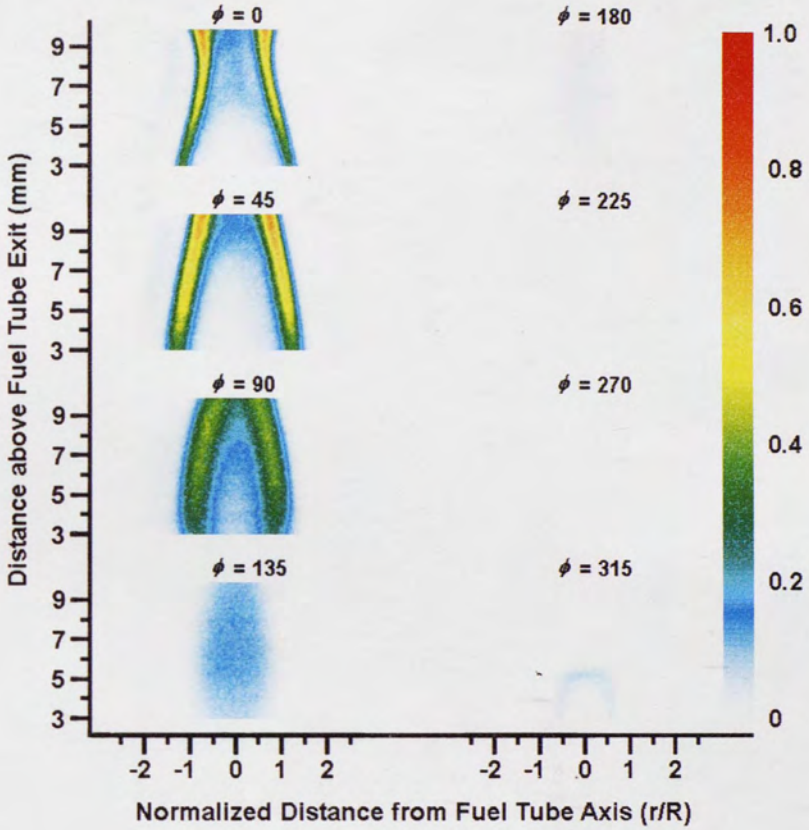

Figure 6-21: Two-dimensional OH field images for 20% He dilution, 100 Hz, high amplitude.

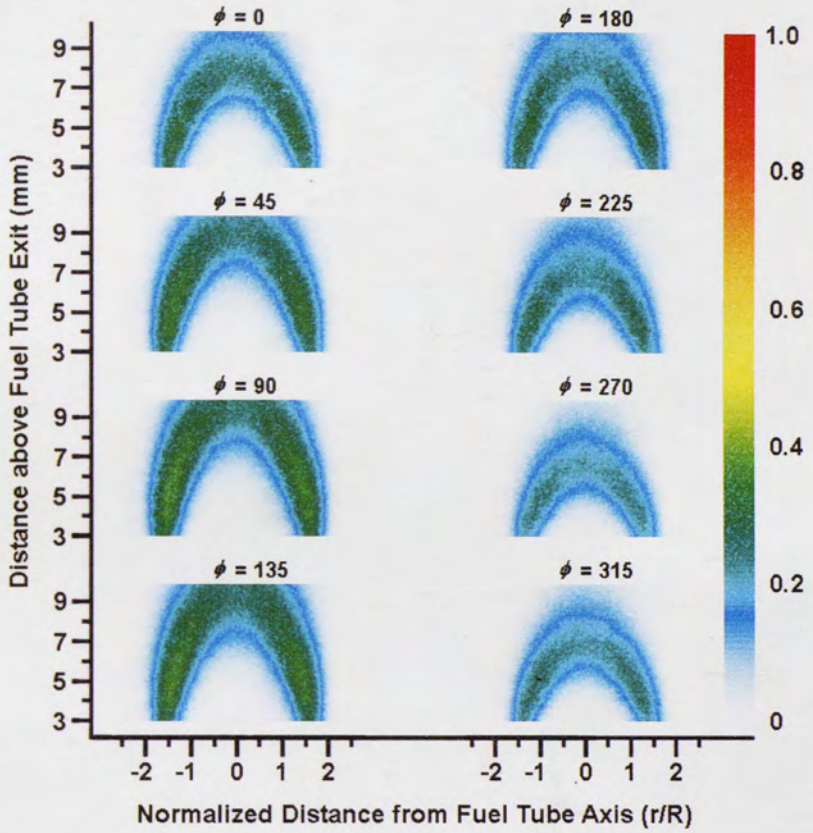

Figure 6-22: Two-dimensional OH field images for 40% Ar dilution, 10 Hz, low amplitude.

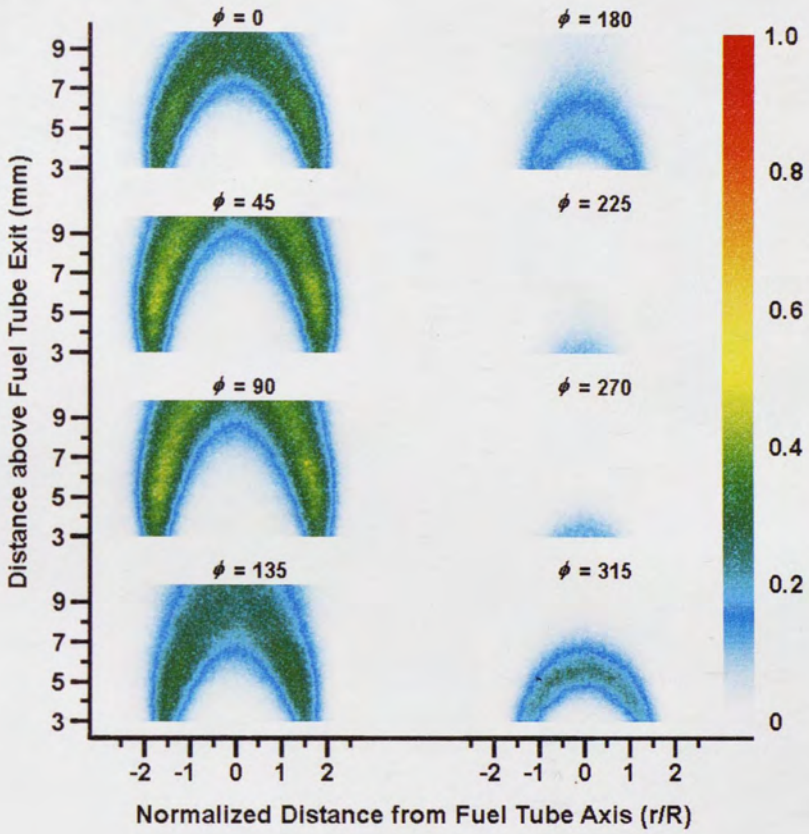

Figure 6-23: Two-dimensional OH field images for 40% He dilution, 10 Hz, low amplitude.

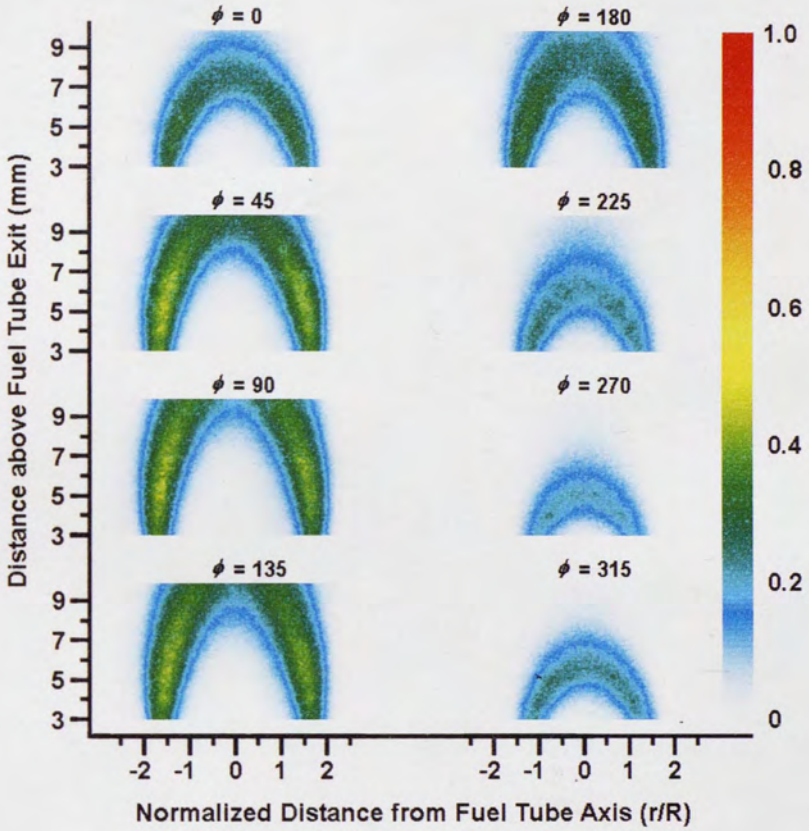

Figure 6-24: Two-dimensional OH field images for 40% Ar dilution, 10 Hz, high amplitude.

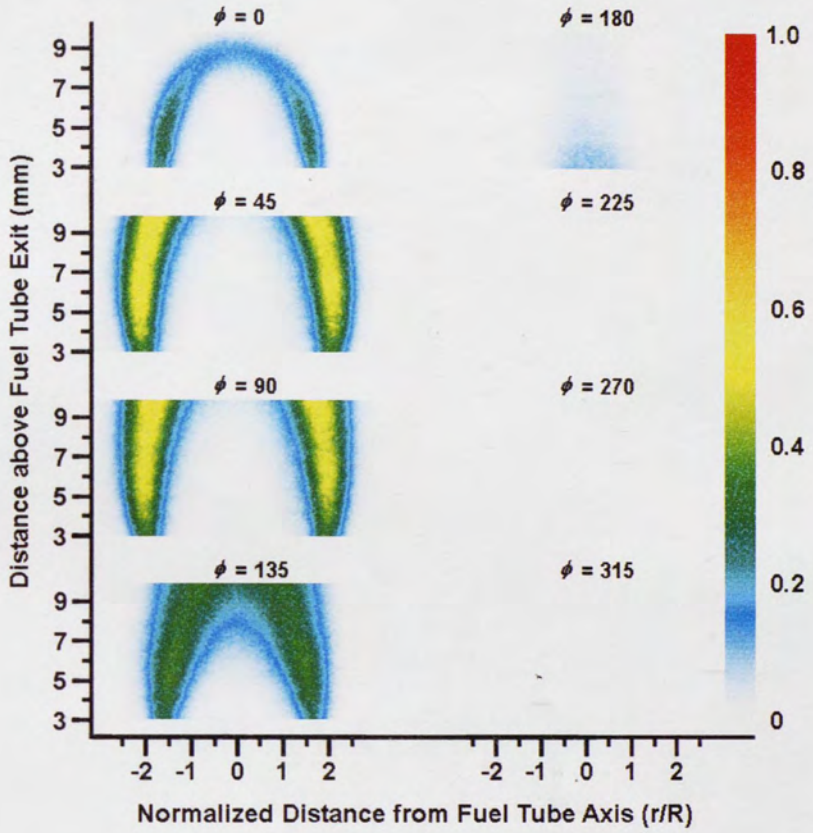

Figure 6-25: Two-dimensional OH field images for 40% He dilution, 10 Hz, high amplitude.

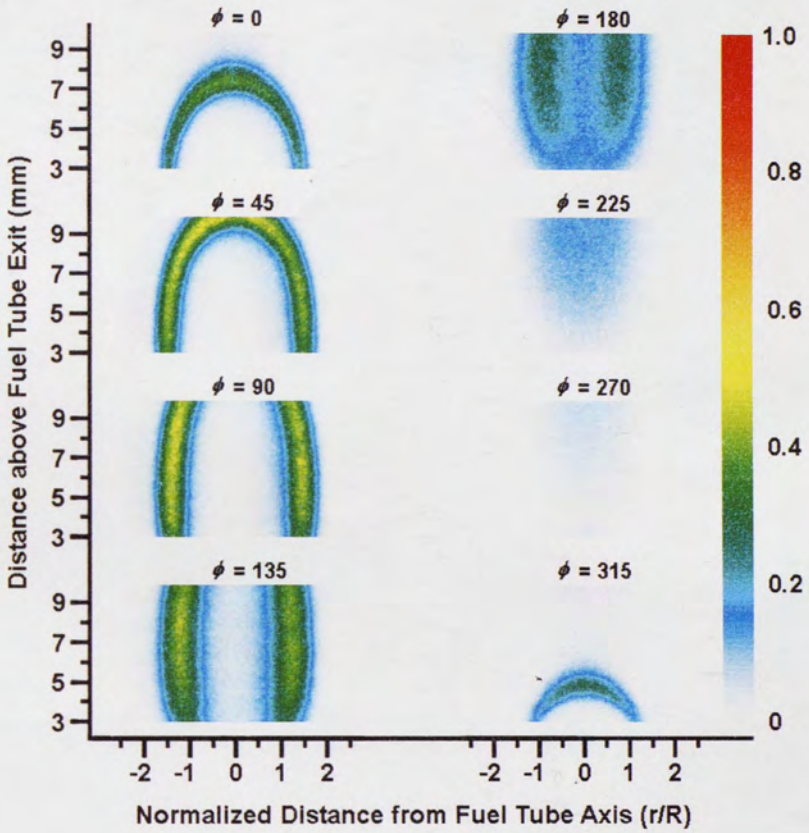

Figure 6-26: Two-dimensional OH field images for 40% Ar dilution, 100 Hz, low amplitude.

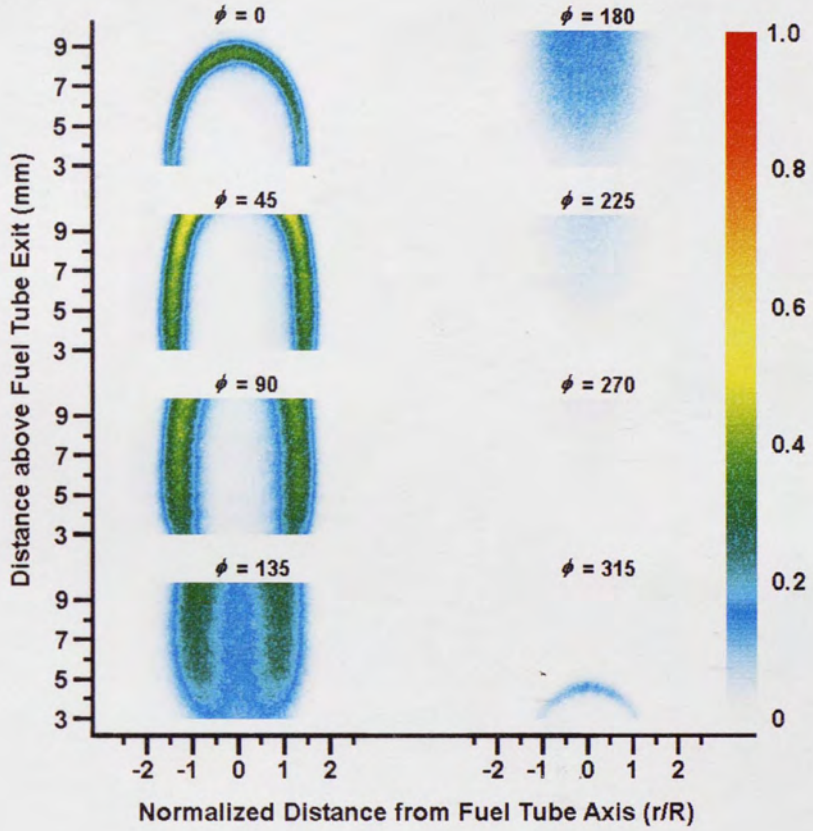

Figure 6-27: Two-dimensional OH field images for 40% He dilution, 100 Hz, low amplitude.

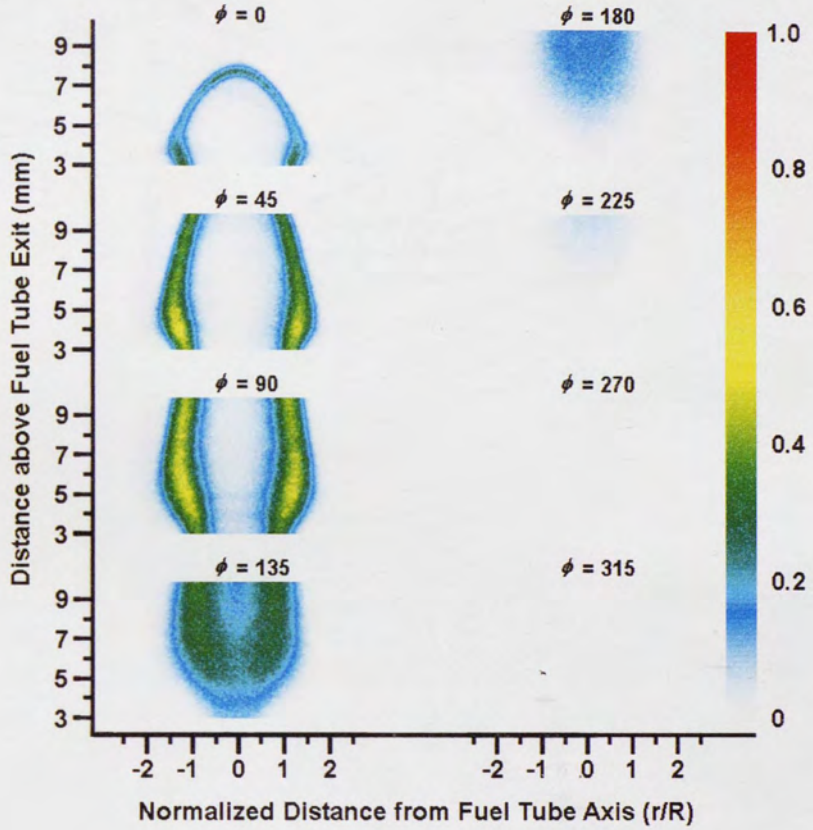

Figure 6-28: Two-dimensional OH field images for 40% Ar dilution, 100 Hz, high amplitude.

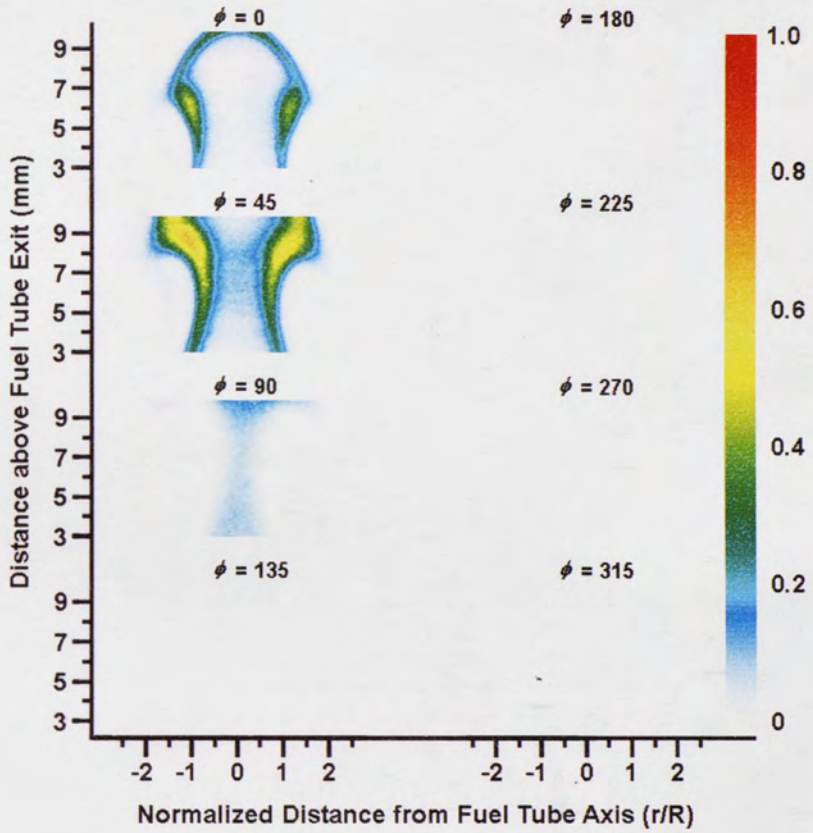

Figure 6-29: Two-dimensional OH field images for 40% He dilution, 100 Hz, high amplitude.

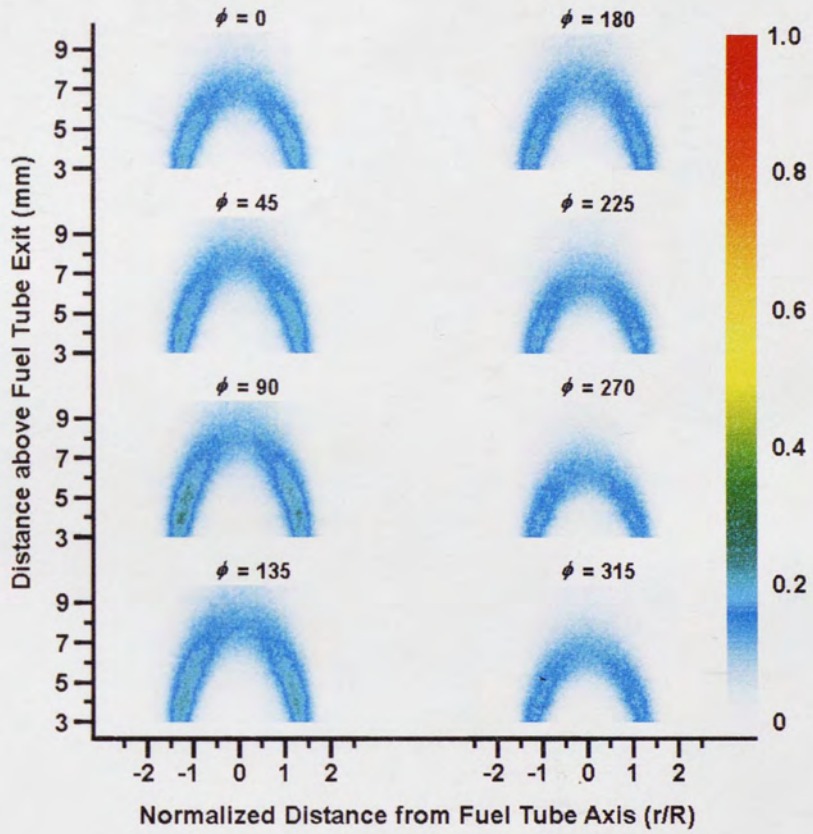

Figure 6-30: Two-dimensional OH field images for 60% Ar dilution, 10 Hz, low amplitude.

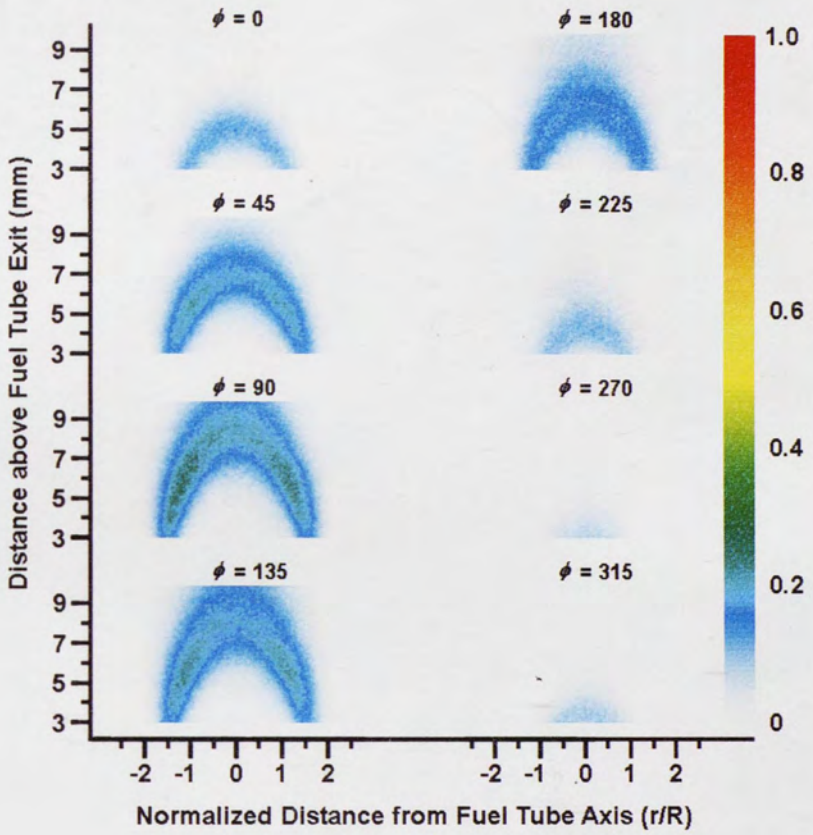

Figure 6-31: Two-dimensional OH field images for 60% He dilution, 10 Hz, low amplitude.

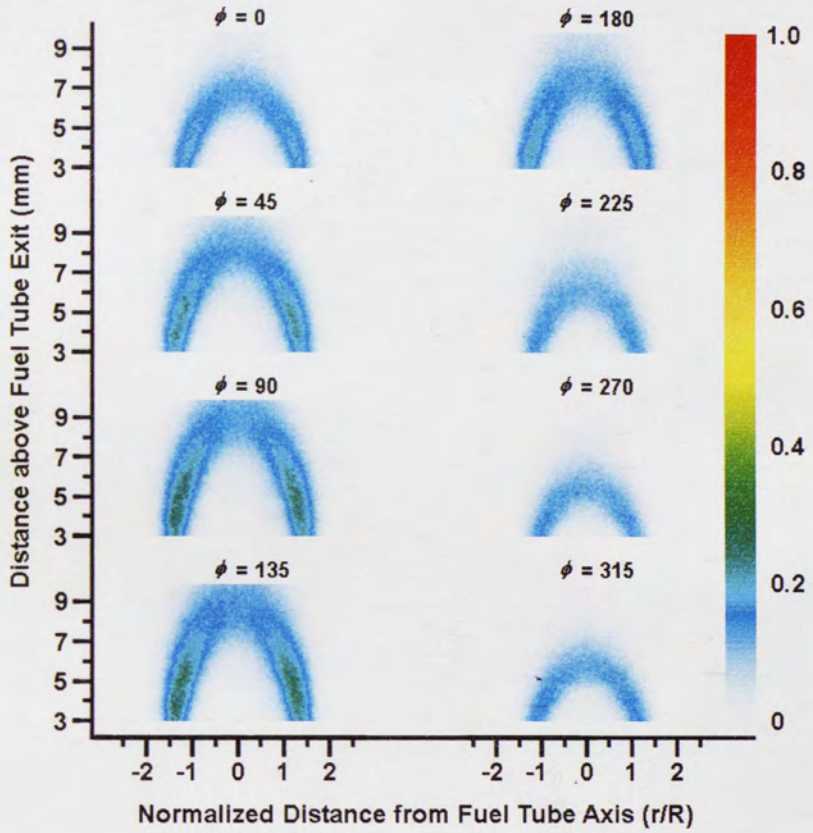

Figure 6-32: Two-dimensional OH field images for 60% Ar dilution, 10 Hz, high amplitude.

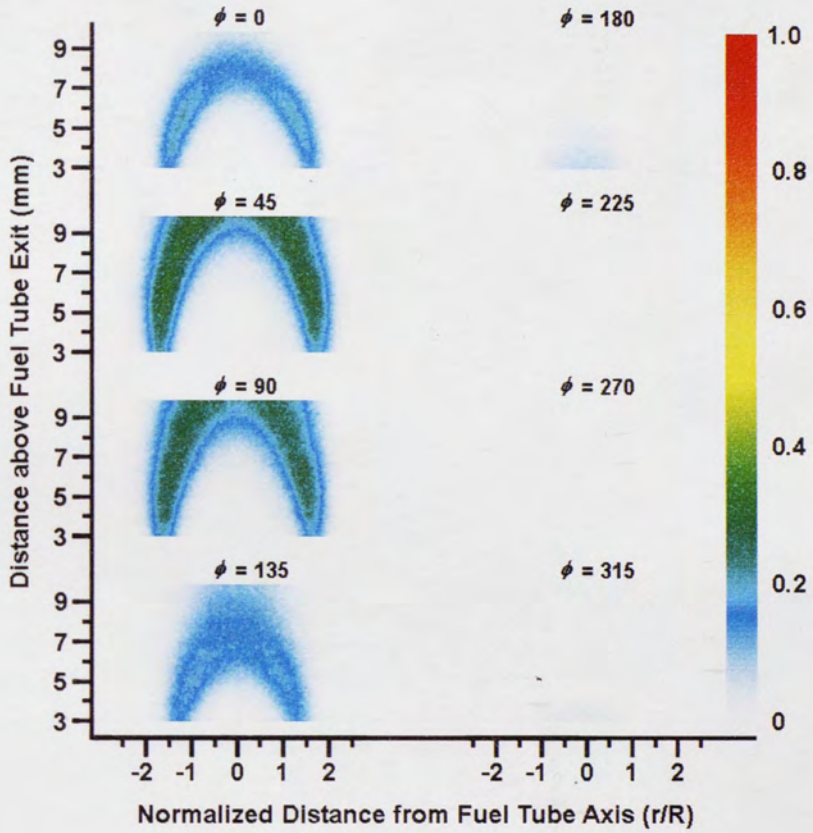

Figure 6-33: Two-dimensional OH field images for 60% He dilution, 10 Hz, high amplitude.

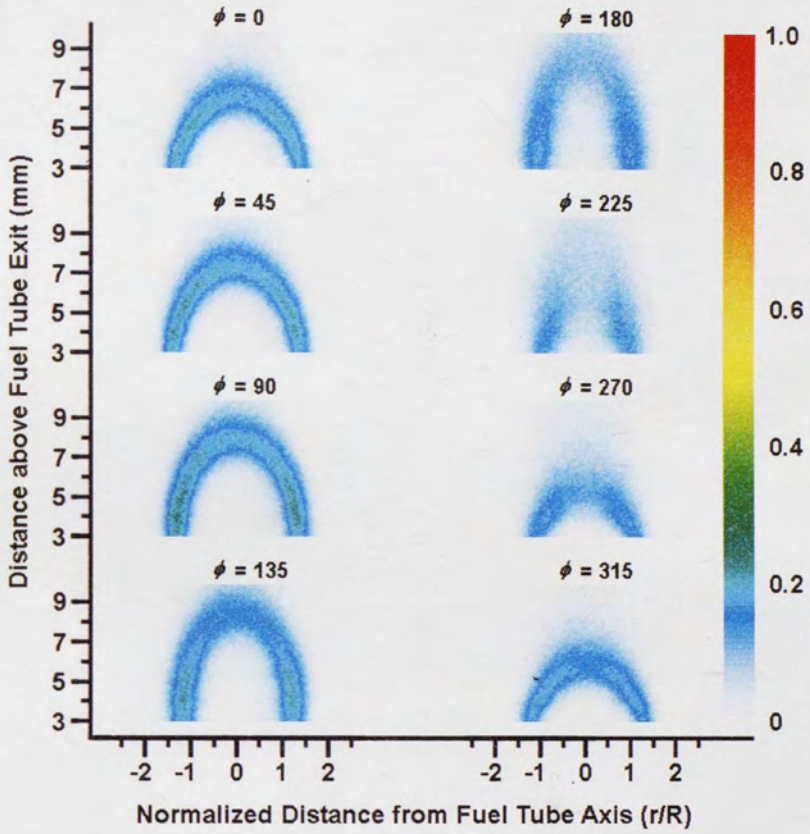

Figure 6-34: Two-dimensional OH field images for 60% Ar dilution, 100 Hz, low amplitude.

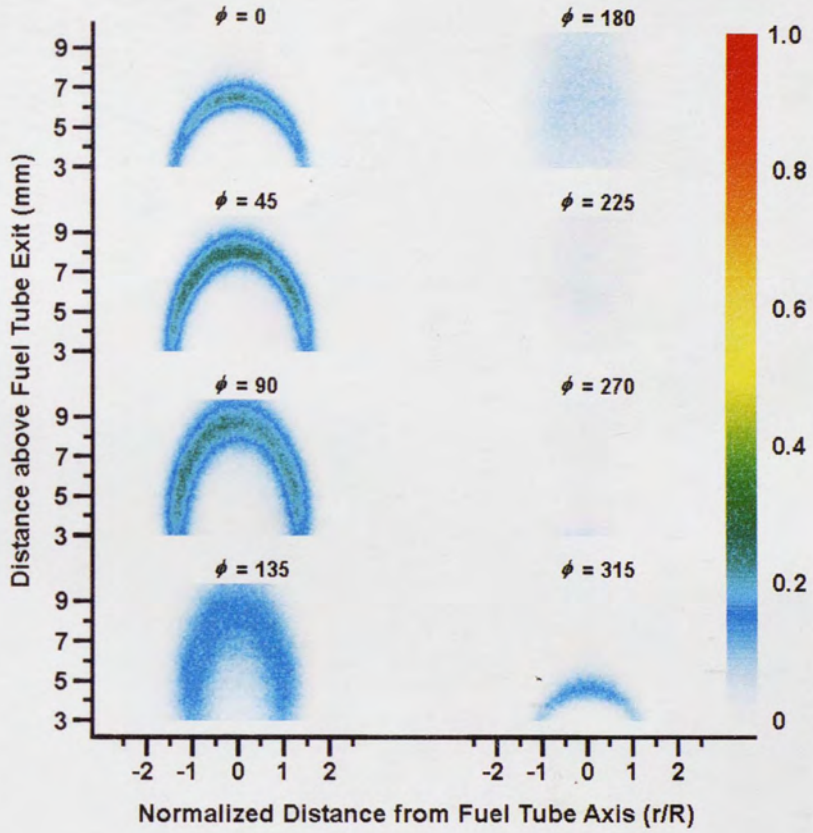

Figure 6-35: Two-dimensional OH field images for 60% He dilution, 100 Hz, low amplitude.

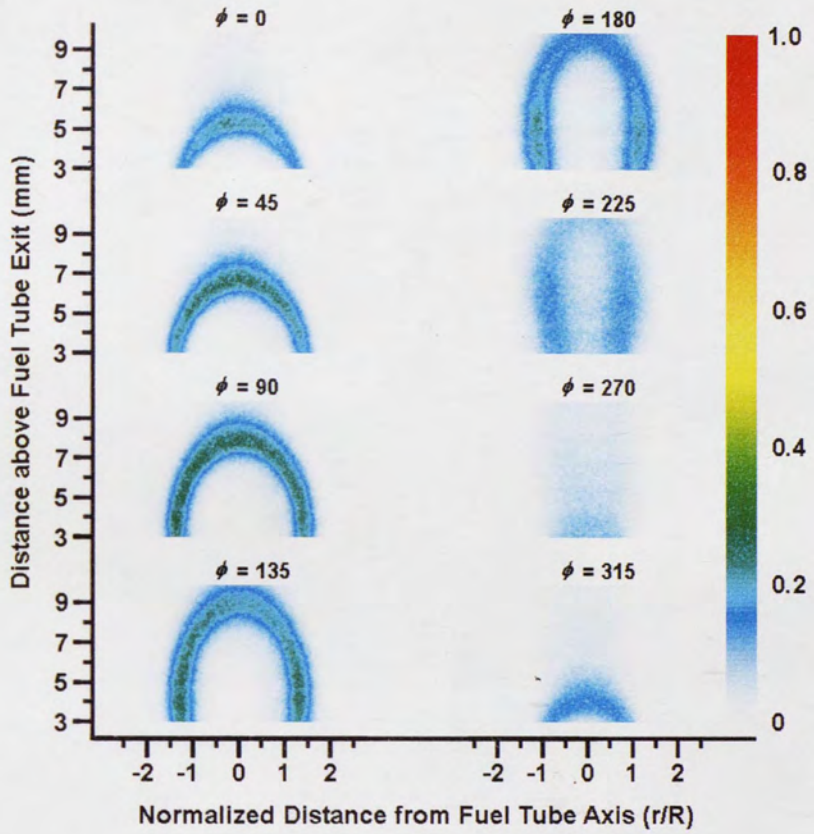

Figure 6-36: Two-dimensional OH field images for 60% Ar dilution, 100 Hz, high amplitude.

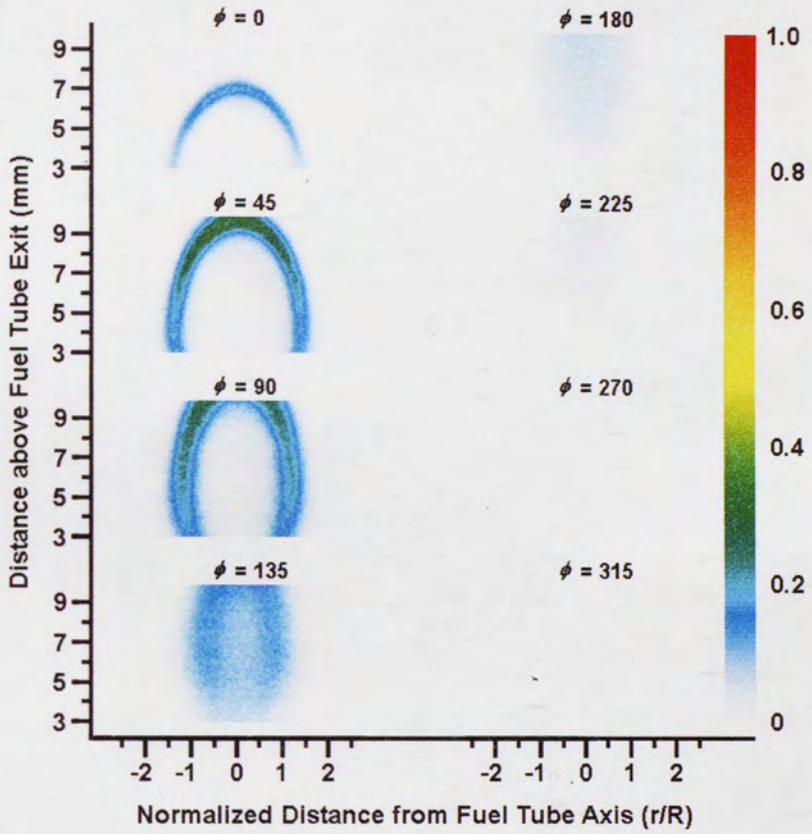

Figure 6-37: Two-dimensional OH field images for 60% He dilution, 100 Hz, high amplitude.

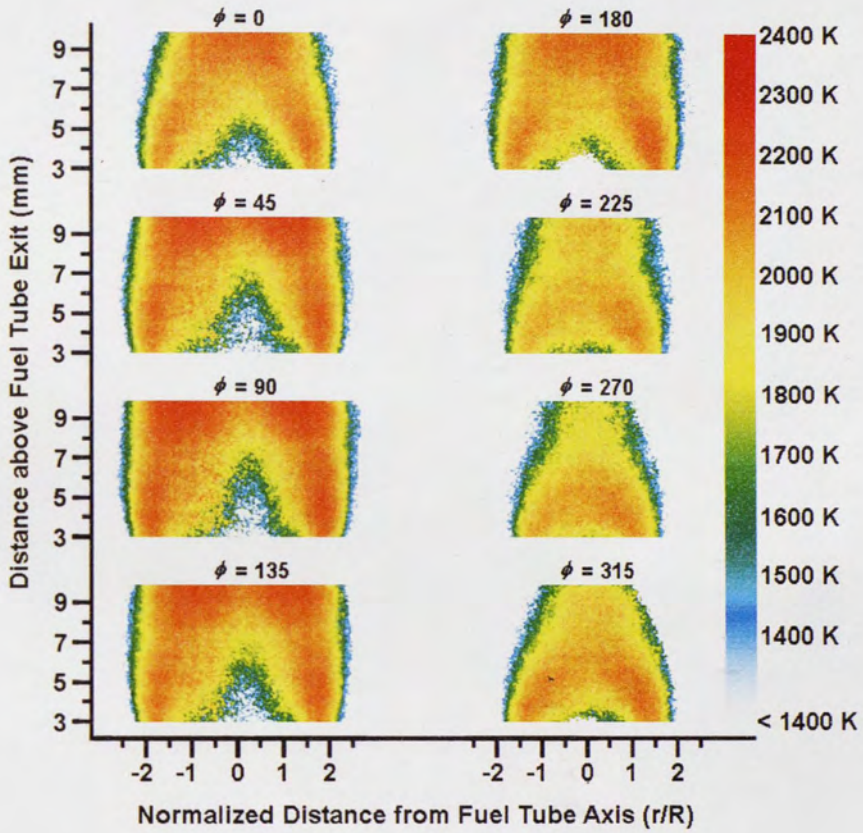

Figure 6-38: Two-dimensional temperature field images for 20% Ar dilution, 10 Hz, low amplitude.

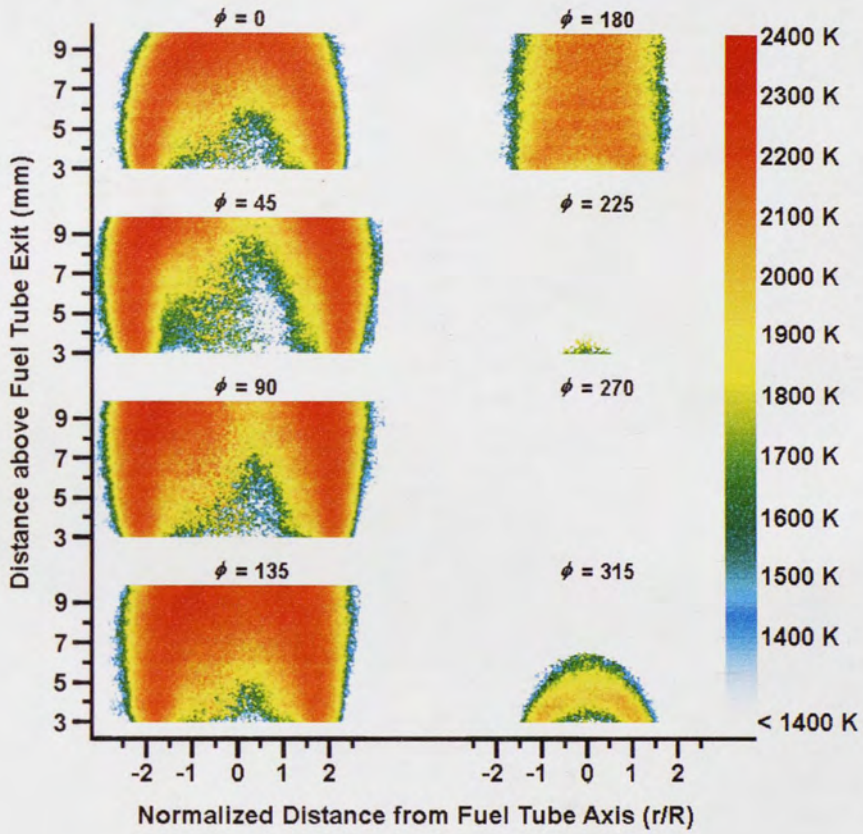

Figure 6-39: Two-dimensional temperature field images for 20% He dilution, 10 Hz, low amplitude.

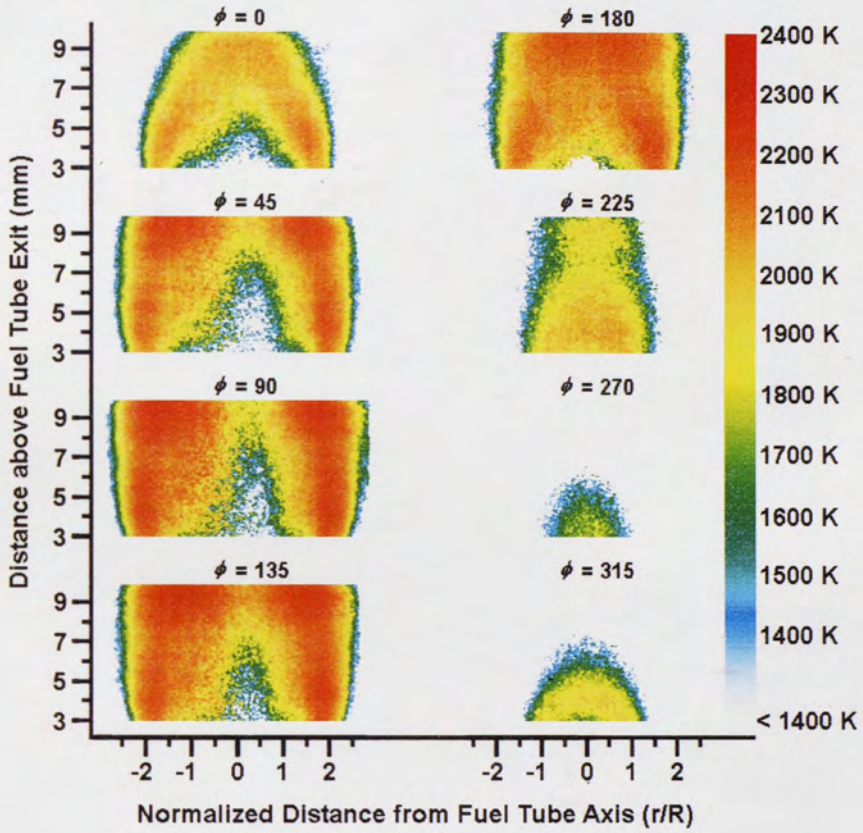

Figure 6-40: Two-dimensional temperature field images for 20% Ar dilution, 10 Hz, high amplitude.

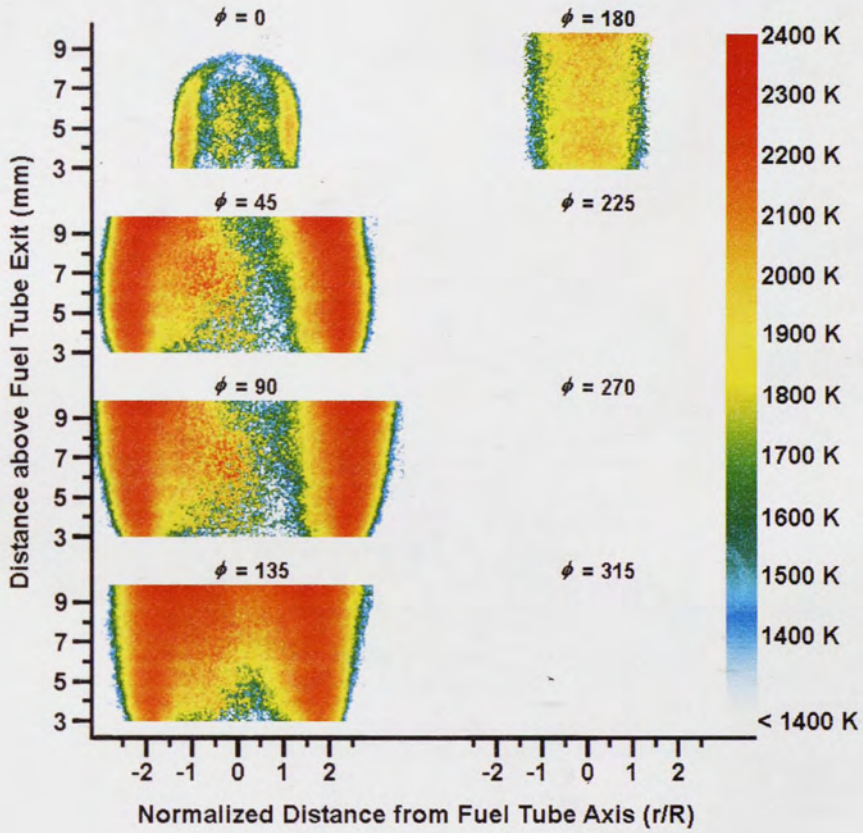

Figure 6-41: Two-dimensional temperature field images for 20% He dilution, 10 Hz, high amplitude.

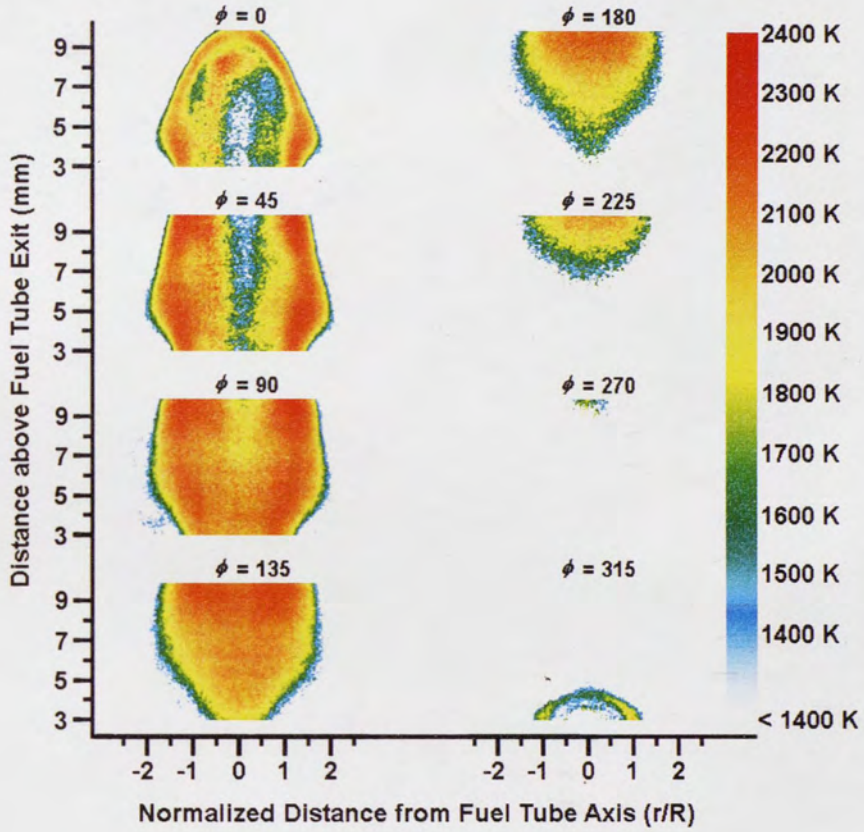

Figure 6-42: Two-dimensional temperature field images for 20% Ar dilution, 100 Hz, low amplitude.

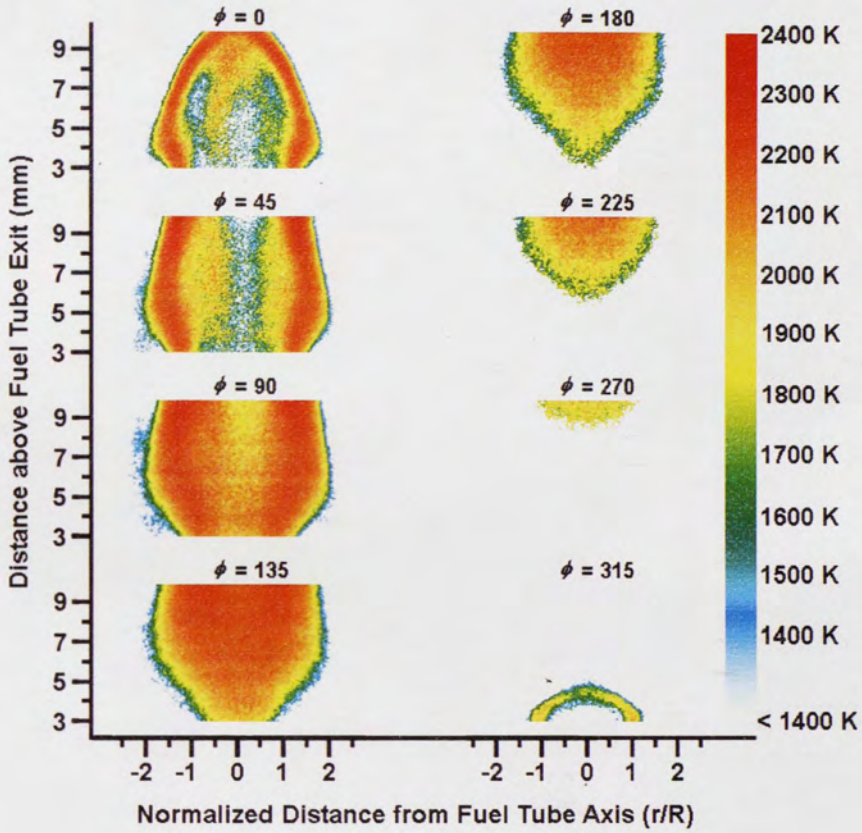

Figure 6-43: Two-dimensional temperature field images for 20% He dilution, 100 Hz, low amplitude.

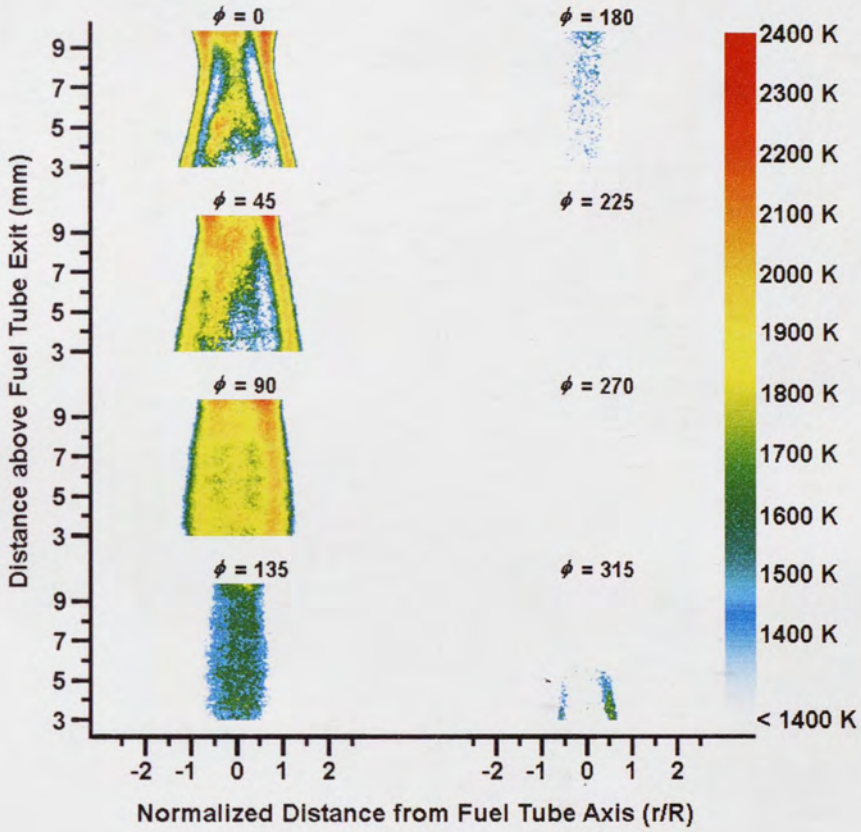

Figure 6-44: Two-dimensional temperature field images for 20% Ar dilution, 100 Hz, high amplitude.

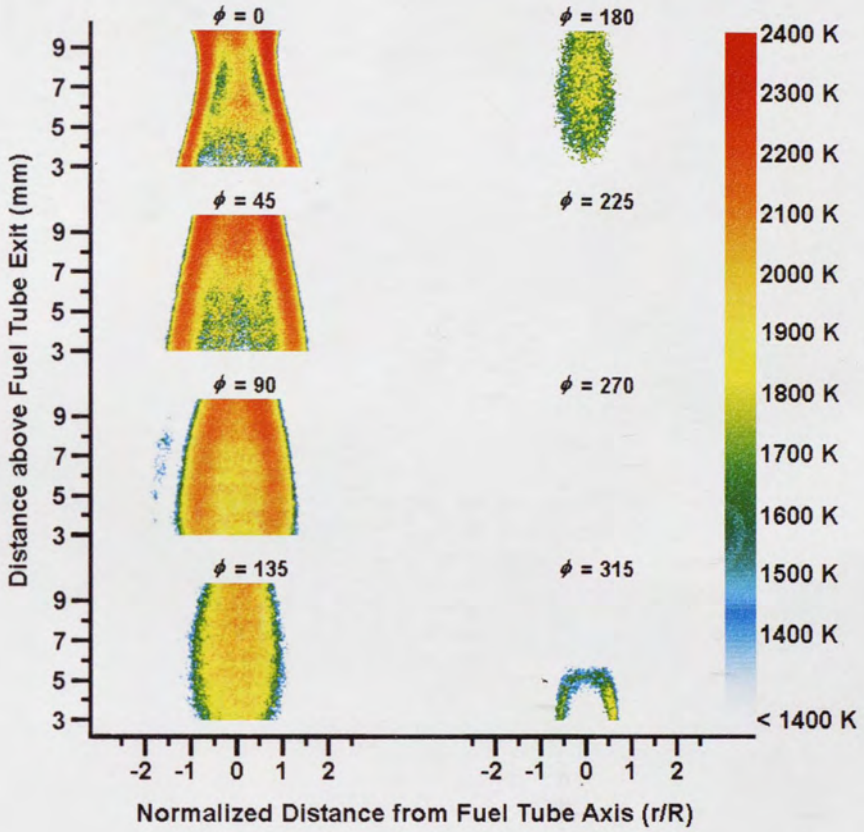

Figure 6-45: Two-dimensional temperature field images for 20% He dilution, 100 Hz, high amplitude.

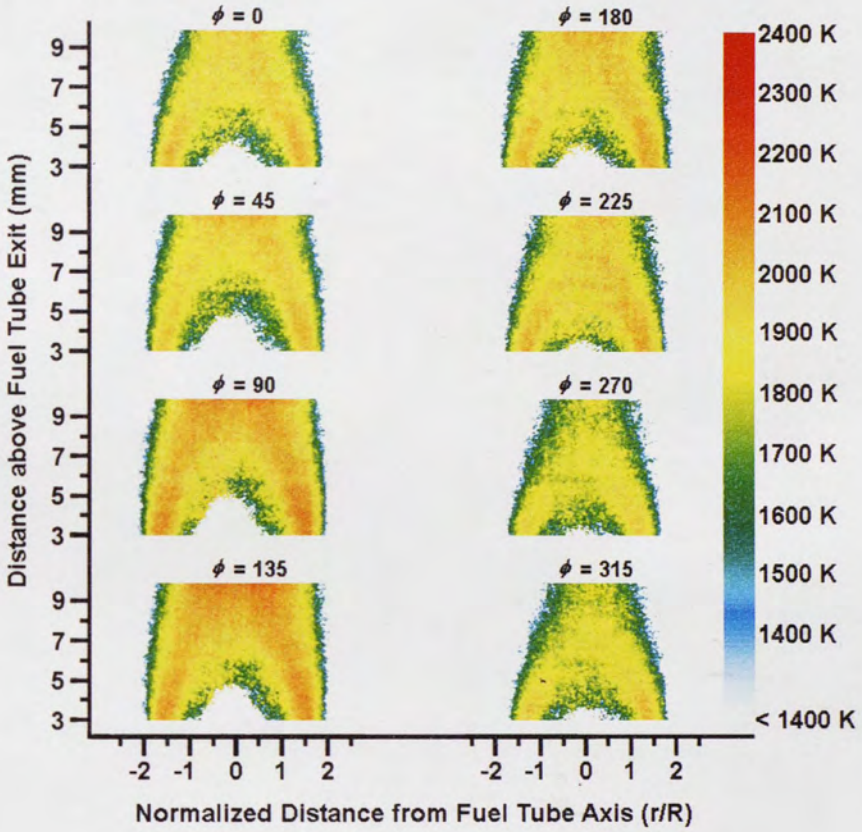

Figure 6-46: Two-dimensional temperature field images for 40% Ar dilution, 10 Hz, low amplitude.

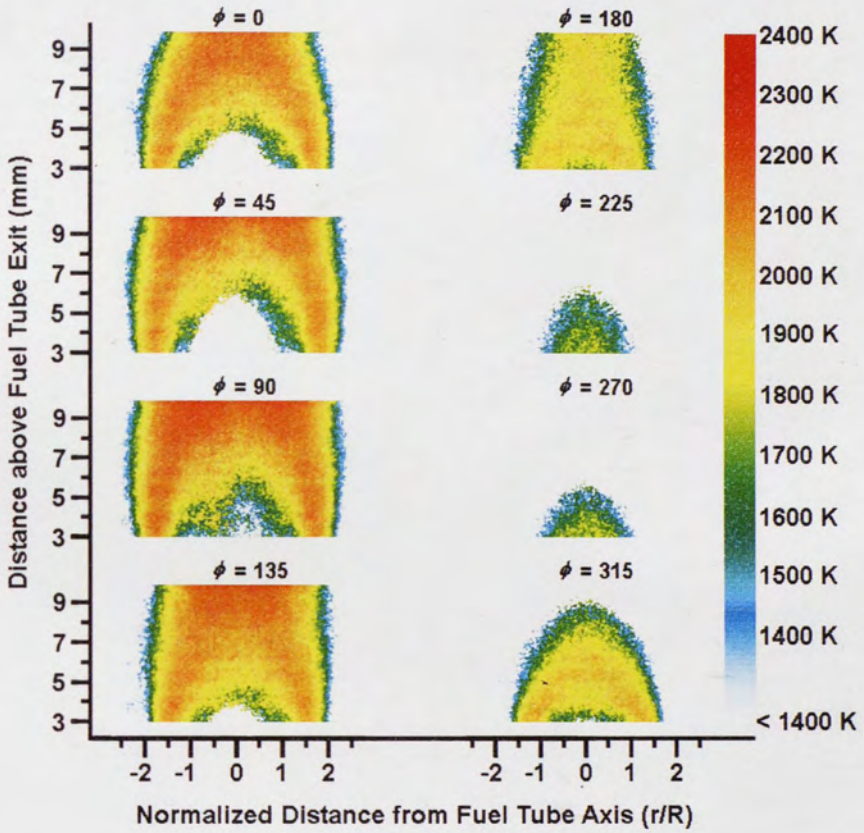

Figure 6-47: Two-dimensional temperature field images for 40% He dilution, 10 Hz, low amplitude.

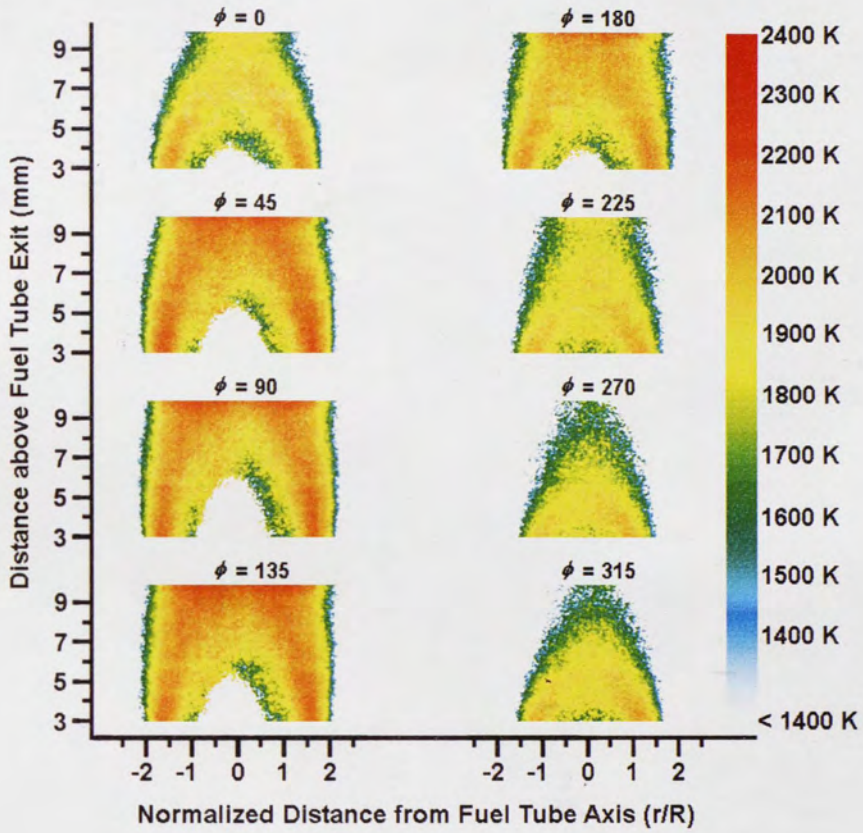

Figure 6-48: Two-dimensional temperature field images for 40% Ar dilution, 10 Hz, high amplitude.

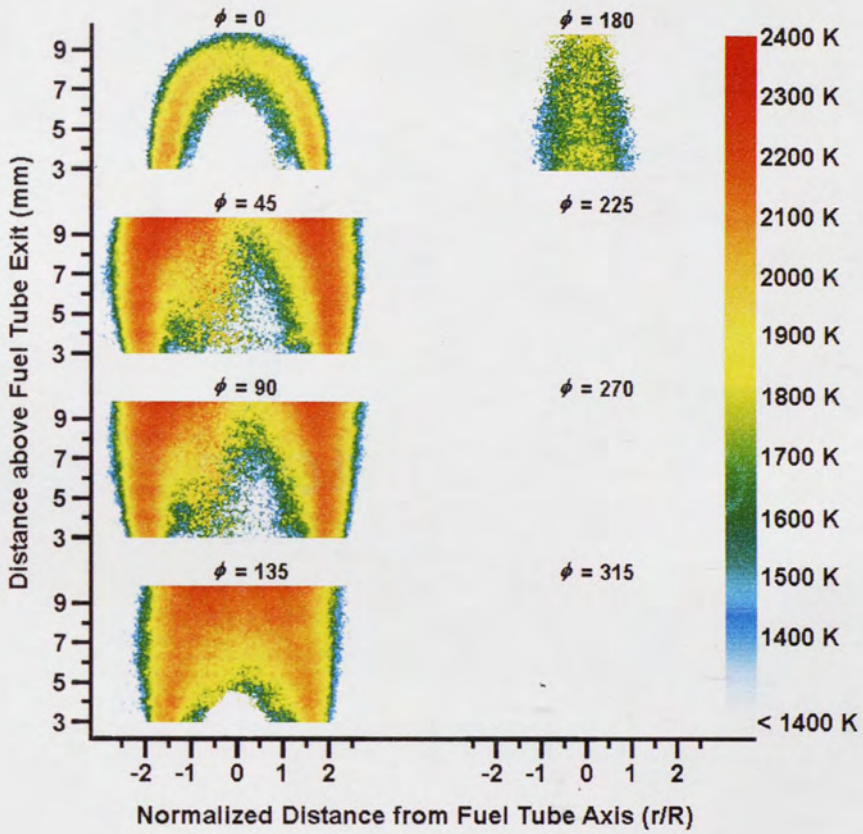

Figure 6-49: Two-dimensional temperature field images for 40% He dilution, 10 Hz, high amplitude.

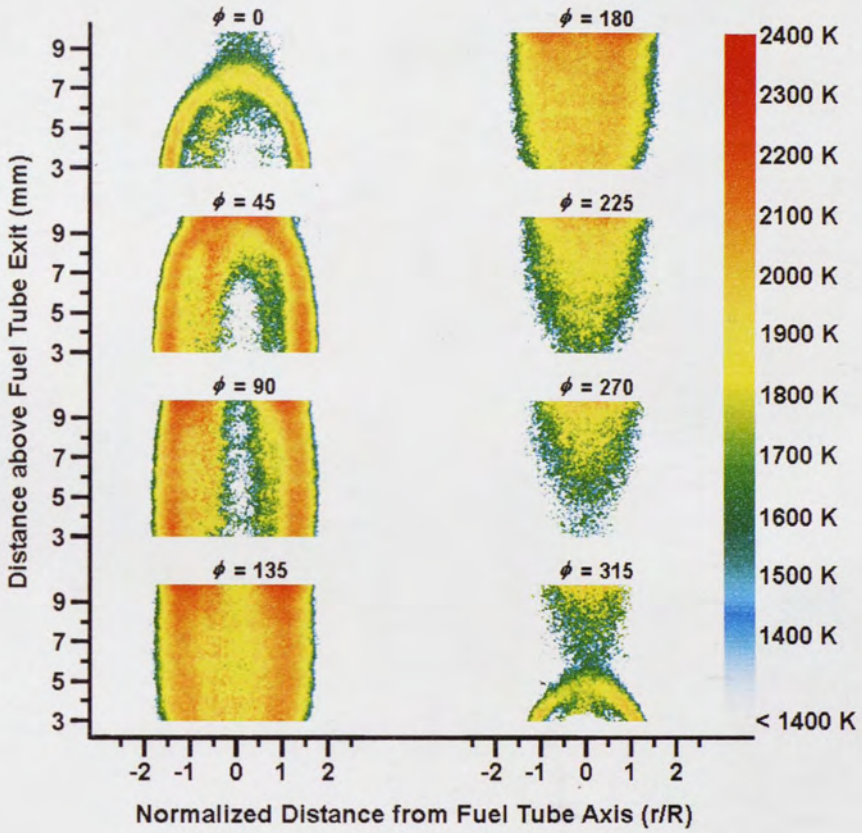

Figure 6-50: Two-dimensional temperature field images for 40% Ar dilution, 100 Hz, low amplitude.

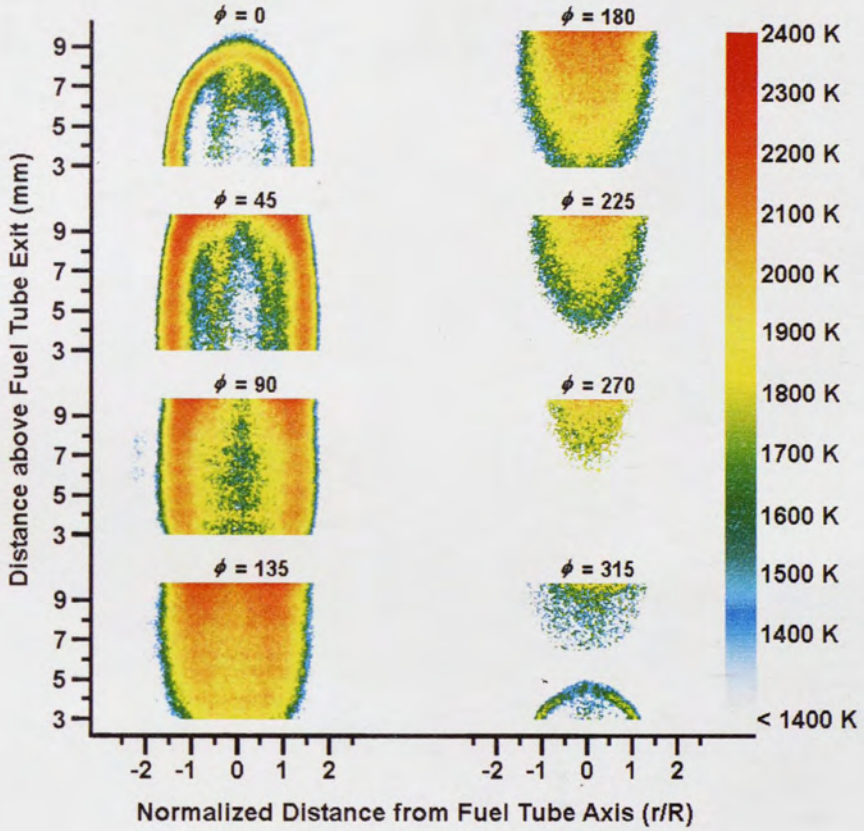

Figure 6-51: Two-dimensional temperature field images for 40% He dilution, 100 Hz, low amplitude.

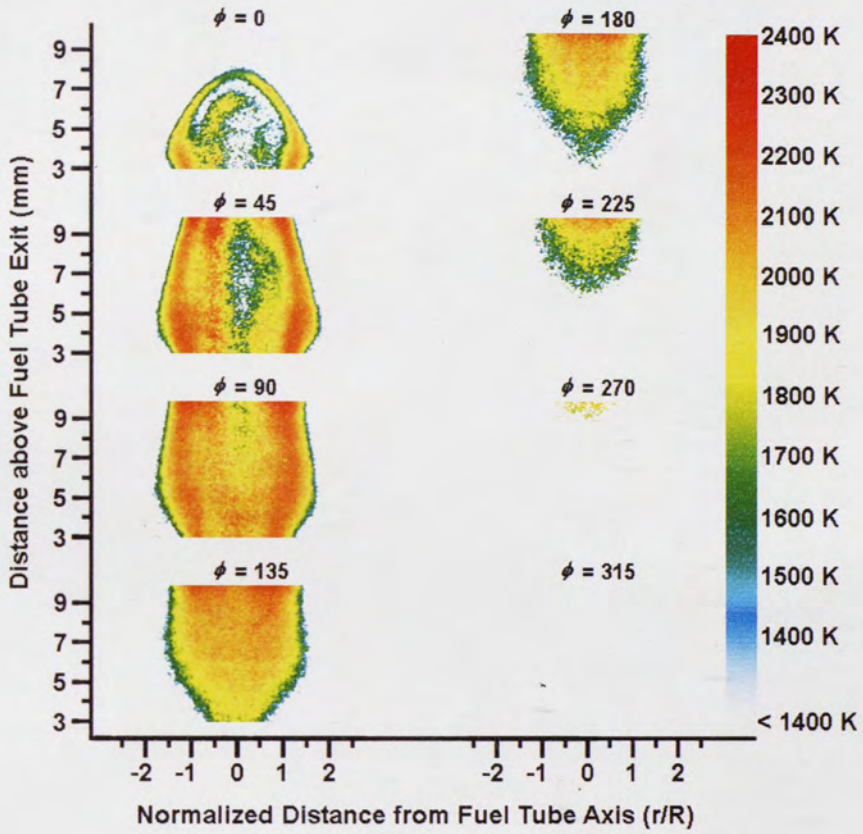

Figure 6-52: Two-dimensional temperature field images for 40% Ar dilution, 100 Hz, high amplitude.

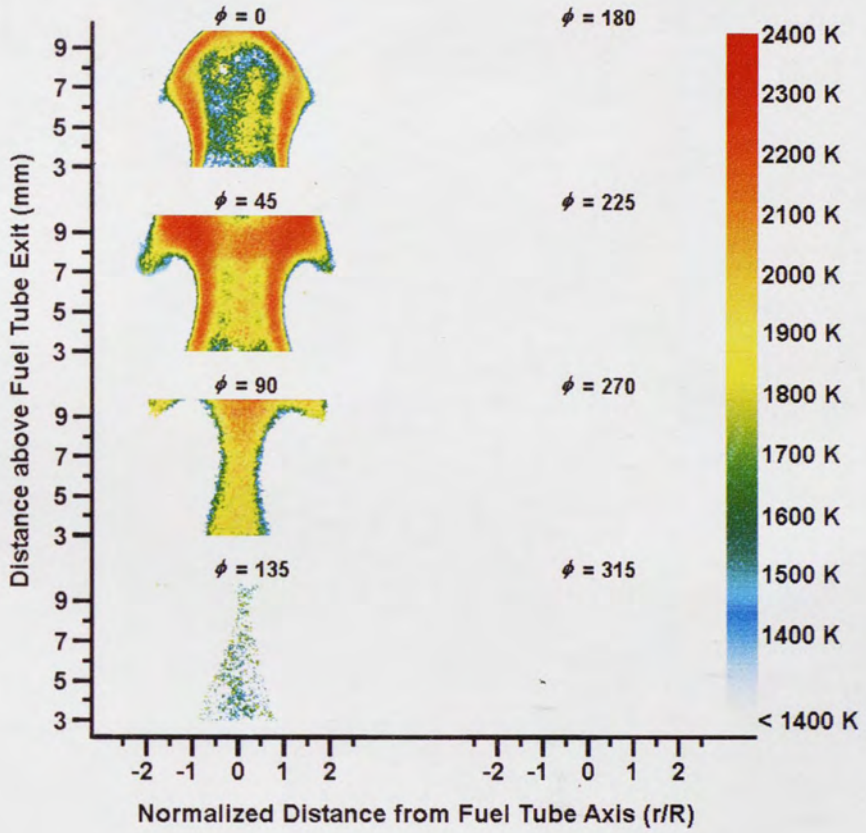

Figure 6-53: Two-dimensional temperature field images for 40% He dilution, 100 Hz, high amplitude.

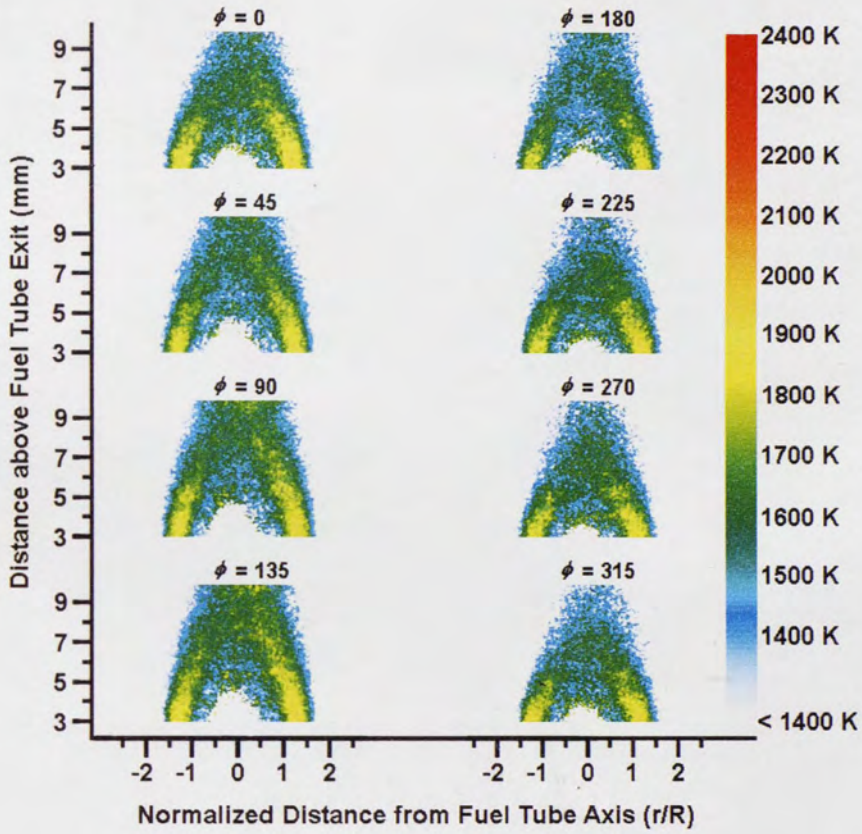

Figure 6-54: Two-dimensional temperature field images for 60% Ar dilution, 10 Hz, low amplitude.

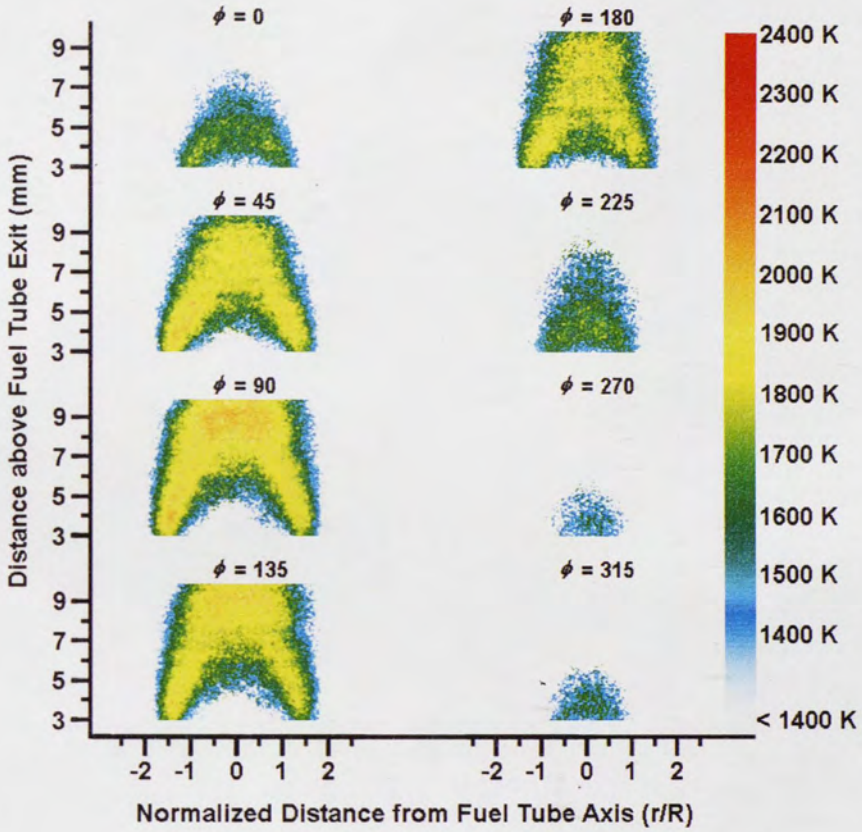

Figure 6-55: Two-dimensional temperature field images for 60% He dilution, 10 Hz, low amplitude.

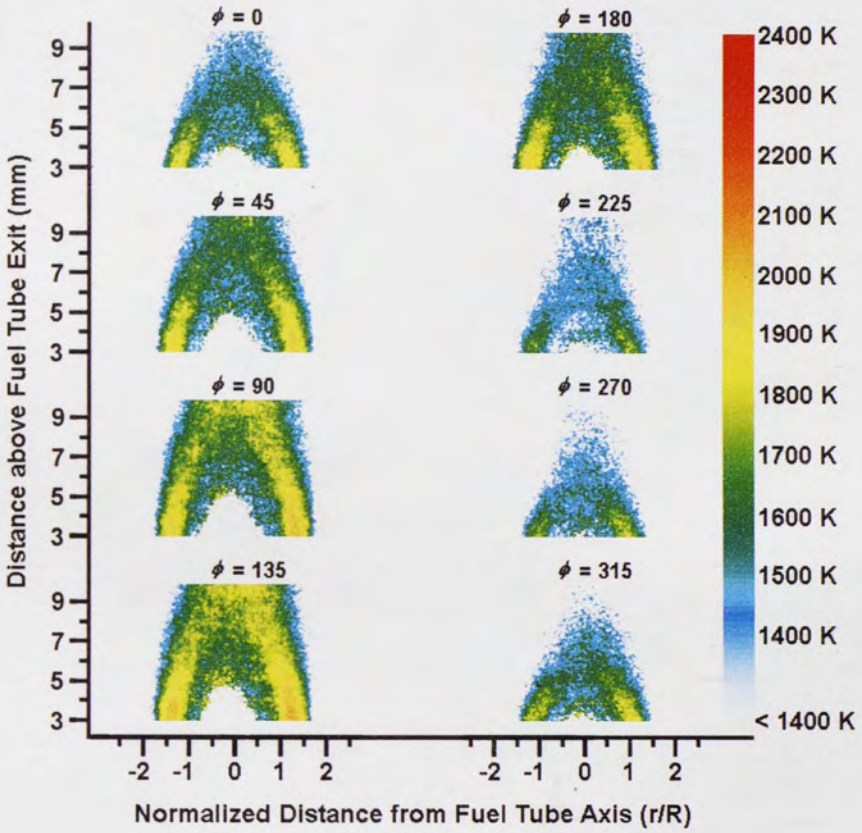

Figure 6-56: Two-dimensional temperature field images for 60% Ar dilution, 10 Hz, high amplitude.

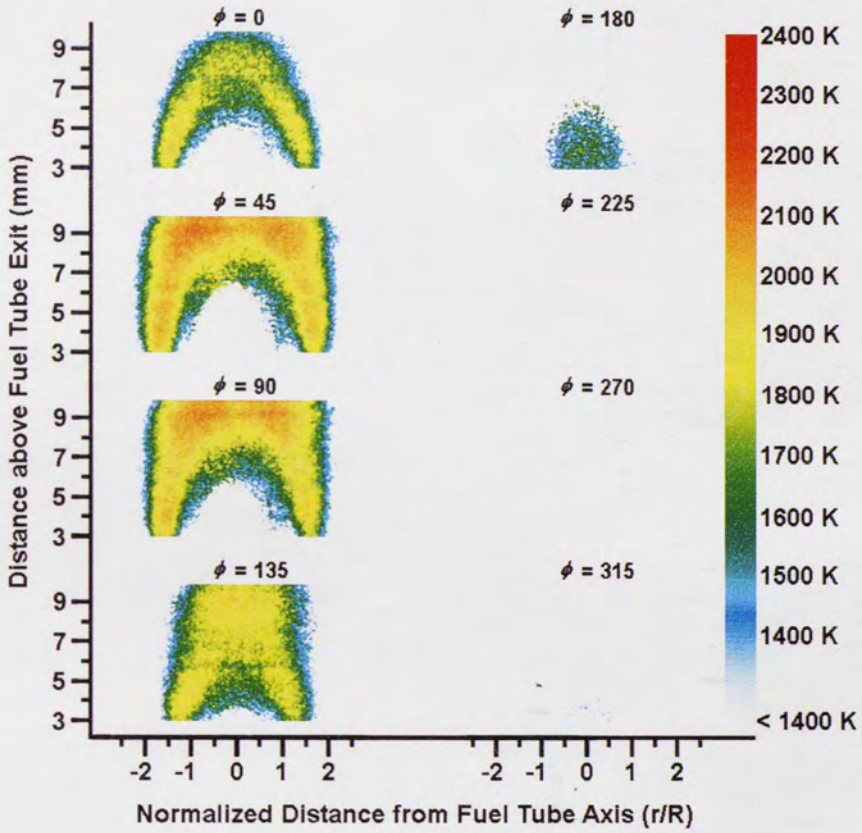

Figure 6-57: Two-dimensional temperature field images for 60% He dilution, 10 Hz, high amplitude.

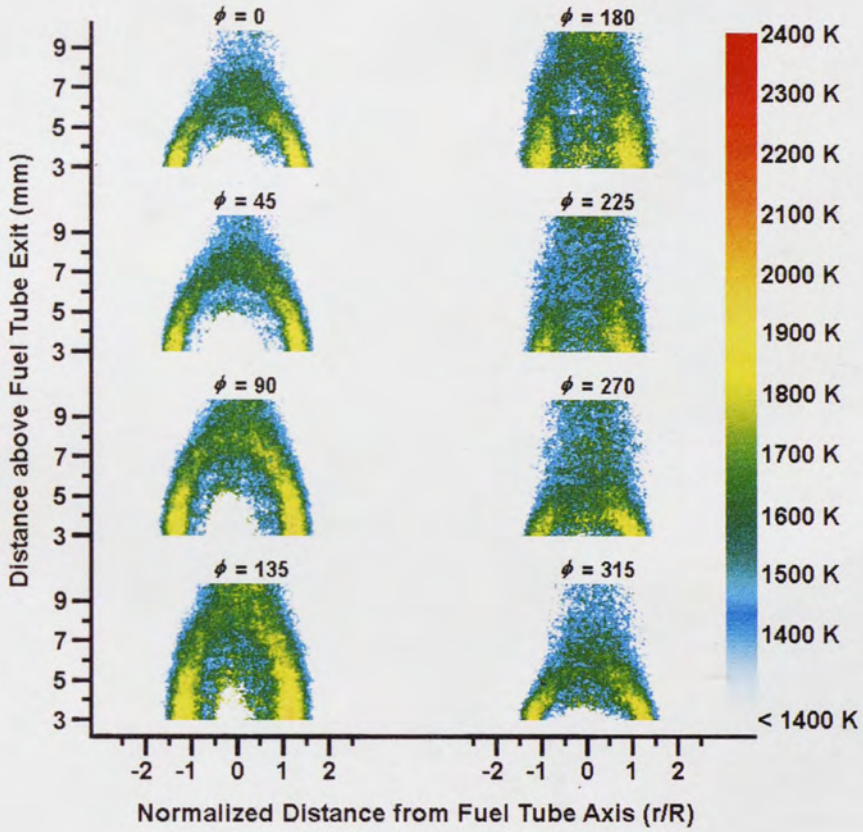

Figure 6-58: Two-dimensional temperature field images for 60% Ar dilution, 100 Hz, low amplitude.

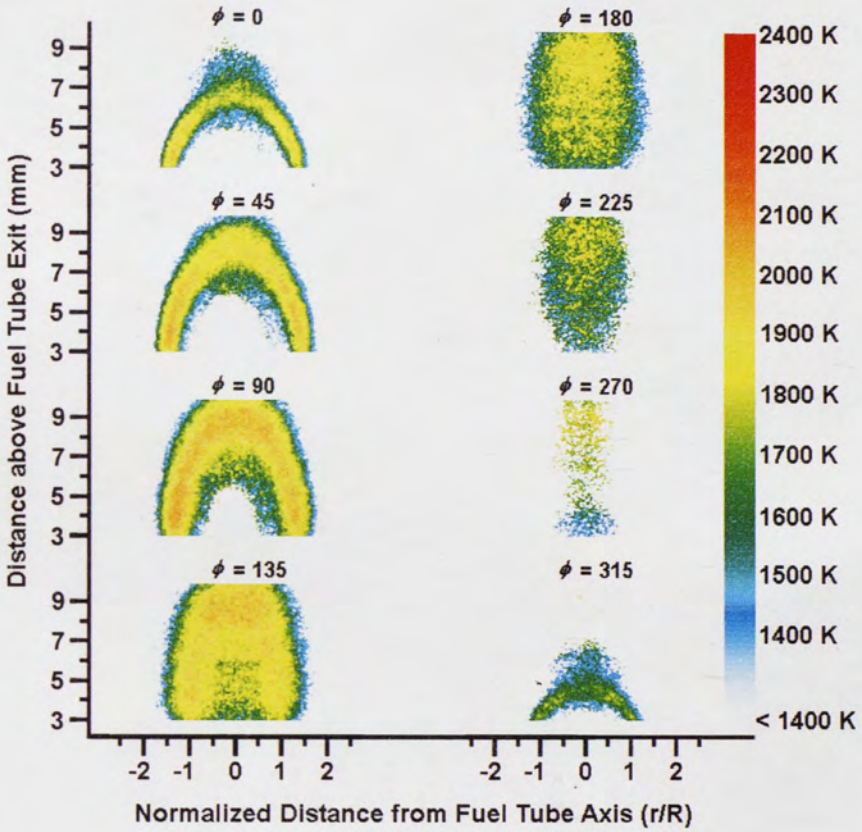

Figure 6-59: Two-dimensional temperature field images for 60% He dilution, 100 Hz, low amplitude.

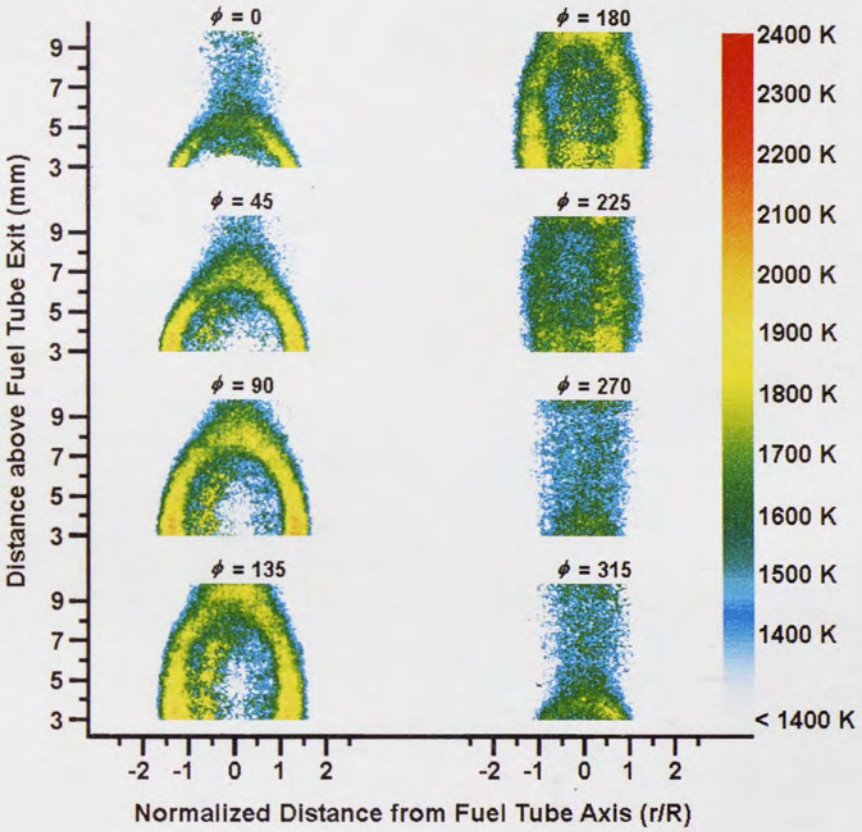

Figure 6-60: Two-dimensional temperature field images for 60% Ar dilution, 100 Hz, high amplitude.

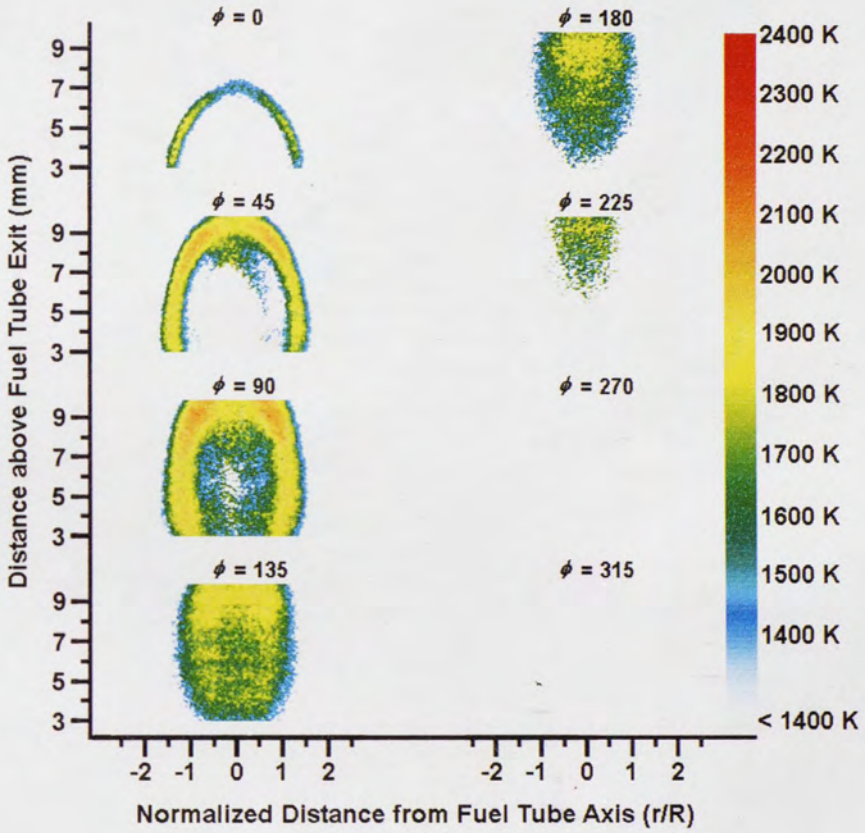

Figure 6-61: Two-dimensional temperature field images for 60% He dilution, 100 Hz, high amplitude.

6.3.2 Steady Flames

Figure 6-12 and Figure 6-13 present the two-dimensional OH and temperature fields, respectively, for steady images. These figures further support the discussion presented in Section 6.2 above. Note that Ar-diluted flames are always longer than He-diluted flames. This can be explained by the fact that H_2 is more diffusive in He than in Ar as shown in Table 6-3. H_2, thus, reaches the flame quicker and the distance from the fuel tube exit needed to consume the fuel is less than for H_2-Ar flames. Note also the curvature effect on OH intensity and temperature near the flame tip of the 60% Ar-diluted flame. Since $Le_F < 1$, there is a strong defocusing effect on the reactant mass reaching the flame tip and, thus, the flame tip temperature is lowered.

Table 6-3: Binary diffusivity of selected molecules at 1500 K in cm^2/s

	H_2	Ar	He	H_2O	O_2	N_2
H_2	---	12.44	23.07	14.05	12.24	11.78
Ar	12.44	---	11.21	4.24	3.13	3.13
He	23.07	11.21	---	13.62	11.06	10.64
H_2O	14.05	4.24	13.62	---	4.30	4.22
O_2	12.24	3.13	11.06	4.30	---	3.23
N_2	11.78	3.13	10.64	4.22	3.23	---

Lewis number effects are also evident in the images corresponding to 20% and 60% dilutions. That is, the maximum intensity and temperature for the 20% Ar-diluted flame is lower than that of the 20% He-diluted flame due to its higher Le_F. Similarly, the maximum intensity and temperature for the 60% Ar-diluted flame (which occurs at the shoulder regions of the flame) is higher than that of the 60% He-diluted flame since $Le_F <$ 1 for the Ar-diluted flame (see Table 6-2).

As discussed in Section 6.2, flames with a 40% dilution level differ in temperature due to the different thermal gradients found in these flames. With the help of the steady OH images, this fact can be shown graphically by considering the shape of the OH profiles in these flames. Figure 6-62 shows the normalized (by their respective maxima) OH profiles of 40% Ar and He-diluted flames taken at a specific location above the fuel tube. As one can see, the profile for the 40% Ar flame is wider than that of the 40% He flame. The wider OH (and, thus, temperature) profile shown in Figure 6-62 supports the argument given above which assumed that the Ar-diluted flame had a smaller thermal gradient. This smaller gradient along with the fact that the thermal diffusivity of 40% Ar mixtures is lower than that of 40% He mixtures (see Figure 6-6) supports the conclusion that the flame temperature of the 40% Ar-diluted flame has to be larger than that of the 40% He-diluted flame. This larger temperature is needed to increase the heat flux and achieve a balance of thermal and mass transfer modes.

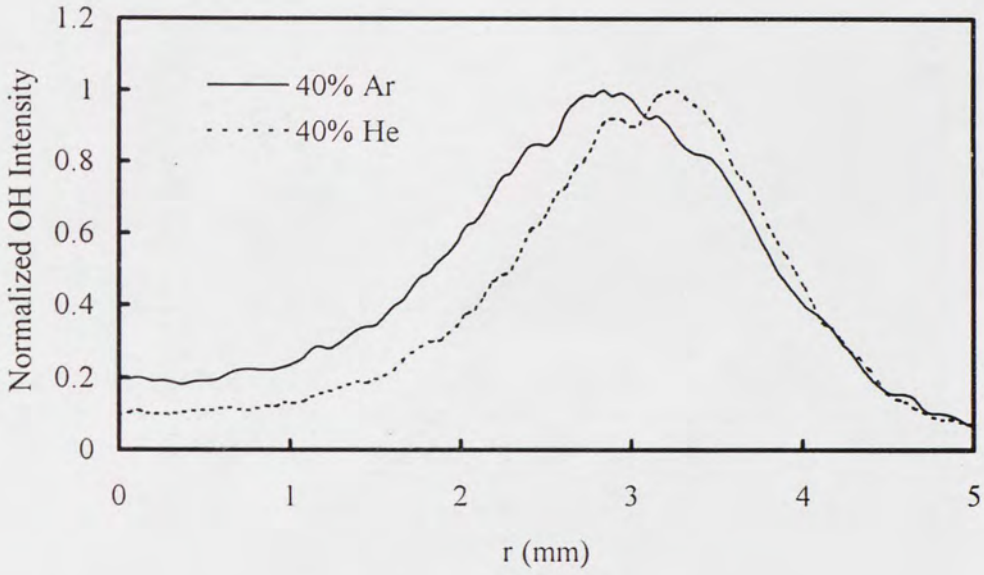

Figure 6-62: Normalized OH profiles (half profile shown) for 40% diluted steady flames at an axial height of 8 mm.

6.3.3 Unsteady Flames

The trends observed from the large image database presented in Figure 6-14 through Figure 6-61 will be summarized here. The effects of flow unsteadiness and flame stretch/curvature will be discussed with emphasis placed on how they couple with mass and thermal transport processes (i.e. Lewis number) ultimately affecting flame temperature and reaction zone structure. It should be noted that the low-speed flames studied in this research are high-Damköhler-number flames, thus any changes in flame temperature of the unsteady flames studied is a result of changes in flame structure and

mass and thermal transport mechanisms as opposed to nonequilibrium chemistry (i.e. incomplete chemical reactions) due to low Damköhler number effects.

6.3.3.1 Unsteadiness Effects

Overall, it is noted that H_2-He flames are more unstable than H_2-Ar flames for the same forcing amplitude. This is the case for all images presented in Section 6.3.1 above regardless of the value of Le_F. This difference in the dynamic behavior of the various fuel mixtures becomes more evident for low frequencies and as dilution increases. This can be explained by the fact that it is easier for hydrogen to diffuse through He than Ar as can be seen in Table 6-3 and as explained below. The difference in viscosity and density of the H_2-Ar and H_2-He mixtures can also be a factor in the observed behavior of the flames due to the variation in momentum transfer from the speaker to the various gases.

As dilution increases, there are more inert species present in the fuel mixture. It appears from the images presented above that, under unsteady conditions, Ar impedes the diffusion of H_2 to the flame zone more than He. When the unsteady flow pushes on the flame, the velocity gradient near the flame zone is dramatically changed. This influences the convective and diffusive mass transport to the flame zone more than the heat being generated at the flame (Hancock, 1996). Essentially, mass diffusion becomes important. Note that at 10 Hz (i.e. low frequency), H_2-He flames move out radially more than H_2-Ar flames and have a slightly larger flame thickness when pulsed at the same amplitude as seen in Figure 6-63. Flame thickness and radial position values reported in this figure

and throughout the remainder of this section were obtained from OH images as illustrated by Figure 6-64. At every location above the burner (i.e. height-above-burner, HAB), the flame location r was determined by locating the maximum OH intensity. The thickness of the flame zone was calculated by measuring the width of the OH peak at a point where the OH intensity was half of the maximum intensity (i.e. full-width-half-magnitude, FWHM).

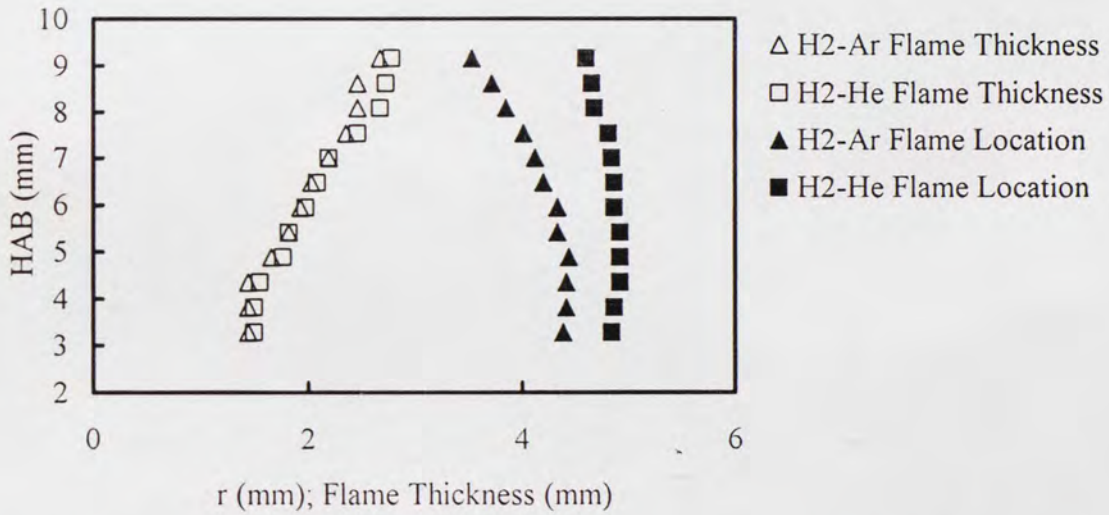

Figure 6-63: Flame thickness and radial position of 20% diluted flames at 10 Hz (low amplitude) at a speaker phase angle ϕ of 45° (see Figure 6-14 and Figure 6-15).

From the above discussion, it is noted that there is an enhanced H_2 mass flux to the flame zone under unsteady conditions and this flux is greater for H_2-He flames due to the difference in mass diffusivity of H_2-He and H_2-Ar mixtures; that is, a larger amount of reactants reach the flame zone in H_2-He flames. Thus, for the same forcing level, the reaction zone of the unsteady H_2-He flames broadens and has to adjust by moving to a

further radial position. This relocation and broadening of the reaction zone is necessary and allows the flame to increase its surface area so that the increased fuel flux can be completely consumed. Other experimental studies on unsteady H_2-N_2 flames have reported an increase in temperature and H_2 mass flux to the flame zone when N_2 was replaced by He (Hancock, 1996; Hancock *et. al.*, 1996).

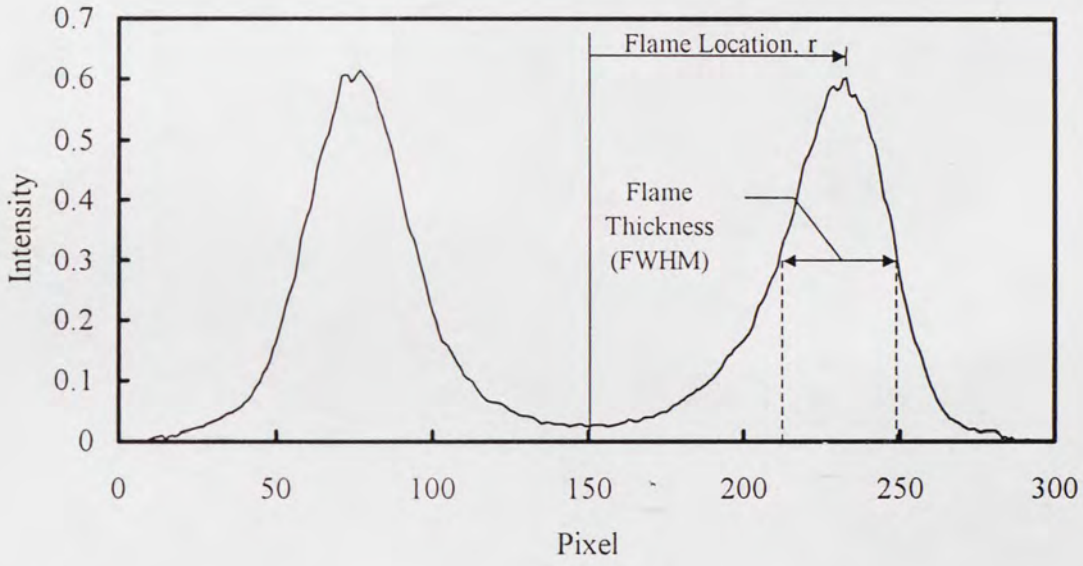

Figure 6-64: Determination of flame location and thickness from OH images.

Recall that, as discussed in Section 6.1, H_2-He flames always extinguished at a lower voltage that H_2-Ar flames. The increased reactant flux to the flame zone in H_2-He flames may be responsible for this. As reactant fluxes increase, the residence time at the flame zone is reduced (Peters, 1984). For high enough reactant fluxes, the residence time

may become shorter than the time necessary for complete chemical reaction, thus, the Damköhler number is reduced and driving the flame to extinction.

The plots in Figure 6-65 through Figure 6-76 show the maximum temperature and OH intensity found at every phase angle within the speaker pulse for all conditions tested. These figures can be found at the end of this section. It can be noted that the change in temperature and OH concentration is nearly sinusoidal (i.e. they follow the speaker excitation). All driven flames exhibit higher local temperatures than their respective undriven steady flame temperatures at some point during the speaker oscillation. This was also observed in the unsteady flame studies of Katta *et. al.* (1994), Katta and Roquemore (1995), and Hancock *et. al.* (1996). For example, see Figure 6-75, which is a phase-temperature plot for 60% diluted flames, pulsed at 10 Hz. At low amplitude, the maximum temperature during the pulse for the He-diluted flame is 2058 K, 178 K higher than the steady value of 1880 K (based on LIF data, see Table 6-2). For the Ar-diluted flame, the maximum temperature is 2006 K whereas the steady temperature is 1969 K. At high amplitude, on the other hand, the maximum temperatures of the He and Ar-diluted flames increase to 2129 K and 2043 K, respectively.

It is of particular importance to note that He-diluted flames always yield higher maximum temperatures than Ar-diluted flames at some point during the pulse cycle. This is true even for 40% and 60% dilutions (see Figure 6-73 through Figure 6-76) where the steady Ar-diluted flames had temperatures greater than He-diluted flames (see Table 6-2). This seems to contradict the Lewis number discussion for steady flames presented in the sections above. It should be noted, however, that, as discussed above, driven flames alter

the way hydrogen reaches the reaction zone as opposed to steady flames. He diffuses rapidly like H_2 and it does not impede the diffusion of H_2 to the flame zone as much as Ar. The concentration gradient of H_2 is increased when the unsteady flow is first introduced and the flame is "pushed out" (i.e. from $\phi = 0^o$ to $\phi = 90^o$); the mass flux of H_2 to the flame is, therefore, greater. Thus, in the driven H_2-He flames, more fuel reaches the flame zone and burning is intensified (see, for example, Figure 6-14 vs. Figure 6-15; Figure 6-24 vs. Figure 6-25; Figure 6-32 vs. Figure 6-33).

Flame structure (as seen in the OH images) is noticeably different at low and high frequencies (e.g. Figure 6-14 and Figure 6-18; Figure 6-25 and Figure 6-29). Flames at low frequency (e.g. Figure 6-14) adjust to the imposed unsteadiness by moving radially outward or inward and have relatively thick flame zones (i.e. low strain rate) compared with flames at high frequency. At high frequency, the flame structure cannot respond fast enough to the rapid hydrodynamic excitation. High frequency flames, thus, do not exhibit the high radial displacement seen in low frequency flames and, overall, their flame thickness is substantially decreased since they adjust to the changing flowfield by either lengthening or compression of the flame zone. In addition, note that, at high frequency, He and Ar-diluted flames have a more similar structure than at low frequency (see Figure 6-26 and Figure 6-27 as opposed to Figure 6-22 and Figure 6-23).

Take, for example, Figure 6-17 and Figure 6-21 which are images of 20% He-diluted flames at 10Hz and 100 Hz, respectively, and high amplitude. Note the difference in the structure of the flame zone. The high frequency flame is much thinner and seems to be stretched. Note that in some cases (see, for example, Figure 6-29) the reaction zone

in high frequency flames is both stretched and compressed due to vortex rollup. In the flames studied in this research, the coflow velocity was high and vortical structures (i.e. rollup) were not as well developed as in other studies (Katta *et. al.*, 1994; Hancock *et. al.*, 1996; Kawabe *et. al.*, 2000; Komiyama *et. al.*, 2001).

This leads to the argument that, at high frequency, the reaction zone is subjected to the highest stretch/strain and it is of interest to investigate the Lewis number effect coupled with the stretch/compression of the flame in these high frequency flames. Flame stretch effects, although present, are not as obvious in low frequency flames. Section 6.3.3.2 below discusses these issues in more detail.

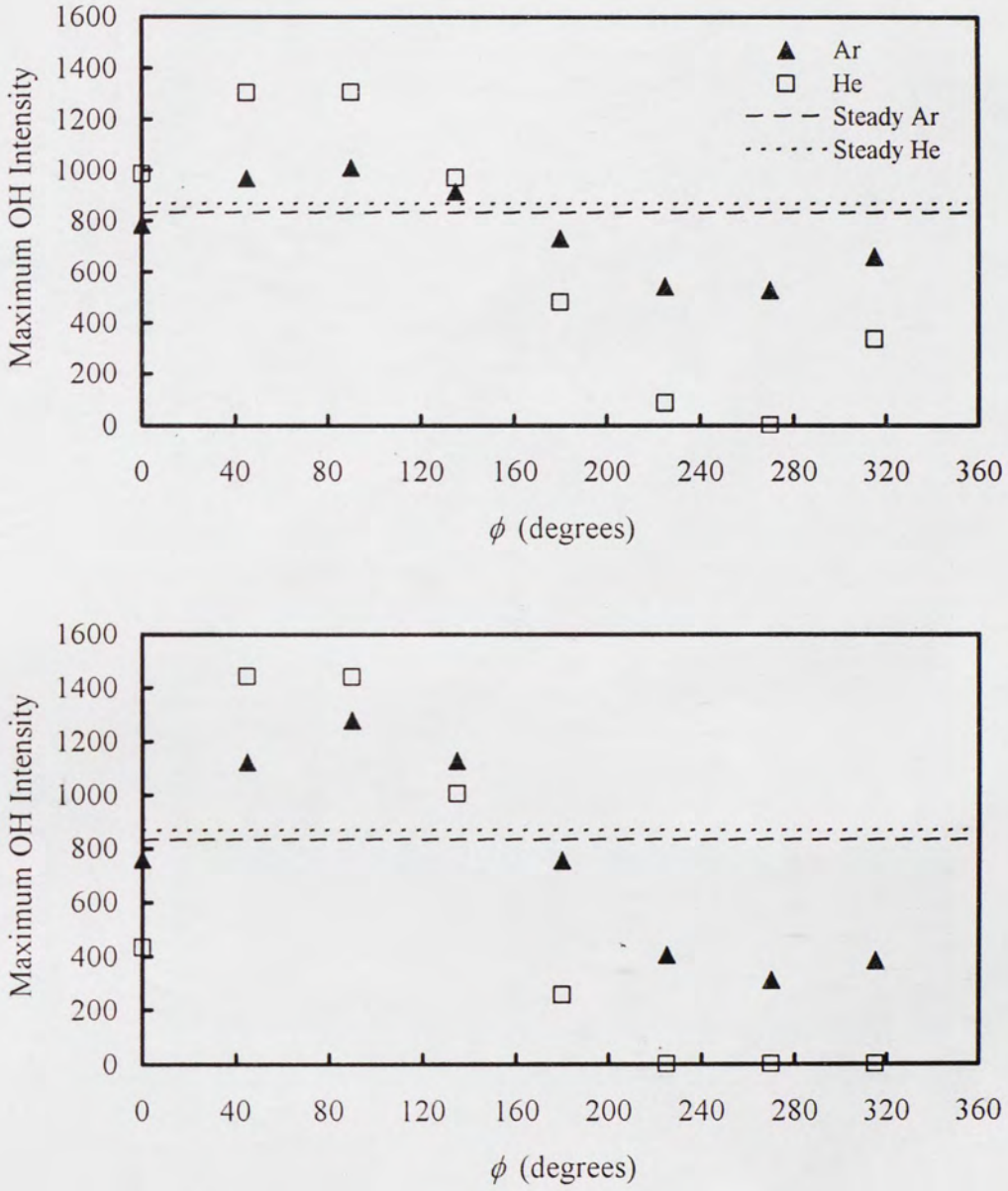

Figure 6-65: OH intensity plots for 20% fuel dilution at a forcing frequency of 10 Hz, top and bottom plots are for low and high amplitudes respectively.

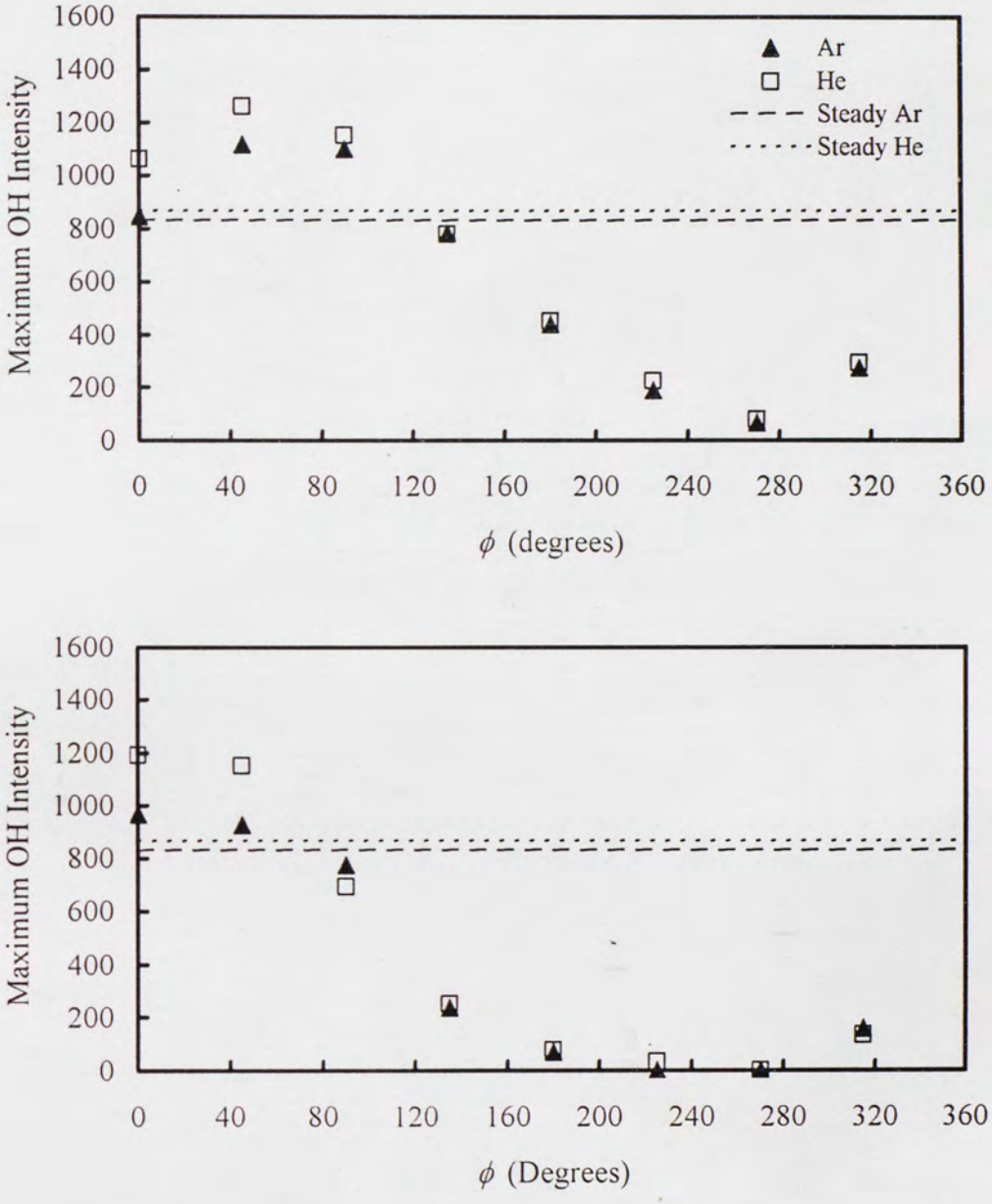

Figure 6-66: OH intensity plots for 20% fuel dilution at a forcing frequency of 100 Hz, top and bottom plots are for low and high amplitudes respectively.

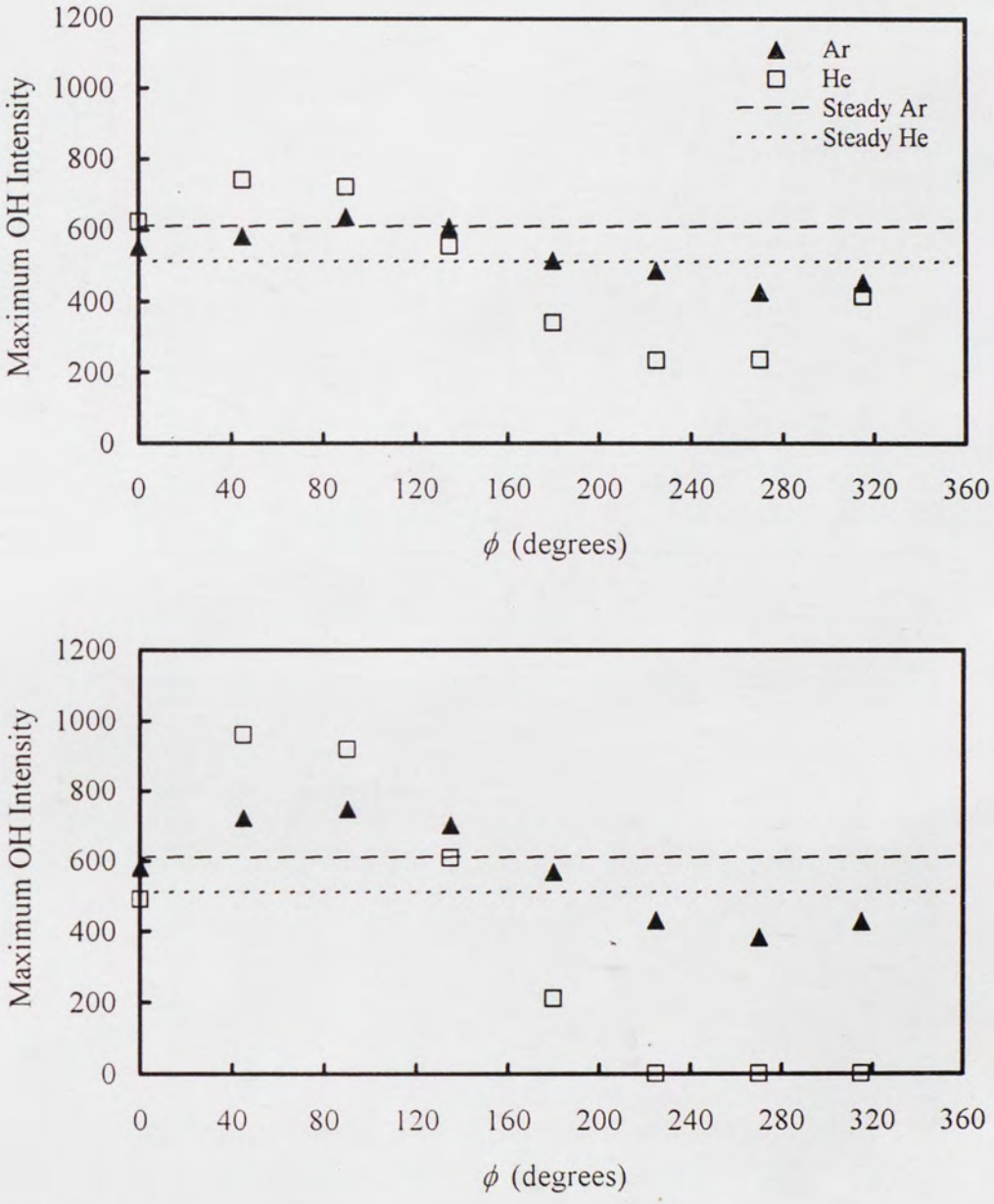

Figure 6-67: OH intensity plots for 40% fuel dilution at a forcing frequency of 10 Hz, top and bottom plots are for low and high amplitudes respectively.

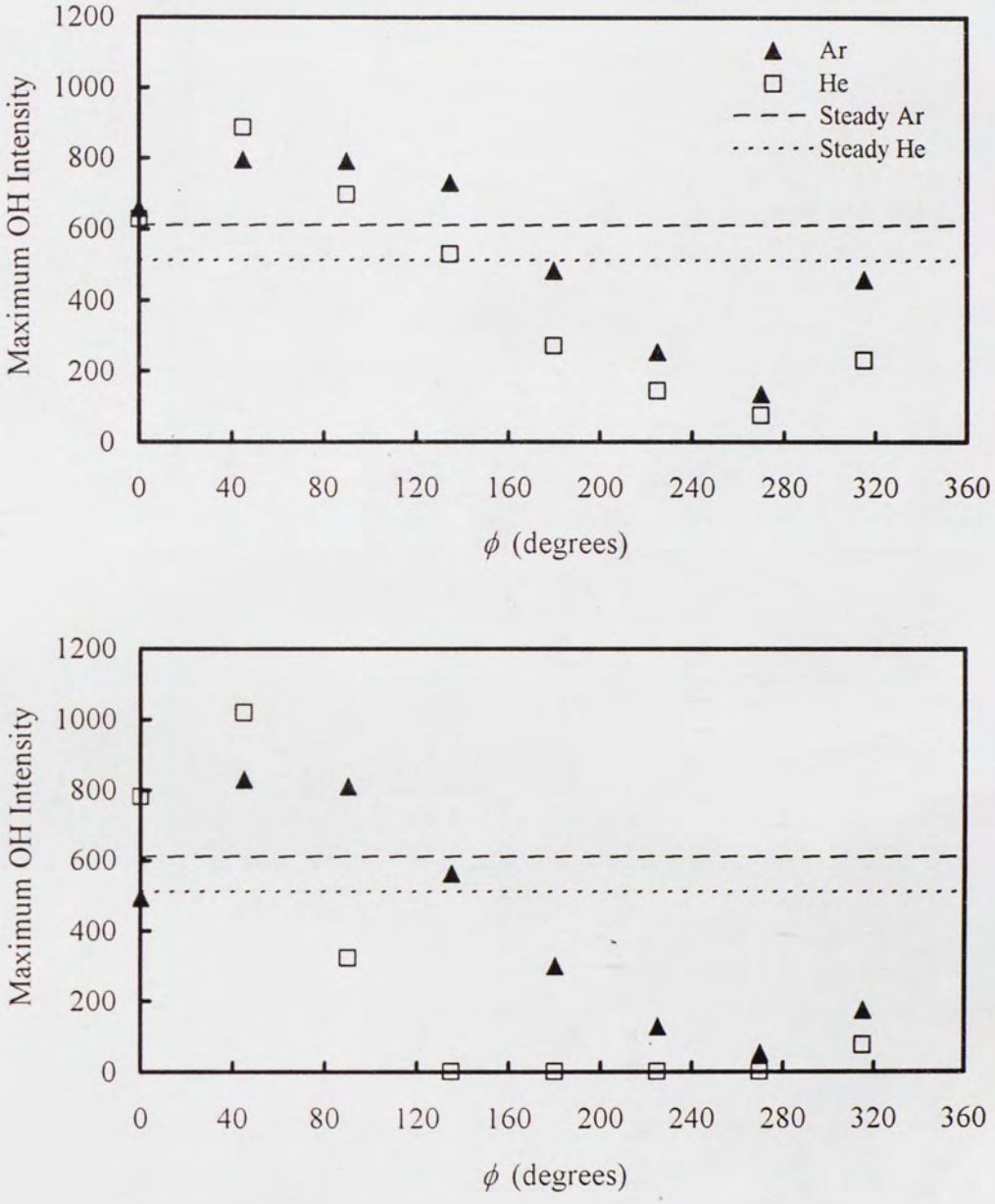

Figure 6-68: OH intensity plots for 40% fuel dilution at a forcing frequency of 100 Hz, top and bottom plots are for low and high amplitudes respectively.

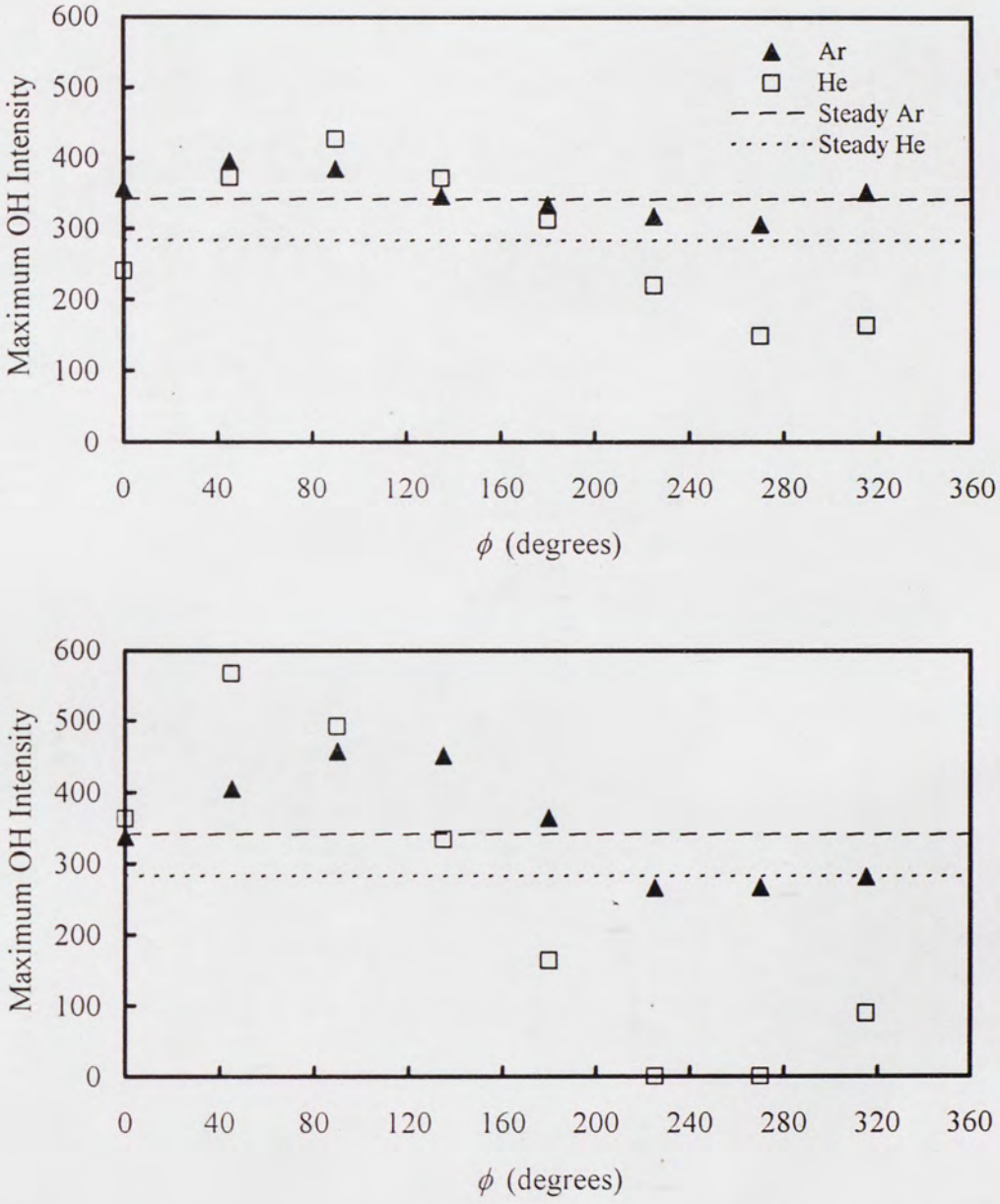

Figure 6-69: OH intensity plots for 60% fuel dilution at a forcing frequency of 10 Hz, top and bottom plots are for low and high amplitudes respectively.

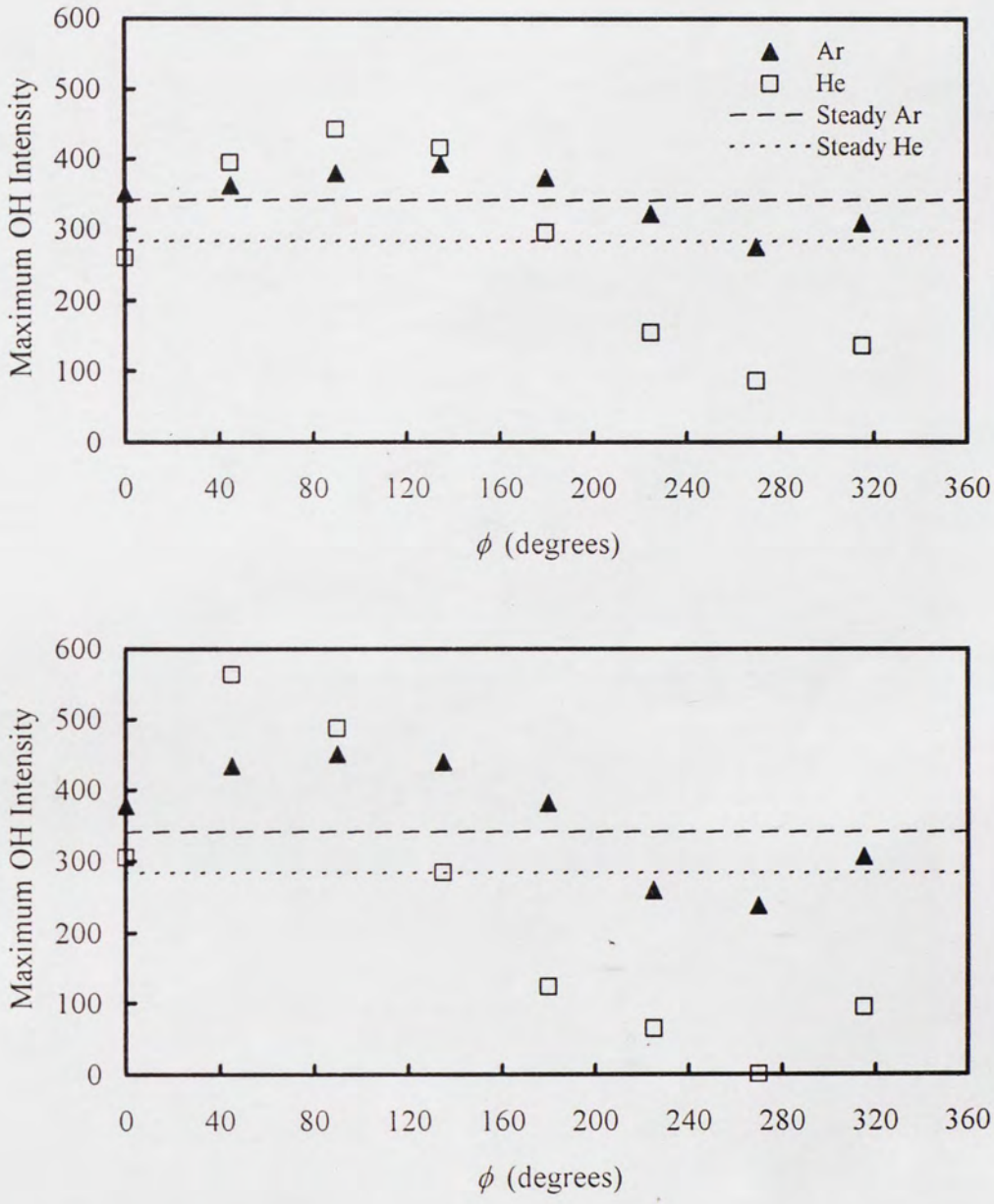

Figure 6-70: OH intensity plots for 60% fuel dilution at a forcing frequency of 100 Hz, top and bottom plots are for low and high amplitudes respectively.

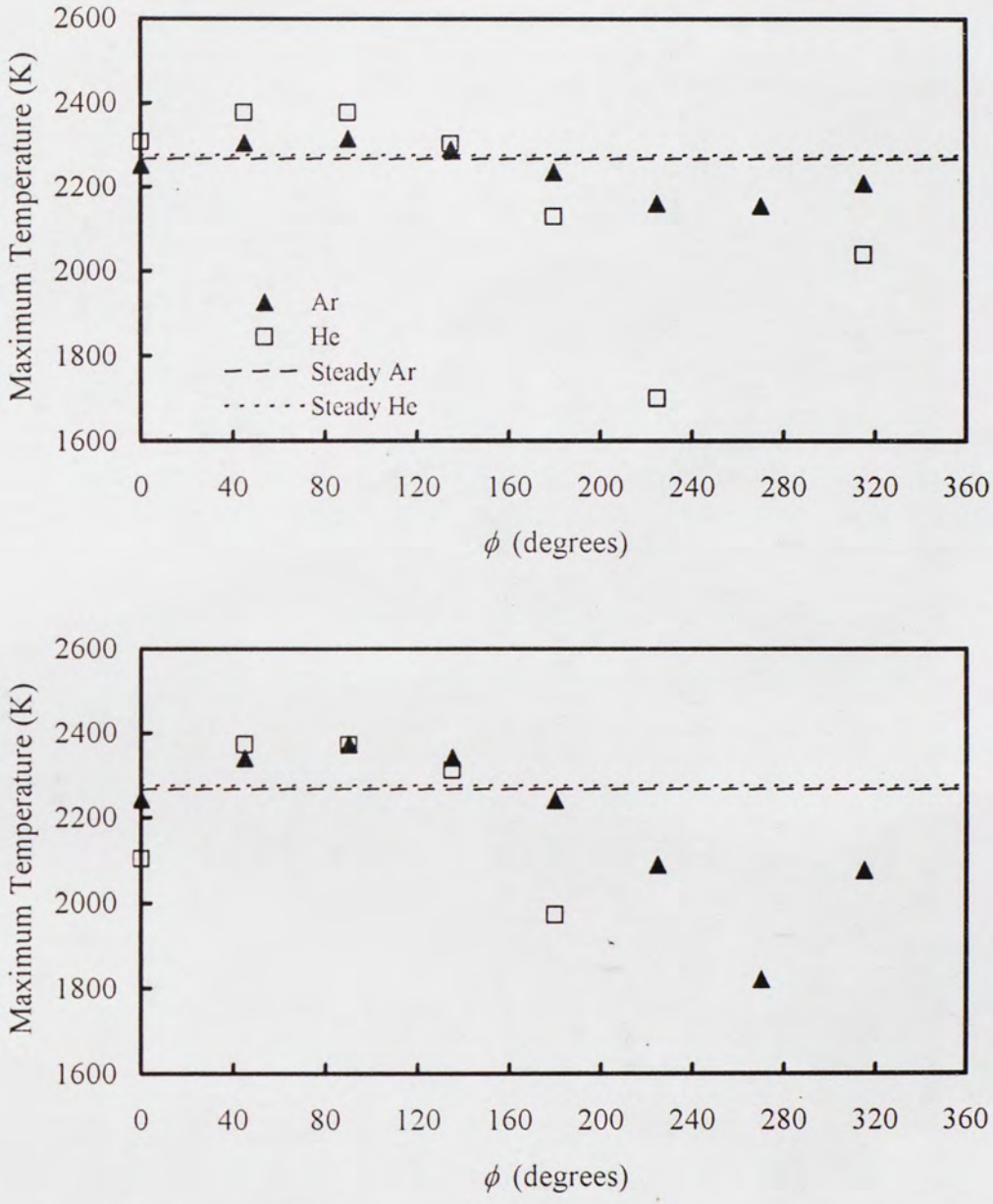

Figure 6-71: Temperature plots for 20% fuel dilution at a forcing frequency of 10 Hz, top and bottom plots are for low and high amplitudes respectively.

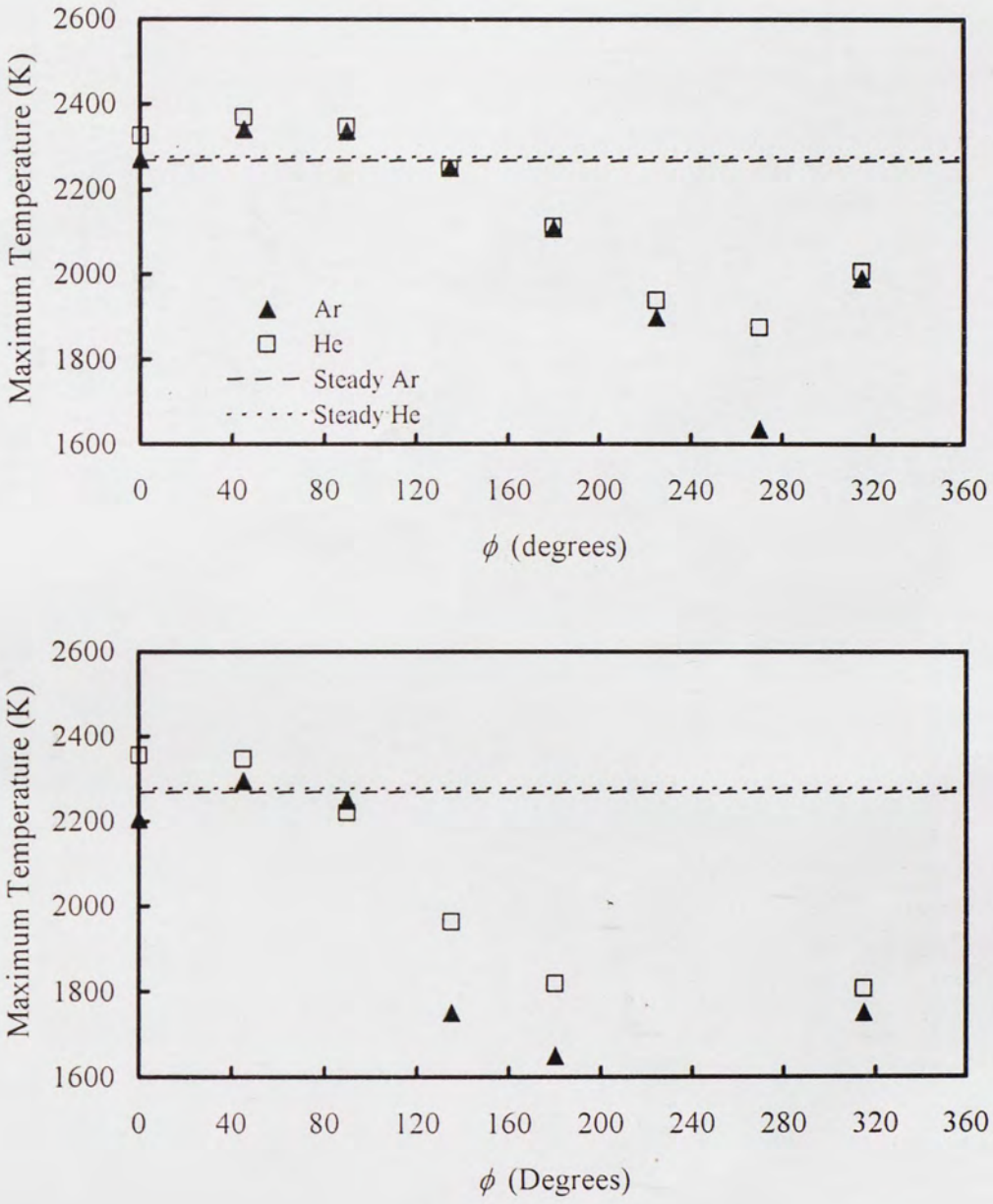

Figure 6-72: Temperature plots for 20% fuel dilution at a forcing frequency of 100 Hz, top and bottom plots are for low and high amplitudes respectively.

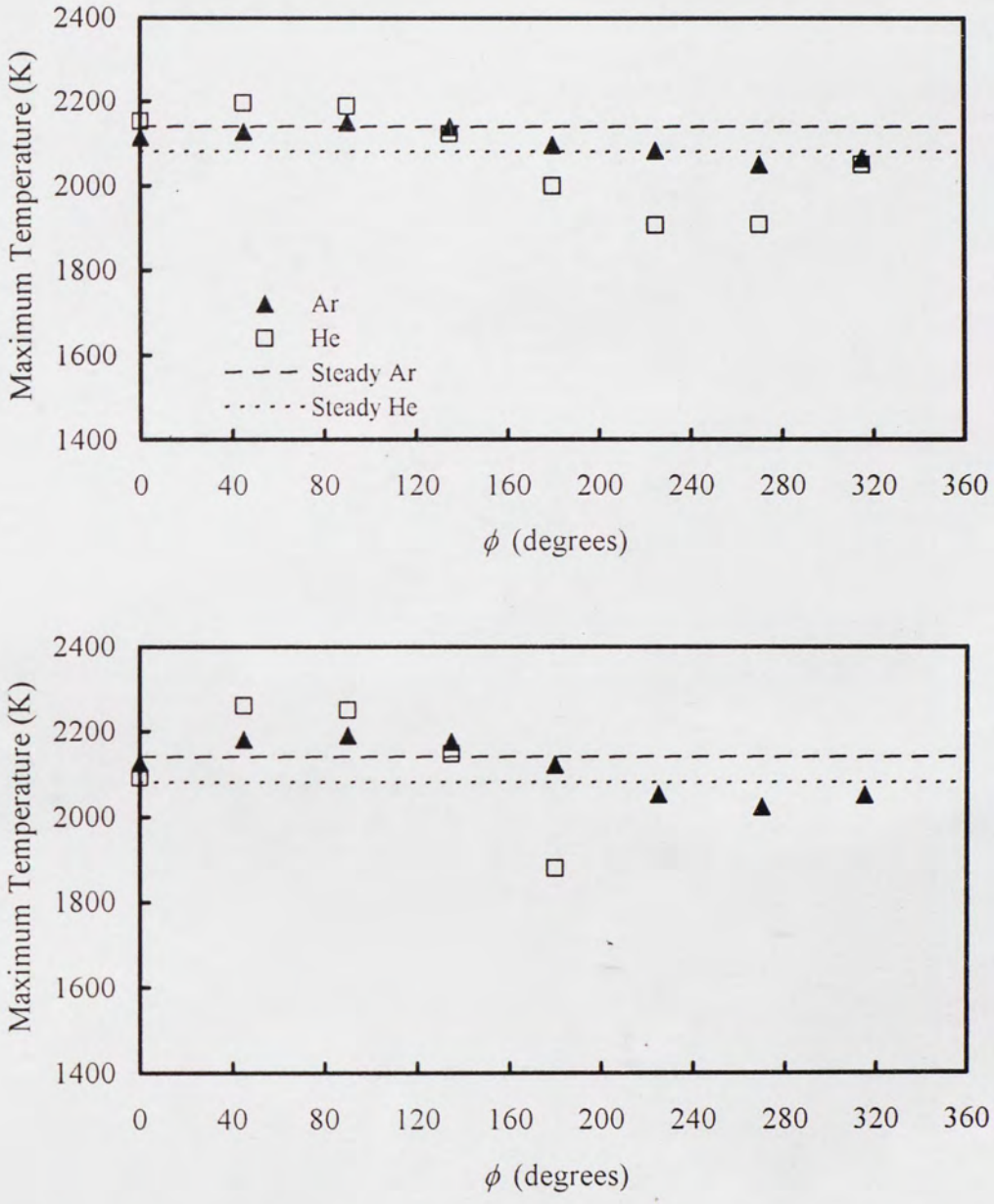

Figure 6-73: Temperature plots for 40% fuel dilution at a forcing frequency of 10 Hz, top and bottom plots are for low and high amplitudes respectively.

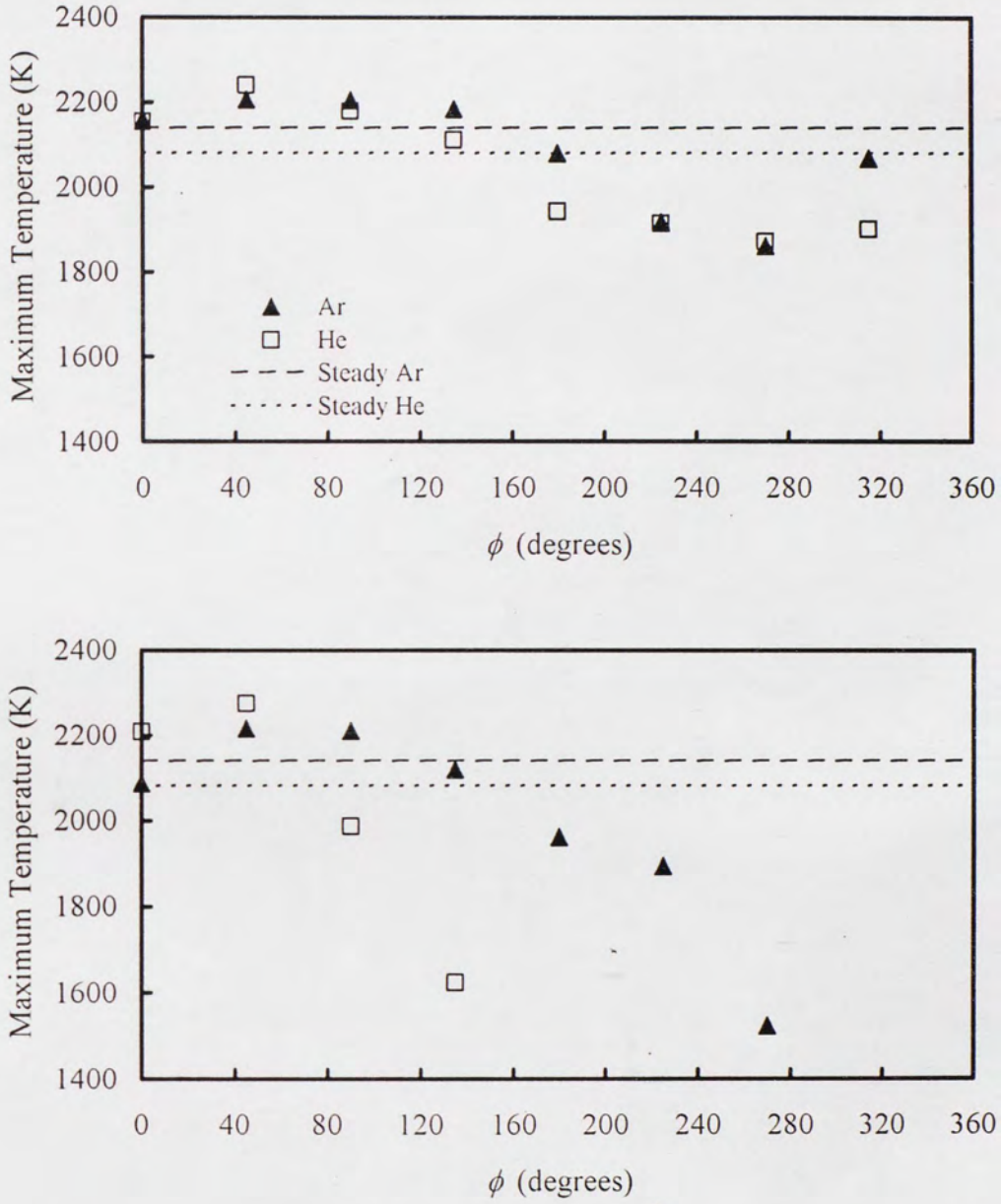

Figure 6-74: Temperature plots for 40% fuel dilution at a forcing frequency of 100 Hz, top and bottom plots are for low and high amplitudes respectively.

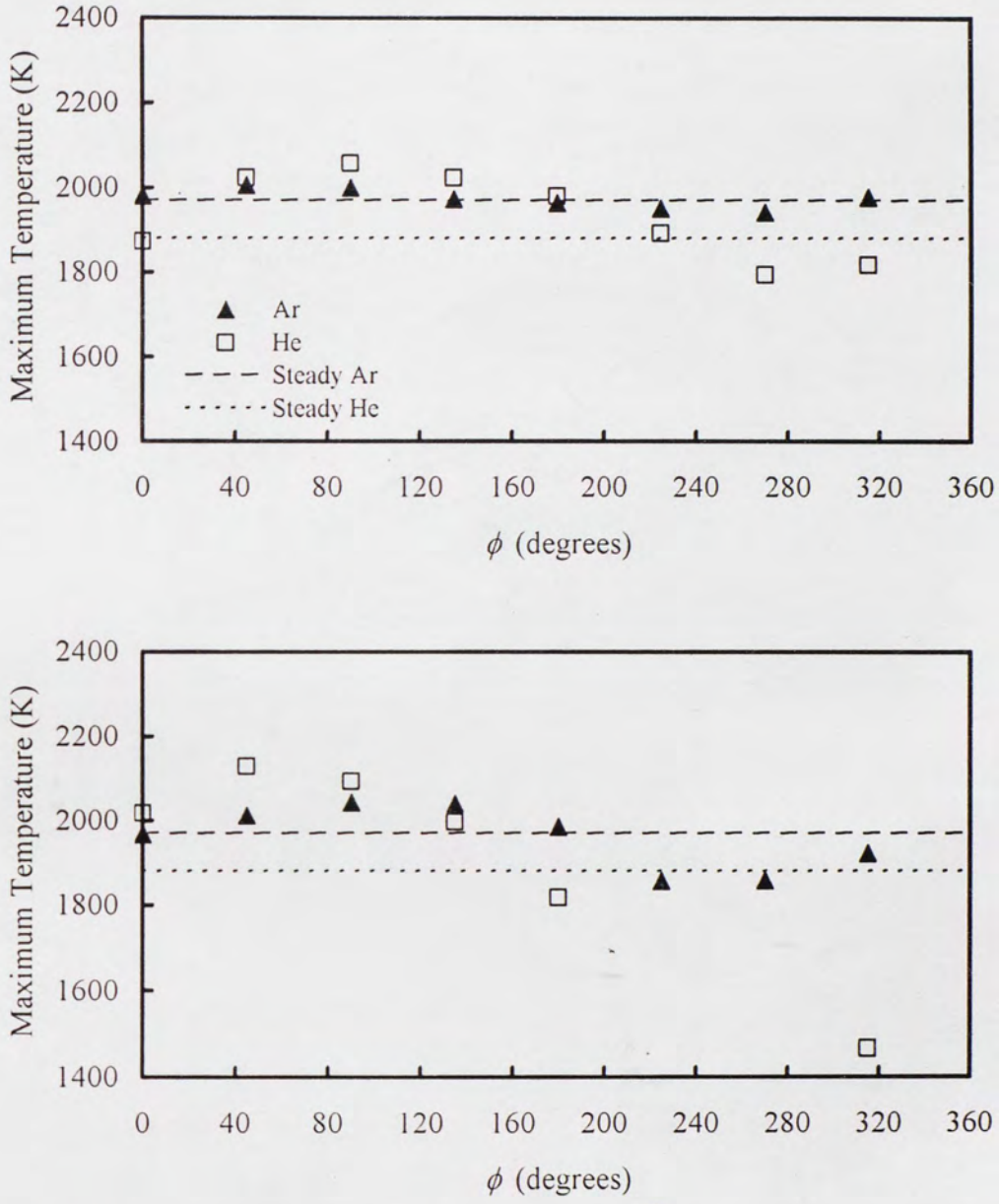

Figure 6-75: Temperature plots for 60% fuel dilution at a forcing frequency of 10 Hz, top and bottom plots are for low and high amplitudes respectively.

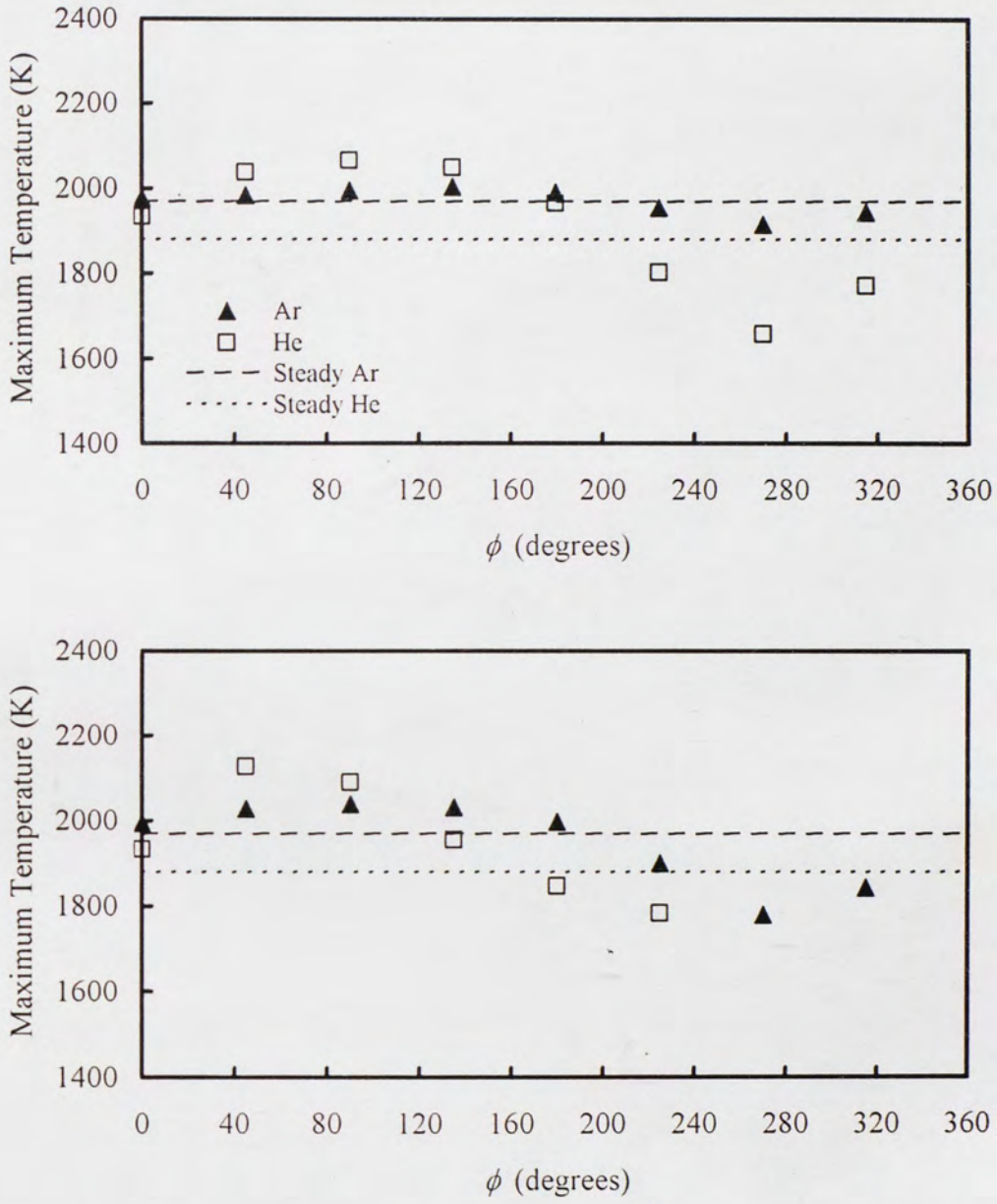

Figure 6-76: Temperature plots for 60% fuel dilution at a forcing frequency of 100 Hz, top and bottom plots are for low and high amplitudes respectively.

6.3.3.2 Effect of Lewis Number and Stretch/Compression/Curvature

At first glance and based on the data presented in Figure 6-14 through Figure 6-76, Lewis number effects are not obvious in the driven flames since the He-diluted flames always exhibit the largest temperature at some point during the speaker oscillation. Take, for example, the 60% diluted flames at 10 Hz (i.e. Figure 6-75). Recall that, in the steady case, the maximum temperature of 60% H_2-Ar flames was higher than that of 60% H_2-He flames (see Table 6-2). In the unsteady case given as an example here, the maximum temperature found during the 10 Hz oscillation of the 60% H_2-He flame is 2058 and 2129 K for low and high amplitudes, respectively. These temperatures are higher than those of the 60% H_2-Ar flame (i.e. 2005 and 2043 K for low and high amplitudes, respectively).

The reason for the increased maximum temperature for the H_2-He flames has been explained in the section above. However, Lewis number effects are indeed present in the unsteady flames studied and can be evidenced by considering one dilution at a time and noting how the imposed unsteadiness changes the flame structure. This change in the reaction zone leads to different changes in temperature depending on whether Le_F is greater or less than unity as discussed below. The next sections will illustrate the effect of $Le_F > 1$ and $Le_F < 1$ in the high as well as in the low frequency flames. Emphasis is placed on the high frequency cases since the observed trends are best represented by these flames.

6.3.3.2.1 High Frequency Flames

Present results (to be discussed below) suggest that flames with $Le_F \geq 1$ (20% He, 40% He, 60% He, 20% Ar, and 40% Ar), when stretched/compressed, decrease/increase in temperature. This follows the flamelet theory of Peters (1984). In the present study, a flame is said to be stretched/compressed when the reaction zone thickness decreases/increases. Consider the thickness of the OH layer in the unsteady images of flames with fuels having $Le_F \geq 1$. When the flame thickness is decreased, the imposed unsteadiness is stretching the flame zone. The opposite is true when the flame thickness increases.

Figure 6-77 shows the flame thickness and temperature of a high frequency H_2-20% Ar flame ($Le_F = 1.389$) pulsed at low amplitude at a specific phase angle ϕ. An image of the corresponding OH field has been embedded for better visualization of the reaction zone. Note how temperature relates to the flame thickness. When the flame thickness decreases, the thermal gradient increases and thus, the thermal flux leaving the flame zone increases as a result. For this $Le_F > 1$ flame, this leads to a lower temperature since thermal diffusivity is higher than mass diffusivity. Similar results for this flame can be expected at high amplitude as shown in Figure 6-78.

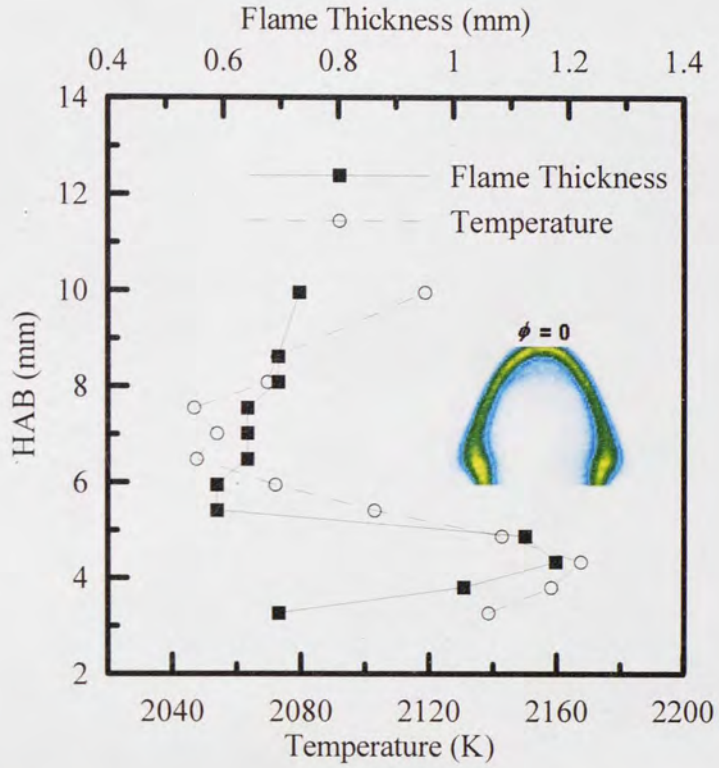

Figure 6-77: Flame temperature and thickness of a 20% Ar flame ($Le_F = 1.389 > 1$) pulsed at 100 Hz, low amplitude (OH field image embedded).

This coupled effect of Le_F and strain affects the flame tip phenomenon present in steady flames. Note that at the flame tip in Figure 6-77 the flame is relatively thin compared with the flame base. The curvature effect at the flame tip which, as explained in Section 6.2, effectively heats the incoming fuel ahead of the flame front for $Le_F \geq 1$ is minimized when the flame is strained. In other words, the largest OH intensity and, therefore, temperature occurs not at the flame tip but at locations where the flame thickness is largest. This is opposite to the steady case where it was shown that the maximum flame temperature occurred at the flame tip for fuel mixtures having $Le_F \geq 1$. Flames with $Le_F \approx 1$ are expected to also behave in this manner as demonstrated by

Figure 6-79 and Figure 6-80. These figures (i.e. Figure 6-77, Figure 6-78, Figure 6-79, and Figure 6-80) are presented here as representative cases; however, the reader is referred to the rest of the figures in Section 6.3.1 above for flames at 100 Hz and $Le_F \geq 1$ which further support the findings described above.

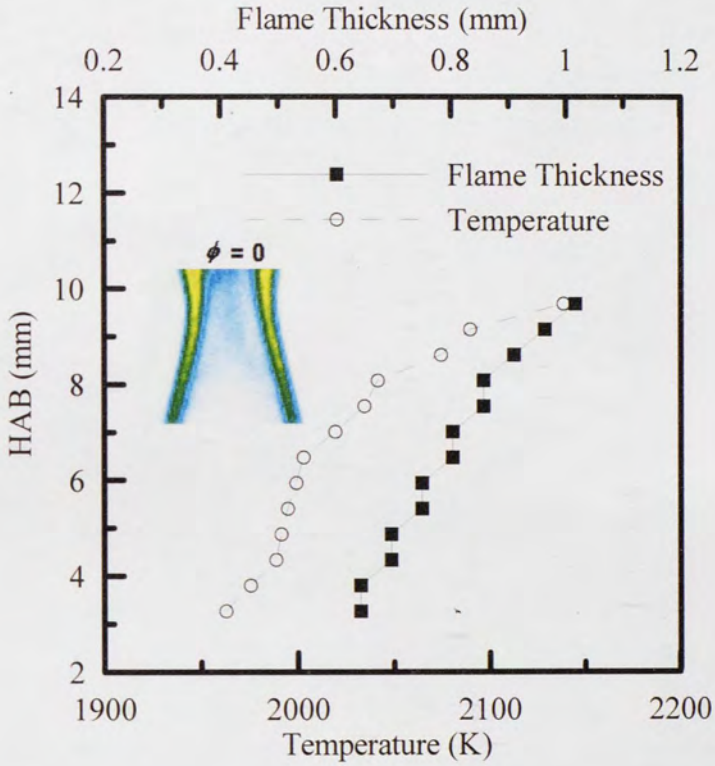

Figure 6-78: Flame temperature and thickness of a 20% Ar flame ($Le_F = 1.389 > 1$) pulsed at 100 Hz, high amplitude (OH field image embedded).

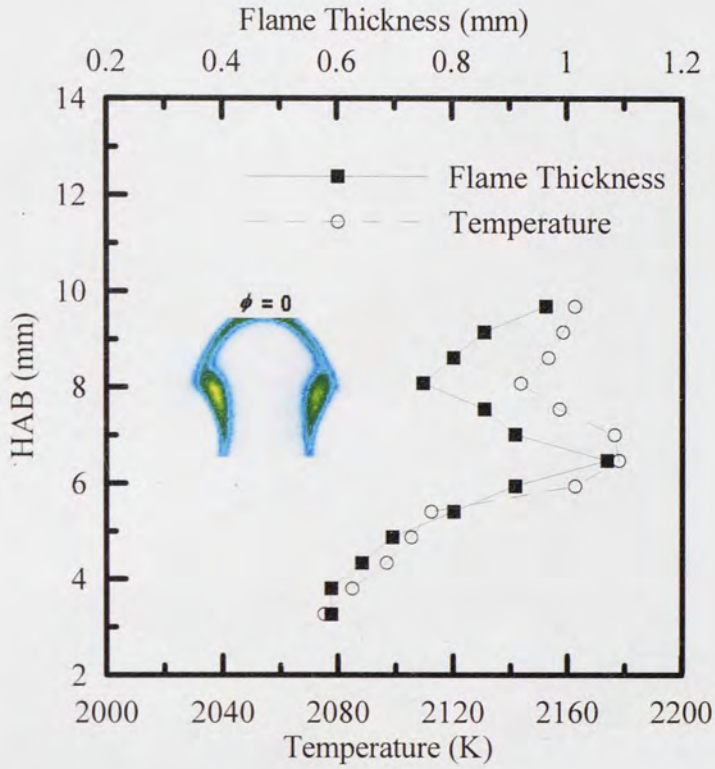

Figure 6-79: Flame temperature and thickness of a 40% He flame ($Le_F = 1.012 \approx 1$) pulsed at 100 Hz, high amplitude (OH field image embedded).

Flames with $Le_F < 1$ at high frequency, on the other hand, exhibit a completely opposite behavior. When the reaction zone is stretched/compressed the temperature increases/decreases. This was also observed by Katta *et. al.*, 1994. This behavior is contrary to what laminar flamelet theory dictates (Peters, 1984). This theory, which arises in an effort to describe turbulent combustion (as discussed in the introduction section of this work), predicts that as a diffusion flame is stretched, the local flame temperature decreases due to an increase in reactant fluxes. If reactant fluxes become too large, the flame will extinguish. This was the case for the unsteady $Le_F \geq 1$ flames presented above but not for the H_2-60% Ar flames (see Figure 6-34, Figure 6-36, Figure

6-60, and Figure 6-58). Thus, there is a limit or domain where the laminar flamelet theory is applicable (Cuenot and Poinsot, 1994). Indeed, laminar flamelet theory has been modified and extended in recent years to include Lewis number effects (Katta and Roquemore, 1995; Pitsch, 2000).

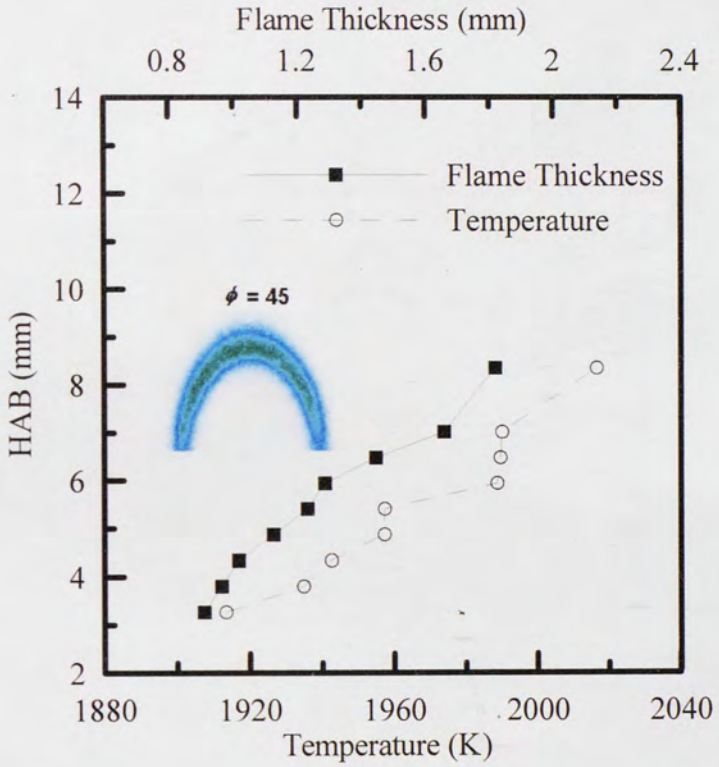

Figure 6-80: Flame temperature and thickness of a 60% He flame ($Le_F = 1.035 \approx 1$) pulsed at 100 Hz, low amplitude (OH field image embedded).

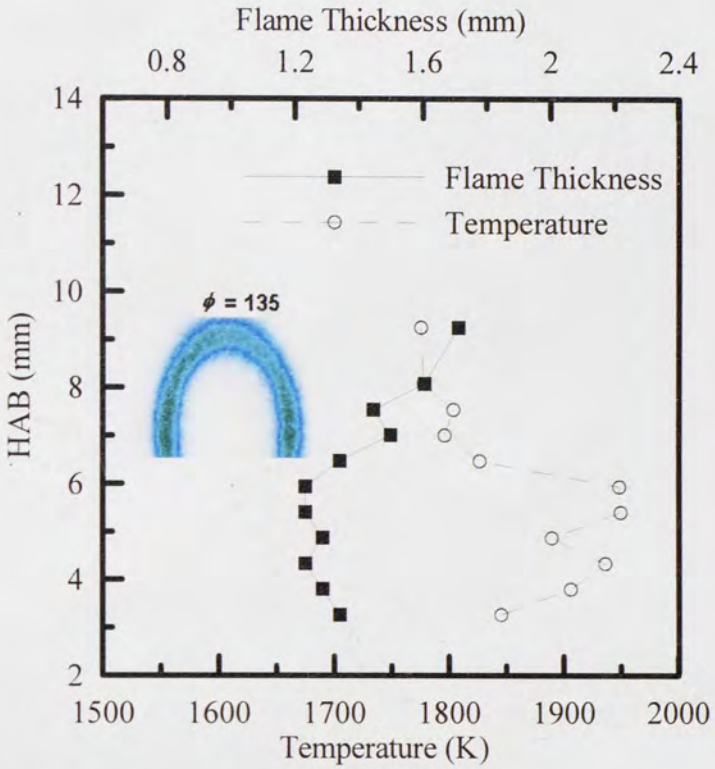

Figure 6-81: Flame temperature and thickness of a 60% Ar flame (Le_F =0.718 < 1) pulsed at 100 Hz, high amplitude (OH field image embedded).

The flame thickness and local temperature of a 60% Ar-diluted flame (Le_F = 0.718) is shown in Figure 6-81. This is a flame at a pulsing frequency of 100 Hz and at high amplitude (i.e. Figure 6-36 and Figure 6-60). Note the location of the maximum temperature, which corresponds with the location at which the flame thickness is minimum. For these $Le_F < 1$ flames, the thermal diffusivity is relatively low (i.e. lower than the mass diffusivity). A decrease in flame thickness increases the thermal and mass gradients at the flame zone. Since the thermal diffusivity is less than the mass diffusivity, the rate at which heat leaves the flame (i.e. heat flux) is less than the rate at which reactants reach the flame. This effectively helps accumulate heat at the flame zone

raising the flame temperature. This is opposite to what was observed for flames with $Le_F \geq 1$. Figure 6-81 is, again, a representative example to support the reasoning above. To further support this argument, consider Figure 6-82 which presents flame thickness and temperature plots for 60% Ar-diluted flames at 100 Hz and low amplitude. The same trend is found in this figure (i.e. decreasing temperature with increasing flame thickness). A similar argument can be given by considering other phases within the speaker pulse (refer to Figure 6-34, Figure 6-36, Figure 6-58, and Figure 6-60).

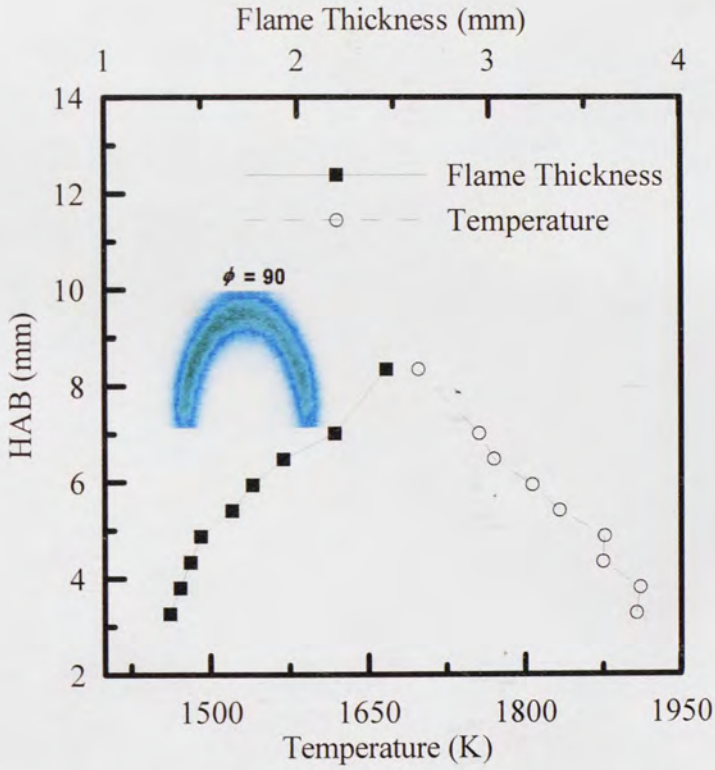

Figure 6-82: Flame temperature and thickness of a 60% Ar flame (Le_F =0.718 < 1) pulsed at 100 Hz, low amplitude (OH field image embedded).

Note that these $Le_F < 1$ high-frequency flames all have well-defined and relatively thin flame tips when compared to their steady counterparts. This is the case, at least, for some phases within the speaker pulse. As was done with the $Le_F \geq 1$ above, it is of interest to investigate how stretching relates to flame curvature at the flame tip. Recall that curvature at the flame tip (i.e. concave towards the incoming fuel) in $Le_F < 1$ flames lowers the flame temperature since the defocusing effect on the incoming reactants is greater than the focusing of heat ahead of the flame tip front (see Figure 6-10).

For $Le_F \geq 1$, it was shown that the maximum flame temperature may occur not at the flame tip (i.e. as in steady $Le_F \geq 1$ flames) but in areas where the flame thickness is largest (see Figure 6-77). When considering the unsteady 60% Ar-diluted flames ($Le_F < 1$), there is no such clear case separating stretch and curvature effects at the flame tip since the flame tip temperature is always lowest in these flames. However, during the flame pulse, the reaction zone at the tip stretches and increases in temperature and it takes a substantial amount of curvature to overwhelm this process (i.e. lower the flame tip temperature). As an example refer to Figure 6-36 which shows the OH field of the 60% Ar flame at 100 Hz and high amplitude. Note how the flame tip intensifies as it thins from $\phi = 0^\circ$ to $\phi = 90^\circ$ and then loses intensity (as seen in the OH image) as curvature increases through the remainder of the pulse.

In order to better illustrate stretch and curvature mechanisms at the flame tip, the amount of curvature that the flame is subjected to was obtained from the OH PLIF images. The flame surface was traced by locating the peak OH intensity as a function of r, the radial distance from the fuel tube centerline, and z, the height above the burner.

The radial location of the flame zone could, therefore, be expressed as a function of z. Since the flame tip structure is not perfectly circular, the average curvature, C, of the flame can be obtained by the following integral (Katta *et. al.*, 2003):

$$C = \frac{1}{r_{max}} \int_{o}^{r_{max}} \frac{dr}{r\sqrt{1+\left(\frac{dr}{dz}\right)^2}} \tag{6.1}$$

Where r_{max} is the maximum radial location of the flame as shown in Figure 6-83. The integral above was evaluated numerically by implementing the trapezoidal rule (Chapra and Canale, 2002) for the 60% Ar-diluted flame at 100 Hz and high amplitude for $0^\circ \leq \phi \leq 180^\circ$ (see Figure 6-36). The results are listed in Table 6-4.

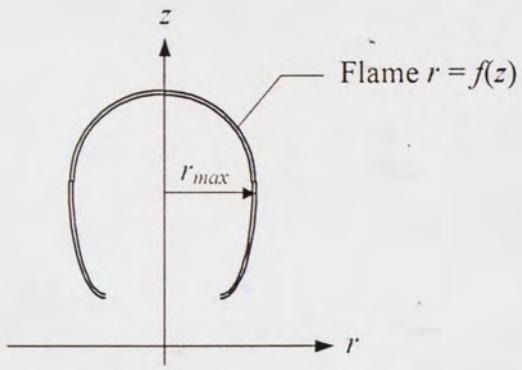

Figure 6-83: Flame curvature schematic.

From Table 6-4 note that as the flame pulse progresses, the curvature always increases. As the flame is stretched from $\phi = 45^\circ$ to $\phi = 90^\circ$ (i.e. flame thickness

decreases), the temperature increases even though curvature increases as well. From $\phi =$ 90° to $\phi = 135°$, the flame thickness remains relatively unchanged, however, the flame temperature at the tip decreases substantially due to the increase in curvature. Thus, flame stretch in $Le_F < 1$ flames is a competing and opposite process to flame curvature as evidenced by the high-frequency images of 60% Ar-diluted flames and the data in Table 6-4.

Table 6-4: Flame tip thickness and curvature effects*

ϕ	Curvature C (mm^{-1})	Flame Thickness (mm)	Maximum OH Intensity	Maximum Temperature (K)
0°	0.217	2.299	0.232	1670
45°	0.258	1.979	0.255	1795
90°	0.314	1.818	0.269	1815
135°	0.402	1.872	0.2162	1788
180°	0.613	2.246	0.166	1766

*For 60% Ar-diluted flames at 100 Hz, high amplitude (see Figure 6-36 and Figure 6-60)

6.3.3.2.2 Low Frequency Flames

It is noted that, although not as obvious, flames at low frequency also exhibit the behavior described above whether $Le_F \geq 1$ or $Le_F < 1$. Low frequency flames, as explained in the previous sections, adjust to the imposed flow oscillation by locating

themselves to further radial positions without a large change in flame thickness. Consider Figure 6-84 through Figure 6-88; these are images of flames at 10 Hz. Note that the 60% Ar-diluted flames ($Le_F = 0.718 < 1$) decrease in temperature as the reaction zone thickens (Figure 6-84 and Figure 6-85). On the other hand, flames at 10 Hz for which $Le_F \geq 1$, exhibit the opposite trend (see Figure 6-86, Figure 6-87, and Figure 6-88). Note that these low frequency flames all have a structure similar to that of the steady flames (i.e. Figure 6-10 and Figure 6-11). It could then be argued that the thickness-temperature trend observed in Figure 6-84 through Figure 6-88 could be due to curvature effects at the flame tip since these low frequency flames seem not to be subjected to the high rates of stretch/strain seen in high frequency flames. Indeed this might be the case since all the flames shown in Figure 6-84 through Figure 6-88 thicken as the tip is approached as steady flames. Therefore, flames with $Le_F < 1$ decrease in temperature whereas temperature increases in $Le_F \geq 1$ flames in the region close to the flame tip which is the trend that was seen in steady flames.

These low frequency flames would have to be pulsed at considerable high amplitudes to determine whether the curvature at the tip is responsible for the temperature trends described above. Consider Figure 6-88 which is 40% He-diluted flame ($Le_F = 1.012$) pulsed at 10 Hz and high amplitude. In this figure, the strength of the pulse has decreased the flame thickness at the tip considerably so that the maximum temperature does not occur at the tip where curvature is strong but where the flame thickness is largest confirming the trends observed in the high frequency flames. Unfortunately, there are no images available in the current data set where flames with Le_F

< 1 (i.e. 60% Ar-diluted flames) at low frequency have a structure similar to that shown in Figure 6-88.

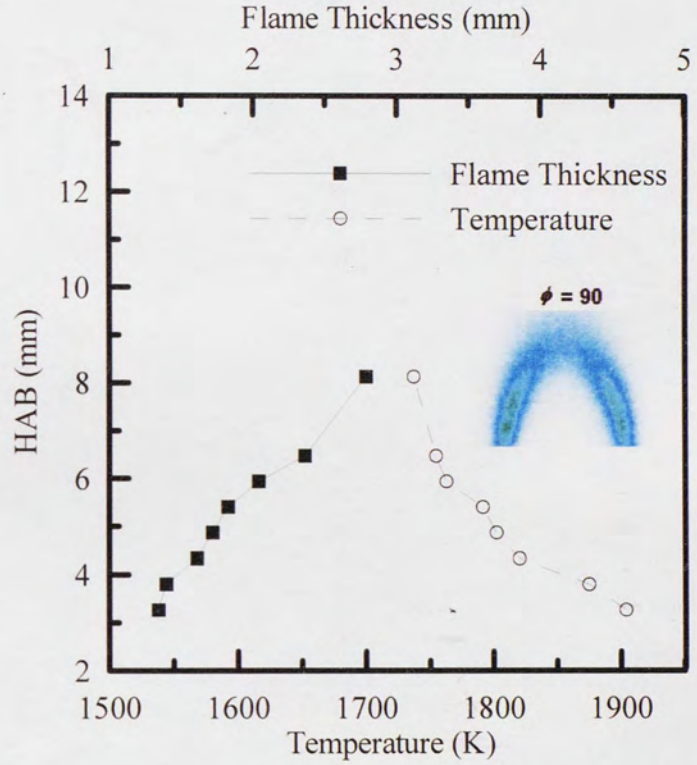

Figure 6-84: Flame temperature and thickness of a 60% Ar flame ($Le_F = 0.718 < 1$) pulsed at 10 Hz, low amplitude (OH field image embedded).

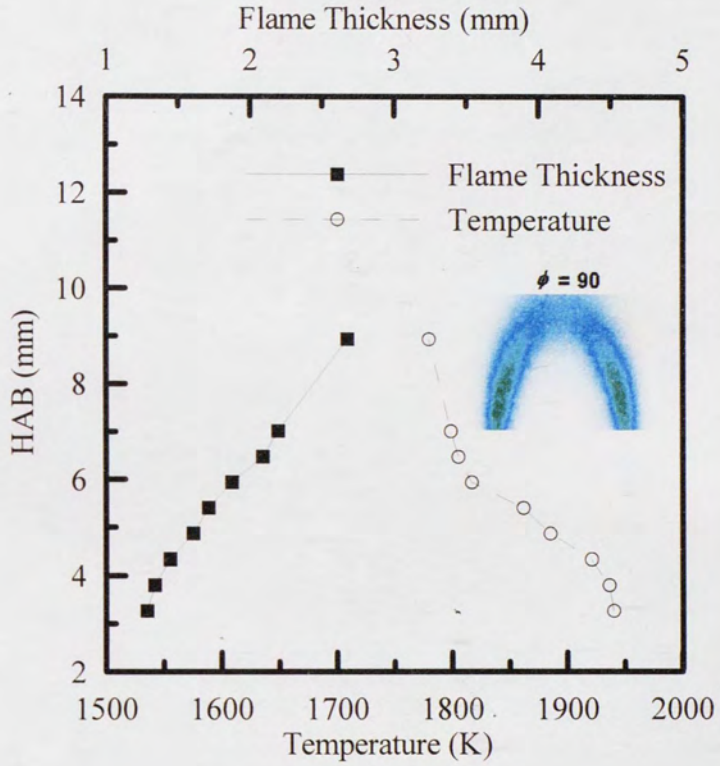

Figure 6-85: Flame temperature and thickness of a 60% Ar flame ($Le_F = 0.718 < 1$) pulsed at 10 Hz, high amplitude (OH field image embedded).

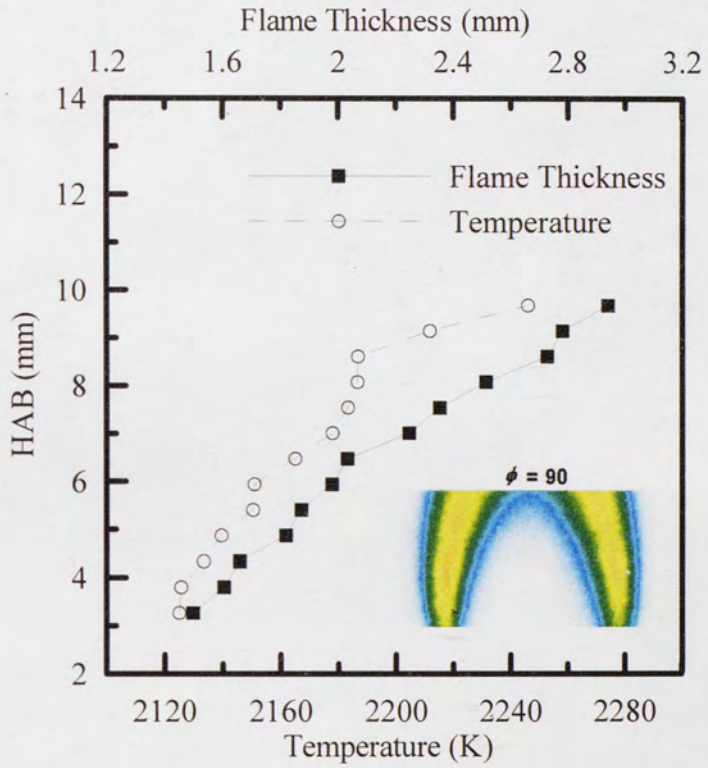

Figure 6-86: Flame temperature and thickness of a 20% Ar flame ($Le_F = 1.389 > 1$) pulsed at 10 Hz, low amplitude (OH field image embedded).

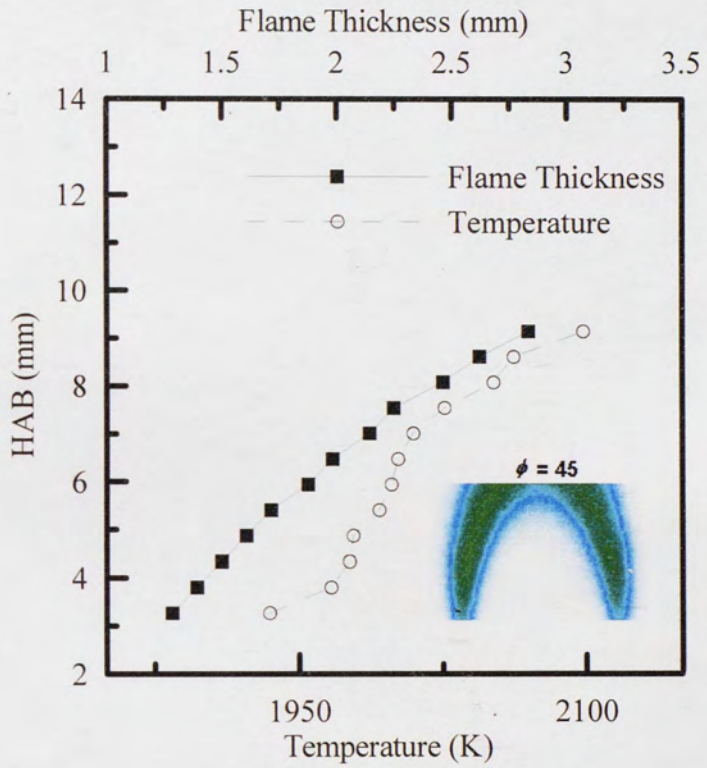

Figure 6-87: Flame temperature and thickness of a 60% He flame ($Le_F = 1.035 \approx 1$) pulsed at 10 Hz, high amplitude (OH field image embedded).

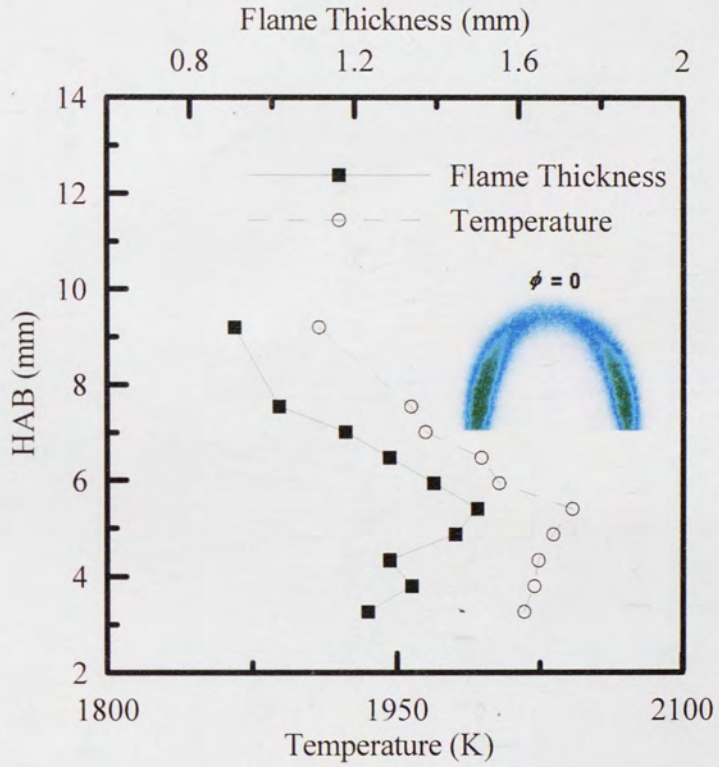

Figure 6-88: Flame temperature and thickness of a 40% He flame ($Le_F = 1.012 \approx 1$) pulsed at 10 Hz, high amplitude (OH field image embedded).

6.4 Summary

Laser-induced fluorescence measurements of OH and temperature have been obtained in steady and unsteady hydrogen jet diffusion flames. Six different flames were investigated having various dilution levels of helium or argon and were driven at two different frequencies and amplitudes. Results show how mass diffusion is of importance in unsteady flames. Lewis number effects are also evident and are affected by the curvature and strain present in high and low frequency flames. This experiment is one of the few studies that provides quantitative linear OH LIF measurements in laminar jet diffusion flames. Not only have measurements been performed in steady flames but in unsteady flow-flame interactions where temperature and OH vary significantly as evidenced by the present results. This constitutes a unique set of data that gives further insight into unsteady thermal and mass transport processes.

7 CONCLUSION AND RECOMMENDATIONS

Diffusion flames are the means by which much of the world's harnessed energy is obtained. For many years these flames have been extensively studied experimentally and computationally; however, their behavior is still not completely understood. The present study adds to the ongoing effort of understanding the complex processes taking place in diffusion flames. Planar laser-induced fluorescence measurements were performed on steady and unsteady laminar hydrogen diffusion flames at various dilution levels with different inert species. A set of detailed gas temperature measurements and reaction zone structure was obtained after the digital image processing of approximately 8,000 laser-induced fluorescence images. The results were related to the mass and thermal properties of the fuel mixtures (i.e. Lewis number). The following is a summary of the major results and conclusions and some recommendations for future work.

7.1 Major Conclusions

- Under unsteady conditions, mass diffusion becomes important in determining flame location, size, and temperature. Dilution with Ar, which is a large, heavy molecule, has the effect of impeding radial diffusion of hydrogen, causing the flame to be thinner and closer to the centerline. For all dilution levels (even 60% dilution which

yields $Le_F < 1$ for the Ar diluted flames), the maximum temperature of the unsteady H_2-He mixtures is always higher than that of H_2-Ar mixtures at some point during the unsteady oscillation cycle. This is due to an increased flux of hydrogen to the flame zone in H_2-He flames under unsteady conditions since H_2 is more diffusive in He than in Ar. H_2-He flames always extinguished at lower forcing voltages than H_2-Ar flames; the increased reactant flux in unsteady H_2-He flames may be one of the factors contributing to this observation.

- Flames disturbed at low frequencies (i.e. low turbulence intensities) respond to the unsteady flowfield by adjusting their radial position outward or inward in a steady manner, as necessary. The flame thickness of these flames does not vary substantially. On the other hand, flames at high frequencies do not respond to the hydrodynamic excitation in the same way as their low frequency counterparts. High-frequency flames adjust to the rapid flowfield changes by considerable thinning (stretch) or widening (compression) of the flame zone.

- Depending on the Lewis number of the fuel mixture, the stretch/compression imparted on the flame by the flow oscillation affects the flame temperature differently. These Lewis number effects were present in low and high frequency flames, however, they were found to be most significant in the high frequency flames. Flames with $Le_F \geq 1$ increased in temperature when compressed and decreased in temperature when stretched. Oppositely, flames with $Le_F < 1$ decreased in

temperature when compressed and increased in temperature when stretched. This result is opposite to the laminar flamelet theory of Peters (1984).

- Curvature was found to influence the temperature of the steady and unsteady flame tips and competed with the stretching effects. Under unsteady conditions, and, more specifically, at high frequencies, the flame tip is stretched during the first stages of the speaker oscillation. For flames with $Le_F \geq 1$, as mentioned above, stretching reduces the flame temperature whereas a concave curvature towards the fuel tends to increase the flame temperature. Stretching in flames with $Le_F < 1$, however, increases the temperature and this process competes with the concave curvature of the flame tip which acts to lower the temperature. It has been shown (for $Le_F < 1$ flames) that even under increasing curvature, if the flame is sufficiently stretched, temperature might increase. On the other hand, a high enough curvature will decrease the flame temperature even when the reaction zone is substantially stretched.

The above results may help the development of computational codes used to model turbulent flames. Based on these results, it is recommended that these models should emphasize mass diffusion of the different fuel species and introduce non-unity Lewis numbers for flames with high levels of turbulence (i.e. high frequency).

7.2 Recommendations for Future Work

- The LDV velocity measurements performed on the burner were done using air at atmospheric conditions. The fuel for the experiments reported herein consisted of various mixtures of hydrogen, argon, and helium. For obvious safety reasons, it was unwise to vent unburned hydrogen into the laboratory to perform the velocity measurements. However, it is noted that using air might be a poor approximation for the unsteady flames since H_2-Ar and H_2-He mixtures have different densities and viscosities and the momentum transfer from the speaker to these gases might vary substantially. Thus, it is recommended that velocity measurements be performed under actual burning conditions so that the combustion processes are occurring while taking the measurements. LDV could still be used, however a different seeding material (i.e. as opposed to atomized water droplets) would have to be selected. A technique such as PIV would be best for this situation. PIV can provide information about the entire flowfield for every phase within the speaker oscillation. This information will be extremely useful since the instant strain rate at the flame zone can be derived from such measurements extending the current analysis to include coupled strain, strech/compression, and curvature effects.

- The effect of the vycor glass, which enclosed the flame on the LIF measurements, should be determined. Due to large room drafts, the glass had to be used in order to assure a repeatable unsteady flame. Images with and without the glass were taken while performing the measurements with no noticeable differences. However, due to

the glass curvature, the vycor glass may act as a lens, which might affect the recorded OH fluorescence images.

- This research experiment was performed at North Carolina State University. The dye laser system used was originally setup to measure fluorescence in hydrocarbon counterflow flames. Thus, laser sheets utilized in this project were short (approximately 10 mm) and the transitions used were strong (needed for hydrocarbon flames). Due to time constraints, the laser system was used as it was. A better setup could be done by expanding the laser sheet to capture as much of the unsteady flames as possible and by selecting transitions with a lower energy separation (in the order of the temperature found in the current unsteady flames) since the hydrogen flames studied do not suffer from soot interference and strong transitions are not needed.

- Numerical combustion codes are sufficiently advanced now and a numerical model of the flames studied in this research would be of extreme importance and benefit. Numerical codes developed by Katta *et. al.* (1994) can be applied and extended in this study.

APPENDIX A: LABVIEW VI DIAGRAMS

Boxcar data acquisition system:

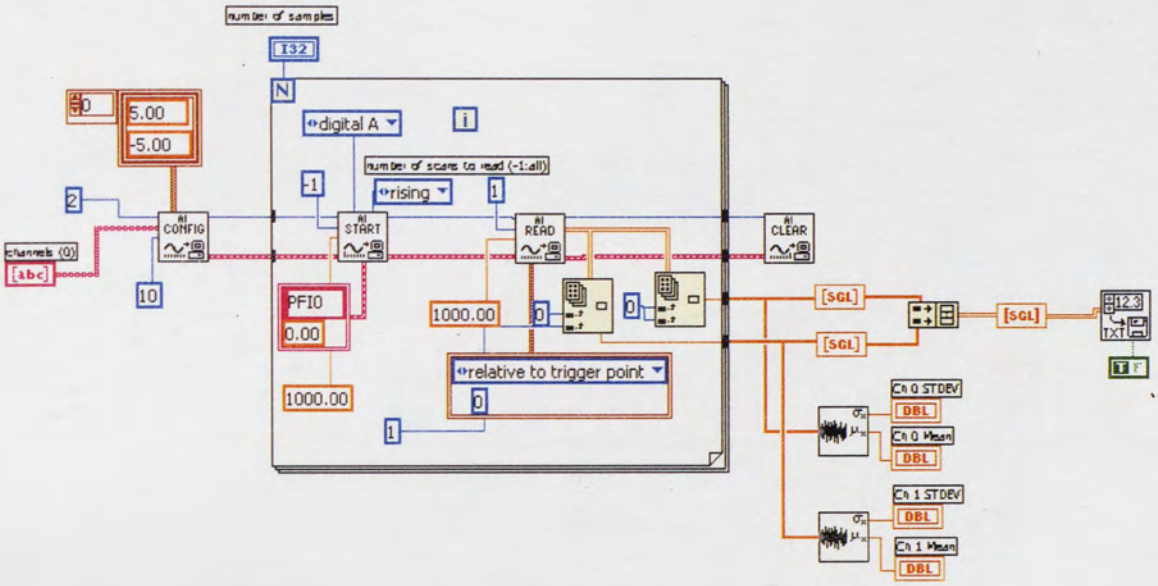

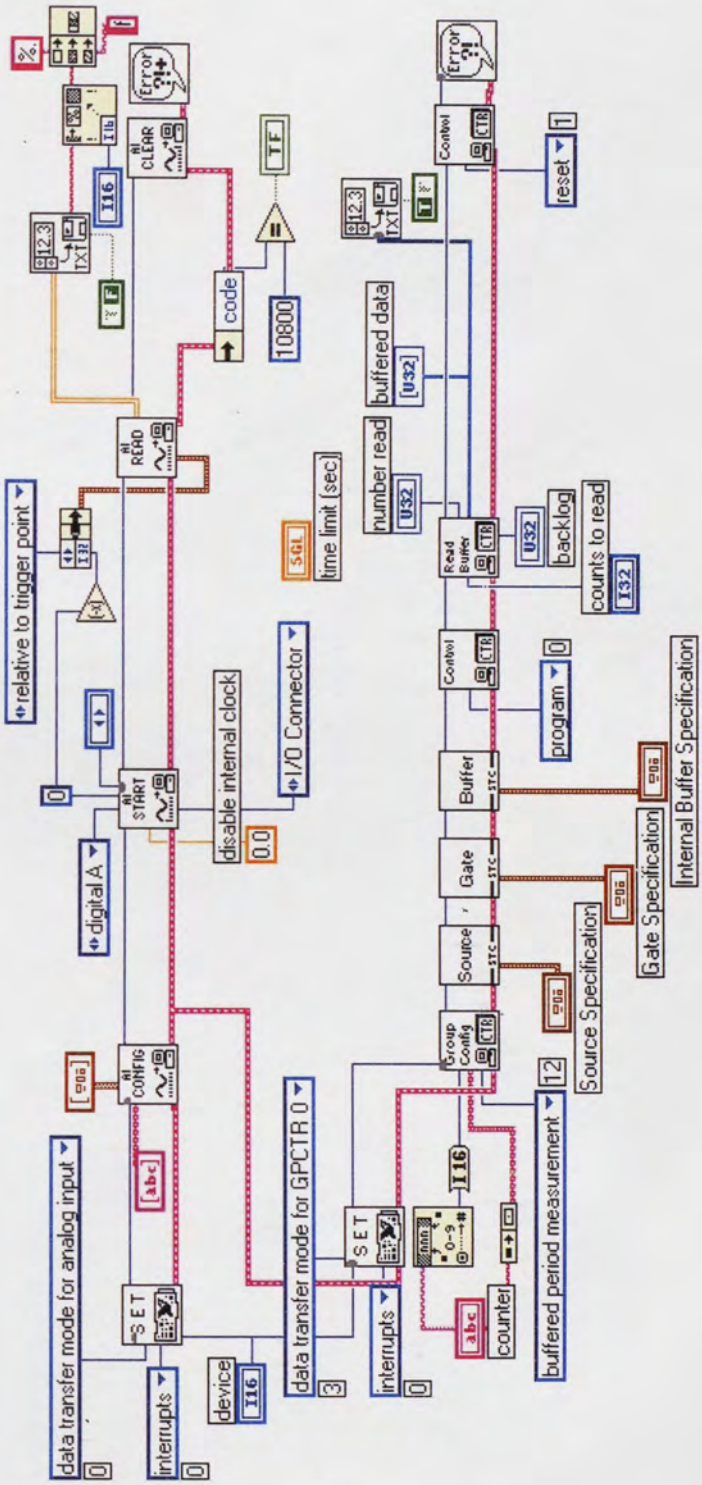
relative to trigger point
digital A
data transfer mode for analog input
interrupts
device
data transfer mode for GPCTR 0
interrupts
counter
buffered period measurement
Source Specification
Gate Specification
Internal Buffer Specification
disable internal clock
I/O Connector
time limit (sec)
code
10800
buffered data
number read
backlog
counts to read
program
reset
AI CLEAR
AI READ
AI START
AI CONFIG
SET
Group Config
Source
Gate
Buffer
Control
Read Buffer

APPENDIX B: FORTRAN PROGRAM (PROFILE IMAGE GENERATOR)

```
PROGRAM PROFILE

* The following program can take either the 1-D beam profile or the 1-D flat field profile and
* generates an image in which every column is the beam profile or every row is the flat field profile
* these images can be used to correct the LIF images for beam profile and camera flat field variation

      REAL IMAGE(135,578)
      INTEGER ANS,K,L
      CHARACTER INPUTF *15,OUTPUTF *15
      WRITE (6,*) 'Input File'
      READ (5,*) INPUTF
      WRITE (6,*) 'Output File'
      READ (5,*) OUTPUTF
      WRITE (6,*) 'Axial (1) or Flat-field (2)?
      READ (5,*) ANS
      OPEN (1,FILE=INPUTF)
      OPEN (2,FILE=OUTPUTF)
      IF (ANS.EQ.1) THEN
        K=135
        L=578
        CALL FLAT(IMAGE,K,L)
        ELSE
          K=578
          L=135
          CALL BEAM(IMAGE,K,L)
      END IF
      CLOSE(1)
      CLOSE(2)
END

**********************************SUBROUTINES**********************************

SUBROUTINE FLAT(IMAGE,K,L)
      REAL IMAGE(135,578)
      INTEGER K,L
      DO 10 I=1,L
        READ (1,'(F6.4)') AXIAL(1,I)
10    CONTINUE
      DO 20 I=1,K
        DO 30 J=1,L
          AXIAL(I,J)=AXIAL(1,J)
30      CONTINUE
20    CONTINUE
      WRITE (2,'(I3,/,I3,/,A1,/)') 578,135,'F'
      DO 40 I=1,K
        WRITE (2,'(L(F6.4,1X),\)') (AXIAL(I,J), J=1,L)
40    CONTINUE
      RETURN
END

------------------------------------------------------------------------------

SUBROUTINE BEAM(IMAGE,K,L)
```

```
      REAL IMAGE(135,578)
      INTEGER K,L
      DO 10 I=1,L
        READ (1,'(F6.4)') AXIAL(I,1)
10    CONTINUE
      DO 20 I=1,L
        DO 30 J=1,K
          AXIAL(I,J)=AXIAL(I,1)
30      CONTINUE
20    CONTINUE
      WRITE (2,'(I3,/,I3,/,A1,/)') 578,135,'F'
      DO 40 I=1,L
        WRITE (2,'(K(F6.4,1X),\)') (AXIAL(I,J), J=1,K)
40    CONTINUE
      RETURN
END
```

REFERENCES

Adrian, R. J. and Yao, C. S. (1987). "Power Spectra of Fluid Velocities Measured by Laser Doppler Velocimetry." *Experiments in Fluids* 5 (1987): 17-28.

Arnold, A., Lange, B., Bouché, T., Heitzmann, T., Schiff, G., Ketterle, W., Monkhouse, P., and Wolfrum, J. "Absolute Temperature Fields in Flames by 2D-LIF of OH Using Excimer Lasers and CARS Spectroscopy." *Berichte der Bunsen-Gesellschaft - Physical Chemistry* 96 (1992): 1388-1393.

Becker, H. A. "Physical Probes." *Instrumentation for Flows with Combustion*. Taylor, A. M. K. P., ed. London: Academic Press, 1993: 53-112.

Benedict, L. H., Nobach, H., and Tropea, C. "Estimation of Turbulent Velocity Spectra from Laser Doppler Data." *Measurement Science and Technology* 11 (2000): 1089-110.

Bergmann, V., Meier, W., Wolff, D., and Stricker, W. "Application of Spontaneous Raman and Rayleigh Scattering and 2D LIF for the Characterization of a Turbulent $CH_4/H_2/N_2$ Jet Diffusion Flame." *Applied Physics B* 66 (1998): 489-502.

Bilger, R. W. "Future Progress in Turbulent Combustion Research." *Progress in Energy and Combustion Science* 26 (2000): 367-380.

Bradley, D. and Matthews, K. J. "Measurement of High Gas Temperatures with Fine Wire Thermocouples." *Journal of Mechanical Engineering* 10 (1968): 299-305.

Burke, S. P., and Schumann, T. F. W. "Diffusion Flames." *Industrial and Engineering Chemistry* 20 (1928): 998-1004.

Bush, W. B., and Fendell, F. E. "On Diffusion Flames in Turbulent Shear Flows." *Acta Astronautica* 1 (1974): 645-666.

Campbell, D. H. "Collisional Effects on Laser-Induced Fluorescence Measurements of Hydroxide Concentrations in a Combustion Environment. 1: Effects for $v' = 0$ Excitation." *Applied Optics* 23 (1984a): 689-703.

Campbell, D. H. "Collisional Effects on Laser-Induced Fluorescence Measurements of Hydroxide Concentrations in a Combustion Environment. 2: Effects for $v' = 1$ Excitation." *Applied Optics* 23 (1984b): 1319-1327.

Cattolica, R. "OH Rotational Temperature from Two-Line Laser-Excited Fluorescence." *Applied Optics* 20 (1981): 1156-1166.

Chaos, M., and Chen, R.-H. "An Experimental Study of Pulsating Instability in Near-limit Laminar Nonpremixed Flames." *Combustion Science and Technology* (2003a); submitted.

Chaos, M., and Chen, R.-H. "Lewis Number Effects in Counterflow Diffusion Flames." *Combustion and Flame* (2003b); in preparation.

Chapra, S. C. and Canale, R. P. *Numerical Methods for Engineers*. 4th ed. New York: McGraw-Hill, 2002.

Cheatham, S., and Matalon, M. "Heat Loss and Lewis Number Effects on the Onset of Oscillations in Diffusion Flames." *Proceedings of the Twenty-Sixth Symposium (International) on Combustion*, Naples, Italy (1996): 1063-1070.

Chen, J.-Y., Chang, W.-C., and Koszykowski, M. L. "Numerical Simulation and Scaling of NO_x Emission from Turbulent Hydrogen Jet Flames with Various Amounts of Helium Dilution." *Combustion Science and Technology* 110-111 (1995): 505.

Chen, J.-Y., Kollmann, W. "PDF Modeling and Analysis of Thermal NO Formation in Turbulent Nonpremixed Hydrogen-Air Jet Flames" *Combustion and Flame* 88 (1992): 397-412.

Chen, R.-H., and Driscoll, J. F. "Nitric Oxide Levels of Jet Diffusion Flames: Effects of Coaxial Air and Other Mixing Parameters." *Proceedings of the Twenty-Third Symposium (International) on Combustion*, Orlans, France (1990): 281-288.

Chen, R.-H., Mitchell, G. B., and Ronney, P. D. "Diffusive-Thermal Instability and Flame Extinction in Nonpremixed Combustion." *Proceedings of the Twenty-Fourth Symposium (International) on Combustion*, Sydney, Australia (1992): 213-221.

Chen, R.-H., Navedo, J. E., and Chew, L. "Effect of Fuel Lewis Number on and Damköhler Number Scaling of Nitric Oxide Emission Level of Burke-Schumann Type Flames." *Combustion Science and Technology* 127 (1997): 293-318.

Chen, Y.-C., and Mansour, M. S. "Measurements of the Detailed Flame Structure in Turbulent H_2-Ar Jet Diffusion Flames with Line-Raman/Rayliegh/PLIF-OH Technique." *Proceedings of the Twenty-Sixth Symposium (International) on Combustion*, Naples, Italy (1996): 97-103.

Chung, S. H., and Law, C. K. "Burke-Schumann Flame with Streamwise and Preferential Diffusion." *Combustion Science and Technology* 37 (1984): 21-46.

Churchill, S. W. and Bernstein, M. "A Correlating Equation for Forced Convection from Gases and Liquids to a Circular Cylinder in Crossflow." *Journal of Heat Transfer, Transactions ASME* 99 (1977): 300-306.

Crosley, D. R. and Smith, G. P. "Rotational Energy Transfer and LIF Temperature Measurements." *Combustion and Flame* 44 (1982): 27-34.

Cuenot, B., and Poinsot, T. "Asymptotic and Numerical Study of Diffusion Flames with Variable Lewis Number and Finite Rate Chemistry." *Combustion and Flame* 104 (1996): 111-137.

Cuenot, B., and Poinsot, T. "Effects of Curvature and Unsteadiness in Diffusion Flames. Implications for Turbulent Diffusion Combustion." *Proceedings of the Twenty-Fifth Symposium (International) on Combustion*, Irvine, California (1994): 1383-1390.

Daily, J. W. "Laser Induced Fluorescence Spectroscopy in Flames." *Progress in Energy and Combustion Science* 23 (1997): 133-199.

Dandy, D. S. *Software Tools*. 29 Jul. 2003. 20 Apr. 2003. <http://grashof.engr.colostate.edu/tools/SoftwareTools.html>

Dieke, G. M., and Crosswhite, H. M. (1962). "The Ultraviolet Bands of OH." *Journal of Quantitative Spectroscopy and Radiative Transfer* 2 (1962): 97-199.

Dimpfl, W. L. and Kinsey, J. L. "Radiative Lifetimes of OH($A^2\Sigma$) and Einstein Coefficients for the A-X System of OH and OD." *Journal of Quantitative Spectroscopy and Radiative Transfer* 21 (1979): 233-241.

Driscoll, J. F., Chen, R.-H., and Yoon, Y. "Nitric Oxide Levels of Turbulent Jet Diffusion Flames: Effects of Residence Time and Damköhler Number." *Combustion and Flame* 88 (1992): 37-49.

Earls, L T. "Intensities in the $^2\Pi$–$^2\Sigma$ Transitions in Diatomic Molecules." *Physical Review* 48 (1932): 423-424.

Eckbreth, A. C. *Laser Diagnostics for Combustion Temperature and Species.* 2nd ed. Amsterdam: Gordon and Breach Publishers, 1996.

Feese, J. J., and Turns, S. R. "Nitric Oxide Emissions from Laminar Diffusion Flames: Effects of Air-Side versus Fuel-Side Diluent Addition." *Combustion and Flame* 113 (1998): 66-78.

Feingold, A. and Gupta, K. G. "New Analytical Approach to the Evaluation of Configuration Factors in Radiation from Spheres and Infinitely Long Cylinders." *Journal of Heat Transfer, Transactions ASME* 92 (1970): 69-76.

Finke, H, and Grünefeld, G. "An Experimental Investigation of Extinction of Curved Laminar Hydrogen Diffusion Flames." *Proceedings of the Twenty-Seventh Symposium (International) on Combustion*, Edinburgh, Scotland (2000): 2133-2140.

Gabriel, R., Navedo, J. E., and Chen R.-H. "Effects of Fuel Lewis Number on Nitric Oxide Emission of Diluted H_2 Turbulent Jet Diffusion Flames." *Combustion and Flame* 121 (2000): 525-534.

Glassman, I. *Combustion.* 3rd ed. San Diego: Academic Press, 1996.

Glawe, G. E., and Shepard, C. E. *Some Effects of Exposure to Exhaust-Gas Streams on Emittance and Thermoelectric Power of Bare-Wire Platinum Rhodium – Platinum Thermocouples.* NACA Technical Note 3253. Washington, 1954.

Goldsmith, J. E. M. and Laurendeau, N. M. "Two-Photon-Excited Fluorescence Measurements of OH Concentration in a Hydrogen-Oxygen Flame." *Applied Optics* 25 (1986): 276-283.

Gutmark, E., Parr, T. P., Hanson-Parr, D. H., and Schadow, K. C. "On the Role of Large and Small-Scale Structures in Combustion Control." *Combustion Science and Technology* 66 (1989): 107-126.

Hancock, R. D.. "Laser Diagnostic Investigation of the Structure of Steady and Driven Hydrogen Jet Diffusion Flames." Diss. University of Illinois at Urbana-Champaign, 1996.

Hancock, R. D., Schauer, F. R., Lucht, R. P., Katta, V. R., and Hsu, K. Y. "Thermal Diffusion Effects and Vortex-Flame Interactions in Hydrogen Jet Diffusion Flames." *Proceedings of the Twenty-Sixth Symposium (International) on Combustion*, Naples, Italy (1996): 1087-1093.

Hanson, R. K., Seitzman, J. M., Paul, P. H. "Planar Laser-Fluorescence Imaging of Combustion Gases." *Applied Physics B* 50 (1990): 441-454.

Hermanson, J. C., Dugnani, R., and Johari, H. "Structure and flame length of fully-modulated, turbulent diffusion flames." *Combustion Science and Technology* 155 (2000): 203-225.

Hermanson, J. C., and Vranos, A. "Combined Effects of Preferential Diffusion and Species Transport in a Strained, Laminar Diffusion Flame." *Combustion Science and Technology* 75 (1991): 339-345.

Hermanson, J. C., and Vranos, A. "Preferential Thermal and Multicomponent Species Transport Effects in Strained Diffusion Flames." *AIAA Journal* 30 (1992): 2982-2985.

Herzberg, G. *Atomic Spectra and Atomic Structure*. New York: Dover, 1944.

Herzberg, G. *Molecular Spectra and Molecular Structure, I. Spectra of Diatomic Molecules*. Cincinnati: Van Nostrand Reinhold Co., 1950.

Holman, J. P. *Experimental Methods for Engineers*. 6th ed. New York: McGraw Hill, Inc., 1994.

Hopkins, K. C., Czerniak, D. O., Youssef, C., Radak, L., and Nylander, J. "NO_x Reduction on Natural Gas-Fired Boilers Using Fuel Injection Recirculation (FIR)-Laboratory Demonstration." *Proceedings of the International Power Generation Conference*, October 6-10, 1991, San Diego, CA. ASME Paper 91-JPGC-EC-3.

Howell, J. R. *A Catalog of Radiation Configuration Factors*. New York: McGraw-Hill, 1982.

Ishizuka, S., and Sakai, Y. "Structure and Tip-Opening of Laminar Diffusion Flames." *Proceedings of the Twenty-First Symposium (International) on Combustion*, Munich, Germany (1986): 1821-1828.

Joulin, G., and Clavin, P. "Linear Stability Analysis of Nonadiabatic Flames: Diffusive-Thermal Model." *Combustion and Flame* 35 (1979): 139-153.

Kaiser, C., Liu, J.-B., and Ronney, P. D. "Diffusive-thermal Instabilitites of Counterflow Flames at Low Lewis Number." *Proceedings of the 38th Aerospace Sciences Meeting & Exhibit*, January 10-13, 2000, Reno, Nevada, AIAA Paper 2000-0576.

Kaplan, C. R., Shaddix, C. R., and Smyth, K. C. "Computations of Enhanced Soot Production in Time-Varying CH_4/Air Diffusion Flames." *Combustion and Flame* 106 (1996): 392-405.

Katta, V. R., and Roquemore, W. M. "On the Structure of a Stretched/Compressed Laminar Flamelet – Influence of Preferential Diffusion." *Combustion and Flame* 100 (1995): 61-70.

Katta, V. R., Carter, C. D., Fiechtner, G. J., Roquemore, W. M, Gord, J. R., and Rolon, J. C. "Interaction of a Vortex with a Flat Flame Formed between Opposing Jets of Hydrogen and Air." *Proceedings of the Twenty-Seventh Symposium (International) on Combustion*, Boulder, Colorado (1998): 587-594.

Katta, V. R., Goss, L. P., and Roquemore, W. M. "Effect of Nonunity Lewis Number and Finite-Rate Chemistry on the Dynamics of a Hydrogen-Air Jet Diffusion Flame." *Combustion and Flame* 96 (1994): 60-74.

Katta, V. R., Meyer, T. R., Gord, J. R., and Roquemore, W. M. "Insights into Non-Adiabatic-Equilibrium Temperatures During Millimeter-Size Vortex/Flame Interactions." *Combustion and Flame* 132 (2003): 639-651.

Kawabe, R., Yatsuda, O., Komiyama, M., Kinoshita, S., and Takagi, T. "Measurements of Two-dimensional Temperature, OH Concentration and Velocity in Diffusion Flames Interacted with Large Scale Vortices." *Proceedings of the 4th JSME-KSME Thermal Engineering Conference*, October 1-6, 2000, Kobe, Japan.

Kee, R. J., Rupley F. M., Miller, J. A, Coltrin, M. E., Grcar, J. F., Meeks, E., Moffat, H. K., Lutz, A. E., Dixon-Lewis, G., Smooke, M. D., Warnatz, J., Evans, G. H., Larson, R. S., Mitchell, R. E., Petzold, L. R., Reynolds, W. C., Caracotsios, M., Stewart, W. E., Glarborg, P., Wang, C., and Adigun, O. *CHEMKIN Collection, Release 3.6.* San Diego, CA: Reaction Design, Inc.,.2000.

Kelman, J. B. and Masri, A. R. "Quantitative Imaging of Temperature and OH in Turbulent Diffusion Flames by Using a Single Laser Source." *Applied Optics* 33 (1994): 3992-3999.

Kent, J. H. "A Noncatalytic Coating for Platinum-Rhodium Thermocouples." *Combustion and Flame* 14 (1970): 279-282.

Kim, J. S., and Lee, S. R. "Diffusional-thermal Instability in Strained Diffusion Flames with Unequal Lewis Numbers." *Combustion Theory and Modelling* 3 (1999): 123-146.

Kim, T. K., Park, J., and Shin, H. D. "Mixing Mechanism Near the Nozzle Exit in a Tone Excited Non-premixed Flame." *Combustion Science and Technology* 89 (1993): 83-100.

Kirkby, L. L., and Schmitz, R. A. "An analytical study of the stability of a laminar diffusion flame." *Combust. Flame* 10 (1966): 205-220.

Komiyama, M., Kawabe, R., Hayashi, A., and Takagi, T. "Extinction and Interruption of Diffusion Flame Interacted with a Large Scale Vortex Measured by Rayleigh Scattering and LIF." *Proceedings of the 6th ASME-JSME Thermal Engineering Joint Conference*, March 16-20, 1997.

Komiyama, M., Kawabe, R., Hayashi, A., Kinoshita, S., and Toshimi, T. "Measurements by Rayleigh Scattering and LIF in Diffusion Flames Interacted with Large Scale Vortices." *Proceedings of the 3rd Asia-pacific Conference on Combustion*, June 24-27, 2001, Seoul, Korea.

Kovács, I. *Rotational Structure in the Spectra of Diatomic Molecules*. New York: Americal Elsevier Publishing Co. Inc., 1969.

Law, C. K. "Dynamics of Stretched Flames." *Proceedings of the Twenty-Second Symposium (International) on Combustion*, Seattle, Washington (1988): 1381-1402.

Law, C. K., and Chung, S. H. "Steady State Diffusion Flame Structure with Lewis number Variations." *Combustion Science and Technology* 29 (1982): 129-145.

Lee, B. M., and Shin, H. D. "Differential Diffusion Effects in H_2/ N_2 Turbulent Nonpremixed Flames." *Combustion Science and Technology* 62 (1988): 311-330.

Lee, J. G., Lee, T.-W., Nye, D. A., and Santavicca, D. A. "Lewis Number Effects on Premixed Flames Interacting with Turbulent Kármán vortex sheets." *Combustion and Flame* 100 (1995): 161-168.

Lee, T.-W., Lee, J. G., Nye, D. A., and Santavicca, D. A. "Local Response and Surface properties of Premixed Flames During Interactions with Kármán vortex sheets." *Combustion and Flame* 94 (1993): 146-160.

Lengel, R. K. and Crosley, D. R. "Energy Transfer in $A^2\Sigma^+$ OH. I. Rotational." *The Journal of Chemical Physics* 67 (1977): 2085-2101.

Lengel, R. K. and Crosley, D. R. "Energy Transfer in $A^2\Sigma^+$ OH. II. Vibrational." *The Journal of Chemical Physics* 68 (1978): 5309-5324.

Lewis, G. S., Cantwell, B. J., Vandsburger, U., and Bowman, C. T. "An Investigation of the Structure of a Laminar Non-premixed Flame in an Unsteady Vortical Flow." *Proceedings of the Twenty-Second Symposium (International) on Combustion*, Seattle, Washington (1988): 515-522.

Lide, D. R., ed. *Handbook of Chemistry and Physics*. 74th ed. Boca Raton: CRC Press, 1993.

Liñán, A. "The Asymptotic Structure of Counterflow Diffusion Flames for Large Activation Energies." *Acta Astronautica* 1 (1974): 1007-1039.

Lucht, R. P., Laurendeau, N. M., and Sweeny, D. W. "Temperature Measurement by Two-Line Laser-Saturated OH Fluorescence in Flames." *Applied Optics* 21 (1982): 3729-3735.

Luque, J., and Crosley, D. R. "LIFBASE: Database and Spectral Simulation Program (Version 1.5)." SRI International Report MP 99-009 (1999).

Meier, U., Kienle, R., Plath, I., and Kohse-Höinghaus, K. "Two-Dimensional LIF Approaches for the Accurate Determination of Radical Concentrations and Temperature in Combustion." *Berichte der Bunsen-Gesellschaft - Physical Chemistry* 96 (1992): 1401-1410.

Mueller, C. J., and Schefer, R. W. "Coupling of Diffusion Flame Structure to an Unsteady Vortical Flow-Field." *Proceedings of the Twenty-Seventh Symposium (International) on Combustion*, Boulder, Colorado (1998): 1105-1112.

Nobach, H. "A Global Concept of Autocorrelation and Power Spectral Density Estimation from LDA Data Sets." *Proceedings of the 10th International Symposium on Applications of Laser Techniques to Fluid Mechanics*, July 10-13, 2000, Lisbon, Portugal.

Nobach, H. *Kern*. 28 Feb. 2003. 10 Mar. 2001 <http://www.nambis.de/programs/kern.html>.

Oyegbesan, A. O., and Algermissen, J. "Numerical Analysis of a Non-equilibrium Turbulent Free Jet Diffusion Flame." *Acta Astronautica* 3 (1976): 281-292.

Palmer, J. L. and Hanson, R. K. "Temperature Imaging in a Supersonic Free Jet of Combustion Gases with Two-Line OH Fluorescence." *Applied Optics* 35 (1996): 485-499.

Peters, N. "Laminar Diffusion Flamelet Models in Non-premixed Turbulent Combustion." *Progress in Energy and Combustion Science* 10 (1984): 319-339.

Peters, N. "Laminar Flamelet Concepts in Turbulent Combustion." *Proceedings of the Twenty-First Symposium (International) on Combustion*, Munich, Germany (1986): 1231-1250.

Pitsch, H. "Unsteady Flamelet Modeling of Differential Diffusion inTurbulent Jet Diffusion Flames." *Combustion and Flame* 123 (2000): 358-374.

Poinsot, T., Veyante, D., and Candel, S. "Quenching Processes and Premixed Turbulent Combustion Diagrams." *Journal of Fluid Mechanics* 228 (1991): 561-606.

Pollock, D. D. *Thermocouples: Theory and Properties*. Boca Raton, FL: CRC Press, Inc., 1991.

Quagliaroli, T. M., Laufer, G., Krauss, R. H., and McDaniel Jr., J. C. "Laser Selection Criteria for OH Fluorescence Measurements in Supersonic Combustion Test Facilities." *AIAA Journal* 31 (1993): 520-527.

Reisel, J. R. and Laurendeau, N. M. "Quantitative LIF Measurements of Nitric Oxide in Laminar High-Temperature Flames." *Energy and Fuels* 8 (1994): 1115-1122.

Renard, P.-H, Rolon, J. C., Thévenin, D., and Candel, S. "Wrinkling Pocket Formationand Double Premixed Flame Interaction Processes." *Proceedings of the Twenty-Seventh Symposium (International) on Combustion*, Boulder, Colorado (1998): 659-666.

Renard, P.-H., Rolon, J. C., Thévenin, D., and Candel, S. "Investigations of Heat Release, Extinction, and Time Evolution of the Flame Surface, for a Nonpremixed Flame Interacting with a Vortex." *Combustion and Flame* 117 (1999): 189-205.

Renard, P.-H., Thévenin, D., Rolon, J. C., and Candel, S. "Dynamics of Flame/Vortex Interactions." *Progress in Energy and Combustion Science* 26 (2000): 225-282.

Roberts, W. L., and Driscoll, J. F. "Laminar Vortex Interacting with a Premixed Flame: Measured Formation of Pockets of Reactants." *Combustion and Flame* 87 (1991): 245-256.

Roberts, W. L., Driscoll, J. F., Drake, M. C., and Goss, L. P. "Images of the Quenching of a Flame by a Vortex – To Quantify Regimes of Turbulent Combustion." *Combustion and Flame* 94 (1993): 58-69.

Roberts, W. L., Driscoll, J. F., Drake, M. C., and Ratcliffe, J. W. "OH Fluorescence Images of the Quenching of a Premixed Flame During an Interaction with a Vortex." *Proceedings of the Twenty-Fourth Symposium (International) on Combustion*, Sydney, Australia (1992): 169-176.

Rolon, J. C., Aguerre, F., and Candel, S. "Experiments on the Interaction Between a Vortex and a Strained Diffusion Flame." *Combustion and Flame* 100 (1995): 422-429.

Rørtveit, G. J., Hustad, J. E., Li, S.-C., and Williams, F. A. "Diluent Effects on NO_x Formation in Hydrogen Counterflow Flames." *Proceedings of the 6th International Conference on Technologies and Combustion for a Clean Environment*, Porto, Portugal, 2001.

Rylander, P. N. *Catalytic Hydrogenation over Platinum Metals*. New York: Academic Press, 1967.

Sakai, Y., Konishi, K., and Ishihara, A. "Tip Opening and Burning Intensity of Bunsen Flames Diluted with Nitrogen." *JSME International Journal, Series B* 39 (1996): 164-184.

Sanders, J. P. H., and Gokalp, I. "Nonequilibrium and differential diffusion effects in turbulent hydrogen diffusion flames." *Journal of Thermophysics and Heat Transfer* 11 (1997): 384-390.

Santoianni, D. A. "Temperature Imaging in Unsteady Propane-Air Counterflow Diffusion Flames Using Planar Laser-Induced Fluorescence of OH." Masters Thesis, North Carolina State University, 1999.

Santoianni, D. A., DeCroix, M. E., and Roberts, W. L. "Temperature Imaging in an Unsteady Propane-Air Counterflow Diffusion Flame Subjected to Low Frequency Oscillations." *Flow, Turbulence and Combustion* 66 (2001): 23-36.

Schauer, F., Hancock, R., Gogineni, S., and Lucht, R. "Vortex-Flame Interactions in Hydrogen Jet Diffusion Flames: A DPIV and DNS Investigation." *Proceedings of the Fluids Engineering Division Summer Meeting*, July 21-25, 1998, Washington, DC.

Seitzman, J. M., and Hanson, R. K. "Planar Fluorescence Imaging in Gases." *Instrumentation for Flow with Combustion*. Taylor, A. M. K. P., ed. London: Academic Press, 1993a: 405-466.

Seitzman, J. M., and Hanson, R. K. "Two-Line Planar Fluorescence for Temporally Resolved Temperature Imaging in a Reacting Supersonic Flow over a Body." *Applied Physics B* 57 (1993b): 385-391.

Seitzman, J. M., Hanson, R. K., DeBarber, P. A., and Hess, C. F. "Application of Quantitative Two-Line OH Planar Laser-Induced Fluorescence for Temporally Resolved Planar Thermometry in Reacting Flows." *Applied Optics* 33 (1994): 4000-4012.

Seitzman, J. M., Miller, M. F., Island, T. C., and Hanson, R. K. "Double-Pulse Imaging Using Simultaneous OH/Acetone PLIF for Studying the Evolution of High-Speed, Reacting Mixing Layers." *Proceedings of the Twenty-Fifth Symposium (International) on Combustion*, Irvine, California (1994): 1743-1750.

Seitzman, J. M., Üngüt, A., Paul, P. H., and Hanson, R. K. "Imaging and Characterization of OH Structures in a Turbulent Nonpremixed Flame." *Proceedings of the Twenty-Third Symposium (International) on Combustion*, Orlans, France (1990): 637-644.

Seshadri, K. and Williams, F. A. "Laminar Flow between Parallel Plates with Injection of a Reactant at High Reynolds Number." *International Journal of Heat and Mass Transfer* 21 (1978): 251-253.

Shaddix, C. R., Harrington, J. E., and Smyth, K. C. "Quantitative Measurements of Enhanced Soot production in a Flickering Methane/Air Diffusion Flame." *Combustion and Flame* 99 (1994): 723-732.

Siegel, R. and Howell, J. R. *Thermal Radiation Heat Transfer*. 4th ed. New York: Taylor & Francis, 2002.

Sivashinsky, , G. I. "Instabilities, Pattern Formation, and Turbulence in Flames." *Annual Review of Fluid Mechanics* 15 (1983): 179-199.

Sivashinsky, G. I. "Diffusional-Thermal Theory of Cellular Flames." *Combustion Science and Technology* 15 (1977): 137-146.

Schlichting, H. *Boundary Layer Theory*. 7th ed. New York: McGraw-Hill, 1979.

Smyth, K. C., Harrington, J. E., Johnsson, E. L., and Pitts, W. M. "Greatly Enhanced Soot Scattering in Flickering CH_4/Air Diffusion Flames." *Combustion and Flame* 95 (1993): 229-239.

Strawa, A. W., and Cantwell, B. J. "Investigation of an Excited Jet Diffusion Flame at Elevated Pressure." *Journal of Fluid Mechanics* 200 (1989): 309-336.

Takagi, T., and Xu, Z. "Numerical Analysis of Laminar Diffusion Flames-Effects of Preferential Diffusion of Heat and Species." *Combustion and Flame* 96 (1994): 50-59.

Takagi, T., Xu, Z., and Komiyama, M. "Preferential Diffusion Effects on the Temperature in Usual and Inverse Diffusion Flames." *Combustion and Flame* 106 (1996): 252-260.

Takagi, T., Yoshikawa, Y., Yoshida, K., Komiyama, M., and Kinoshita, S. "Studies on Strained Non-Premixed Flames Affected by Flame Curvature and Preferential Diffusion." *Proceedings of the Twenty-Sixth Symposium (International) on Combustion*, Naples, Italy (1996): 1103-1110.

Takahashi, F., and Katta, V. R. "Unsteady Extinction Mechanisms of Diffusion Flames." *Proceedings of the Twenty-Sixth Symposium (International) on Combustion*, Naples, Italy (1996): 1151-1160.

Thévenin, D., Renard, P. H., Fiechtner, G. J., Gord, J. R., and Rolon, J. C. "Regimes of Non-Premixed Combustion." *Proceedings of the Twenty-Eight Symposium (International) on Combustion*, Edinburgh, Scotland (2000): 2101-2108.

Touloukian, Y. S. and Ho, C. Y., eds. *Thermophysical Properties of Matter: Thermal Radiative Properties-Metallic Elements and Alloys*. Vol. 7. New York: Wiley, John & Sons, Inc., 1970. 13 vols.

Turns, S. R. "Understanding NO_x Formation in Nonpremixed Flames: Experiments and Modeling." *Progress in Energy and Combustion Science* 21 (1995): 361-385.

Vilimpoc, V., and Goss, L. P. "SiC-Based Thin-Filament Pyrometry: Theory and Thermal Properties." *Proceedings of the Twenty-Second Symposium (International) on Combustion*, Seattle, Washington (1988): 1907-1914.

Vincenti, W. G., and Kruger, C. H. *Introduction to Physical Gas Dynamics*. New York: John Wiley, 1965.

Vranos, A., Knight, B. A., Proscia, W. M., Chiapetta, L., and Smooke, M. D. "Nitric Oxide Formation and Differential Diffusion in a Turbulent Methane-Hydrogen Diffusion Flame." *Proceeding of the Twenty-Fourth Symposium (International) on Combustion*, Sydney, Australia (1992): 377-384.

Whiting, E. E., Paterson, J. A., Kovács, I., and Nicholls, R. W. "Computer Checking of Rotational Line Intensity Factors for Diatomic Transitions." *Journal of Molecular Spectroscopy* 47 (1973): 84-98.

Williams, F. A. "Progress in Knowledge of Flamelet Structure and Extinction." *Progress in Energy and Combustion Science* 26 (2000): 657-682.

Williams, F. A. *Combustion Theory*. 2nd ed. Menlo Park: Benjamin/Cummings, 1985.

Yoshida, K., and Takagi, T. "Transient Local Extinction and Reignition Behavior of Diffusion Flames Affected by Flame Curvature and Preferential Diffusion." *Proceedings of the Twenty-Seventh Symposium (International) on Combustion*, Naples, Italy (1998): 685-692.

Yoshida, K., and Takagi, T. "Unsteady Behavior of Locally Strained Diffusion Flames Affected by Curvature and Preferential Diffusion." *Proceedings of the 5th ASME/JSME Joint Thermal Engineering Conference*, March 15-19, 1999, San Diego, California.